



Co-combustion of diesel and gaseous
fuels with exhaust emissions analysis
and in-cylinder gas sampling

Midhat Talibi

Submitted in partial fulfilment of the requirements
for the degree of Doctor of Philosophy
at University College London,
University of London.

October 2015

I, Midhat Talibi confirm that the work presented in this thesis is my own. Where information has been derived from other sources, I confirm that this has been indicated in the thesis.

Dated: 14/10/2015

Abstract

The development of novel strategies for improved efficiency and ‘cleaner’ emissions from internal combustion engines requires new insights into the processes of energy release and in-cylinder species formation from future sustainable fuels.

This work presents an experimental investigation carried out on a compression-ignition engine to study the co-combustion of diesel fuel with various gaseous fuels, including hydrogen, methane-hydrogen mixtures, biogas and biogas-hydrogen mixtures. In addition, a novel in-cylinder gas sampling and analysis system, developed during the project, was used to extract samples from the engine cylinder during combustion of these gaseous fuels at various stages of the engine cycle, with two sampling location arrangements relative to the diesel fuel spray. Furthermore, the co-combustion of hydrogen and diesel fuel was investigated with the engine intake air boosted and simulated EGR applied.

It was found that exhaust NO_x emissions were minimal at low engine loads when in-cylinder gaseous fuel-air stoichiometry was quite lean, but increased rapidly when the combined temperatures from gaseous fuel and diesel fuel co-combustion exceeded the threshold of NO_x formation temperatures. The eventual level of exhaust particulate mass emissions was observed to be dependent on two competing factors; the aspirated gaseous fuel reduced the intake oxygen concentration resulting in increased soot formation rate, while thermal soot oxidation rates increased due to higher gaseous fuel combustion temperatures. During the early stages of combustion (10 CAD ATDC), the in-cylinder NO_x concentration was observed to be higher in the region between two sprays, relative to that within the spray core. This is attributable to a higher proportion of the aspirated gaseous fuel mixture being located between two sprays, resulting in higher gas temperatures from combustion, and hence elevated NO_x formation rates. In the later stages of combustion there was much less distinction in the concentration of species between the two sampling locations.

Acknowledgements

Firstly, I would like to acknowledge the contributions of my supervisors Dr. Ramanarayanan Balachandran and Professor Nicos Ladommatos towards the fulfilment of this work. My sincerest thanks to Dr. Balachandran for providing me with the opportunity to pursue a PhD degree at UCL, for helping me secure funding for the same and for his invaluable support and counsel throughout the years. I am immensely grateful to Prof. Ladommatos for his vision, ideas, knowledge, technical expertise, practical assistance and wise support that I have benefited from throughout the course of this project. Without his invaluable guidance, this work would not have been possible.

Thanks are also due to UCL Overseas Research Scholarships, BP Global Fuels Ltd., Cella Energy and Innovate UK for their financial contributions towards the project.

I am very grateful to all the staff and students at UCL Mechanical Engineering for their assistance and encouragement.

A special mention to all those with whom I have shared the Fuels, Engines and Combustion Laboratory at UCL. Thank you to Dr. Paul Hellier for his valuable expertise and immense help in and out of the laboratory. Thank you to Dr. (to be) Aadil Dowlut and Dr. Taaha Hussain for introducing me to the laboratory and for inclining me towards undertaking a PhD degree. Thank you to Dr. Priyesh Patel for showing me the ropes during the early days of the project. Last but not the least, thank you to Dr. Baptiste Duboc, Dr. Mart Magi, Dr. Aaron Eveleigh and Dr. (to be) Elina Koivisto for their assistance, for the long discussions on various engineering and non-engineering topics, and most of all, for making the entire experience a pleasurable one.

Finally, I am greatly indebted to my parents, Drs. Shiraz and Shama Talibi, and my sister, Ms. Farah Talibi, whose unceasing support, constant encouragement and unwavering optimism have helped me throughout and allowed me to reach where I am today. Thank you for believing in me and being patient with me.

Contents

List of Figures	9
List of Tables	17
Nomenclature	18
1 Introduction	20
1.1 Motivation.....	20
1.2 Aims and objectives	26
1.3 Structure of the thesis.....	27
2 Literature Review	29
2.1 Fundamentals of compression-ignition combustion	29
2.2 Emissions formation in compression-ignition combustion	36
2.2.1 Oxides of nitrogen (NO _x).....	36
2.2.2 Carbon monoxide	44
2.2.3 Unburned hydrocarbons	45
2.2.4 Particulates.....	47
2.3 Methods of production of hydrogen, natural gas and biogas.....	53
2.3.1 Hydrogen and natural gas	53
2.3.2 Biogas	55
2.4 Co-combustion of fuel mixtures in CI engines	58
2.4.1 Hydrogen-diesel fuel mixtures	58
2.4.2 Hydrogen-methane-diesel fuel mixtures.....	63
2.4.3 Biogas-diesel fuel mixtures	73
2.5 Engine in-cylinder gas sampling	80
2.6 Conclusions	89
2.7 Gap analysis.....	92
3 Experimental setup	94
3.1 Single-cylinder engine	95
3.2 Common rail fuel injection system.....	101
3.3 Intake air supercharger system	104

3.4	Gas delivery system	106
3.5	Exhaust and in-cylinder gas composition analysis system.....	108
3.5.1	CO and CO ₂	110
3.5.2	O ₂	113
3.5.3	Unburned THC.....	114
3.5.4	NO and NO _x	114
3.5.5	Particulates.....	116
3.6	Instrumentation and data acquisition systems	119
3.6.1	Control of diesel fuel injection pressure, timing and duration	119
3.6.2	Monitoring, control and acquisition of engine data.....	120
3.6.3	Control and monitoring of MFCs.....	125
3.6.4	Exhaust analyser data acquisition.....	127
3.7	In-cylinder gas sampling valve system.....	129
3.7.1	Sampling valve tip.....	130
3.7.2	Valve actuation system	131
3.7.3	Construction materials	136
3.7.4	Installation of the sampling valve in the engine head.....	137
3.7.5	Shape and volume of an engine in-cylinder gas sample.....	139
3.7.6	Dilution tunnel	142
3.7.7	Control and monitoring system for the sampling valve	144
3.7.8	Verification of dilution ratio results with sample bag.....	149
3.8	High pressure low volume fuel system (HPLVFS).....	151
4	Effect of hydrogen-diesel fuel co-combustion on exhaust emissions with verification using an in-cylinder gas sampling technique	164
4.1	Experimental procedure	165
4.1.1	Experimental set 1: Exhaust emission tests	165
4.1.2	Experimental set 2: In-cylinder gas sampling tests	167
4.2	Results and Discussion.....	170
4.2.1	Combustion characteristics.....	170
4.2.2	Gaseous emissions of CO, THC and CO ₂	174
4.2.3	NO _x emissions	177

4.2.4	Nitrogen dilution experiments.....	182
4.2.5	Particulate emissions.....	185
4.2.6	In-cylinder gas sample analysis.....	191
4.3	Conclusions.....	198
5	Influence of methane-hydrogen mixtures on combustion and emission characteristics, and in-cylinder gas composition	201
5.1	Experimental procedure.....	202
5.1.1	Experimental set 1: Exhaust emission tests (using CH ₄ -H ₂ mixtures).....	203
5.1.2	Experimental set 2: In-cylinder gas sampling tests (using CH ₄ -H ₂ mixtures).....	207
5.1.3	Experimental set 3: In-cylinder gas sampling tests (using CH ₄).....	209
5.2	Results and discussion.....	211
5.2.1	Combustion characteristics.....	211
5.2.2	CO ₂ , CO and unburned THC exhaust gas emissions.....	216
5.2.3	NO _x exhaust gas emissions.....	218
5.2.4	Particulate exhaust emissions.....	221
5.2.5	In-cylinder gas sample composition (using CH ₄ only - Experimental set 3).....	226
5.2.6	In-cylinder gas sample composition (using CH ₄ -H ₂ mixtures).....	235
5.3	Conclusions.....	243
6	Experimental investigation on the combustion and exhaust emission characteristics, and in-cylinder gas composition, of hydrogen enriched biogas mixtures in a diesel engine	246
6.1	Experimental procedure.....	247
6.1.1	Experimental set 1: Exhaust emission tests (using CH ₄ -CO ₂ -H ₂ mixtures).....	247
6.1.2	Experimental set 2: In-cylinder gas sampling tests (using CH ₄ -CO ₂ -H ₂ mixtures).....	251
6.1.3	Experimental set 3: Exhaust emissions from real biogas.....	255
6.2	Results and discussion.....	257
6.2.1	Combustion characteristics.....	257

6.2.2	CO ₂ , CO and unburned THC exhaust gas emissions	263
6.2.3	NO _x exhaust gas emissions	266
6.2.4	Particulate exhaust emissions.....	270
6.2.5	In-cylinder gas sample composition.....	274
6.2.6	Exhaust emissions from real biogas.....	280
6.3	Conclusions	283
7	The influence of hydrogen-diesel co-combustion on an EGR applied, intake air boosted CI engine	286
7.1	Experimental procedure	287
7.2	Results and Discussion.....	292
7.2.1	Combustion characteristics.....	292
7.2.2	Exhaust gas emissions	296
7.2.3	Optimum H ₂ operating window based on exhaust gas emissions results	307
7.3	Conclusions	309
8	Conclusions and recommendations for future work	311
8.1	Conclusions and summary	311
8.1.1	Literature review	311
8.1.2	Co-combustion of hydrogen and diesel fuel.....	312
8.1.3	Co-combustion of CH ₄ -H ₂ mixtures with diesel fuel.....	314
8.1.4	Co-combustion of CH ₄ -CO ₂ -H ₂ mixtures (simulating H ₂ enriched biogas) with diesel fuel	316
8.1.5	Summary of conclusions	317
8.2	Claims of originality.....	320
8.3	Recommendations for future work.....	323
	Appendix A	324
	Appendix B	325
	Appendix C	336
	Appendix D	344
	References	353

List of Figures

Figure 1.1: Progressive reduction in the pollutant emission limits from diesel engine exhausts based on the European emission standards.....	23
Figure 2.1: Diesel conceptual model describing fuel mixing and combustion, up to the end of injection (Dec 1997; Musculus et al. 2012)	32
Figure 2.2: Typical heat release rate (J/deg) curve of a DI compression-ignition engine showing the different phases of combustion (SOI-start of fuel injection, EOI-end of fuel injection) (Heywood 1988).....	33
Figure 2.3: Schematic showing the sequential pathway of soot formation from gas/liquid phase to agglomerated solid particles (Tree & Svensson 2007)	47
Figure 2.4: Typical size distribution of particulates from diesel engine exhaust (Kittelson 1998)	51
Figure 3.1: Schematic showing a section through the cylinder head and crankcase of the research engine (Schönborn 2009)	98
Figure 3.2: 58x wheel and shaft encoder mounted on the front end of the crankshaft	99
Figure 3.3: The lubricating oil and coolant system of the research engine (Ricardo 1986)	100
Figure 3.4: Schematic of the common-rail fuel delivery system, including the heat exchanger	102
Figure 3.5: Servo-hydraulic solenoid-injector; (1) Fuel return, (2) Solenoid coil, (3) Solenoid armature, (4) Valve ball, (5) Valve control chamber, (6) Nozzle needle pressure shoulder, (7) Injector nozzle holes, (8) Outlet restrictor, (9) High pressure port, (10) Inlet restrictor, (11) Valve plunger (Bosch 2004)	103
Figure 3.6: Schematic of the intake air supercharger system (air boost system) mounted on the single cylinder engine.....	104
Figure 3.7: Schematic of the gas delivery system, and subsequent aspiration with the engine intake air	106
Figure 3.8: Horiba MEXA 9100 HEGR main analyser rack	110
Figure 3.9: Schematic demonstrating the operating principle of the NDIR CO and CO ₂ analyser (Horiba Instruments 1984)	111
Figure 3.10: Schematic demonstrating the operating principle of the magneto-pneumatic O ₂ analyser (Horiba Instruments 1984).....	113
Figure 3.11: Schematic showing the flow of sample through the DMS500 (Cambustion 2011).....	117
Figure 3.12: Classifier column of the DMS500 (Cambustion 2011)	118
Figure 3.13: Screenshot of the fuel injection control program, Emtronix EC-Lab	119

Figure 3.14: Screenshot of NI LabVIEW program showing pressure traces and other engine parameters	123
Figure 3.16: Screenshot of NI LabVIEW program showing heat release trace other combustion characteristics	124
Figure 3.16: Screenshot of NI LabVIEW program showing the various temperature readings as well as the PID controls for the proportional solenoid valves	124
Figure 3.17: Screenshot of the MFC control and monitoring NI LabVIEW program	126
Figure 3.18: Screenshot of the NI LabVIEW emissions monitoring program	127
Figure 3.19: Screenshot of the Cambustion DMS500 particle spectrometer PC interface program	128
Figure 3.20: Simplified diagram of the in-cylinder sampling valve showing the gas flow from within the cylinder to the sample outlet port.....	130
Figure 3.21: Valve lift duration and gas flow rate through the valve of the gas sampling valve at 10Hz operating frequency and 40 bar air pressure on the valve face	136
Figure 3.22: Schematic showing (a) plan view and (b) cross-sectional side view of the relative locations of the injector, the sampling valve at maximum in-cylinder penetration and the piston at TDC	137
Figure 3.23: Actual sample volume shape at inlet of a poppet-type sampling valve (Zhao & Ladommatos 2001)	139
Figure 3.24: Schematic of the heated dilution tunnel with the various gas access points (Length of tunnel – 950 mm, Diameter of tunnel – 28 mm)..	143
Figure 3.25: Screenshot of the NI LabVIEW program to control solenoid valves installed on dilution tunnel	144
Figure 3.26: Crank angle resolved supply voltage and valve lift trace. A – poppet valve opening time delay, B – valve sampling duration	147
Figure 3.27: Control and monitoring system of the sampling valve.....	148
Figure 3.28: Comparison of in-cylinder gas sample composition obtained using the dilution tunnel and sample bag, as well as exhaust emissions for (a) CO ₂ , (b) CO and (c) NO _x	149
Figure 3.29: Schematic showing fuel flow in the high pressure low volume fuel system	154
Figure 3.30: Cross-sectional (a) front view and (b) side view of the assembly of the high pressure fuel system	155
Figure 3.31: Isometric view of (a) custom designed port connectors and (b) two-part high pressure in-line fuel filter housing	160
Figure 3.32: Cross-sectional view of the fuel system with the special cap showing (a) piston position with the top O-ring exposed and (b) piston completely removed from the main cylinder	163

Figure 4.1: (a) Percentage energy from H ₂ and (b) concentration of H ₂ in the intake air at various engine loads and fixed diesel injection periods	166
Figure 4.2: Schematic showing (a) sampling arrangement one and (b) sampling arrangement two relative to the diesel fuel sprays; changes to the position of the spray relative to the valve location was achieved by rotating the fuel injector	169
Figure 4.3: (a) Heat release rate curves and combustion characteristics (b) duration of ignition delay, (c) apparent net peak heat release rates (J/deg) and (d) indicated thermal efficiency of the engine at various engine loads and H ₂ -diesel fuel proportions	170
Figure 4.4: Variation in exhaust emissions of (a) carbon monoxide (CO), (b) unburned total hydrocarbons (THC) and (c) carbon dioxide (CO ₂) at various engine loads and H ₂ -diesel fuel proportions	174
Figure 4.5: Variation in (a) exhaust emissions of nitrogen oxides (NO _x) and (b) adiabatic flame temperatures at various engine loads and H ₂ -diesel fuel proportions. The temperatures were calculated using GASEQ software at an initial pressure of 40 bar and initial temperature of 600 K	177
Figure 4.6: Exhaust emissions of nitrogen oxides (NO _x) at constant engine loads and variable H ₂ -air equivalence ratio (ϕ_{H_2})	180
Figure 4.7: Exhaust emissions of NO _x at constant engine loads and varying percentage reduction in intake O ₂ due to the aspirated H ₂ or N ₂ (assuming 21% O ₂ in ambient air)	182
Figure 4.8: Variation in exhaust emissions of total particulate mass ($\mu\text{g}/\text{cc}$) at various engine loads and H ₂ -diesel fuel proportions	185
Figure 4.9: Comparison of the percentage reduction in total particulate mass with percentage reduction in the carbon content of the combustible mixture at constant engine loads	187
Figure 4.10: Exhaust NO _x emissions against PM emissions at constant engine loads with varying proportions of H ₂ and diesel fuel	189
Figure 4.11: Measurement of (a) in-cylinder unburned total hydrocarbon (THC) concentration, (b) total particulate mass (TPM), (c) carbon dioxide (CO ₂) concentration and (d) nitrogen oxide (NO _x) concentration in gas samples collected at (i) 10 CAD, (ii) 25 CAD and (iii) 40 CAD ATDC at fixed diesel with increasing amounts of H ₂ and variable engine loads (engine speed 1200 rpm) with two sampling arrangements (Figure 4.2)	191
Figure 5.1: Percentage energy from H ₂ for (a) 0 bar and (b) 1.5 bar pilot diesel fuel IMEP, at various engine loads (IMEP) and CH ₄ -H ₂ mixture ratios	205
Figure 5.2: Schematic showing (a) sampling arrangement one and (b) sampling arrangement two relative to the diesel fuel sprays; changes to the	

position of the spray relative to the valve location was achieved by rotating the fuel injector	208
Figure 5.3: Heat release rate curves for a fixed engine load of 4 bar IMEP, for the two pilot diesel fuel IMEPs of 0 and 1.5 bar and two CH ₄ -H ₂ mixture proportions	211
Figure 5.4: Combustion characteristics (a) and (b) duration of ignition delay, and (c) and (d) peak heat release rates for the two pilot diesel fuel IMEPs of 0 and 1.5 bar, and at various engine loads and CH ₄ -H ₂ mixture proportions	213
Figure 5.5: Variation in the exhaust emissions of (a) carbon dioxide (CO ₂), (b) unburned total hydrocarbons (THC) and (c) carbon monoxide (CO) for the two pilot diesel fuel IMEPs, at various engine loads and CH ₄ -H ₂ mixture proportions	216
Figure 5.6: Variation in the exhaust emissions of oxides of nitrogen (NO _x) for the two pilot diesel fuel IMEPs, at various engine loads and CH ₄ -H ₂ mixture proportions	218
Figure 5.7: Exhaust emissions of total particulate mass for the two pilot diesel fuel IMEPs, at various engine loads and CH ₄ -H ₂ mixture proportions	221
Figure 5.8: Comparison of percentage reduction in total particulate mass with percentage reduction in the carbon content of the combustible mixture at constant engine loads and for a fixed pilot diesel fuel IMEP of 1.5 bar	223
Figure 5.9: Measurement of in-cylinder (a) carbon dioxide (CO ₂) concentration, (b) unburned total hydrocarbon (THC) concentration, (c) nitrogen oxide (NO _x) concentration and (d) total particulate mass (PM) in gas samples collected at (i) 10 CAD, (ii) 25 CAD and (iii) 40 CAD ATDC at fixed pilot diesel fuel IMEP of 1.5 bar with increasing amounts of H ₂ or CH ₄ and variable engine loads with two sampling arrangements (Figure 5.2)	226
Figure 5.10: Measurement of carbon dioxide (CO ₂) concentration in in-cylinder gas samples collected between -20 and 100 CAD ATDC with two sampling arrangements (Figure 5.2), at a fixed pilot diesel fuel IMEP of 1.5 bar, two different CH ₄ -H ₂ mixture proportions and an overall engine load of 4 bar IMEP	235
Figure 5.11: Measurement of carbon monoxide (CO) concentration in in-cylinder gas samples collected between -20 and 100 CAD ATDC with two sampling arrangements (Figure 5.2), at a fixed pilot diesel fuel IMEP of 1.5 bar, two different CH ₄ -H ₂ mixture proportions and an overall engine load of 4 bar IMEP	237
Figure 5.12: Measurement of unburned hydrocarbon (THC) concentration in in-cylinder gas samples collected between -20 and 100 CAD ATDC with	

two sampling arrangements (Figure 5.2), at a fixed pilot diesel fuel IMEP of 1.5 bar, two different CH ₄ -H ₂ mixture proportions and an overall engine load of 4 bar IMEP	238
Figure 5.13: Measurement of oxides of nitrogen (NO _x) concentration in in-cylinder gas samples collected between -20 and 100 CAD ATDC with two sampling arrangements (Figure 5.2), at a fixed pilot diesel fuel IMEP of 1.5 bar, two different CH ₄ -H ₂ mixture proportions and an overall engine load of 4 bar IMEP	240
Figure 6.1: Percentage energy supplied to the engine from the different CH ₄ -CO ₂ and CH ₄ -CO ₂ -H ₂ mixtures for (a) 0 bar and (b) 1.5 bar pilot diesel IMEP, at various engine loads (IMEP)	251
Figure 6.2: Schematic showing (a) sampling arrangement one and (b) sampling arrangement two relative to the diesel fuel sprays; changes to the position of the spray relative to the valve location was achieved by rotating the fuel injector	254
Figure 6.3: Schematic of the Sistema Biobolsa biodigester system, including feed stocks and use of outputs (Biobolsa 2015)	255
Figure 6.4: Heat release rate curves for an engine load of 4 bar IMEP, for a pilot diesel fuel IMEP of 0 bar and various CH ₄ -CO ₂ -H ₂ mixture proportions (v/v)	257
Figure 6.5: Combustion characteristics for the two pilot diesel fuel IMEPs of 0 and 1.5 bar, at various engine loads and CH ₄ -CO ₂ -H ₂ mixture proportions: (a) and (b) duration of ignition delay; (c) and (d) time of peak heat release rate; (e) and (f) peak heat release rates	259
Figure 6.6: Variation in the exhaust emissions of (a) carbon dioxide (CO ₂), (b) carbon monoxide (CO) and (c) unburned total hydrocarbons (THC) for the two pilot diesel fuel IMEPs, at various engine loads and CH ₄ -CO ₂ -H ₂ mixture proportions	263
Figure 6.7: Variation in the exhaust emissions of oxides of nitrogen (NO _x) for the two pilot diesel fuel IMEPs, at various engine loads and CH ₄ -CO ₂ -H ₂ mixture proportions	266
Figure 6.8: Exhaust emissions of total particulate mass for the two pilot diesel fuel IMEPs, at various engine loads and CH ₄ -CO ₂ -H ₂ mixture proportions	270
Figure 6.9: Comparison of percentage reduction in total particulate mass with percentage reduction in the CH ₄ content (fuel carbon) of the combustible mixture at constant engine loads and for a fixed pilot diesel IMEP of 0 bar.	272
Figure 6.10: Measurement of in-cylinder carbon dioxide (CO ₂) concentration for (a) 60CH ₄ :40CO ₂ and (b) 60CH ₄ :40CO ₂ + 15% H ₂ mixtures in gas samples collected at (i) 10 CAD, (ii) 25 CAD and (iii) 40 CAD ATDC at a fixed	

pilot diesel fuel IMEP of 1.5 bar with increasing amounts of CH ₄ -CO ₂ -H ₂ mixtures and variable engine loads with two sampling arrangements (Figure 6.2)	274
Figure 6.11: Measurement of in-cylinder unburned total hydrocarbon (THC) concentration for (a) 60CH ₄ :40CO ₂ and (b) 60CH ₄ :40CO ₂ + 15% H ₂ mixtures in gas samples collected at (i) 10 CAD, (ii) 25 CAD and (iii) 40 CAD ATDC at a fixed pilot diesel fuel IMEP of 1.5 bar with increasing amounts of CH ₄ -CO ₂ -H ₂ mixtures and variable engine loads with two sampling arrangements (Figure 6.2)	276
Figure 6.12: Measurement of in-cylinder nitrogen oxide (NO _x) concentration for (a) 60CH ₄ :40CO ₂ and (b) 60CH ₄ :40CO ₂ + 15% H ₂ mixtures in gas samples collected at (i) 10 CAD, (ii) 25 CAD and (iii) 40 CAD ATDC at a fixed pilot diesel IMEP of 1.5 bar with increasing amounts of CH ₄ -CO ₂ -H ₂ mixtures and variable engine loads with two sampling arrangements (Figure 6.2)	277
Figure 6.13: Exhaust emissions of (a) CO ₂ , (b) CO, (c) unburned THC, (d) particulates and (e) NO _x for two real biogas samples for a fixed flow rate of biogas to the engine and various engine loads. For comparison, the exhaust emissions from diesel fuel only engine operation (no biogas addition) are also shown.	280
Figure 7.1: H ₂ flow rates (l/min) and (b) power content of H ₂ (kW) at constant engine loads and varying percentage energy from H ₂	290
Figure 7.2: Duration of ignition delay for three intake air boost-engine load combinations, at constant percentage reductions in intake O ₂ and varying percentage energy from H ₂	292
Figure 7.3: Peak heat release rates (J/deg) for three intake air boost-engine load combinations, at constant percentage reductions in intake O ₂ and varying percentage energy from H ₂	294
Figure 7.4: Specific emissions of carbon dioxide (CO ₂) for three intake air boost-engine load combinations, at constant percentage reductions in intake O ₂ and varying percentage energy from H ₂	296
Figure 7.5: Specific emissions of unburned total hydrocarbons (THC) for three intake air boost-engine load combinations, at constant percentage reductions in intake O ₂ and varying percentage energy from H ₂	297
Figure 7.6: Specific emissions of oxides of nitrogen (NO _x) for three intake air boost-engine load combinations, at constant percentage reductions in intake O ₂ and varying percentage energy from H ₂	299
Figure 7.7: Specific emissions of total particulate mass for three intake air boost-engine load combinations, at constant percentage reductions in intake O ₂ and varying percentage energy from H ₂	301

Figure 7.8: Particulate number distribution for 1.33 bar intake air pressure – 8.5 bar IMEP engine load, at various percentage reduction in intake O ₂ and varying percentage energy from H ₂	303
Figure 7.9: Particulate number distribution for 1.67 bar intake air pressure – 10 bar IMEP engine load, at various percentage reduction in intake O ₂ and varying percentage energy from H ₂	303
Figure 7.10: Particulate number distribution for 1.99 bar intake air pressure – 11.5 bar IMEP engine load, at various percentage reduction in intake O ₂ and varying percentage energy from H ₂	304
Figure 7.11: Typical size distribution of diesel exhaust particulates (Kittelson et al. 2002)	304
Figure 7.12: Specific emissions of NO _x and total particulate mass (TPM) for constant intake air pressure - engine load combinations and varying % energy from H ₂ , at an intake O ₂ reduction level of 1%.	308
Figure 7.13: Specific emissions of NO _x and CO ₂ for constant intake air pressure - engine load combinations and varying % energy from H ₂ , at an intake O ₂ reduction level of 1%.	308
Figure A.1: Diesel fuel flow rate (ml/min) at different engine load (bar IMEP) for a single cylinder, half-litre engine at an engine speed of 1200 rpm ..	324
Figure B.1: Typical net heat release rate (J/deg) from diesel fuel combustion, showing the start of combustion (SOC) as the point (in CAD) when the heat release first becomes positive after fuel burning	330
Figure C.1: One of the two intake valves on the 1 st cylinder of the engine head replaced by a dummy valve with threaded hole for the sampling valve	336
Figure C.2: Tip of the gas sampling valve protruding through the dummy valve in the cylinder head.....	336
Figure C.3: A small part at the edge of the piston bowl (of diameter 15 mm and depth 10 mm) was removed to prevent the sampling valve tip from hitting the piston	337
Figure C.4: Heated dilution tunnel (insulated) with various electromagnetic solenoid valves to control gas flows in and out of the tunnel	337
Figure C.5: The gas sampling valve mounted on the engine cylinder head. A bracket was used to reduce the stress on the long valve stem due to engine vibrations	338
Figure C.6: The amplifier electronics box and power supply for the LVDT proximity sensor mounted on the gas sampling valve	338
Figure C.7: Adjustable power supply for the electromagnetic actuation system of the gas sampling valve	339

Figure C.8: Kistler charge amplifier (type 5018) for use in conjunction with the piezoelectric transducer mounted on the engine head to measure in-cylinder gas pressure	339
Figure C.9: Bronkhorst EL-Flow thermal mass flow controllers which precisely meter the amount of gas being supplied to the engine	340
Figure C.10: Positive displacement air flow meter (Romet G65) to measure the volumetric flow rate of intake air being supplied to the engine.....	340
Figure C.11: Intake air boot system including the electric motor, supercharger and charge air cooler (which is a heat exchanger for maintaining intake air temperature)	341
Figure C.12: Potentiometer controller to control the speed of the electric motor, which drives the supercharger in the intake air boost system	341
Figure C.13: Single cylinder, compression-ignition engine assembly	342
Figure C.14: Emtronix electronic engine control unit and heated tunnel PID control box	342
Figure C.15: Exhaust gas emissions analyser rack (Horiba MEXA-9100HEGR)	343
Figure C.16: Particulate spectrometer (Cambustion DMS500)	343
Figure C.17: Engine dynamometer speed, and oil and coolant level and temperature control unit	343
Figure D.1: Certificate of analysis for the fossil diesel fuel used in the experiments presented in this thesis (page 1 of 2)	344
Figure D.2: Certificate of analysis for the fossil diesel fuel used in the experiments presented in this thesis (page 2 of 2)	345
Figure D.3: Calibration certificate for the Kaman 1U1 proximity sensor mounted on the in-cylinder gas sampling valve	346
Figure D.4: Calibration certificate for the Kistler piezoelectric pressure transducer mounted on the cylinder head to measure in-cylinder gas pressure .	347
Figure D.5: Calibration certificate for the damping vessel which is part of the intake air system.....	348
Figure D.6: Thermal mass flow controller 1 calibration certificate for H ₂	349
Figure D.7: Thermal mass flow controller 2 calibration certificate for CO ₂ (page 1 of 2).....	350
Figure D.8: Thermal mass flow controller 2 calibration certificate for N ₂ (page 2 of 2)	351
Figure D.9: Thermal mass flow controller 3 calibration certificate for CO ₂	352

List of Tables

Table 3.1: Single cylinder engine specifications.....	97
Table 3.2: Estimates of the gas sample flow rates and volumes for different sampling conditions at an engine speed of 1200 rpm	140
Table 3.3: Standard deviation (st.dev.) in the valve opening and closing instants (CAD) at different valve operating parameters.....	148
Table 4.1: Test parameters used in the exhaust emission experiments.....	166
Table 4.2: Diesel fuel only engine loads (IMEP) and the corresponding diesel fuel injection periods (μ s).....	166
Table 4.3: Gaseous sample extraction time CAD ATDC during the engine cycle and the corresponding sampling window in CAD.....	169
Table 5.1: Test parameter matrix for the exhaust emission experiments	206
Table 5.2: Properties of diesel fuel, hydrogen and methane at 1 atm and 300 K (Karim 2003; Saravanan & Nagarajan 2008a; Chong & Hochgreb 2011)	206
Table 5.3: In-cylinder gas sample extraction timings in CAD ATDC during the engine cycle and the corresponding sampling windows in CAD	210
Table 6.1: Test parameter matrix for the exhaust emission experiments	250
Table 6.2: Important properties of diesel fuel, CH ₄ , CO ₂ and H ₂ at 1 atm and 300 K (Karim 2003; Saravanan & Nagarajan 2008a)	251
Table 6.3: In-cylinder gas sample extraction timings in CAD ATDC during the engine cycle and the corresponding sampling windows in CAD	254
Table 6.4: Test parameter matrix for biogas-diesel fuel co-combustion tests (*the balance was assumed to be made up of inert components)	256
Table 7.1: Combined EGR and intake air boost test operating condition matrix showing different intake air boost/ engine load combinations (and corresponding power developed by the engine in kW) at various EGR ratios and engine speed 1200 rpm.....	289
Table 7.2: Properties of diesel fuel and hydrogen at 1 atm and 300 K (Karim 2003; Saravanan & Nagarajan 2008a)	290

Nomenclature

ATDC	after-top-dead-centre
atm	standard atmosphere
BTDC	before-top-dead-centre
CAD	crank angle degree
cc	cubic centimetre
CFD	computational fluid dynamics
CH ₄	methane
CI	compression ignition
CO	carbon monoxide
CO ₂	carbon dioxide
DAQ	data acquisition
D _p	Particle diameter
EGR	exhaust gas recirculation
FID	flame ionization detector
H ₂	hydrogen
HO ₂	hydroperoxyl
HPLVFS	high pressure low volume fuel system
IMEP	indicated mean effective pressures
MFC	mass flow controller
N ₂	nitrogen
NO	nitric oxide
NO ₂	nitrogen dioxide

NO _x	nitrogen oxides
O ₂	oxygen
OH	hydroxyl
PID	proportional integral derivative
PM	particulate mass
ppm	parts per million
ppr	pulses per revolution
rpm	revolutions per minute
SI	spark ignition
SOC	start of combustion
SOI	start of injection
TDC	top-dead-centre
THC	total hydrocarbons
TPM	total particulate mass
Φ_{CH_4}	methane-air equivalence ratio
Φ_{D}	diesel-air equivalence ratio
Φ_{H_2}	hydrogen-air equivalence ratio

1 Introduction

1.1 Motivation

Since the inception of the internal combustion engine during the late 19th century, improvements in durability, reliability and increased power output capability had been the primary focus of the evolution of engine design and technology. However, in the last few decades the spotlight has shifted towards not only optimising the engine in-cylinder reactions to utilise fuel more efficiently, but also producing ‘cleaner’ exhaust emissions. The need for greater fuel efficiency was bolstered during the Arab oil embargoes in the mid-1970s which saw an almost 300% increase in the price of crude oil. Additionally, population-based epidemiological studies have shown that long-term exposure to high levels of air pollutants can cause a range of adverse effects including exacerbation of asthma, interference with lung function, increase in respiratory and cardiovascular complications and increased risk of

mortality (COMEAP 1998; COMEAP 2001; WHO 2006). A recent report by Public Health England estimated the fraction of mortality attributable to current levels of anthropogenic particulate matter air pollution from around 2.5% in the rural areas of Scotland to over 8% in some of the most polluted boroughs of London (Gowers et al. 2014). Studies also suggest that atmospheric fine particulate matter of aerodynamic diameters less than 10 μm (PM10) and 2.5 μm (PM2.5) are associated with the incidence of lung cancer (Pope et al. 2002; Raaschou-Nielsen et al. 2013). In 2013, an assessment conducted by the European Study of Cohorts for Air Pollution Effects (ESCAPE) involving nine European countries showed that lung cancer rate rose by 22% for every increase of 10 $\mu\text{g}/\text{m}^3$ of PM10, while for the smaller PM2.5 the increase was 36% per 10 $\mu\text{g}/\text{m}^3$, as they can penetrate deeper into the lungs (Raaschou-Nielsen et al. 2013). Furthermore, the concentration of atmospheric CO_2 , which is a greenhouse gas and a by-product of fossil fuel combustion, has risen steeply recent times; atmospheric CO_2 levels have risen by 36% in the last 250 years, with half of that rise occurring only in the last three decades (Somerville et al. 2007). According to a report by the UK Department of Climate and Energy Change, published in 2015, CO_2 accounted for 82% of the total UK greenhouse gas emissions in 2013 (DECC 2015). This has resulted in the increased accumulation of the CO_2 in the atmosphere resulting in an alarming rise in global warming.

Therefore, concerns over hazardous health effects of fossil fuel by-products, poor air quality and greenhouse gas emissions have resulted in the imposition of stringent legal limits around the world on pollutant emissions from internal combustion engines. This legislation, addressing environmental concerns, is designed to reduce the exhaust emissions of toxic pollutants. As an example, compression ignition engines have become increasingly popular due to their higher thermal efficiencies and relatively stable combustion characteristics; however, at the same time, they suffer from drawbacks of undesirably high emissions of nitrogen oxides (NO_x) and particulate matter (PM) (Tsolakis & Hernandez 2005). As a result, the current European emission regulations (Euro 6) impose substantial reductions in the permitted levels of NO_x and PM exhaust emissions from diesel vehicles, as compared to previous emission standards (Figure 1.1). Furthermore, the commitment to increase the amount of renewable fuels used for transportation to 10% by 2020 (European Parliament 2009) has pressed the need to find suitable long-term replacements for conventional fossil fuels, and has raised interest in the research and development of sustainable and cleaner burning fuels for internal combustion engines.

Hydrogen (H₂) has long been recognized as a potential ‘green’ fuel for internal combustion engines as it does not produce any carbon emissions (such as CO, CO₂ and soot) from combustion. This makes H₂ an excellent candidate as a renewable fuel resource in terms of helping to meet the strict emission controls and potentially

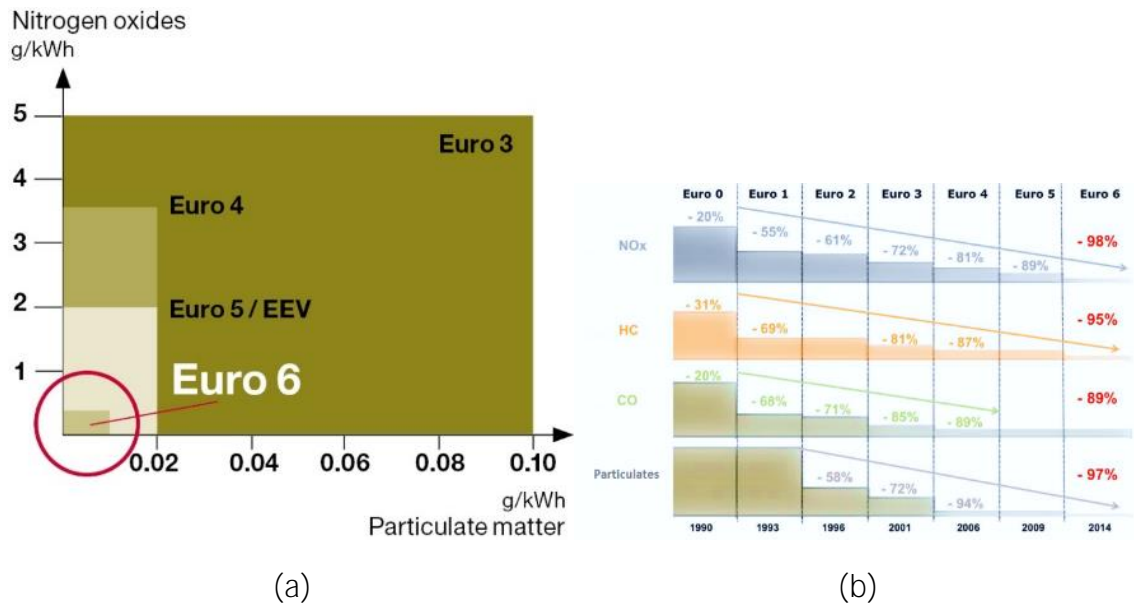


Figure 1.1: Progressive reduction in the pollutant emission limits from diesel engine exhausts based on the European emission standards

reduce the demand for conventional fossil fuels. However, the viability of H_2 as a fuel is critically dependent on a number of other factors including its production, storage, portability, transport and purity. Karim (2003) and Klell et al. (2012) have discussed all these factors in detail in his review on the limitations associated with the widespread application of H_2 as a fuel resource. Since H_2 does not occur in its free state naturally, it has to be produced from various sources which requires both energy and financial resources. H_2 of sufficiently high purity can be produced through the electrolysis of water, and if the electric energy used for this process is generated from thermal power stations which burn fossil fuels, the overall efficiency of H_2 production becomes lower than 35%. The power station also produces CO_2 when burning fossil fuels, and therefore, such use of H_2 , for example in cities, merely displaces the CO_2 emissions from cities to power stations. The storage and portability of adequate quantities of H_2 for practical applications presents another

barrier yet to be overcome. H_2 can be stored as a compressed gas in cylinders at extremely high pressures, however this would add to the total weight and bulkiness of the fuel supply system. In addition, the cost of compressing H_2 to such high pressures could potentially make the entire process economically unfeasible. Other mechanisms of transporting H_2 include using various metal hydrides which allow the controlled release of H_2 , trapping H_2 within special alloys of certain metals (palladium-copper) or carrying it as a cryogenic liquid; all these technologies are still at various phases of development and could potentially increase the availability of H_2 as a fuel in internal combustion engines in the near future (Karim 2003).

Hydrogen fuel cell vehicles have been gaining widespread attention in recent times due to recent advances in fuel cell technology combined with their potential to reduce our dependence on fossil fuels and substantially decrease pollutant emissions (Zamel & Li 2006; Schafer et al. 2006). Studies comparing the energy use and exhaust pollutant emissions of IC engine vehicles and hydrogen fuel cell vehicles over their entire life-cycle show lower energy consumption and reduced pollutant emissions in the case of fuel cell vehicles (Zamel & Li 2006). However a lot of issues have to be addressed before fuel cell vehicles can achieve significant penetration into the existing vehicle market which include reduction in initial cost, political motivation, infrastructure for the supply of hydrogen of sufficient purity, technological limitations, etc. (Weiss et al. 2000; Kreith & West 2004). Therefore, a short- and long-term strategy for reducing fossil fuel dependence and emissions

should include both the improvement of IC engines and the simultaneous research and development of hydrogen fuel cells (Schafer et al. 2006).

The key to exploring novel strategies for improved efficiency and reduced pollutant emissions lies in comprehensively understanding the processes taking place in the engine combustion chamber. The measurement of exhaust emissions provides important information about the combustion characteristics of the fuel being combusted, but additional knowledge of the in-cylinder species being formed and their reaction mechanisms has also become essential for the development of future combustion systems.

1.2 Aims and objectives

The overarching aim of the project was to gain a comprehensive understanding of the combustion and emission characteristics of various sustainable gaseous fuels in a compression ignition engine, with a particular focus on the variations in in-cylinder gas composition as the combustion process progressed. To that end, the specific objectives of the project may be described as follows:

- The development and commissioning of a novel in-cylinder gas sampling system, consisting of a timed, high-speed gas sampling valve and a heated dilution tunnel; and the deployment of the system in a single cylinder research engine.
- The development of a control and monitoring system that allowed gas samples to be extracted from the engine cylinder during combustion, at selected discrete sampling windows, at any desired crank angle in the engine cycle.
- An experimental investigation of H₂-diesel fuel co-combustion in (a) a naturally aspirated diesel engine and (b) with the diesel engine intake air boosted and simulated EGR applied; for these tests the H₂ supply to the engine was varied from low levels to predominantly H₂ combustion.
- The study of the synergy between methane and hydrogen by supplying CH₄-H₂ blends to the engine and assessing heat release rates, ignition delay periods, exhaust pollutant emissions and the temporal evolution of in-cylinder species.

- The effect of combusting hydrogen enriched biogas in a diesel engine to determine whether the absorption of thermal energy by the inert carbon dioxide (CO_2) in the biogas could be countered by the addition of H_2 to the biogas.

1.3 Structure of the thesis

The thesis is divided into nine chapters, which may be summarised as follows:

Chapter 2 is a review of the technical literature pertaining to the various subjects investigated in this thesis. The initial sections of the review provide fundamental details of the compression-ignition combustion process and the reaction mechanisms involved in the formation processes of the regulated diesel engine pollutants. The later sections examine past research on using various gaseous fuels in diesel engines and explore published work on in-cylinder gas sampling techniques.

Chapter 3 provides a description of the various experimental apparatus and systems used during this project. These comprise of the single cylinder research diesel engine and its fuel injection system, the air super charging system, the intake gas delivery system, the exhaust gas analysing systems, the instrumentation and data acquisition systems and, importantly, the in-cylinder gas sampling and analysis system developed during the project.

Chapter 4 describes the methods of mathematical analysis carried out on the experimental data in order to extract, from the recorded data, further information regarding in-cylinder combustion behaviour.

Chapter 5 presents an experimental investigation of hydrogen-diesel fuel co-combustion carried out on the diesel engine when running in naturally aspirated mode.

Chapter 6 describes the experiments conducted using CH₄-H₂ mixtures of various proportions, with two different pilot ignition diesel fuel flow rates.

Chapter 7 describes the experimental study carried out using a variety of simulated biogas and hydrogen-enriched biogas mixtures, with two different pilot ignition diesel fuel flow rates.

Chapters 5, 6 and 7 also include a substantial amount of results acquired with the in-cylinder gas sampling system which allowed greater insights to be obtained into the temporal and spatial development of the combustion process.

Chapter 8 describes a study of H₂-diesel fuel co-combustion with the diesel engine intake air boosted and simulated EGR applied.

Chapter 9 provides a summary of the conducted research work whilst outlining the main conclusions. Additionally, the novel aspects of this research, the academic publications produced from this work and some recommendations for future work are also presented.

2 Literature Review

This chapter presents a survey of the technical literature pertaining to the various subjects investigated in this thesis. The initial sections of this chapter describe the compression-ignition combustion process and the reaction mechanisms involved in the formation processes of the regulated diesel engine pollutants. The later sections examine past research on burning various gaseous fuels in compression-ignition engines and provide a review of the work carried out by past researchers using in-cylinder gas sampling techniques.

2.1 Fundamentals of compression-ignition combustion

The detailed understanding of the combustion processes in a compression-ignition engine is of paramount importance for the development of comprehensive qualitative and quantitative relationships between fuel spray behaviour, flame structure and fuel burning rate, and pollutants formation. In the 1970s, attempts

were made by several investigators (Chiu et al. 1976; Faeth 1977) to develop models for diesel spray mixing and to describe the nature of combustion processes in diesel engines. Chiu et al. (1976) investigated transient fuel sprays in a high pressure, high temperature chamber and proposed a diesel spray model consisting of the fuel rich diesel core surrounded by diesel fuel-air mixtures of progressively leaner equivalence ratios. The non-uniformity in stoichiometry in the outer spray region exists due to the different degrees of entrainment of air into the spray. Faeth (1977) looked into the steady state aspect of compression-ignition combustion and described the spray structure as a diesel fuel rich central core, surrounded by a layer of diesel fuel and entrained air mixture, where combustion occurred upon the mixture reaching an appropriate stoichiometry. The lack of advancement in computational capabilities and optical diagnostic technologies prevented a detailed correlation of the spray and flame structure with combustion stoichiometry, flame temperatures and cylinder wall interactions. In recent years, the understanding of in-cylinder processes associated with diesel spray combustion has been greatly improved due to conceptual models of diesel combustion, such as the one proposed by Dec (1997), who utilised laser-imaging diagnostics to provide a temporal description of diesel fuel consumption and define zones of varying fuel-air mixture stoichiometry in the flame structure, as well as detail the location of various burning processes that occur within these zones (Flynn et al. 1999). The events occurring

during diesel combustion, as proposed by this conceptual model (Dec 1997), have been summarised in Figure 2.1 and are discussed in detail in the following paragraphs.

Diesel combustion commences with the injection of diesel fuel at a high pressure (500 -1000 bar), through a narrow injector orifice into the cylinder of an engine which contains compressed intake air at a temperature higher than the ignition temperature of the fuel. As diesel fuel is injected into the cylinder, it entrains the surrounding hot air and undergoes atomisation and droplet formation. The fuel droplets encounter aerodynamic resistance, slow down, gain heat from the entrained air and evaporate in the process. High-speed imaging of the fuel injection process showed that the fuel jet length is limited due to this vaporisation process. The fuel vapour gets pushed to the periphery of the spray by the later-injected fuel which forms a narrow core densely filled with liquid fuel droplets (Heywood 1988). Rayleigh scatter images showed (Figure 2.1, number 2) that the layer downstream of this core has a well-defined boundary and consists of a uniform fuel rich diesel fuel-air mixture with an equivalence ratio of between two to four, and that there is only a very narrow fringe of stoichiometric mixture at this edge.

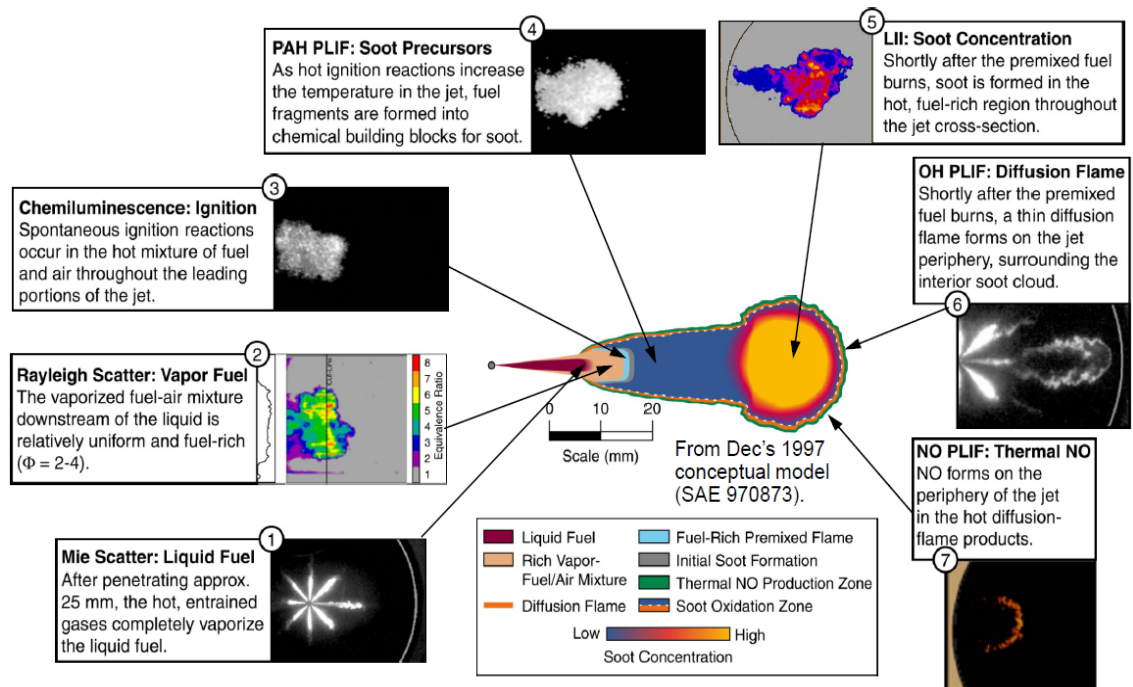


Figure 2.1: Diesel conceptual model describing fuel mixing and combustion, up to the end of injection (Dec 1997; Musculus et al. 2012)

The fuel vapour gets blown around by the swirling motion of the air, and the turbulent environment inside the chamber promotes the mixing of fuel vapour with the intake charge mainly in the regions between the individual sprays. The mixing process of fuel vapour with air and the energy transferred to the fuel from the hot air initiates the chemical breakdown of the fuel molecules; the kinetic reaction mechanisms between fuel and air molecules in the entrained air govern the duration of ignition delay. Ignition delay is defined here as the duration in CAD between the start of diesel fuel injection (SOI) and the start of combustion (SOC). SOI is taken to be the time when the actuation signal is sent to the injector, whereas the SOC is defined as the first incidence of detectable heat release following autoignition of the diesel fuel (Figure 2.2). Autoignition first occurs around fuel vapour-air pockets

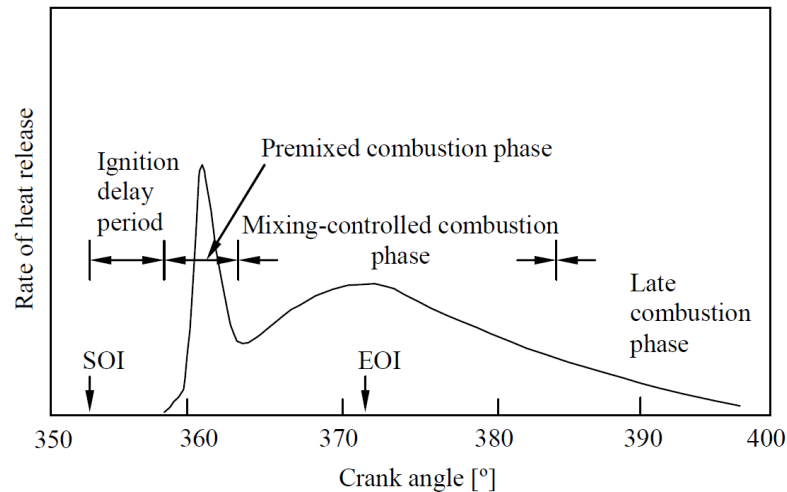


Figure 2.2: Typical heat release rate (J/deg) curve of a DI compression-ignition engine showing the different phases of combustion (SOI-start of fuel injection, EOI-end of fuel injection) (Heywood 1988)

of the appropriate stoichiometry and temperature, which have had time to mix during the ignition delay period; therefore, this phase is generally referred to as the premixed combustion phase (Heywood 1988). The rapid chemical energy release, following ignition, is accompanied by a significant rise in the combustion chamber temperature, resulting in high in-cylinder gas pressures, characteristic of the high peak heat release rates of the premixed combustion phase (Figure 2.2). Dec (1997) employed the use of natural flame chemiluminescence to detect the beginning of heat release, and reported that chemiluminescence is first observed in the fuel vapour regions near the injector tip, and it progressively increases in intensity downstream of the injector tip, with the highest levels of chemiluminescence detected in the solely vapour zone in the leading portion of the jet (Figure 2.1-number 3). Furthermore, chemiluminescence was detected at multiple points throughout the leading edge of the fuel-air mixture, providing evidence that diesel

fuel ignition occurs at numerous multiple locations spontaneously where fuel and air have mixed to within flammability limits.

During the initial stages of premixed combustion, as the heat release rate rises steeply, fuel molecules break down into smaller chain hydrocarbons and intermediate radicals, some of which subsequently polymerise to form polyaromatic hydrocarbons (PAH). These PAHs are precursors to soot, and were detected by Dec (1997) using planar laser induced fluorescence (PLIF) (Figure 2.1-number 4).

The conceptual model by Dec (1997) of diesel combustion describes the premixed fuel vapour-air pockets having an equivalence ratio between one to one-and-a-half.

In-cylinder gas sampling studies indicating high levels of CO within the flame enveloped spray (Heywood 1988) provide further evidence that the premixed burn phase comprises mainly of the combustion of a fuel rich mixture. As premixed burning proceeds, small soot particles begin to appear in the fuel rich regions, as evidenced by laser induced incandescence images obtained by Dec (1997) (Figure 2.1-number 5). Subsequent detection of larger soot particles, using Rayleigh light scattering (Dec 1997) at the periphery of the premixed combustion zone, suggests that soot particles undergo growth as they move towards the edge of the rich premixed flame.

As combustion proceeds during the premixed burn phase, a thin diffusion flame develops along the periphery of the premixed burn region now. As the premixed

phase is completed, a fully developed diffusion flame encompasses the entire downstream region of the spray cone and extends upstream along the jet as far as the flame lift off point. This is referred to as the diffusion burn, or mixing rate controlled phase (Figure 2.2), and the heat release during this phase is limited by the rate at which the fuel and air sufficiently mix to combustible levels. Therefore, this phase of combustion is characterised by lower heat release rates and occurs over a longer period of time as compared to the premixed combustion phase. The existence of a diffusion flame was indicated by the presence of OH radicals observed by Dec (1997) using planar laser induced fluorescence (PLIF) (Figure 2.1-number 6). OH radicals occur in regions where the fuel-air mixture is close to stoichiometric (Turns 1996). No OH radicals were detected during the initial premixed burn phase, when the mixture stoichiometry was between two and four. Following peak heat release, OH radicals were first observed in small pockets along the contours of the premixed burn region. These radicals were subsequently seen encompassing the flame front and extending up to just downstream of the injector tip.

PLIF measurements done for the detection of nitrogen oxide (NO) by Dec & Canaan (1998) provided further evidence of the presence of a diffusion flame (Figure 2.1-number 7). NO formation is normally favoured in a high temperature environment, which can be found in a diffusion flame region due to the fuel and air mixture equivalence ratio being near stoichiometric (Heywood 1988). Work done

by Flynn et al. (1999), using planar laser induced Rayleigh scattering (PLIR), demonstrates the stoichiometry of the premixed burn region to be fuel rich, and hence not at sufficient temperatures to initiate significant NO formation. Dec & Canaan (1998) reported that NO was not present in the initial fuel rich premixed burn region, but started appearing at the periphery of the spray jet, following the formation of a diffusion flame.

Combustion is completed during the late diffusion stage (Figure 2.2) which is the period following the end of fuel injection (EOI) and the end of the main diffusion phase, during which the remaining fuel evaporates and burns along with soot particles and products of fuel rich combustion (Heywood 1988).

2.2 Emissions formation in compression-ignition combustion

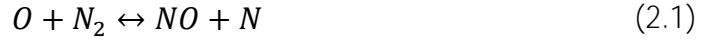
The discussion in the previous section implies a critical relationship between the diesel fuel combustion process and the accompanying formation of pollutant emissions. The following sections describe the production of both gaseous and particulate emissions formed during diesel combustion.

2.2.1 Oxides of nitrogen (NO_x)

The principal reaction mechanisms that lead to the production of oxides of nitrogen have been detailed in the following paragraphs.

The formation of nitrogen oxide (NO) via the oxidation of atmospheric nitrogen (N₂) with the oxygen (O₂) in the air was first described by Zeldovich et al. (1947).

Bowman (1973) built upon this work and defined the reaction mechanism popularly known as the “thermal” or “Zeldovich” mechanism, that is,



Lavoie et al. (Lavoie et al. 1970) studied NO formation using spectroscopy and suggested that the following reaction between atmospheric nitrogen and hydroxyl (OH) radicals contributed significantly to the Zeldovich mechanism of NO formation especially for near stoichiometric and rich mixtures.



The three reactions collectively form the extended Zeldovich mechanism as defined by Miller & Bowman (1989), who carried out extensive work to measure the kinetic rate constants that determine the rate of NO formation via this mechanism. The rate of initial NO formation may therefore be expressed as follows,

$$\frac{d[NO]}{dt} = \frac{6 \times 10^{16}}{T^{1/2}} \exp\left(\frac{-69,090}{T}\right) [O_2]_e^{1/2} [N_2]_e \quad (2.4)$$

where the units of the above equation are $mol/cm^3.s$.

The reactions of the extended Zeldovich mechanism are highly thermally sensitive and take place at temperatures of more than 1800 K, with conditions of high temperatures and high O_2 concentrations resulting in high NO formation rates, as

evidenced in Equation 2.4 (Bowman 1975). Therefore, the formation of NO during diesel fuel combustion tends to take place in the post flame gases to a large extent, as the residence time of the high pressure combustion gases at the flame front is insufficient for NO reactions to undergo completion. Additionally, the gases produced during early combustion reach significantly higher temperatures during the later stages of combustion, thereby enhancing NO production (Heywood 1988). Thermal NO formation rates tend to peak at near stoichiometric fuel-air mixtures, predominantly due to high gas temperatures present under such conditions (Heywood 1988; Turns 1996).

The rate of NO formation is of paramount importance in diesel combustion as it determines the final concentration of NO in the engine exhaust gas. Since the fuel oxidation reactions, as well as changes in the combustion chamber conditions, proceed significantly faster than the overall NO formation rate, the concentration of NO within the chamber is largely controlled by the kinetics of the extended Zeldovich reaction mechanism, rather than by equilibrium NO_x chemistry. Additionally, due to the relatively slow rate of decomposition of NO, as compared to the rate of cooling of post combustion gases during the expansion stroke, NO is not allowed to return to its equilibrium concentration corresponding to the in-cylinder conditions, and the NO chemistry is effectively 'frozen' or 'arrested' before significant decomposition of NO back to N_2 and O_2 can occur.

The formation of NO via the “prompt” mechanism, involving the reaction of fuel hydrocarbon radicals with molecular N₂ is another pathway for the production of NO. While most investigations have been able to explain NO concentrations entirely by the thermal (Zeldovich) mechanism, some studies reported higher NO levels than expected due to the thermal mechanism alone, especially at fuel rich conditions (Bowman 1975). The most significant reason for this discrepancy was believed to be that of “prompt” NO formation as suggested by Fenimore (1971), who compared the expected NO concentration formed via the thermal mechanism with results of NO levels in the adiabatic and non-adiabatic flames of methane and ethylene. Through this study Fenimore (1971) observed that, while post combustion NO formation was predominantly via the thermal mechanism, there was some NO formation during the fuel rich combustion stage. He proposed a reaction mechanism involving the breakdown of N₂ and its reaction with hydrocarbon radicals, as the alternative thermal mechanism (which requires high O₂ concentrations to initiate) appeared implausible in the fuel rich zone. The prompt mechanism is significantly faster than the thermal mechanism, and becomes particularly important during the fuel rich combustion stage ($\phi_{H_2} > 0.8$) when there is a high concentration of short-chain hydrocarbon radicals (Miller & Bowman 1989). The following two reactions are the most likely path to the degradation of molecular N₂ and the formation of

cyano compounds, which subsequently react with O, H and OH radicals to form NO (Fenimore 1971; Miller & Bowman 1989; Turns 1996),



Fuel bound nitrogen can also be responsible for the formation of NO during diesel combustion. Miller & Bowman (1989) report that the addition of small amounts of nitrogen to fuel can lead to a significant increase in exhaust NO levels, and discuss in detail the mechanism for this reaction, which proceeds via intermediate species such as NH_3 , NH_2 , HCN, etc. The reaction rates for this mechanism occur very fast, are comparable to fuel breakdown and oxidation rates and are entirely dependent on local combustion conditions (Fenimore 1972).

The decomposition of nitrogen dioxide (NO_2) into nitrogen oxide (NO) may also contribute towards the final concentration of NO in the exhaust gas. Bowman (1975) reported the rate of conversion of NO_2 to NO to be five times as quick as the rate of NO formation, and proposed the following reaction pathways for the formation of NO_2 and its subsequent decomposition into NO in the flame front during diesel combustion,



Based on chemical equilibrium conditions in post combustion gases, Heywood (1988) reported that the ratio of the concentrations of NO_2 to NO should be negligible. However, studies have shown the NO_2 concentration in diesel engine exhaust gas to be between 10 to 30 % of the total concentration of the oxides of nitrogen in the exhaust gas (Hilliard & Wheeler 1979). It was suggested that this was due to the quenching of the post combustion gases by the bulk cylinder gases during the expansion stroke, which effectively “froze” the NO_2 decomposition reaction mechanism. Evidence of this was provided by Hilliard & Wheeler (1979) who reported higher exhaust NO_2 levels at combustion conditions which were particularly conducive to quenching of the hot post combustion gases (due to the colder excess intake charge). The collective concentrations of NO and NO_2 are generally referred to as oxides of nitrogen (NO_x).

Extensive work has been carried out to understand the effect of heat released during the premixed burn phase and mixing-controlled diffusion phase of diesel combustion on the formation rates of NO_x . The heat released during the premixed phase of combustion is highly dependent on the ignition delay of the fuel, as it determines the time allowed for the fuel and air to mix and the volume of sufficiently mixed fuel-air mixture at the start of combustion. It has been observed by several investigators that an increase in the heat released during premixed burn phase of diesel combustion leads to higher NO_x concentrations in the exhaust gas due to

higher peak in-cylinder gas temperatures reached (Heywood 1988; Turns 1996; Ladammatos, Parsi, et al. 1996). This is because heat release occurs at a significantly more rapid rate during the premixed combustion phase as compared to the mixing-controlled combustion phase (Figure 2.2). This leads to a relatively short combustion event, occurring very close to the top-dead-centre (TDC) position, where the volume of the combustion chamber and energy losses to the chamber walls are at a minimum. Verbiezen et al. (2007) reported an increase in average in-cylinder temperature and an accompanying rise in exhaust and in-cylinder NO_x concentrations, as the diesel fuel injection timing was advanced. Ladammatos et al. (1996) reported a good correlation between the peak global in-cylinder temperature reached during the engine cycle and the relative fraction of fuel burned during the premixed combustion phase. Higher gas temperatures result in higher NO_x formation rates via the extended Zeldovich mechanism as discussed earlier in this section. The higher temperatures occurring during the premixed burn phase not only affect temperatures during the later stages of premixed combustion, but also cause an increase in gas temperatures during the mixing-controlled phase, in which a majority of NO_x is believed to be formed. Also, the occurrence of peak in-cylinder gas temperatures earlier during the engine cycle increases the duration of high temperature environment which is favourable to NO_x formation. Szybist et al. (2007) reported the time of peak global in-cylinder temperature to be a major factor

in determining NO_x formation rates, as peak temperatures occurring later in the engine cycle reduce the time available for NO_x production before temperatures fall below the levels required for the NO_x reaction to proceed (Heywood 1988).

Another factor which can influence the formation of NO_x in diesel engines is exhaust gas recirculation (EGR) which has been reported to be very effective in reducing exhaust NO_x levels (Ladommatos, Balian, et al. 1996; Ladommatos et al. 2000). An extensive study was carried out by Ladommatos et al. (2000) to decouple the various effects (dilution, thermal, chemical, etc.) which EGR has on NO_x formation rates and reaction mechanisms during diesel combustion. The study concluded that the thermal effect of EGR was dominant in reducing NO_x by decreasing adiabatic flame temperatures. The reduction in temperatures was due to decreasing the amount of O_2 in the intake charge, thereby forcing the fuel to interact with a larger amount of intake charge (to find O_2 to react with) and undergo higher heat losses in the process. This lead to a reduction in post-combustion gas temperatures and hence a decrease in NO formation rates via the thermal (Zeldovich) mechanism. Other consequences of EGR such as the change in the heat capacity of the intake charge (brought about by the change in composition of the intake charge) or the chemical effect of the additional CO_2 or water vapour on the NO_x reaction mechanism, were reported to have a secondary role in reducing NO_x formation rates.

2.2.2 Carbon monoxide

The formation of CO occurs due to the incomplete fuel combustion, that is, incomplete oxidation of fuel bound carbon, typically due to fuel-rich combustion and the unavailability of sufficient O₂. Bowman (1975) compared in-cylinder CO concentrations with those in the exhaust at various engine speed/load conditions, and found the in-cylinder concentrations to be higher, from which he concluded that the rate of CO formation and oxidation is kinetically controlled. Bowman (1975) suggested that CO formation begins during the initial stages of fuel oxidation. Further oxidation of CO to CO₂ occurs primarily by OH radicals; however, the rate of this conversion is lower than the rate of CO formation. The oxidation of CO to CO₂ by O₂ radicals is considered unlikely due to the extremely low rates of reaction Bowman (1975).

Based on literature, the formation of CO can occur through three principal mechanisms (Turns 1996). Firstly, CO may be formed during combustion of rich fuel-air mixtures, where lack of O₂ availability prevents complete oxidation of carbon atoms to CO₂. In diesel engines this may occur in the local diesel fuel rich pockets, which fail to mix adequately with air and undergo incomplete combustion. Secondly, CO formation can occur due to dissociation of CO₂ at high temperatures. The CO formed by this process usually oxidises to CO₂ if the mixture cools at a sufficiently slow rate and time is allowed for chemical equilibrium conditions to be established. However, the rapid mixing of combustion gases with the unreacted in-

cylinder charge and the relatively quick decline in the temperature of the combustion gas mixture during the expansion stroke can quench the conversion of CO to CO₂. Thirdly, the CO may be formed as an intermediate during the fuel oxidation process, which is quenched due to turbulent mixing of the combustion gases with the cooler in-cylinder gases, resulting in a rapid decrease in in-cylinder gas temperature. Further oxidation of the intermediate CO would therefore be 'frozen', with the CO persisting to the engine exhaust.

Despite these three mechanisms contributing to CO formation, the CO concentration in diesel exhaust gas is considered to be low as compared to other pollutant species, and hence is not deemed to be major problem (Heywood 1988).

2.2.3 Unburned hydrocarbons

Unburned total hydrocarbon (THC) emissions from diesel engines depend greatly on engine operating conditions, and different hydrocarbon (HC) formation mechanisms become important at different engine modes. Heywood (1988) outlined two primary routes by which hydrocarbon fuel would avoid the normal combustion process, either completely or partially, and persist to the exhaust: overlean fuel-air mixtures and undermixed considerably rich fuel-air mixtures. Overleaning occurs close to the spray boundary where the fuel injected at the start of injection mixes with the air beyond the lean limit of combustion. The fuel-air mixture becomes too lean to either auto-ignite or to sustain a propagating flame front. This fuel-air mixture can only be oxidised by the relatively slow thermal-oxidation reactions

which are unable to complete (before the expansion stroke begins and in-cylinder gas temperatures plummet), resulting in unburned fuel, fuel decomposition products and partially oxidised fuel products escaping the chamber. Undermixing occurs either if fuel enters the combustion chamber at low velocity and often late in the combustion process, for example from the injector nozzle sac, or excess fuel enters the chamber during transients when the engine undergoes an acceleration process. Similar to overleaning, fuel that has not mixed completely with air (undermixed) will not be able to auto-ignite or support a fast reaction front, and will therefore not undergo complete oxidation. It has been determined through experimentation that, at light engine load conditions, undermixing produces considerably less unburned HC as compared to overleaning (Yu & Shahed 1981). A third source of unburned HC, as identified by Heywood (1988), can be from flame quenching at the cylinder walls. Combustion chamber wall temperatures and the degree of spray impingement on the chamber walls significantly affect the degree of HC emissions due to quenching. Experiments have shown a 30% reduction in unburned HC emissions when coolant and lubricating oil temperatures were increased from 40°C to 90°C (Heywood 1988).

2.2.4 Particulates

Particulate refers to the combination of soot and other solid or liquid phase materials that might be absorbed onto soot, such as unburned hydrocarbons, lubricating oil, bound water and fuel derived sulphates (Lee et al. 1998). Soot is considered to be the insoluble part of particulates, and has been defined by Tree & Svensson (2007) as a solid substance consisting of approximately eight parts carbon and one part hydrogen. Over the years, the fundamentals of soot formation and oxidation, and the mechanisms of various processes involved, have been described in detail by several investigators (Palmer & Cullis 1965; Smith 1981; Haynes & Wagner 1981; Glassman 1989). More recently, Tree & Svensson (2007) conceptualised the five key processes that lead to the formation of soot particles from either liquid or vapour phase hydrocarbons: pyrolysis, nucleation, coalescence, surface growth and agglomeration. These processes are shown in a sequential schematic in Figure 2.3 and are described in detail in the following paragraphs.

Soot formation begins with the process of pyrolysis, an endothermic reaction whereby the hydrocarbon fuel breaks down in the presence of high temperatures, to produce species including unsaturated hydrocarbons, polyacetylenes, and

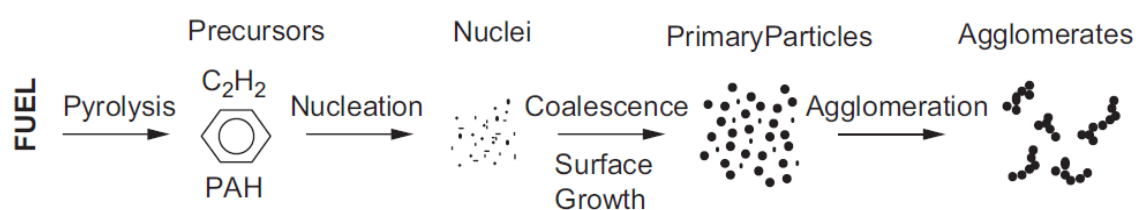


Figure 2.3: Schematic showing the sequential pathway of soot formation from gas/liquid phase to agglomerated solid particles (Tree & Svensson 2007)

eventually, mono-aromatic and polycyclic aromatic hydrocarbons (PAH). Reactive radicals such as hydrogen are important in accelerating the pyrolytic process. This is followed by nucleation of these species, leading to the formation of initial solid particles from gas phase hydrocarbons, by the addition of small aliphatic hydrocarbon molecules to larger aromatic structures. These initial particles have diameters (D) ranging between 1.5 and 2 nm. The nucleation process occurs at temperatures ranging between 1300 and 1600 K, and in the presence of high radical concentrations. Surface growth follows, which involves gas phase hydrocarbons (mainly acetylene) attaching to the reactive sites on the nascent particles. The rate of surface growth reduces with increasing particle size and decreasing availability of reactive sites, and is also less dependent on temperature and radical concentration as compared to nucleation. The total particulate mass significantly increases during this process, while the total number of particles is approximately maintained. The two terminal processes of soot formation are coalescence (coagulation) and agglomeration; coalescence is the joining of two spherical particles to form a new larger spherical primary particle (of diameter 20 – 70 nm), while agglomeration is primary particles clumping together forming agglomerates of diameter 100 nm or greater, while maintaining their individual shape. These two processes result in an increase in particle size and a decrease in the total number of particles, while the total particulate mass is approximately maintained. A sixth

process that occurs simultaneously with the other five is soot oxidation, involving the conversion of solid carbon particles and partially pyrolysed hydrocarbons back to CO, CO₂, H₂ or H₂O. The rate of soot oxidation is significant in determining eventual particulate emissions, and is highly dependent on temperature as well as oxygen availability, as will be discussed in detail in the following paragraph.

In the past, researchers have carried out experiments to try and determine the impact of various physical factors on particulate emissions, and a review of these effects has been documented by Tree & Svensson (2007). The effects of oxygen and temperature on soot production are quite difficult to isolate due to their interdependence. An increase in flame temperature results in an increase in the rates of both soot formation and oxidation. However, with increasing temperature, the rate of soot oxidation rises more rapidly than the rate of soot formation, resulting in a net decrease of soot concentration in the flame. If oxygen is present, as in the case of premixed flames, an increase in temperature can enhance soot oxidation rates more than soot pyrolysis rates. On the other hand, under low oxygen conditions (for example, in diffusion flames) an increase in temperature tends to only increase soot pyrolysis rates. OH oxidation is the primary driver for soot oxidation under rich or stoichiometric conditions, whereas O₂ oxidation dominates at lean conditions. Incipient soot formation has been observed to occur at above 1650 K, while oxidation of soot particles and its precursors initiates at temperatures

above 1300 K (Kent & Wagner 1985). From these observations, Kent & Wagner (1985) implied that in order to prevent soot formation entirely either the flame temperatures should be kept below 1650 K, or the soot oxidation zone, located in the lean region of the flame, should be kept at temperatures above 1300 K to allow oxidation of previously formed soot particles. The effect of in-cylinder pressure and specific volume are not easy to define due to the wide-ranging effects that in-cylinder pressure has on diffusivity and flame structure (Glassman & Yetter 2008a; Glassman & Yetter 2008b). However, it has been suggested that an increase in in-cylinder pressure is likely to increase the rate of molecular collisions, hence enhancing rates of reaction.

Advancing the fuel injection timing has been reported to result in a decrease in particulate emissions (Kamimoto & Kobayashi 1991). On one hand, an advance in fuel injection timing increases soot formation during the early stages of the combustion process, since much of it now occurs under higher temperatures and pressures. On the other hand, since the combustion process has been advanced, more time is now available for soot oxidation to occur at sufficiently higher temperatures during the late combustion and post combustion stages. Time availability for soot oxidation has been determined to be the primary factor between this trade-off, resulting in a net decrease in particulate emissions (Tree & Svensson 2007). Exhaust gas recirculation (EGR) has also been determined to have a

significant effect on the particulate emissions from an engine. Comprehensive experiments done by Ladommatos et al. (2000) have shown that the progressive introduction of EGR substantially increases particulate emissions, and has been attributed to the displacement of intake air, and hence, the reduction in O_2 availability for the oxidation of soot and its precursors.

Measurements of the size distribution of particles in a diesel engine exhaust have been carried out by researchers employing a variety of methods (Dolan & Kittelson 1978; Khatri et al. 1978; Amann & Siegl 2008), and the diameters of particles have been found to vary between 5 nm to an excess of 10 μm (Kittelson 1998). From their observations (Kittelson 1998) proposed that the distribution of diesel exhaust particles is trimodal, with the three modes being: nucleation mode particles (5 – 50 nm diameter), accumulation mode particles (100 – 300 nm diameter) and the coarse mode particles (2 – 10 μm diameter) as shown in Figure 2.4.

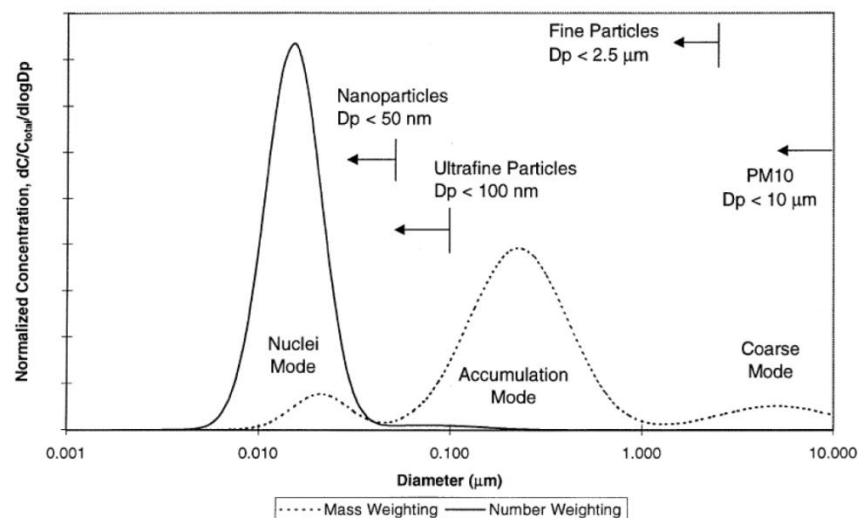


Figure 2.4: Typical size distribution of particulates from diesel engine exhaust (Kittelson 1998)

It can be observed from Figure 2.4, that the majority of the particles (i.e. the particle number weighting) are concentrated in the nucleation mode, which only counts for between 1% and 20% of the total particulate mass. The bulk of the mass comes from the smaller number of relatively large particles of the accumulation mode, which make up 60 – 94% of the total particulate mass. Similar to the nucleation mode, the particles in the coarse mode make up 5 – 20% of the total particulate mass (Kittelson 1998). The nucleation mode particles consist primarily of condensed phase hydrocarbons, the accumulation mode particles are predominantly made of clusters of soot particles, while the coarse mode particles are understood to be agglomerates of the accumulation mode particles (Kittelson 1998).

Mayer et al. (1980) conducted experiments to determine the contribution of engine lubricating oil to the exhaust particulate mass and concluded that 1.5 – 25% of the particulate mass could be attributed to the lubricating oil, and that the percentage contribution increased with increasing engine speed. The author also observed that the contribution of the lubricating oil to the particulate matter was in the form of adsorbed hydrocarbons on the soot surface, rather than part of the carbonaceous components of particulates, suggesting that lubricating oil does not participate significantly in the soot particle formation process.

2.3 Methods of production of hydrogen, natural gas and biogas

2.3.1 Hydrogen and natural gas

Klell et al. (2012) published a review on the various production, storage and distribution methods of hydrogen and methane in terms of composition, safety, regulations and infrastructure. The following sections briefly describe the different ways of generating or procuring natural gas and hydrogen, summarized from the work of Klell et al. (2012).

Natural gas is typically found as a fossil fuel or produced as a component of biogas generated via the gasification of biogenic material. The possible sources of biogenic material can be waste organic residuals from industrial processes, animal excrements, or agricultural and municipal waste products. Various gasification techniques can be employed to generate either a methane (CH₄) rich or a hydrogen (H₂) rich biogas; CH₄ proportions of 80% by volume can be achieved by fermentation, while pyrolysis can produce biogas with up to 46% H₂ by volume. Higher H₂ concentrations in the final product can be achieved by using chemical procedures like the pressure-swing-adsorption technique, which utilises high pressure to adsorb gases on materials which have a high affinity for that particular gas species (Lively et al. 2012).

Steam reforming of natural gas can be used to produce H₂; this is an endothermic reaction in which water and methane react together at 800°C to produce a synthesis

gas consisting mainly of H_2 and CO . The volumetric proportion of H_2 in this wet synthesis gas can be up to 50%, and higher H_2 concentrations can be achieved by employing additional chemical procedures such as water-gas shift reaction (Chianese et al. 2015) and pressure-swing-adsorption technique. The water-gas shift reaction is the reaction between CO and water vapour to form CO_2 and H_2 . Commercial steam reforming facilities are able to generate H_2 at very high rates of up to 100,000 Nm^3/h with energy conversion efficiencies ranging between 75% and 80%.

Water can be separated into its constituents, H_2 and O_2 , if a sufficiently high voltage is applied, via a process known as electrolysis. This process happens in an electrochemical cell, which is supplied with water, and H_2 and O_2 evolve at the cathode and anode respectively. Large scale alkaline H_2 electrolyzers are capable of producing 30,000 Nm^3/h of H_2 at an energy conversion efficiency of about 70%, while small scale H_2 production uses PEM (proton exchange membrane) electrolysis and can produce H_2 at a rate of 0.5 – 10 Nm^3/h with an efficiency of up to 50%. More recently, solar and wind power plants have started generating H_2 through electrolysis. During periods of high energy production and low electricity demand, the electrical energy being produced can be used to generate H_2 which can then be utilised to power IC engines or introduced into the natural gas grid during periods of peak energy demand.

2.3.2 Biogas

Biogas is typically produced via anaerobic digestion, which involves the multi-staged decomposition of bioorganic waste matter by bacteria, in the absence of oxygen, to form gaseous by-products. These gaseous by-products consist primarily of CH₄ and CO₂, with trace amounts of other gases present. The following account detailing the various stages of biogas production has been summarized from a review by Barik & Murugan (2014). The first stage of biogas production is the bacterial hydrolysis of large organic polymers into smaller monomers which involves the breaking down chains of complex organic molecules (cellulose, lipase, protease and amylase) into simple sugars, amino acids and fatty acids. The process of acidogenesis follows, where the simple monomers are converted to volatile fatty acids (VFA). Additionally, hydrogen and acetate is also produced during these initial stages, due to the action of fermentative bacteria, which can be directly used by the methanogens. The volatile fatty acids, produced during the initial hydrolytic reactions, need to undergo further catabolism before they can be acted upon by methanogens. This is done by the obligate hydrogen-producing acetogenic bacteria, which convert the VFAs into primarily acetic acid as well as CO₂, H₂ and acetate. It is necessary to maintain a low partial pressure of H₂ in the digester, as the metabolism of the acetogenic and hydrogen producing bacteria is severely affected by H₂ accumulation. Weiland (2010) suggested adding hydrogen producing bacteria to the digester feedstock to increase biogas production. The final stage is called

methanogenesis or biomethanation, where methanogens (or methanogenic archaea) make use of the intermediate products from the preceding stages, such as acetate, and convert them into CH_4 and CO_2 , while other bacteria consume the hydrogen to produce CH_4 (Ferrer et al. 2008). Trace amounts of hydrogen sulphide (H_2S) are also produced due to action of sulphate-reducing bacteria on intermediates.

The composition of the produced biogas depends on the feedstock material fed to the digester and on the digestion technique applied. As compared to natural gas, which has a very low CO_2 content (0.67 – 1%), the volumetric proportion of CO_2 in biogas can vary between 25% and 50%. Biogas also has a higher content of impurities such as N_2 , H_2S and NH_3 as compared to natural gas. The higher concentrations of CO_2 and impurities in biogas reduce its calorific value, necessitating the need to clean the biogas post-production, in order to reduce the concentration of contaminants in the biogas (Yang, Ge, et al. 2014). *Pressurised water scrubbing (PWS)* is the most commonly used biogas cleaning technique, in which pressurised biogas (900 – 1200 kPa) is flown counter currently to the flow of water. CO_2 and H_2S are separated from the biogas due to their higher water solubility relative to CH_4 ; the subsequently dried biogas can contain > 96% CH_4 (Patterson et al. 2011). *Pressure swing adsorption (PSA)* is another extensively used biogas cleaning method which, as described in the preceding section, relies on the selective adsorbent properties of a material to capture preferred gases. The

adsorbent materials are designed to have specific pore sizes, enabling them to selectively adsorb molecules smaller than the designed pore size. Zeolite, carbon molecular sieve and silica gel are some commonly used adsorbents for biogas cleaning, which are able to capture CO₂, O₂ and N₂, thereby enriching the CH₄ content of the biogas. *The amine absorption method* is used to remove CO₂ from gas streams, as amine solvents, such as alkanolamines, are able to selectively absorb CO₂. Furthermore, since amine solvents have a much higher solubility of CO₂, as compared to CH₄, the cleaned biogas can contain 96 – 98% CH₄ by volume. The *membrane permeation technique* works on the principle that when a gas mixture is pressurised, gases with higher permeability (for example, due to their small molecular size) can be transported through a membrane while gases with lower permeability are retained (Lie et al. 2007). This method is used to remove impurities such as CO₂, O₂ and H₂O from biogas (Kimura & Walmet 2006), and is preferred due to its safety, scale-up flexibility, operational simplicity, and no requirement for hazardous chemicals (Yang, Ge, et al. 2014). Other less commonly used biogas cleaning methods include temperature swing absorption (TSA) (Clause et al. 2004; Shao et al. 2012), cryogenic techniques (Patterson et al. 2011; Yang, Ge, et al. 2014) and biofilters (Yang, Wang, et al. 2014).

2.4 Co-combustion of fuel mixtures in CI engines

2.4.1 Hydrogen-diesel fuel mixtures

Hydrogen (H_2) is a 'zero' carbon fuel and therefore produces no carbon-bearing products such as particulate matter, total hydrocarbons (THC), carbon monoxide (CO) or carbon dioxide (CO_2) from combustion (Karim 2003). However, hydrogen has an appreciably lower cetane number than diesel fuel (Karim 2003) and is not ignitable merely by means of compression in modern diesel engines, and therefore it requires an ignition source. In the case of a diesel engine, the hydrogen can either be aspirated into the engine or injected directly into the cylinder, while the auto-ignition of diesel fuel spray can act as a pilot to ignite the hydrogen (Lambe & Watson 1993; Lilik et al. 2010). Hydrogen requires a very low amount of energy to ignite but has high flame propagation rates within the engine cylinder in comparison to hydrocarbon fuels, even at lean mixture conditions. The high flame speeds are a result of the fast and thermally neutral branching chain reactions of H_2 as compared to the relatively slower and significantly endothermic chain reactions associated with hydrocarbon fuel combustion (Karim 2003). Gaseous H_2 does not experience problems associated with liquid fuels, such as vapour lock, cold wall quenching, inadequate vaporization and poor mixing (Akansu 2004).

Heat release rates from H_2 -diesel fuel co-combustion tend to be higher than those for diesel fuel combustion, resulting in a shorter duration of combustion with less heat transfer to the surroundings, and can improve thermal efficiencies (Saravanan

& Nagarajan 2008b; Masood et al. 2007; Christodoulou & Megaritis 2013). However, Masood et al. (2007) and Christodoulou & Megaritis (2013) reported a small deterioration in thermal efficiency when operating the engine with a H₂-diesel fuel mixture, at low load and low speed conditions, which they attributed to the incomplete burning of all the hydrogen aspirated into the engine.

A considerable number of studies (Varde & Varde 1984; Lambe & Watson 1993; Saravanan & Nagarajan 2008a; Saravanan & Nagarajan 2008b; Christodoulou & Megaritis 2013) reported a reduction in PM emissions when H₂ was used as a secondary fuel in a diesel engine, which they ascribed to a number of factors; firstly, increased oxidation of particulates due to higher in-cylinder temperatures that result from increased heat release rates, secondly the overall reduction in the carbon-hydrogen ratio of the combined H₂-diesel fuel, and thirdly the formation of OH radicals from H₂ combustion which also enhance PM oxidation. Tomita et al. (2001) reported a reduction in smoke to near zero levels at all diesel injection timings and at all equivalence ratios of hydrogen. Tsolakis & Hernandez (2005) used reformed exhaust gas recirculation (REGR) to introduce hydrogen rich gas to the engine intake air and reported a reduction in the total number and mass of PM emissions, but no effect was noted on the particle size distribution compared to standard diesel operation. Some investigators reported an increase in PM emissions at high engine loads (Lilik et al. 2010; Varde & Varde 1984). When H₂ is aspirated

into the engine via the engine inlet manifold, it displaces some of the intake air and can reduce the power density of the engine. At high load operating conditions, which are accompanied by high levels of H₂ substitution, the intake air becomes increasingly vitiated, slowing the rate of carbon oxidation reactions, which can result in a rise in PM emissions.

NO_x emissions have been reported to increase as stoichiometric H₂-air ratios are approached, and reach a peak value at an equivalence ratio of 0.9 (Brunt et al. 1998; Naber 1998). The faster burning rates of H₂ relative to fossil diesel (Saravanan & Nagarajan 2008b) and the resulting higher in-cylinder temperatures, especially when operating with near-stoichiometric H₂-air mixture conditions, has been suggested by some investigators to give rise to increased NO_x exhaust emissions (Tsolakis & Hernandez 2005; Varde & Varde 1984). Conversely, other investigators, such as Lambe & Watson (1993) and Tomita et al. (2001), have reported considerable reductions in NO_x emissions with H₂-diesel fuel co-combustion, at certain load conditions with relatively advanced diesel fuel injection timings. Saravanan & Nagarajan (2008a;2008b) conducted co-combustion experiments, at various engine loads, during which diesel fuel was replaced with H₂ while keeping the engine speed constant. Significant reductions in NO_x emission levels were observed, at low engine loads, when 30% of the initial volume of diesel fuel was replaced with H₂ in the intake air (keeping the engine speed constant), which these

authors attributed to lean burn combustion. An 80% reduction in NO_x emissions was reported by Saravanan & Nagarajan (2008a;2008b), at high engine loads, with 90% of the diesel fuel volume replaced by hydrogen. At full load engine operating conditions, NO_x emissions were reported by Saravanan & Nagarajan (2008a;2008b) to marginally increase. Lilik et al. (2010) noted that the engine used by Saravanan & Nagarajan (2008a;2008b) produced NO_x at an order of magnitude higher than usually emitted by modern diesel engines, and any decrease in NO_x could therefore be a result of enhanced turbulent in-cylinder mixing.

Masood et al. (2007) and Masood & Ishrat (2008) carried out computational H₂-diesel fuel co-combustion studies and validated the findings against experimental results. Both the computational and experimental NO_x emission results showed an overall decrease in NO_x with increasing H₂ addition except for a marginal increase in NO_x reported in the experimental data at high H₂ substitution levels. The overall decrease in NO_x with increasing H₂ substitution was attributed to the increase in mole fraction of water vapour in the combustion products produced from H₂ combustion, absorbing energy released from combustion and reducing peak combustion temperatures.

Lilik et al. (2010) substituted up to 15% of energy from diesel fuel by H₂ aspirated into the engine intake air. Two engine speeds (1800 rpm and 3600 rpm) and two engine loads (25% and 75% of the maximum output) were investigated, and while

it was observed that the effect of H₂ substitution on NO_x emissions was minimal, a greater increase at low engine loads was reported compared to high engine loads with the addition of H₂. Considering only the NO component of the total NO_x emissions, increased H₂ substitution led to decreasing levels of NO emissions especially at low load. However, NO₂ emissions were observed to increase, when the ratio of H₂ in the intake charge was increased, most significantly at high engine load. This reduction in NO/NO₂ ratio was verified using numerical modelling and was attributed to the increased availability of the HO₂ radicals with increasing H₂ addition and subsequent reaction of HO₂ with NO. The numerical model also showed that the spatial temperature distribution in the cylinder was relatively unaffected by H₂ combustion, and it was therefore suggested that the observed changes in NO_x were not the result of changes in thermal NO. The authors attributed the small reduction in the overall NO_x emissions to the slight increase in ignition delay causing a small shift in the combustion phasing towards the expansion stroke and, therefore, generally lower in-cylinder gas temperatures.

More recently Christodoulou & Megaritis (2013) conducted H₂-diesel fuel co-combustion engine tests where up to 8% by volume of the intake air was replaced with hydrogen. At low load conditions, no significant changes in NO_x emissions were reported with the introduction of H₂, which was attributed to the smaller thermal boundary layer of the hydrogen flame and the relatively cooler engine walls

which enhanced heat rejection and offset the higher adiabatic flame temperature of hydrogen. At higher load conditions and increasing displacement of diesel fuel with H₂, NO_x emissions increased due to elevated flame temperatures.

2.4.2 Hydrogen-methane-diesel fuel mixtures

Besides hydrogen, natural gas (NG) stands out as another potential alternative for the currently used petroleum-based fuels, since natural gas burns more cleanly than any other fossil fuel releasing relatively few by-products into the atmosphere as pollutants (Akansu 2004). This is because, typically, up to 99% of the total volume of NG is methane (CH₄), with the remaining made up of constituents such as ethane, propane, butane, and inert gases like nitrogen, helium, carbon dioxide, hydrogen sulphide and sometimes water (DeLuchi et al. 1988; Weaver 1989). CH₄ has a H-C ratio of 4:1, and therefore upon combustion releases 25% less CO₂ than conventional fossil fuels for the same energy release in internal combustion engines. CH₄ has a high octane number (120-130) that allows for increased compression ratios without risk of autoignition resulting in thermal efficiencies comparable to those of IC engines (Diéguez et al. 2014).

Hydrogen and methane are complimentary fuels in many aspects, as is evident from their physical and chemical properties (Karim 2003; Klell et al. 2012). CH₄ is a relatively stable molecule and has an ignition energy requirement which is approximately 15 times greater than that of H₂. CH₄ can be difficult to combust

completely in an engine or catalyse using exhaust after treatment systems. On the other hand, H_2 can act as a combustion stimulant accelerating CH_4 combustion.

A major drawback of operating engines on lean mixtures of methane and air is the associated low flame propagation velocity which can result in incomplete combustion, increased cycle-to-cycle variation and occasional flame failure (Diéguez et al. 2014). Some improvements in the burning rate of CH_4 can be brought about by optimizing the spark timing or increasing turbulence, which comes at a cost of excessive heat losses through cylinder walls, as well as increased peak cylinder gas temperatures and thus higher NO_x emissions (Akansu et al. 2007). One approach to enhancing the combustion process, without adversely affecting emission levels, is to add a small amount of H_2 to CH_4 . H_2 has a flame speed about six times higher than CH_4 at atmospheric conditions (42 cm/s for CH_4 and 230 cm/s for H_2), and approximately eight times higher at the high engine pressure and temperature operating conditions. Nagalingam et al. (1983) conducted SI engine tests using natural gas supplemented by H_2 and concluded that while the engine power output was reduced due to the lower volumetric heating value of H_2 (2.8 MJ/dm³ at 350 bar, 25°C) as compared to CH_4 (11.6 MJ/dm³ at 350 bar, 25°C), the considerably higher flame speed of H_2 meant that less spark advance was required to produce maximum brake torque (MBT). Hence the very high flame speed of H_2 allows shorter combustion duration leading to higher peak cylinder pressures and heat

release rates and smaller time interval between fuel ignition and peak heat release, as compared to CH₄. On the other hand, the presence of CH₄ in H₂-CH₄ mixtures reduces the risk of combustion anomalies such as backfire and knock, usually associated with H₂ (Demuyne et al. 2009; Verhelst et al. 2010). CH₄ has a relatively low flammability range (4.4 – 15% v/v in air at 1 bar and 25°C) which can limit improvements in fuel efficiency and NO_x emissions that are possible at lean air/fuel ratios, whereas, hydrogen has a broad flammability limit of 4 – 76% v/v in air at 1 bar and 25°C. The addition of H₂ to CH₄ can, therefore, significantly widen the flammability limits and allow engine operation at leaner air/fuel ratios. Hence, it can be seen that the use of blends of CH₄ and H₂ as fuel can yield beneficial synergetic effects, which might not be achievable if the two gaseous fuels are used individually.

There is considerable literature available, spanning a couple of decades, relating to the use of CH₄-H₂ mixtures in SI engines; more recently, studies have been conducted using CH₄-H₂ mixtures in CI engines, with the diesel fuel acting as an ignition source (pilot ignition). The following paragraphs will briefly look at literature pertaining to CH₄-H₂ combustion in SI engines, before discussing in detail investigations conducted on CI engines, since they are more relevant to the study currently being carried out in this thesis.

Investigators studying the combustion and emission characteristics of CH₄-H₂ mixtures in SI engines used mixtures with various proportions of CH₄ and H₂ (from H₂ rich to CH₄ rich mixtures), at a variety of CH₄-H₂/air equivalence ratios, engine loads and engine speeds, and arrived at the following unanimous conclusions. NO_x emissions increased with increasing proportion of H₂ in the mixture; however, NO_x emissions were seen to decrease to extremely low levels by employing lean burn (possible due to the wide flammability limits of H₂), EGR or exhaust after treatment techniques. Unburned hydrocarbons, CO₂ and CO emissions decreased with increasing H₂ content due to direct displacement of CH₄ with 'zero' carbon H₂. The thermal efficiency of the engine was observed to increase only at certain operating conditions (30 CAD BTDC spark timing and 20% H₂ in the mixture). The knock resistance characteristics of CH₄ were not significantly affected by the addition of small amounts of H₂. The overall brake specific fuel consumption (BSFC) decreased with increasing H₂ proportion in the mixture. The optimum concentration of H₂ in the CH₄-H₂ mixture, to achieve an increase in brake power output but still avoid knock, was proposed to be about 20 – 30% by volume of H₂. However, the costs of CH₄-H₂ mixtures were considerably higher as compared to CH₄ rich natural gas. (Nagalingam et al. 1983; Swain et al. 1993; Wallace & Cattelan 1994; Raman et al. 1994; Hoekstra 1995; Liu & Karim 1995; Karim et al. 1996; Larsen & Wallace 1997; Van Blarigan & Keller 1998; Shrestha 1999; Das 2000; Bauer 2001b; Bauer

2001a; Akansu 2004; Akansu et al. 2007; Kahraman et al. 2009; Thurnheer et al. 2009; Diéguez et al. 2014).

Based on their experience with the behaviour of CH₄-H₂ mixtures in SI engines Sierens & Rosseel (2000) proposed a strategy for the effective use of CH₄ and H₂ in engines by adjusting the hydrogen proportion as function of engine load. At low loads, pure H₂ could be used at high air-fuel ratios ($\lambda > 2$), at intermediate loads a methane rich CH₄-H₂ mixture (20:80 H₂:CH₄ by volume at $\lambda > 1.5$) could be used to keep in-cylinder gas temperatures and hence NO_x emissions at low levels. However, exhaust after-treatment techniques would need to be employed to lower CO and unburned HC emissions to acceptable levels. At full load nearly pure methane would have to be used to achieve high brake mean effective pressures.

The use of CH₄-H₂ mixtures to reduce the toxic pollutant emissions has recently attracted the attention of vehicle manufactures and transport operators. Tests were conducted at the ENEA Casaccia Research Centre by Genovese et al. (2011), whereby two public transit urban buses were fuelled with H₂-CH₄ mixtures of varying H₂ proportions (0 – 25% by volume of H₂), and then taken through a series of road tests representative of the urban and suburban drive cycles. The authors presented the following key findings from the experiments: an increase in engine efficiency due to an improvement in energy performance was observed at low levels of H₂ addition, and an improvement of 4% in energy consumption was observed at

5% H₂ proportion. However the authors did point out that this improvement was accompanied by a 1 CAD decrease in spark ignition advance, and if spark timing were to be optimized the change in efficiency could be different. A reduction in CO₂ emissions, beyond that expected due to simple carbon displacement was observed with increasing H₂ proportion; this was thought to be an effect of the enhanced fuel efficiency, and hence decreased carbon emission products. A similar effect of a reduction in unburned HC was also observed with increasing H₂. However, NO_x emissions were seen to increase with increasing H₂, as a result of higher flame temperatures of H₂.

McTaggart-Cowan et al. (2009) used a Cummins ISX series heavy-duty, single-cylinder diesel engine, with direct injection capabilities for both diesel and gaseous fuels, to investigate the combustion and emission characteristics of CH₄-H₂ mixtures pilot ignited with diesel fuel. From the study it was determined that the H₂ addition enhances the ignitability of the in-cylinder fuel mixture, resulting in shorter ignition delays. At low loads, the addition of H₂ not only improved the rate of burning during the partially premixed stage, but also reduced cycle-to-cycle variability. At high loads, a reduction in peak heat release rates was observed due to H₂ having a lower energy density. There was no significant influence of H₂ on the duration of combustion at both low and high loads. It was speculated by the authors that the overall duration of combustion is primarily dependent on the turbulent mixing rate,

and is not particularly sensitive to the fuel mixture composition. The observed decrease in CO, unburned HC and PM emissions due to H₂ addition was more, than would result merely from the lower carbon content of the fuel. This was attributed to improved combustion stability and hence, enhanced fuel oxidation rates. NO_x emissions were observed to increase at all engine load conditions tested, which was attributed not only to hydrogen's higher flame temperatures, but also to the effect of H₂ on the NO formation chemistry. Similar work was done by Gatts et al. (2010) by adding H₂ on a natural gas-diesel fuel heavy duty engine, with comparable observations reported. Additionally, Gatts et al. (2010) also reported that the low combustion efficiency of natural gas was primarily due to CH₄ remaining unburned in the combustion chamber, which showed an improvement up on the addition of H₂.

Imran et al. (2014) carried out a study on a single cylinder, direct injection compression ignition engine, which was run separately on natural gas (NG) and hydrogen with the pilot liquid fuel serving as the ignition source. The study investigated the effects of changing pilot fuel quantity (diesel fuel and rape methyl ester (RME)) on various combustion and emission parameters. Dual fuel combustion of NG-pilot fuel exhibited an increase in ignition delay as compared to single fuelling combustion of pilot fuel under similar operating conditions. A reduction in ignition delay was observed as the quantity of pilot fuel was increased.

Similar reductions in ignition delay with increasing pilot fuel quantities were also observed with H₂-pilot fuel mixtures. At higher engine speeds and dual fuel operation of NG-pilot fuel, the specific NO_x emissions were found to be proportional to the quantity of pilot fuel injected. However, at lower engine speeds a pilot fuel quantity threshold was observed where maximum NO_x emissions were measured, with lower NO_x levels observed at any other pilot fuel setting. A similar threshold phenomenon against engine speed was observed in the case of unburned HC. In the case of H₂-pilot fuel mixtures, the NO_x emissions demonstrated opposing trends at different engine speeds. At lower speeds specific NO_x emission decreased with increasing pilot fuel quantity, whereas, at high speeds NO_x levels were observed to increase with increasing quantity of pilot fuel.

Pichayapat et al. (2014) investigated the emission characteristics of hydrogen and compressed natural gas mixtures (HCNG) with diesel fuel pilot ignition in a EURO 4 standard, four cylinder, direct injection diesel engine at different engine speeds ranging from 800 to 4000 RPM. The authors demonstrated that the use of HCNG mixtures is safe in a diesel engine at the tested engine operating conditions. A reduction in emission levels was observed with the use HCNG-diesel fuel blends as compared to diesel fuel only operation; a 12.97% reduction in CO emissions, a 15.84% reduction in unburned HC emissions, a 1.16% reduction in NO_x emission

and a 9.14% reduction in PM emissions were observed with the HCNG-diesel fuel mode at all the tested speeds.

A similar study was also conducted by Zhou et al. (2014) investigating the effects on engine performance and pollutant emissions, of H₂ only, CH₄ only and CH₄-H₂ mixtures co-combusting with diesel fuel in a four cylinder, 4.334 litre CI engine. The authors reported that the combustion efficiency of the gaseous fuels was highly dependent on engine load; the addition of gaseous fuels reduced peak in-cylinder gas pressure and peak heat release rates at low loads and them at high loads (with the engine torque kept constant when adding gaseous fuels). The addition of CH₄ to H₂ was observed to make H₂ combustion smoother, and the authors suggested this could improve engine operational safety and mechanical durability. An increase in break specific fuel consumption and a decrease in brake thermal efficiency were reported by the authors when either CH₄ or H₂ was added to the engine, especially at lower loads. The decrease in efficiency observed, when using H₂-diesel fuel as compared to diesel only operation, was in contrary to other reported studies in literature, and the authors speculated this could be an effect of the extremely small quenching distance of H₂ leading to a higher thermal losses from the H₂ flame as compared to the diesel only flame. The brake thermal efficiency was observed to be higher for H₂-CH₄-diesel fuel blends as compared to CH₄-diesel fuel blends, attributable to the higher flame speeds of H₂ (relative to CH₄). CO and unburned

HC emissions were observed to be higher for CH₄-diesel fuel mixtures as compared to diesel fuel only operation. This was attributed to the partial oxidation of CH₄ and some of the CH₄ not combusting in the engine and persisting to the exhaust. Since the CH₄ was being aspirated into the engine, and hence forming a near homogenous mixture with the intake air, the likelihood of the diesel fuel flame being able to ignite almost all the intake CH₄ is considered to be highly improbable. As expected, the replacement of either diesel fuel or CH₄ by H₂, lead to a reduction in the emissions of CO and unburned HC, due to displacement of carbon-containing fuel. A considerable rise in NO_x emissions was reported when using CH₄-diesel fuel or H₂-diesel fuel mixtures, as compared to diesel fuel only operation. NO_x emissions were observed to decrease as H₂ was gradually replaced by CH₄, due to lower combustion temperatures of CH₄. It was suggested that a H₂ rich mixture (30CH₄-70H₂) improves engine performance and lowers CO and unburned HC emissions, whereas, a CH₄ rich mixture (70CH₄-30H₂) is effective in limiting NO_x formation rates and increasing combustion stability (avoiding phenomena such as uncontrolled pre-ignition of H₂). Particulate emissions reduced when H₂ was added to CH₄-diesel fuel combustion; this observation agrees with the results of Wang et al. (2009), which suggest that H₂ moves the CH₄ oxidation path towards a lower carbon reaction path, and hence reduces soot formation rates.

2.4.3 Biogas-diesel fuel mixtures

Biogas is considered to be a carbon-neutral fuel since the carbon emitted when biogas undergoes combustion comes from plant matter that fixed this carbon from atmospheric carbon dioxide (via the natural carbon cycle). The primary component of biogas is CH_4 (50-80% by volume depending on the method of production of biogas), which is a greenhouse gas (GHG) and has a global warming heating factor of about 20 times higher than CO_2 . Burning biogas converts the CH_4 to CO_2 , thereby reducing the GHG impact on the environment by about 20 times. Since biogas production involves extracting the CH_4 out of organic waste products and burning it to release energy (waste products that could otherwise degrade in open environment), direct emissions of CH_4 into the atmosphere can be avoided. The use of biogas as fuel has the potential to reduce the demand on conventional fossil fuels (Bora et al. 2014; Yang, Ge, et al. 2014).

The use of biogas as fuel in diesel engines is particularly suitable, as biogas has a relatively high octane number of about 130 (due to the presence of CH_4), thereby exhibiting greater resistance to phenomena such as knock and autoignition, and making it appropriate for use in engines with high compression ratios (Tricase & Lombardi 2009; Sahoo et al. 2009). Since biogas has an autoignition temperature of 1087 K (Bora et al. 2014), and the air temperature reached at the end of the compression stroke in a CI engine is about 600 K, a small quantity of liquid fuel is needed to pilot ignite the biogas in a diesel engine. Consequently, this allows

burning very lean or diluted biogas and air mixtures, resulting in low temperature combustion, and hence reduced NO_x emissions. Additionally, since biogas has lower carbon content compared to conventional diesel fuel, the use of biogas as the primarily fuel, with only a small amount of pilot diesel fuel, results in a significantly lower carbon pollutant emissions (CO_2 and particulates). Therefore biogas-diesel fuel co-combustion in CI engines has potential both economically and environmentally, providing low pollutant emission combustion while still maintaining diesel fuel comparable efficiencies (Yoon & Lee 2011; Bora et al. 2014). There have been many studies conducted in the past investigating the practical advantages of utilizing biogas in CI engines, as well as studying the combustion characteristics of biogas obtained from various feedstock materials. Bari (1996) studied the effect of CO_2 concentration in biogas run diesel engine. An increase in BSFC was reported for CO_2 concentrations above 20 – 30 % by volume in the biogas, as CO_2 acts as an inert gas in the combustion chamber, absorbing energy from the combustion flame and affecting the burning velocity of the biogas-air mixture. However, a slight decrease in BSFC was seen below 20% CO_2 concentration, which was speculated to be due to oxygen radicals, released via dissociation of CO_2 , reducing ignition delay and enhancing carbon oxidation. Henham & Makkar (1998) did similar tests, making use of simulated biogas to represent the varying quality of biogas, in terms of $\text{CH}_4:\text{CO}_2$ ratios, available from

different sources. The effect of CH₄ proportion in biogas and of the quantity of pilot fuel was studied on a two-cylinder diesel engine, over a range of engine speeds and loads. The results indicated the possibility of 60% substitution of diesel fuel with biogas without knock, however, the thermal efficiency was observed to drop as diesel fuel was replaced with biogas. Duc & Wattanavichien (2007) reported no deterioration in performance of a premixed charge biogas-diesel fuelled indirect injection engine at all the tested engine speeds. At low engine loads, the energy conversion efficiency was seen to be less compared to diesel only mode, but was comparable to diesel fuel conversion efficiency at high loads. Additionally, lower exhaust gas temperatures were reported for biogas-diesel dual fuel combustion at all engine loads and speeds, while high cooling water and lubricating oil temperatures were observed at high engine loads and high engine speeds. Tippayawong et al. (2007) successfully ran long duration endurance tests (about 2000 hours) on a small direct injection diesel engine operating on biogas-diesel fuel mixtures, to demonstrate the feasibility of using biogas in real-world situations. Maizonnasse et al. (2013) suggested heating the biogas before it enters the engine is a potential way to increase its combustion efficiency.

Other investigations have also examined the effect of biogas-diesel co-combustion on exhaust gas emissions. Bedoya et al. (2009) tested the performance of a DI diesel engine with simulated biogas (60% CH₄ - 40% CO₂), utilising a supercharger and a

Kenics mixer system in the intake. The authors reported that the supercharged mixing system allowed almost complete diesel substitution by biogas (except for a small quantity of pilot fuel), increased thermal efficiency and reduced CH₄ and CO exhaust gas emissions. Yoon & Lee (2011) carried out an experimental investigation comparing combustion and emission characteristics of an engine operating on biogas-fossil diesel and biogas-biodiesel mixtures (dual fuel mode); the biodiesel was 100% methyl ester of soybean oil. An increase in ignition delay was observed for the dual fuel mixtures, as compared to diesel fuel only engine operation. This was attributed to the relatively low charge temperatures of the biogas-air mixture and high specific heat capacity of the biogas; the exhaust gas temperatures for the dual fuel engine operation were found to be lower than single fuel modes as well for the same reason. Both NO_x and particulate emissions were relatively low under dual fuel operation; the low NO_x emissions were attributed to the reduced in-cylinder gas temperatures, whereas the reduction in soot emissions was speculated to be due to the lower carbon content of biogas. A significant increase in HC and CO emissions was observed when running the engine in dual fuel mode. The increase in HC was attributed to unburned biogas in the combustion chamber persisting to the exhaust. From his investigation on biogas-diesel fuel co-combustion, Makareviciene et al. (2013) proposed that additional modifications to the engine, such as the use of EGR and optimization of diesel injection timing, are necessary to gain further

benefit from biogas. He reported that an engine with these modifications, running on biogas (95%CH₄-5%CO₂) and diesel fuel mixtures, gives thermal efficiencies comparable to that from diesel only operation, similar smoke levels in the exhaust, and a reduction of 1.5 times in diesel fuel consumption and exhaust NO_x emissions with negligible increases in HC and CO emissions. Bora et al. (2014) conducted experiments to determine the effects of changing the compression ratio (CR) on a biogas-diesel fuel mixture fuelled engine. A decrease in the minimum quantity of pilot diesel fuel, required to ignite the biogas, was observed with increasing CR. While a reduction in CO and unburned HC was observed, the NO_x and CO₂ exhaust emissions were reported to have sharply risen as the CR was increased. The authors suggested that since the combustion and emission characteristics of a biogas fuelled engine seemed to be a function of CR, higher CR engines should be explored to achieve the maximum advantage from biogas. Mustafi et al. (2013) carried out a comparative study between biogas and natural gas fuelled engines and reported a 12% reduction in NO_x and a 70% reduction in PM mass emissions for the gas-diesel dual fuel operation relative to diesel only combustion. Although unburned HC emissions increased in the case of both the gaseous fuels, the HC emissions were higher for biogas fuelling due to the presence of CO₂. An increase in BSFC and in the duration of ignition delay was observed when biogas was introduced in the

engine; the increases in BSFC and ignition delay were found to be proportionate to the amount of CO₂ present in the exhaust gas.

The increase in ignition delay when running CI engines on biogas-diesel fuel mixtures is disadvantageous as it results in higher premixed combustion and peak heat rates, leading to a reduction in engine efficiency, increase in exhaust emission levels (such as NO_x) and a possibility of causing damage to mechanical parts of the engine (Gunea et al. 1998; Agarwal & Assanis 1998; Stelmasiak 2002). The ignition delay increases due to displacement of intake air O₂ by the aspirated biogas, resulting in lower effective temperatures during compression and a reduced quantity of reactive radicals available at the start of combustion (SOC). Cacua et al. (2012) tried to overcome this problem by increasing the O₂ concentration in the intake air up to 27% by volume. A reduction in ignition delay was observed at all O₂ enrichment levels due to the higher amount of O₂ available for the combustion process. At the highest level of O₂ enrichment and 40% load condition, a 28% increase in thermal efficiency was observed (relative to non-enriched air), attributed to the increased rate of oxidation reactions and high flame propagation velocities. Considerable decrease in the exhaust emissions of methane and CO were also reported for all levels of O₂ enrichment.

Much emphasis is being placed nowadays on the extraction of biodiesel from non-edible seeds such as *Pongamia pinnata* (Karanja), *Scheleicheraoleosa* (Kusum) and

Madhuca indica (Mahua) (Raheman & Ghadge 2007). After oil is extracted from these seeds, the de-oiled seed cakes (which form about 75% of the total mass) are considered a waste by-product with potential to create environmental problems by releasing various toxic pollutant gases into the atmosphere. Barik & Murugan (2014) demonstrated the potential of the *Pongamia pinnata* de-oiled cake to produce biogas with approximately 73% CH₄ concentration (by volume), via anaerobic digestion. This biogas was tested in a DI diesel engine and the combustion and emission characteristics of the biogas-diesel fuel mixture were compared to diesel fuel only operation. A 36% increase in BSFC, while a 6.2% reduction in BTE was reported when using biogas-diesel fuel mixtures as compared to only diesel fuel. A significant reduction in NO, CO₂ and smoke emissions, but a considerable increase in CO and unburned HC was observed when diesel fuel was partly substituted by the biogas. The authors suggested that the use of biogas in diesel engines is desirable as it reduces exhaust emissions, decreases consumption of conventional diesel fuel and utilises energy stored in organic bio-waste.

2.5 Engine in-cylinder gas sampling

New insights about the diesel combustion process with modern combustion systems require knowledge of how combustion progresses within the engine cylinder. High pressure and temperature studies inside engine combustion chambers are particularly challenging due to extremely short reaction rates, with unsteady environment conditions posing further complications. Attempts to follow the course of engine in-cylinder combustion and evolution of intermediate species have been carried out by a number of investigators by means of both optical and physical sampling techniques. The application of optical diagnostic methods, despite possessing the advantages of higher spatial and temporal resolution, and being of a non-intrusive nature (Nowak et al. 2008), are particularly difficult to apply in diesel engines, as robust optical access to the combustion chamber is required. Considerable density and composition gradients of species concentrations can occur across the cylinder and the wide-ranging spectrum of blackbody radiation from carbon soot particles can eclipse spectral radiations emitted by other in-cylinder species (Turns 1996). Furthermore, optically accessible engines often run at lower compression ratios than commercial engines and are not sufficiently suited for running continuous, long duration tests, not only because of possible thermal fatigue but also because the optical windows can get covered with combustion deposits and require cleaning at frequent intervals (Zhao & Ladommatos 2001). Physical sampling techniques, where samples are extracted after combustion, have

been applied to shock tubes and rapid compression machines which replicate some of the characteristics of combustion in an engine (Roblee 1961; Beeley et al. 1980; Shiga et al. 2002; Würmel et al. 2007; Thi et al. 2014; Gowdagiri et al. 2014). Similarly, many research and commercial engines readily allow analysis of the composition of the engine exhaust. Since only the end products of the combustion process can be sampled and analysed, these methods do not provide significant insight as to the composition histories of the combustion and pollutant intermediates. Total cylinder dumping has been used as a method of extracting time-resolved in-cylinder gas samples and involves the rapid emptying of the entire contents of the cylinder during combustion, at a selected crank angle, into a sample collection bag or vessel (Voiculescu & Borman 1978; Liu & Kittelson 1982; Kittelson et al. 1986; Kittelson et al. 1988; Pipho et al. 1992). Since the entire contents of the combustion chamber are extracted, this technique is not able to provide spatially resolved in-cylinder information (Zhao & Ladommatos 2001).

Timed, fast in-cylinder sampling is an attractive approach that can provide spatially and time-resolved quantification of stable species formed in the course of combustion. With this approach, sampling can be timed so that the extraction of the gas sample from the cylinder occurs at a specific narrow crank angle window. In-cylinder gas sampling valves have been employed in internal combustion engines to improve understanding of various physical and chemical processes associated with combustion; such as the phenomena of knock in spark-ignition (SI) engines

(Lovell et al. 1927) and diesel fuel-air mixture distribution in compression-ignition (CI) engines (Nightingale 1975; Bennethum et al. 1975; Rhee et al. 1978). In recent years, advanced gas sampling techniques have been developed with the aim of comprehensively understanding the in-cylinder processes which lead to pollutant emissions such as NO_x and PM, and therefore develop methods of reducing the formation of these emissions. Heywood et al. (1980) carried out in-cylinder gas sampling experiments in a single cylinder spark-ignited CFR engine in order to investigate the contribution of unburned hydrocarbons, from the quench layers on the cylinder head and upper portion of the cylinder liner, to the exhaust emissions. Matsui et al. (1979) developed a special gas sampling cylinder head insert (with dual functionality as both a spark plug and a gas sampling valve) and used it to measure local fuel mixture concentrations within the spark electrode spacing, at the instant of spark discharge. Helium gas was used as a carrier gas for the collected gas sample and it was observed that the cyclic variation in fuel concentration at the electrode spacing increased with increasing percentage of EGR supplied to the engine. Turns & Borman (1980) investigated, in a steady flow rig, the extent to which a sampling valve can disturb the in-cylinder gas motion. Two types of in-cylinder gas sampling probes were used, one having intermittent and the other continuous sampling flow action. It was observed that the probe diameter affected the measured species concentration, by altering the fuel diffusion process. These

results are in agreement with similar studies carried out previously by various other investigators (Fristrom et al. 1957; Yanagi 1977; Hayhurst et al. 1977).

Aoyagi et al. (1980) used an electro-magnetic needle-type sampling valve (Tsukasa Sokken GSD-1A) in a direct injection compression-ignition (CI) engine to investigate the effects of injection timing, swirl ratio and combustion chamber shape on the formation processes of NO and soot. NO was observed to form during the early and middle stages of combustion at high in-cylinder pressures and temperatures, and peak NO concentrations were reached as in-cylinder mixture ratios neared stoichiometric conditions. Soot was reported to form rapidly during the initial stages of combustion in fuel rich zones within the flame, and was later oxidized due to the entrainment of air in the flame. Optimum swirl conditions were found to produce a more homogenous distribution of fuel and air throughout the combustion chamber, resulting in lower soot levels. Similar studies were conducted by Fujiwara et al. (1984) in which gas composition analysis was performed using gas chromatographic techniques, while a transmission electron microscope was employed to examine soot concentration and size distribution, and the spatial dispersion of soot particulates.

Liu et al. (1984) used a total cylinder sampling technique to study the effects of engine load, equivalence ratio, fuel injection timing and percentage EGR on NO_x levels within the cylinder of a passenger-type, single cylinder, indirect injection CI engine. The sampling valve used an explosively actuated cutter to cut a diaphragm

sealing the pre-chamber, when the sample was required to be collected; the valve has been described in detail by Liu & Kittelson (1982). Nitrogen gas was used to dilute the sample in order to arrest the chemical reactions, and the diluted sample is filled into a Teflon sampling bag for analysis. NO_x concentrations were observed to increase after the end of the ignition delay period and reach a maximum at 10 CAD ATDC, and then decay towards exhaust concentrations. Peak NO_x concentrations increased by 45% when equivalence ratio was increased from 0.38 to 0.94. The ratio of peak in-cylinder NO_x to exhaust NO_x emissions increased with increasing engine load. Advancing of fuel injection timing led to an increase in both peak and exhaust NO_x concentrations, i.e. a 33% increase in exhaust NO_x and a 50% increase in peak in-cylinder NO_x concentration was observed when the fuel injection timing was advanced by 10 CAD. The addition of 11.5% EGR decreased NO_x concentrations by 33%. The experimental results were in good agreement with model predictions made using stochastic combustion models for this engine (Liu & Kittelson 1982).

Barbella et al. (1989) used a stainless steel, water cooled, electro-magnetic needle-type sampling valve to collect in-cylinder gas samples in order to study the composition histories of soot, light and heavy hydrocarbons and NO_x emissions in a direct-injection CI engine. Liquid and gas chromatographic techniques were applied to analyse the chemical transformations that paraffinic, and mono-aromatic and poly-aromatic compounds in diesel fuel undergo during combustion. Samples

were collected every cycle and sampling durations of 1 ms at an engine speed of 1200 rpm were achieved. The concentration of heavy hydrocarbons decreased during early stages of combustion and their profile matched the consumption of fuel. Paraffinic and aromatic fuel compounds decreased rapidly during injection and a concurrent increase in oxygenated fuel compounds was observed. The total PAH concentration was seen to reduce during the early stages of combustion and a preferential conversion of light alkylated PAHs was observed. NO_x formation occurred mainly in the premixed burning phase in the presence of high pressures and temperatures reaching peak values during the diffusion burning phase of combustion. Maximum soot concentration was also observed in the diffusion burning phase. Heavy hydrocarbons were detected during the late part of the cycle and their similarity with the original fuel suggested that part of the later-injected fuel quenched on the chamber walls and survived oxidation.

Ozasa et al. (1991) used an electromagnetically actuated needle-type sampling valve similar to the one used by Aoyagi et al. (1980), in conjunction with a catalytic oxygen sensor, in a single cylinder, 4-stroke, dual spark plug SI engine. The sampling valve was installed in place of one of the spark plugs and the effect of swirl ratio on the air-fuel mixture strength (measured using the oxygen sensor) near the spark plug was investigated. The swirl ratio was varied by using three different piston bowl shapes. The global air-fuel ratio was found to be similar to the local mixture strength at the spark plug for all three piston bowl shapes and decreased

as the engine cycle progressed due to air entrainment. The fuel injection timing significantly influenced the air-fuel ratio but only for the piston bowl shapes which maintained the swirl motion. NO_x emissions were also seen to vary significantly with fuel injection timing but only for piston bowl shapes which maintained the swirl ratio of the combustion chamber. It was suggested that NO_x emissions were considerably dependent on the homogeneity of the air-fuel mixture in the combustion chamber.

Zhao et al. (1996) developed an in-cylinder poppet-type gas sampling valve, based on the percussion principle, with an electromagnetically actuated armature and a proximity sensor to measure valve lift. This sampling valve was used to extract in-cylinder gaseous samples from a direct injection CI engine, at various instants during the engine cycle, so as to follow the in-cylinder composition histories of NO_x , CO, CO_2 and soot emissions. NO_x concentrations were found to increase rapidly after combustion and reached peak levels within 1 ms of the start of combustion before subsequently declining to similar concentration levels as those measured in the engine exhaust. EGR was seen to be very effective in reducing NO_x concentration in the in-cylinder gases. However, EGR also resulted in a significant increase in soot concentrations, with the peak particulate concentration in the cylinder found to be at least 20 times greater than the exhaust particulate concentration. Electron microscopy and chemical speciation techniques were also employed to assess soot particulate sizing; individual soot spherules appeared to be

larger at 40 CAD ATDC relative to those observed at 10 CAD ATDC and 150 CAD ATDC.

Kato et al. (1997) applied an in-cylinder gas sampling technique to determine the concentrations of the soluble organic fractions (SOF) and the insoluble fractions (ISF) of PM at different locations within the combustion chamber. High concentrations of SOF and ISF were reported when sampling along the spray flame axis, with both SOF and ISF concentrations higher when sampling closer to the chamber wall.

More recently, Nowak et al. (2008) utilized a gas sampling technique to measure the in-cylinder concentrations of various stable intermediate species during the HCCI combustion cycle and provide insights on fuel oxidation. The sampling probe featured an in-built N₂ dilution system and channels for oil circulation to regulate valve temperature, and was installed in the spark plug hole of a CFR engine; sampling times of 0.6 ms were achieved with satisfactory repeatability. The maximum concentration of combustion products observed during the high temperature reaction regime, and the major species produced during these reactions, were found to be the same as those measured in the exhaust gas. Of the exhaust THC concentrations, 70% were reported to be unburned fuel species mostly from the in-cylinder surface boundary layer, where low temperatures prevented oxidation. Dumitrescu et al. (2009) carried out a computational study to determine the optimum sampling valve design (including the method of surface cooling and inert

gas flow specification) required to arrest the reaction chemistry in an extracted sample for high resolution determination of particulate loading. The authors suggested that the sample valve length should be kept as short as possible to prevent adherence of soot on the valve inner walls, and the flow of an inert gas was necessary to quench sample reactions as valve wall cooling alone was insufficient in this respect.

2.6 Conclusions

The following conclusions can be reached from the discussion on the processes involved in diesel fuel combustion and emissions formation in a compression ignition engine:

- The diesel fuel combustion process can be divided into multiple stages: the ignition delay period which consists of low temperature fuel breakdown, while the air entrains into the injected diesel fuel spray, followed by autoignition at multiple sites where the fuel and air had mixed within combustible limits prior to autoignition, accompanied by a rapid discharge of heat energy during the premixed stage, and the remaining fuel combusting during the diffusion-controlled stage.
- A variety of optical techniques, including laser diagnostic methods (PLIF, Rayleigh scattering, chemiluminescence, etc.), were used to provide an in-cylinder timeline of diesel fuel consumption and define zones of varying fuel-air mixture stoichiometry in the flame structure.
- The formation of NO_x via the thermal (Zeldovich) mechanism, which involves the breakdown of atmospheric N_2 , is the dominant NO_x reaction mechanism in compression ignition engines. NO_x formation rates are kinetically controlled, and are highly dependent on in-cylinder gas temperatures and on the concentrations of N_2 and O_2 in the gas mixture.

- Soot formation in compression ignition engines commences with the process of fuel pyrolysis (fuel breakdown) followed by the formation of nuclei which act as reactive sites for the addition of gaseous hydrocarbon radicals (surface growth). The processes of coalescence and agglomeration follow, whereby particles clump together to form larger particles. The process of soot oxidation occurs concurrently with soot formation, and is significant in determining the ultimate soot emissions.
- The distribution of diesel exhaust particle size is trimodal: nucleation mode particles (5 – 50 nm diameter), accumulation mode particles (100 – 300 nm diameter) and the coarse mode particles (2 – 10 μm diameter).

From the literature available and previous studies conducted on the co-combustion of diesel fuel with a variety of gaseous fuel mixtures, the following conclusions can be made:

- The use of H_2 as fuel is beneficial in IC engines as it does not produce carbon-bearing pollutants from combustion. A review of literature suggests that the co-combustion of diesel fuel with H_2 has a varying effect on NO_x emissions, the primary reason for this lack of clarity being the different engine operating conditions used.
- Methane and hydrogen have a lot of complimentary properties; methane has a narrow flammability limit, low flame propagation velocity, high ignition energy requirement and excellent anti-knock properties, while relatively,

hydrogen has a wide flammability limit, high flame speeds and high adiabatic flame temperatures, but can suffer from anomalies such as knock and backfiring. The use of hydrogen-methane mixtures in IC engines has the potential to yield beneficial effects from their synergy.

- The combustion of biogas releases carbon dioxide that was originally fixed by the plant matter during photosynthesis, via the natural carbon cycle. The combustion of biogas decreases atmospheric CH₄ emissions, reduces liquid fuel consumption, allows lean burn operation, emits less carbon pollutants than the liquid fuel equivalent and under certain engine operating conditions is able to provide comparable thermal efficiency.

From previous investigations conducted using in-cylinder sampling techniques in IC engines, the following conclusions can be reached:

- In-cylinder gas sampling is an invaluable technique that can provide quantitative insight about the diesel combustion process and the evolution of intermediate species that ultimately form pollutants.
- A wide variety of timed gas sampling valves (needle type, poppet valve type, hydraulic actuation, electromagnetic actuation, etc) have been used by previous investigators in both SI and CI engines to extract in-cylinder gas samples for analysis, when investigating gasoline and diesel fuel combustion, respectively.

- The in-cylinder gas sampling methods have been used in conjunction with gas analysers, electron microscopy and chemical speciation techniques, and gas chromatographs and mass spectrometers, to analyse the constituents of the collected in-cylinder gas sample.

2.7 Gap analysis

A review of literature on in-cylinder gas sampling systems shows that it is quite an effective method for determining the change in the composition of the in-cylinder gases as the engine cycle progresses. The current method of collecting in-cylinder samples involves filling a bag which takes both time and can result in the condensation of low boiling point species in the sample, as the collected sample in the bag cools down to room temperature. There is a need to develop a sampling system which would (a) reduce the time for which the samples are collected from the engine cylinder and (b) reduce the duration between extraction and analysis of the samples.

The literature on H₂-diesel co-combustion suggests a varying effect on exhaust emissions, particularly NO_x and particulate exhaust emissions, with some researchers observing a significant increase in NO_x emissions with the addition of H₂ while others reporting a decrease in NO_x emissions. These conflicting reports could be due to different test conditions adopted by different researchers and therefore there is a need to undertake a comprehensive study on H₂-diesel co-

combustion whereby the amount of H_2 supplied to the engine varies from additive levels to the engine running primarily on H_2 .

A review of literature suggests that engines operating on CH_4 and biogas (typically CH_4 - CO_2 mixtures) suffer from issues such as increased ignition delay periods, low peak heat release rates, increased cycle to cycle variation and the occasional flame failure. The addition of H_2 to both CH_4 and biogas has the potential to counter these issues, since H_2 requires a very low amount of energy to ignite but has significantly higher flame propagation speeds (as compared to CH_4 and biogas).

3 Experimental setup

The present chapter describes the experimental facility including the single cylinder engine and the various systems that were utilised with the engine in order to conduct the experiments described in this work. These include the following systems: engine common-rail fuel injection, air super charging, gas delivery, exhaust gas analysis, instrumentation and data acquisition, and a high pressure low volume fuel system for use with non-conventional liquid fuels. The single cylinder engine, the common-rail fuel system and the air supercharging system were in place at the beginning of this project, while the rest of the systems were developed during the course of the project. Also described in the present chapter is the development of the design and manufacture of a novel in-cylinder gas sampling and analysis system which allowed the extraction of gas samples from within the combustion chamber of a running engine, and means of analysing their composition.

3.1 Single-cylinder engine

For the purpose of this work, a custom built 4-stroke single cylinder research engine with direct fuel injection was utilised. The cylinder head, intake manifold, fuel injector, piston and connecting rod (along with the associated bearings) were taken from a production 2.0 litre four cylinder turbocharged automotive diesel engine (Ford Duratorq 2.0 CD132 130PS), in order to preserve realistic engine geometry. The cylinder head was mounted on an engine crankcase (Ricardo Hydra), with an adapter plate used to adapt the production four cylinder head into a single cylinder arrangement. The combustion chamber of the engine comprised of a flat roof with four valves (two intake and two exhaust) and a centrally located fuel injector, in conjunction with a ω shaped bowl piston. A schematic of the section through the engine head and crankcase is shown in Figure 3.1, and the specifications for this engine are listed in Table 3.1. The engine crankshaft was connected directly to a David McClure dynamometer, which can motor the engine up to 5000 rpm. When the engine is firing, the dynamometer is able to hold the engine at a constant speed, by absorbing and adjusting the torque resistance offered to the engine. The dynamometer is not configured for transient operation, and is therefore more suitable for experiments run at constant speeds. The dynamometer was driven by the thyristor power unit and controlled by a Cussons test-bed control rack. A 58x tooth wheel with a Hall Effect sensor and shaft encoder were fitted on the front end of the crankshaft (Figure 3.2). Additionally, a camshaft sensor mounted on the

cylinder head provided a reference signal when the piston was at top dead centre (TDC). The signals from the crankshaft and camshaft sensors were used by the injection control systems, to control the timing and duration of fuel injection. The crankshaft encoder provided 1800 pulses per revolution as well as a reference signal per revolution to indicate piston TDC, both of which were used for the data acquisition system.

A high pressure and temperature piezoelectric pressure transducer (Kistler 6056A) was used in conjunction with a charge amplifier (Kistler 5018) to measure in-cylinder pressure. The pressure transducer was installed where the glow plug is normally mounted in the production head, and a glow plug adapter (manufactured by Kistler) was used to house the pressure transducer in the engine head. As the in-cylinder pressure transducer was of the piezoelectric type, it required reference to a known absolute pressure. This was accomplished by setting the in-cylinder pressure, once every engine cycle when the piston was at BDC, to the inlet manifold pressure which was measured with a piezoresistive pressure transducer (Druck PTX 717-3275) installed 160 mm upstream of the inlet valves.

Engine head model	Ford Duratorq
Engine crankcase model	Ricardo Hydra
Number of cylinders	1
Bore	86 mm
Stroke	86 mm
Swept volume	499.56 cm ³
Compression ratio (geometric)	18.3 : 1
Maximum in-cylinder pressure	150 bar
Piston design	Central ω - bowl in piston
Fuel injection pump	Delphi single-cam radial-piston pump
High pressure common rail	Delphi solenoid controlled, 1600 bar max.
Diesel fuel injector	Delphi DFI 1.3 6-hole solenoid valve injector
Electronic fuel injection system	1 μ s duration control
Crank shaft encoder	1800 ppr, 0.2 CAD resolution

Table 3.1: Single cylinder engine specifications

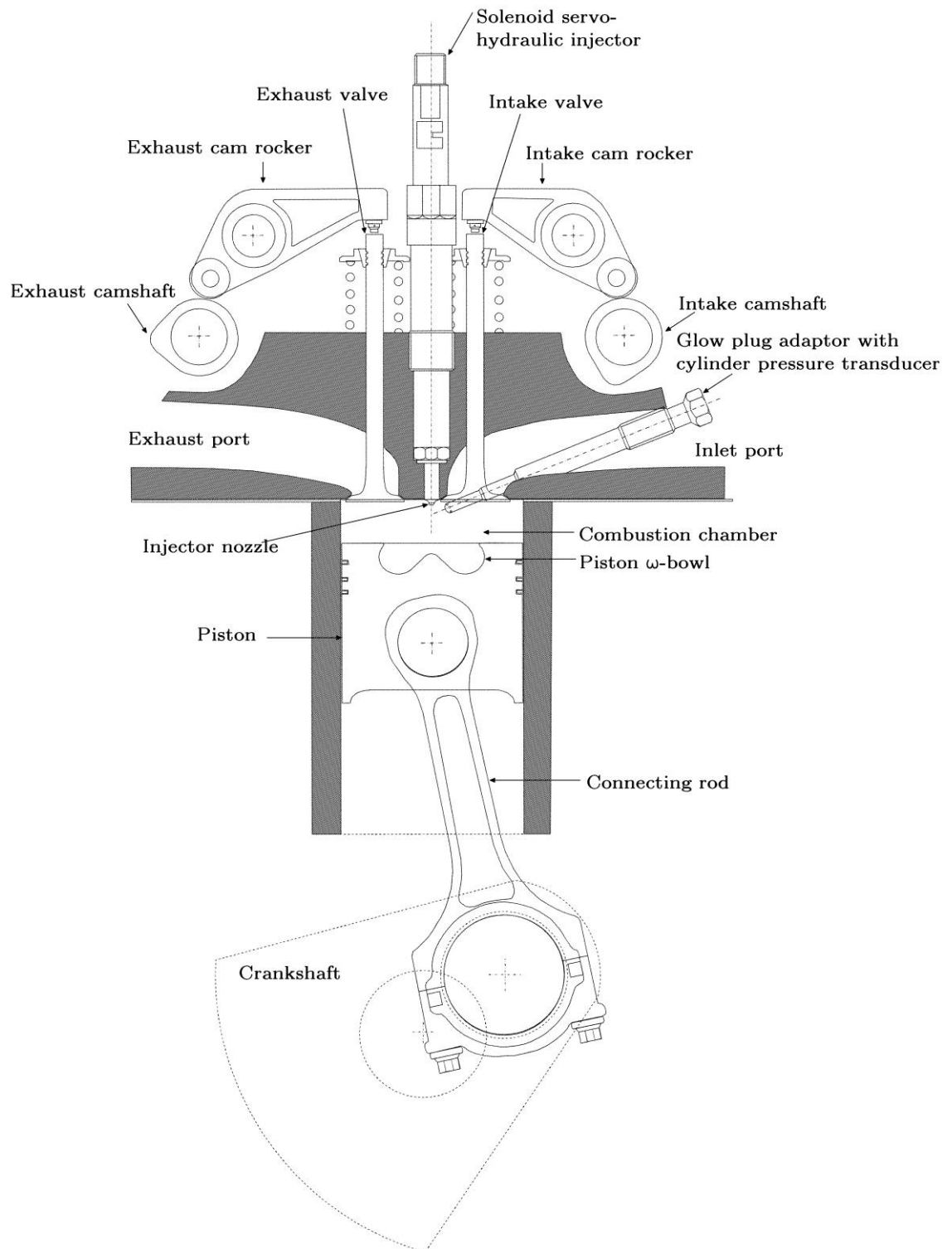


Figure 3.1: Schematic showing a section through the cylinder head and crankcase of the research engine (Schönborn 2009)

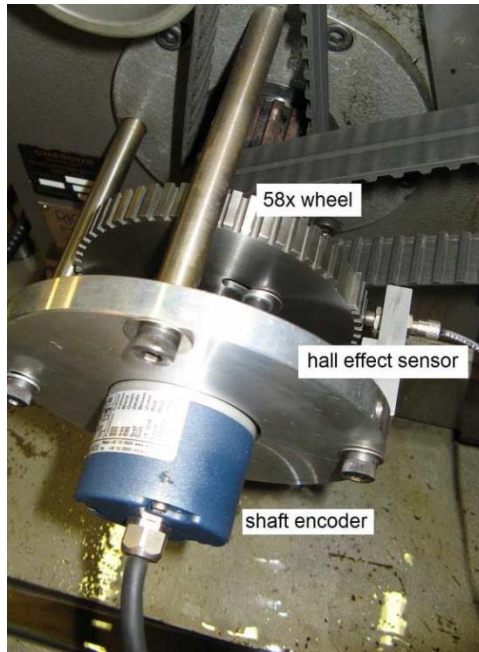


Figure 3.2: 58x wheel and shaft encoder mounted on the front end of the crankshaft

The engine can be run naturally aspirated as well as with the intake air pressurised (boosted) using an air supercharged system. When the engine was operated in naturally aspirated mode, the engine intake air was inducted from the surrounding atmosphere, through a filter, a positive displacement volumetric air flow meter (Romet Type G65) and a plenum (damping chamber), before entering the intake manifold. Flexible hosing of diameter 52 mm was used to connect the various components of the air intake system. A piezoresistive pressure transducer (Druck PTX 717-3257) and a K-type thermocouple were placed at the inlet of the air flow meter, to enable conversion of volumetric flow rates to mass flow rates.

The exhaust gas exited from the exhaust port of the engine and was conveyed to a silencer through a steel tube of diameter 53 mm, and then evacuated from the silencer by the extraction system of the laboratory. The exhaust pressure (measured

head, however the coolant circuit was not pressurised. Various sensors placed around the test bed measured the oil temperature and pressure and the coolant temperature and level, and in the case of any fault the engine was shut off automatically. Figure 3.3 shows the oil and coolant system which is a part of the Cussons test-bed.

3.2 Common rail fuel injection system

A high pressure common-rail fuel injection system, similar to those found on many modern automotive compression-ignition engines, was used with the engine. The fuel injection system consisted of a header tank, high pressure fuel pump, common rail, heat exchanger and fuel injector. Figure 3.4 shows the schematic of the fuel injection system, including the heat exchanger used for cooling the fuel.

The header tank (volume 2 litres) was mounted 350 mm above a crankshaft driven, self-lubricating fuel pump (Delphi 33100-4X400), so that diesel fuel flow to the pump could be assisted by gravity. An inline fuel filter (Delphi HDF924) was installed between the header tank and fuel pump to remove any particles in the diesel fuel which could potentially block the injector nozzle holes. The fuel was pumped into the high-pressure common rail (Delphi B47KA, maximum operating pressure 2200 bar) where the pressure was regulated by means of a pulse-width modulated pressure relief valve (PRV), installed at one end of the common rail. A pressure transducer was installed on the other end of the common rail and was used in

conjunction with the PRV to keep the pressure in the common rail at the level set by the user. The low pressure spill from the fuel pump, common rail and injector was combined and cooled by a counter-flow stainless-steel nickel fuel heat exchanger which utilized water as the cooling fluid. Cooling the spill is necessary as the fuel gets heated up due to compression in the fuel pump and the common rail. The flow rate of water to the heat exchanger was controlled by a proportional solenoid valve, and the voltage supplied to the proportional valve was automatically regulated by a closed loop feedback system, based on the temperature of the fuel spill. The cooled-down fuel spill was subsequently fed back into the fuel supply circuit upstream of the fuel pump.

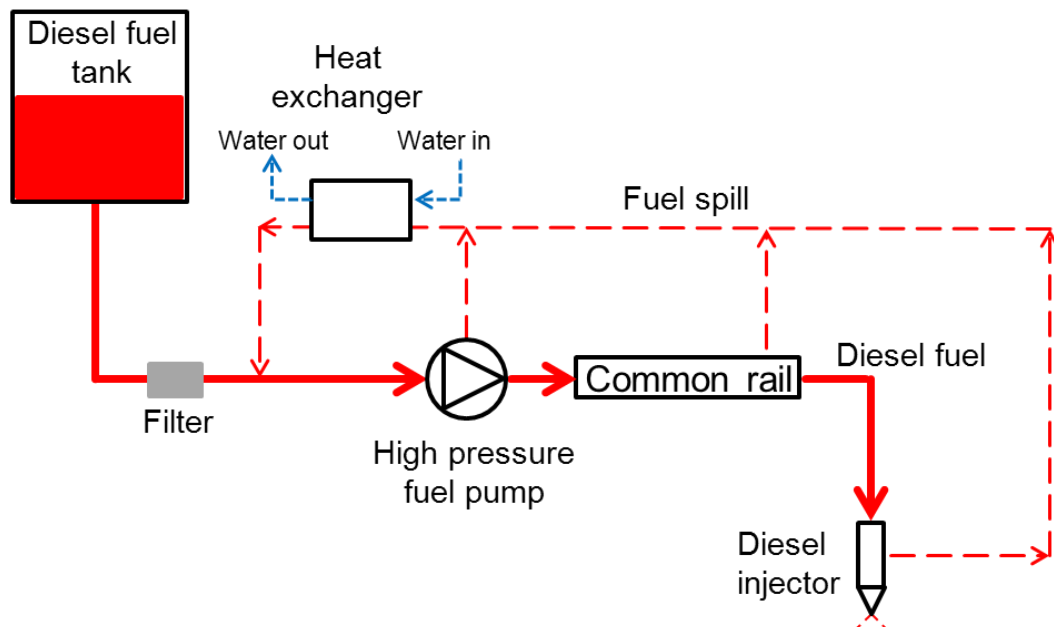


Figure 3.4: Schematic of the common-rail fuel delivery system, including the heat exchanger

A servo-hydraulic solenoid valve diesel fuel injector was used for the experiments, which had six holes in the nozzle, each of 154 μm diameter. Figure 3.5 shows the main features of servo-hydraulic fuel injector and operating principle of such an injector is described in the following lines. The high pressure fuel from the common rail (9) acts on the back of the needle and on the shoulder (6). When current is supplied to the solenoid (2), the valve ball (4) opens the valve control chamber (5) and fuel at the back of the valve plunger (11) bleeds into the fuel return (1). This relieves the pressure acting at the back of the needle, and the higher pressure acting on the nozzle needle pressure shoulder (6) rapidly lifts the needle, letting fuel through the nozzle holes (7). Injection parameters such as response time and needle lift of the injector can be finely-tuned through optimization of the size of the outlet (8) and inlet (10) restrictors.

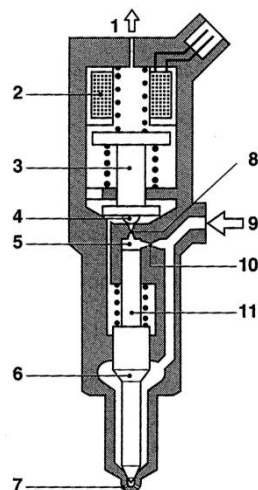


Figure 3.5: Servo-hydraulic solenoid-injector; (1) Fuel return, (2) Solenoid coil, (3) Solenoid armature, (4) Valve ball, (5) Valve control chamber, (6) Nozzle needle pressure shoulder, (7) Injector nozzle holes, (8) Outlet restrictor, (9) High pressure port, (10) Inlet restrictor, (11) Valve plunger (Bosch 2004)

3.3 Intake air supercharger system

An intake air supercharger system was deployed on the single-cylinder research

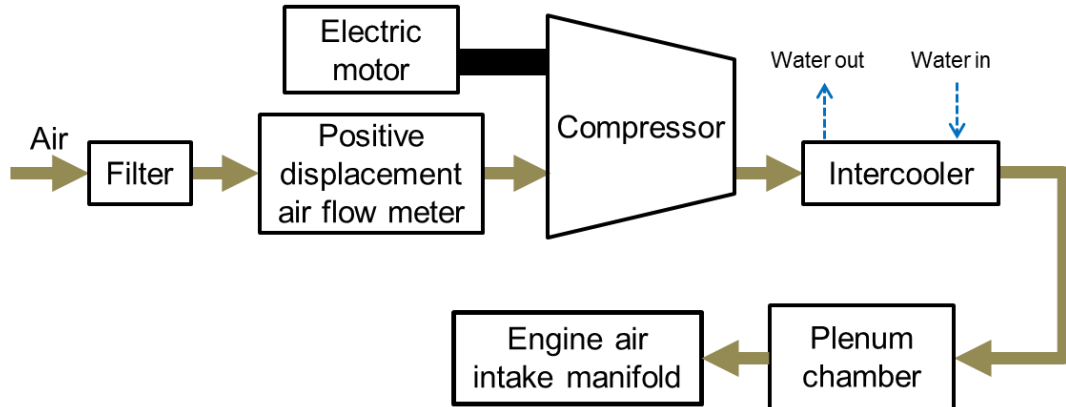


Figure 3.6: Schematic of the intake air supercharger system (air boost system) mounted on the single cylinder engine

engine to create test conditions that match a modern turbocharged engine, while allowing for independent control of intake air pressure and temperature. A schematic of the supercharger system, along with the associated air and water flows, is shown in Figure 3.6. The system contained a rotary screw super charger (Eaton, model M45), which was driven by an ABB variable speed electric motor via a drive belt. The rotational speed of the electric motor was controlled by a thyristor system with a signal voltage of 0-10V adjusted by means of a potentiometer. A relay switch was included in the supercharger electric circuit which cut power to the electric motor in the event of the engine being stopped either manually or due to any failure. This was done to prevent pressure build up downstream of the supercharger, in the event of the engine suddenly stopping. The air flow rate was determined using a positive displacement volumetric air flow meter (Romet Type G65), mounted before the supercharger, which has been described previously in Section 3.1. A Bowman

charge-air intercooler (which used laboratory water as the cooling fluid) was installed downstream of the supercharger in order to regulate the temperature of the pressurised air from the supercharger, and hence of the engine intake air. The flow rate of water to the intercooler was controlled by a proportional solenoid valve, and the voltage supplied to the proportional valve was automatically regulated by a closed loop feedback system, based on the temperature of the air. A plenum chamber with a volume of 50 litres (approximately 100 times engine displacement) was used as a damping box to dampen any pressure fluctuations from the supercharger. For safety reasons, the plenum chamber was fitted with three fast-acting pressure relief valves in order to vent the system quickly if the pressure in the chamber rose above 4 bar. A pressure transducer installed in the intake manifold (described in Section 3.1) was used to determine the inlet air pressure, and the speed of the electric motor was varied to adjust this pressure level.

3.4 Gas delivery system

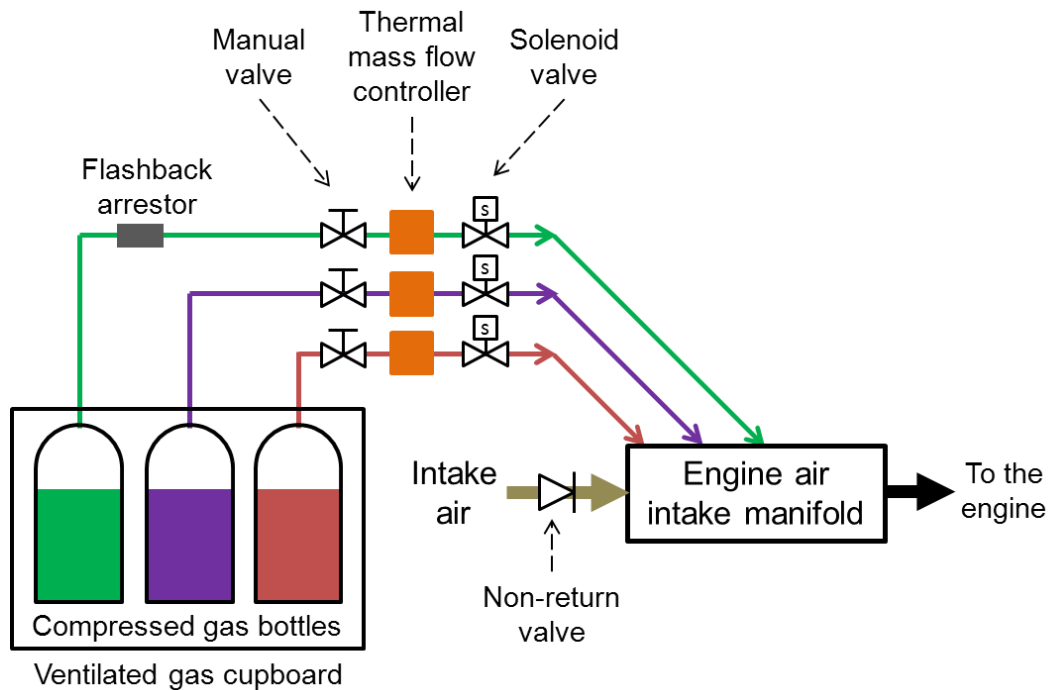


Figure 3.7: Schematic of the gas delivery system, and subsequent aspiration with the engine intake air

A major part of this project involved co-combusting diesel fuel and various gaseous fuels such as H_2 and CH_4 , and on occasion running the engine entirely on the gaseous fuel with the diesel acting a pilot ignition source. For this purpose, a gas delivery system was set up so as to safely transport the gas from the compressed gas bottles to the engine intake manifold, where it mixed with the engine intake air and was aspirated into the cylinder; a schematic of this setup is shown in Figure 3.7. Three thermal mass flow controllers (MFC), manufactured by Bronkhorst, were used to remotely control the flow rate of different gases, allowing mixtures of up to three gases to be supplied to the engine. Thermal MFCs make use of the heat conductivity of the gases to determine mass flow. Within the MFC unit, a flow resistance splitter (restrictor) placed in the primary flow path of the gas causes the

gas to flow through a secondary narrower pathway (by-pass) which houses the sensor. The sensor makes use of heaters and differential temperature measurement to provide a signal that is proportional to the gas flow in the by-pass. The ratio of the flow in the primary path through the restrictor and flow in the by-pass is precisely known and is kept constant. The electrical circuits within the MFC make use of the sensor signal and flow ratio to determine the mass flow rate of the gas. The flow rate can be varied by changing the size of the orifice in the flow control element of the MFC. The orifice size is changed by means of a solenoid-controlled valve plunger, which changes position based on the voltage signal supplied to the coil winding around the valve stem. All the three MFCs were calibrated to operate at 1 to 8 bar gauge inlet pressure and 0 - 1.5 bar gauge outlet pressure, and had an accuracy of $\pm 0.1\%$ of the full-scale reading. Two of the MFCs were a similar model (EL-FLOW F201AV-70K) and were calibrated to measure Ar, CH₄, C₂H₆, CO, CO₂, H₂, He, N₂, N₂O, air and O₂ up to a maximum flow rate equivalent to 70 l/min air flow. The third MFC (EL-FLOW F202AV-M20) could go up to higher flow rates, equivalent to 200 l/min air flow, and was calibrated to measure CO₂, N₂ and air. This MFC was typically used to simulate EGR like conditions in the engine, by aspirating large quantities of inert gases like CO₂ or N₂ with the engine intake air. However, all three MFCs could be used with a variety of other gases/gas mixtures by applying a conversion factor which could be obtained from an online Bronkhorst gas flow conversion tool.

Hand-operated ball valves were installed before the MFCs to manually shut off the gas flows when the setup was not in use. Electronically operated solenoid valves were mounted downstream of the MFCs, and relay switches placed in the electric circuit cut power to the solenoid valves (causing them to shut close, and hence stopping gas flow into the engine) in the event of the engine being stopped either manually or due to any failure. The pipes feeding the gas into the intake manifold were biased in the direction of flow (Figure 3.7), in order to reduce the likelihood of back flow. Additionally, a spring loaded non-return full-flow valve was installed upstream of the intake manifold to prevent gases from flowing back into the plenum chamber (Figure 3.6). The non-return valve opened at a very low pressure of 25 mbar in the air forward direction, and hence the pressure drop across the valve was insignificant. As an additional safety precaution, flashback flame arrestors were installed in the gas supply lines which carried flammable gases such as H_2 or CH_4 .

3.5 Exhaust and in-cylinder gas composition analysis system

The composition of the exhaust and in-cylinder gas (henceforth referred to as ‘sample’) was determined using an automotive exhaust gas analyser rack (Horiba MEXA 9100 HEGR) and a particulate spectrometer (Cambustion DMS500). The main analyser rack (Figure 3.8) was capable of measuring the concentrations present in the sample of the following species: CO, CO_2 , EGR CO_2 , THC, O_2 , NO and NO_x . While all the other analysers were located within the main rack, the fast

ionization detector (FID) sensor and the associated oven, which measured THC concentrations, was housed separately, and the signals from the FID were fed into the main analyser rack. The gas sample was conveyed from the engine to the analysers by means of two heated lines, which were maintained at 190°C to prevent condensation of any low boiling point species in the sample. One of the heated lines carried the gas sample to the main analyser rack where it was subjected to filtering and condensation of water vapour and gaseous hydrocarbons (by using coolers which reduced the temperature of the sample to 5°C before entering the individual analysers, while the other conveyed the sample to the FID for THC measurement. The following sections describe the operating principles of the various gas and particulate analysers.

3.5.1 CO and CO₂

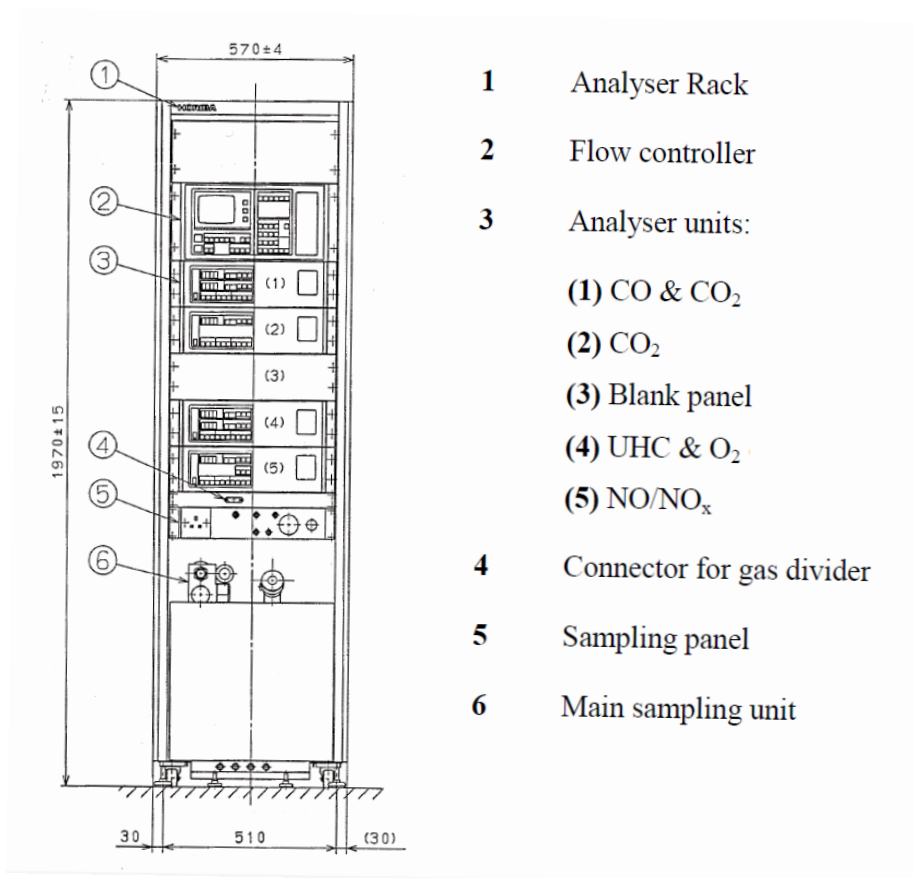


Figure 3.8: Horiba MEXA 9100 HEGR main analyser rack

The concentration of CO and CO₂ in the gas sample was measured using a non-dispersive infrared (NDIR) absorption analyser (Horiba AIA-120), located in one of the drawers of the analyser rack. This technique utilised the absorption of wavelength-specific infrared energy by CO and CO₂, and the degree of absorption was proportional to the concentration of the molecule present in the sample, at constant known pressure and temperature.

In a basic single NDIR detector system, as shown in Figure 3.9, two cells are placed in parallel with the sample gas flowing through one of the cells and an infrared-non absorbing gas (N₂) flowing through the other. An infrared beam passes through

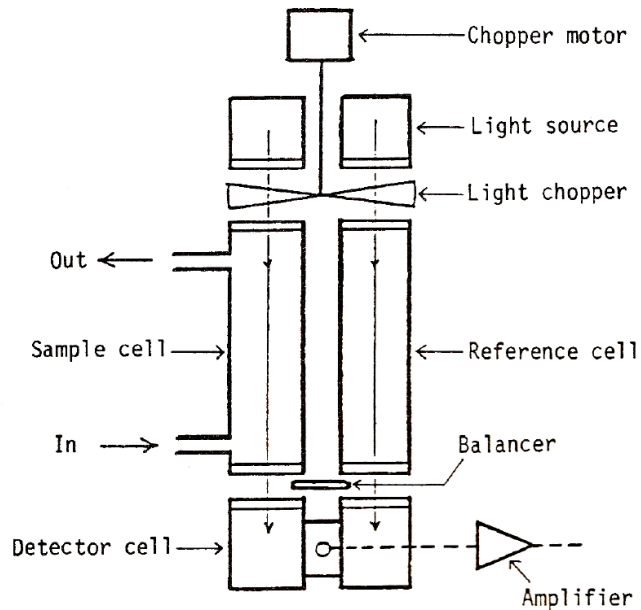


Figure 3.9: Schematic demonstrating the operating principle of the NDIR CO and CO₂ analyser (Horiba Instruments 1984)

both cells simultaneously, then exits the cells and enters a hermetically sealed detection cell. The frequency of the infrared beam is modulated by varying the speed of a rotating chopper wheel, and the intensity of the beam entering the detection cell is dependent on the level of absorption of the beam by CO or CO₂ in the sample. The beams result in the deflection of a metallic membrane within the detector, with the amount of deflection being proportional to the energy of the infrared beam. The deflection is measured by a capacitive sensor and a proportionate electrical output signal produced (Horiba Instruments 1984).

Two NDIR units were used in the analyser for measurement of different ranges of CO and CO₂. The first unit employed a dual detector system in order to be able to measure very low concentrations of CO (<3000 ppm) with a high accuracy. The two detectors were placed in series, with the first detector featuring infrared

transparent windows to allow the infrared beam to exit the first and enter the adjacent second detector cell. The first detector responds primarily to the sample and contributes only a small portion of the output signal produced by an interferent species (such as CO₂ in the case of CO detection). The second detector behaves in the opposite manner, and hence the eventual compensated composite signal that is produced has a very low influence from the interferent. The second unit is capable of simultaneously measuring CO₂ and higher concentrations of CO (>3000 ppm) and employs a stacked detector system. It is possible to measure the concentrations of both molecules from the same sample using two separate detector cells, if both species are present in similar concentrations in the sample, as the absorption wavelengths of CO and CO₂ do not overlap (Horiba Instruments 1984).

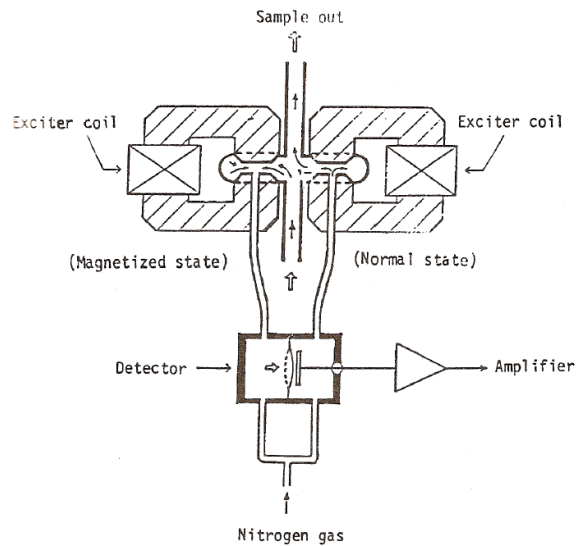
3.5.2 O₂

Figure 3.10: Schematic demonstrating the operating principle of the magneto-pneumatic O₂ analyser (Horiba Instruments 1984)

A magneto-pneumatic analyser (Horiba FMA-125) was used to determine the concentration of O₂ in the gas sample. The measurement was based on the principle that O₂ possesses a significantly higher paramagnetic susceptibility than the other gases present in the sample. Within the analyser, the sample gas flows past a pair of poles which are alternately magnetised by electromagnetic excitation of the coils. O₂ molecules are attracted towards the magnetised pole, which disrupts the flow of N₂ through the orifice located within the magnetic pole. The flow of N₂ through the orifice in the non-magnetized pole is not restricted, and the pressure differential of the N₂ between the two poles is converted by a detector (a condenser microphone) to an electrical signal proportional to the concentration of O₂ in the sample (Horiba Instruments 1984).

3.5.3 Unburned THC

The level of unburned total hydrocarbons (THC) is determined using a flame ionisation detector (FID) which consists of a controller module (Horiba FMA-125) located in the main rack and an external heated oven (Horiba FIA OV-04), which houses the FID sensor and is kept at 190°C. The gas sample passes through a hydrogen and air flame, located in the oven, resulting in the breakdown of hydrocarbon bonds into positive ions and electrons. Two electrodes, with opposing polarities, are positioned at either end of the flame and the ionisation of hydrocarbons results in a current being generated across the electrodes. The magnitude of the generated current is proportional to the number of carbon atoms ionised (Horiba Instruments 1984).

3.5.4 NO and NO_x

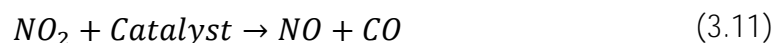
A chemiluminescent analyser (Horiba CLA-150) was used to measure the concentration of NO and NO_x in the gas sample. The gas sample is mixed with ozone (O₃) and fed into an evacuated reaction chamber to allow the NO and O₃ to react under reduced pressure conditions, resulting in the formation of NO₂. About 10% of the NO₂ formed is initially in an electrically excited state, and emits photons as it reverts back to the unexcited state (Equations 3.1 and 3.2). The resulting luminescence is proportional to the concentration of NO in the sample and is measured by a photosensitive diode, which produces a signal output. The reaction

chamber is kept evacuated using a vacuum pump (part of main analyser rack); the reduced pressure also decreases collisions between excited NO_2 and other molecules (for example, air molecules) thereby reducing interference from other species present in the sample.



(Where h = Plank's constant, f = frequency of light in Hz, * denotes the excited state)

The amount of NO_2 can also be measured using the chemiluminescent analyser by passing the entire gas sample through a NO_2 heated catalyst, prior to the sample entering the reaction chamber. The NO_2 dissociates in the presence of a heated catalyst to form NO,



The total NO concentration in the gas sample after passing through the NO_2 converter consists of the original NO and the converted NO (from NO_2). Thus, it is possible to detect the total level of NO_x in the gas sample by using the NO_2 converter. The analyser can be switched between NO and NO_x detection modes by routing the gas sample either directly to the reaction chamber or via the NO_2 to NO converter (Horiba Instruments 1984).

3.5.5 Particulates

A differential mobility particle spectrometer (Cambustion DMS500) was used to determine the number, size and mass of particles ranging between 5 and 1000 nm diameter. The operating principle of the particle spectrometer is to classify the particles according to their specific ratio of electric charge to aerodynamic drag.

Figure 3.11 shows the flow of the gas sample through the particle spectrometer.

The gas sample is carried from the sampling point on the engine to a heated remote cyclone (kept at 80°C) via a stainless steel pipe of length 250 mm. In the remote cyclone, the gas is diluted with heated dry compressed air at a ratio of 5:1 (ratio of air to sample) which serves two purposes: firstly, the dilution reduces the water dew point of gas sample to below the ambient operating condition of the instrument and secondly, diluting the sample reduces the particle concentration in the gas sample, thereby decreasing particle accumulation and extending instrument service intervals. The compressed air is carried to the remote cyclone via a heated line which was 5 m in length and maintained at 80°C. Additionally, the remote cyclone has an orifice fitted which removes, and thus prevents, particles greater than 1 µm in size from passing through. The pressure downstream of the orifice (and throughout the instrument) is maintained at an absolute pressure of 0.25 bar by an external vacuum pump. The sample is then carried from the remote cyclone via the heated line (in a separate PTFE pipe to the compressed air pipe for the remote cyclone) to a second dilution system, a rotating disc diluter, where the sample is

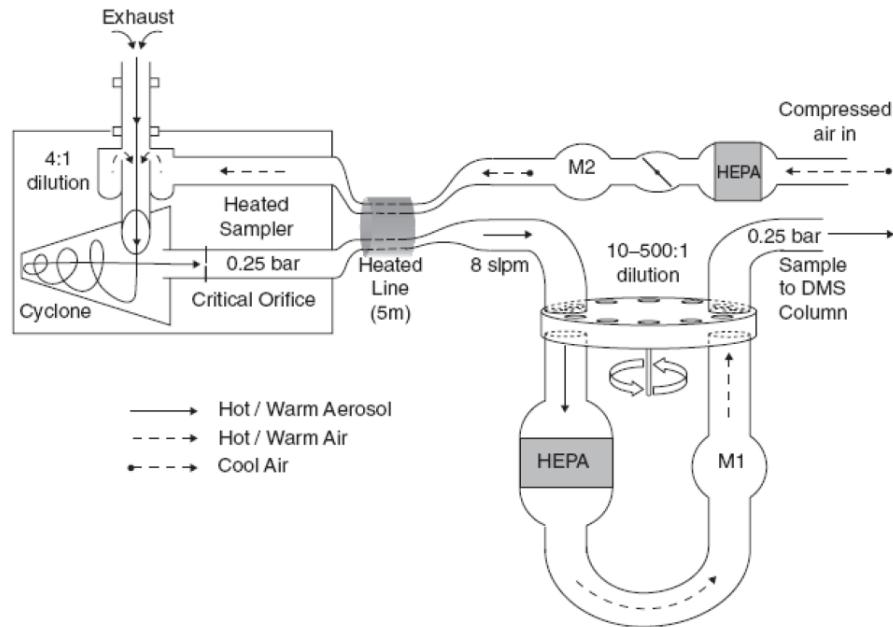


Figure 3.11: Schematic showing the flow of sample through the DMS500 (Cambustion 2011)

diluted by a ratio of 200:1 by compressed air. The flow rates of the dilution air and of the gas sample streams following dilution are precisely measured in order to be able to calculate the actual dilution ratios. After passing through the secondary diluter, the sample flows through a corona discharge charger, which adds a negative charge to the particles in the gas sample, and then into the classifier column (particle sizer) (Cambustion 2011).

The classifier column consists of a uniform cylindrical column of air flowing around a central high voltage electrode and surrounded by a sheath of particle free air. The sheath is surrounded by twenty two grounded rings, and the high voltage potential of the central electrode caused particles to deflect towards these rings as the sample gas passes through the classifier. The location at which the particle impacts inside the classifier, and hence the ring up on which the particle discharges, is determined

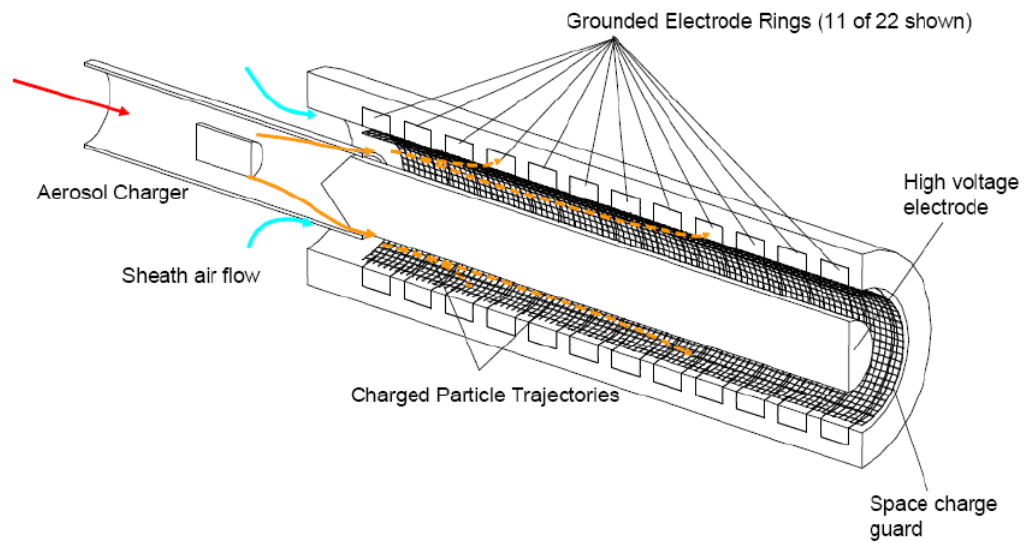


Figure 3.12: Classifier column of the DMS500 (Cambustion 2011)

by the mobility of the particles, and therefore depends on the size of the particle and the magnitude of charge it holds. The aerodynamic drag on the particles can be related to the particle diameter (assuming a spherical shape) and will thus affect the velocity of the particle as it travels through the classifier. Therefore by comparing the discharge current and ring location of particles in the gas sample to those of known particle sizes, the charge and diameter of the particles in the gas sample can be determined (Cambustion 2011). The total mass of particulates can be determined by making assumptions regarding the shape and density of the particles, and previous work has shown that a good estimate of the diesel particulate mass can be obtained from the particle mobility diameter (Park et al. 2003; Symonds et al. 2007).

3.6 Instrumentation and data acquisition systems

3.6.1 Control of diesel fuel injection pressure, timing and duration

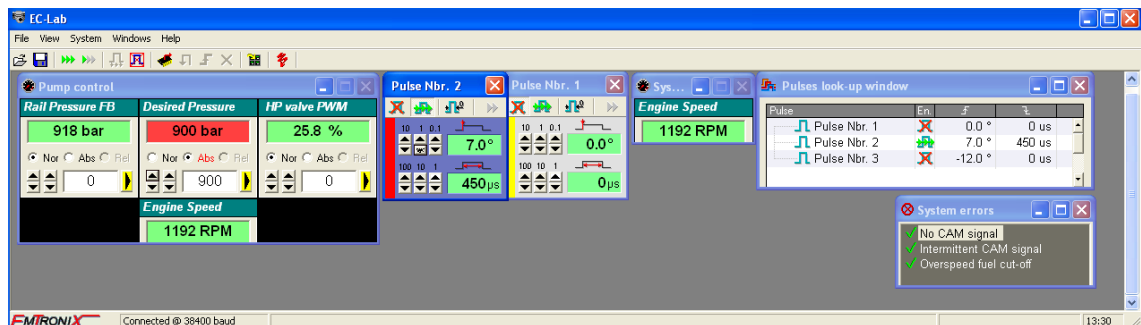


Figure 3.13: Screenshot of the fuel injection control program, Emtronix EC-Lab

The fuel pressure at the injector, the timing of the fuel injection and its duration were all controlled by multi-microprocessor electronic control system (Emtronix EC-GEN-500) in conjunction with a dedicated software program (Emtronix EC Lab) for PC interface. Signals from the Halls effect sensor mounted on the 58x flywheel and from the camshaft sensor were used by the Emtronix system to calculate engine speed as well as control the timing of fuel injection based on the piston TDC position. The common rail pressure, and hence the fuel injection pressure, was also regulated by the Emtronix unit by sending a pulse-width-modulated (PWM) current, of constant frequency and amplitude, with a varying ‘on’ period to the pressure relief valve (PRV) on the common rail, depending on the feedback signal received from the pressure transducer mounted on the common rail. The desired common-rail pressure, fuel injection timing (with reference to TDC) and duration of fuel injection could be set by the user to accuracy of ± 1 bar, ± 0.1

CAD and $\pm 1 \mu\text{s}$, respectively, on the EC Lab program. Additionally the Emtronix system allowed multiple injections, of up to 8 fuel injections, in an engine cycle.

3.6.2 Monitoring, control and acquisition of engine data

Engine experimental data was monitored in real-time and logged using data acquisition hardware from National Instruments (NI DAQ), which was used in conjunction with graphical programming software, NI LabVIEW. Bespoke and comprehensive NI LabVIEW programs were developed by the author in-house to acquire signals from various sensors, display engine parameters in real time, send signals to instruments, and process and log the acquired data. Multiple NI DAQ systems were used to record different sets of data as described in the following paragraphs.

A high speed data acquisition card, NI PCI-6254, was utilised to acquire pressure data from the various pressure transducers mounted in different locations on the engine (described in Section 3.1). The DAQ card had 16 multiplexed differential analogue input channels with a peak sampling rate of 1.25 MS/s (mega samples per second) served by a single analogue to digital converter, and 48 digital channels which could be used as either inputs or outputs. Data was acquired at a resolution of 0.2 CAD and was displayed and logged as one complete engine cycle, with the signals from the crankshaft encoder and from the camshaft sensor being utilised to accurately time the data with respect to engine piston TDC position. The once per crankshaft rotation signal from the encoder was synchronised through a solid state

AND logical control gate with once per camshaft rotation signal, to obtain a once per engine cycle reference signal. The LabVIEW program used this reference signal as a trigger to initiate an execution loop and start acquiring data samples for a single engine cycle. When the next reference signal was received, indicating the start of the subsequent engine cycle, the current execution loop stopped and new loop initiated. Additionally, the crankshaft encoder also supplied 1800 pulses per revolution which was used as the timing base; this meant that data samples were recorded every 0.2 CAD, and that 7200 samples were acquired every engine cycle. The following pressures were acquired (crank-resolved to 0.2 CAD) within this execution loop: in-cylinder pressure, air inlet pressure, air intake manifold pressure, exhaust gas pressure and fuel common-rail pressure. Engine geometry parameters were preloaded on the LabVIEW program, and were used to calculate various combustion characteristics (crank-resolved) in real time to allow better experimental control. These included: indicated mean effective pressures (IMEP), apparent heat release rates, time of start of combustion, time of peak heat release rate, cumulative heat release, total mass fraction burnt, pressure against volume (p-V) diagrams, global in-cylinder temperatures and entropy. The entropy and temperature data was used to determine the actual position of the piston TDC, according to the method described by Tazerout et al. (1999), since the reference TDC signal from the shaft encoder was not aligned with the actual piston TDC.

The misalignment between the two TDC positions could then be corrected by applying a crank angle offset between the reference trigger signal and piston TDC. Low pass filters could also be optionally applied to the acquired data to remove noise on the signals due to electrical interference from other equipment in the test cell. An ensemble average of the acquired raw data and of the processed combustion characteristics could be obtained and logged for a pre-set number of engine cycles. The LabVIEW program created a date stamped folder when it was started, and the logged files were stored in the folder in a sequential manner. A second execution loop consisted of a counter which measured the time between successive TDC reference signals to calculate engine speed. A third execution loop used the digital output channels of the NI DAQ card to send OPEN (5 V) or CLOSE (0 V) signals to electromagnetic solenoid valves (via solid state relays) installed at the access points of a dilution tunnel, which is part of the in-cylinder sampling system (as described in Section 3.7). Figure 3.14 and Figure 3.16 show PC screenshots of the NI LabVIEW program.

A second low speed data acquisition card, NI PCIe-6323, was used which was capable of sampling data at a rate of 250 kS/s (kilo samples per second) and had 16 differential analogue input channels, as well as 4 analogue output channels. This card (along with a dedicated NI LabVIEW program) was used to acquire temperature data and air flow rate readings. As this data varied relatively slowly

(as compared to the pressure data), there was no need have synchronization with the engine cycle and the data acquisition rate was fixed at a 1000 Hz. The collected temperature data was averaged and displayed every 100 samples, thus giving an apparent sampling frequency of 1 sample per second. This was done to reduce the effect of electronic noise on the thermocouple signal and reduce the amount of recorded data to a reasonable level. Audible and visual alarms were also configured in the LabVIEW program in case of significant deviation of temperatures from their expected (pre-set) values. The volumetric and mass flow rates of the intake air were also displayed in real-time, with the pressure and temperature readings at the air inlet used to calculate mass flow rate values.

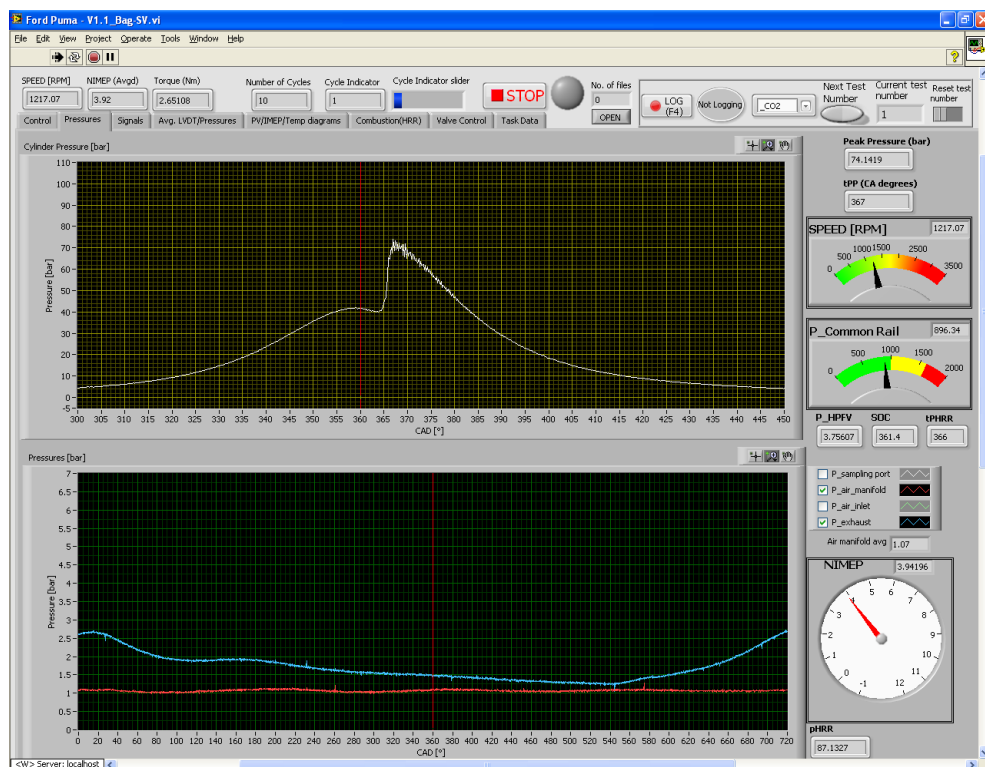


Figure 3.14: Screenshot of NI LabVIEW program showing pressure traces and other engine parameters

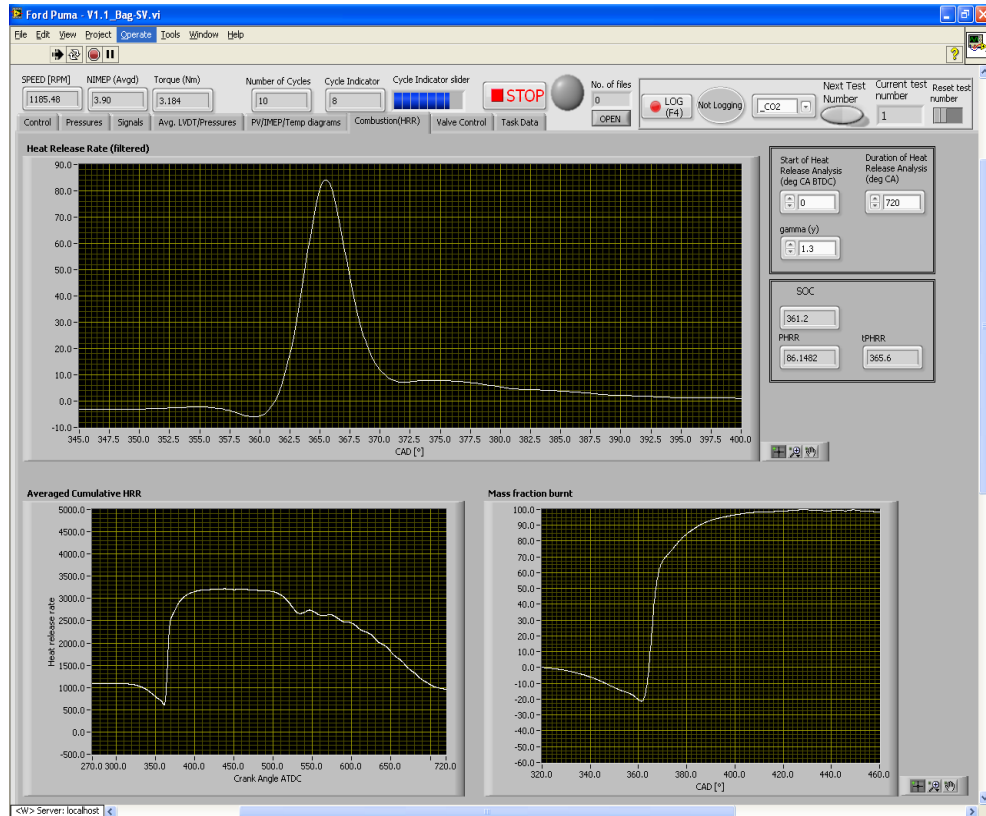


Figure 3.16: Screenshot of NI LabVIEW program showing heat release trace other combustion characteristics

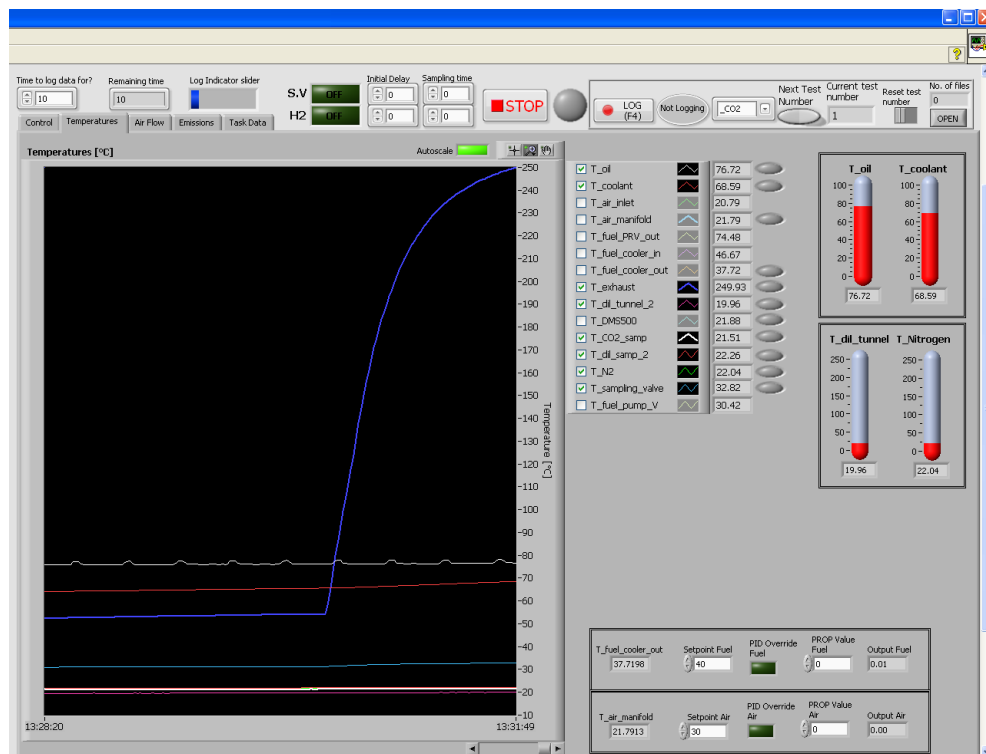


Figure 3.16: Screenshot of NI LabVIEW program showing the various temperature readings as well as the PID controls for the proportional solenoid valves

The analogue output channel of the NI PCIe-6323 was used to send an ‘on-off’ signal to the electromagnetic solenoid of the in-cylinder sampling valve (via a relay).

The charging duration of supplied current to the solenoid of the sampling valve could be varied by varying the duration of the ‘on’ period of the ‘on-off’ signal. The in-cylinder sampling valve and its control system will be described in detailed in Section 3.7.

A NI USB-6009 card with two analogue output channels (0 – 5 V) was used to set voltages for two proportional solenoid valves which controlled the water flow rate for the fuel cooler (Section 3.2) and for the supercharger intercooler (Section 3.3).

A PID control system program was written in NI LabVIEW for this purpose, and the output signals from the USB-6009 card were passed through a solid state amplifier, since the operating voltage of the proportional valve was higher (0 – 24 V) than the maximum voltage output from the card.

3.6.3 Control and monitoring of MFCs

The gas mass flow controllers used to control the flow rate of gases (such as H₂ and CH₄) into the engine. They were controlled and monitored using a combination of NI VISA drivers (which allow RS232 input signals to be read in LabVIEW) and suite of add-ins specially developed by Bronkhorst for use in the LabVIEW environment. Using these tools, a comprehensive program was developed by the author, which not only allowed the user to remotely set the gas flow rate through the MFC (by sending a signal to the proportional solenoid valve which controls the

orifice size), but also monitor the actual flow rate in real time (from the thermal sensor as described in Section 3.4). Additionally, the program allowed the user to select the calibration curve for a specific gas to be used in the MFC, as well as choose the most appropriate range within the operating limits of the MFC. A stop switch was configured within the program which immediately reset all the MFCs to their closed (zero flow) position if the gas flow rates went above pre-set values. A substantial amount of work for this thesis involved utilising more than one MFC at a time in order to feed gas mixtures into the engine. Furthermore, the test procedure was designed to vary the flow rate of the gas mixture (and keep the mixture composition constant) to achieve certain engine loads (IMEP). Controlling all three MFCs individually to attain a specific IMEP, while at the same time maintaining a constant mixture composition, was considered an inefficient and uneconomical way of conducting tests. Therefore, the LabVIEW program was

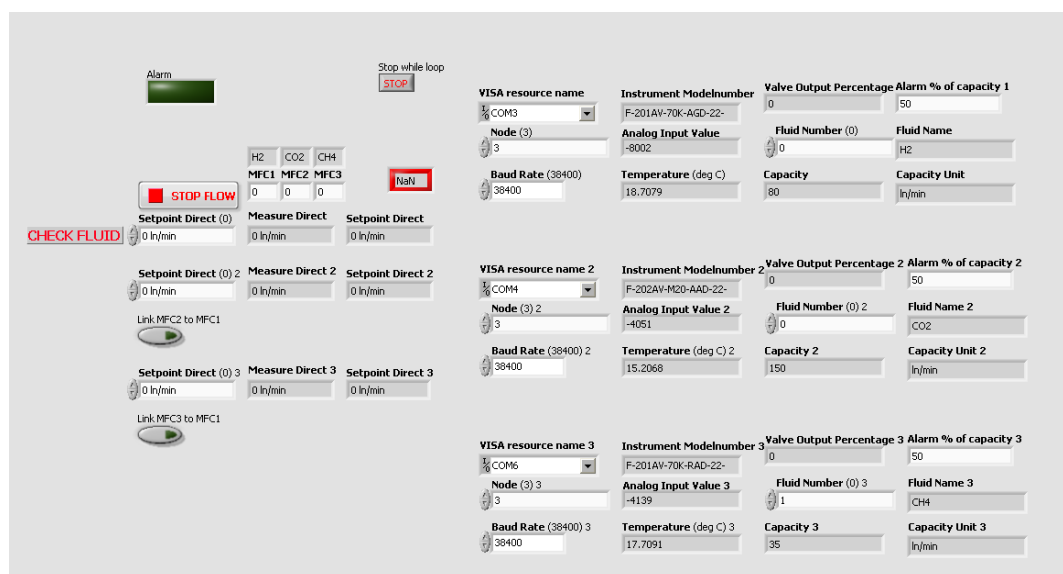


Figure 3.17: Screenshot of the MFC control and monitoring NI LabVIEW program

further configured to optionally link the signal outputs (which control the orifice size) of two or more MFCs. The required percentage composition of the gas mixture and the flow rate through one of the MFCs has to be fed into the program, and the flow rates of other linked MFCs are adjusted automatically based on the mixture ratios. A screenshot of the described program can be seen in Figure 3.17.

3.6.4 Exhaust analyser data acquisition

In order to read in the data generated by the gas analyser rack (Horiba MEXA 9100HEGR) into a PC, a GPIB to USB module (NI GPIB-USB-HS) was used. A LabVIEW program was developed by the author, using NI GPIB drivers, which allowed real-time monitoring and logging of the emissions data generated by the analysers. A screenshot of the LabVIEW emissions program is shown in Figure 3.18.

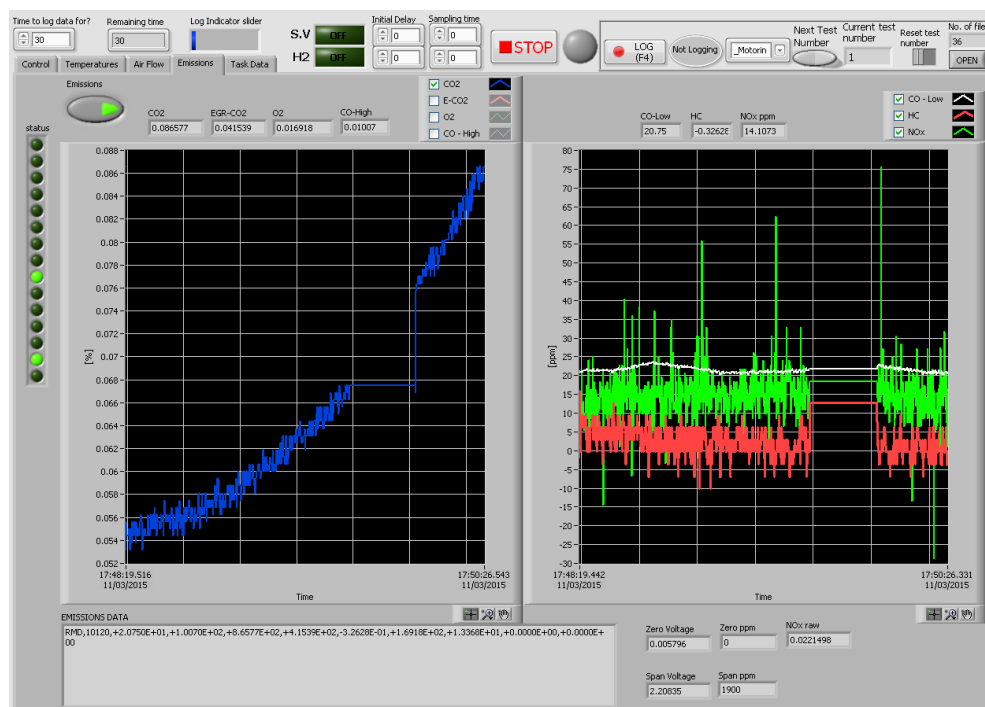


Figure 3.18: Screenshot of the NI LabVIEW emissions monitoring program

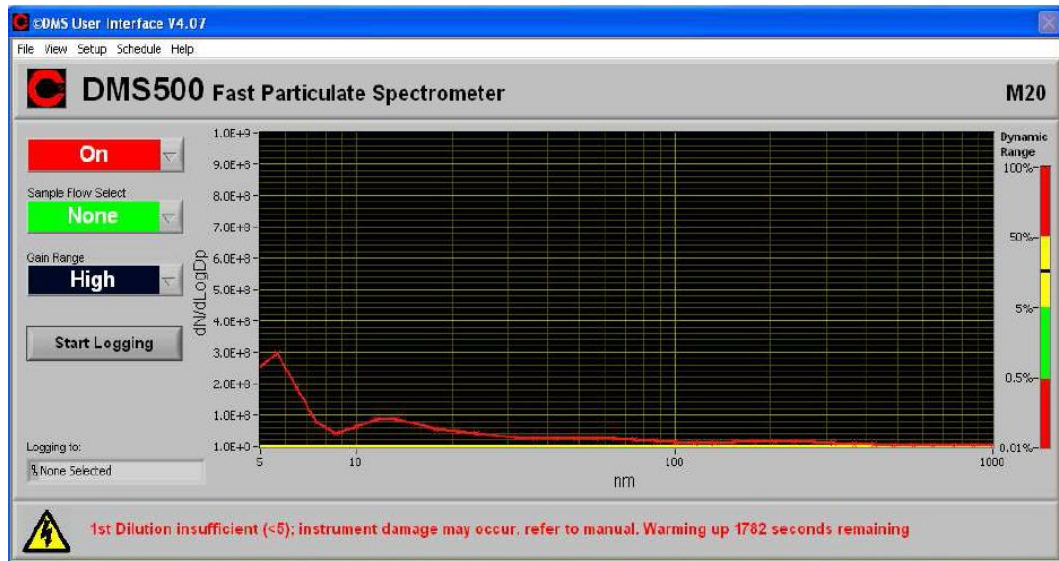


Figure 3.19: Screenshot of the Cambustion DMS500 particle spectrometer PC interface program

The particulate spectrometer (Cambustion DMS500) was controlled using a dedicated PC interface program supplied by Cambustion (DMS User Interface V4.10). The program allowed the user to switch the instrument ON and OFF, warm up the instrument prior to use, set the sample flow to OPEN or CLOSE, clean the instrument with compressed air after use, set the gain for the data being acquired, change the temperatures and dilution ratios of the different components in the instrument and record the acquired data. Additionally, the program also displayed the size distribution of the particles in real-time and the level of saturation of the particle detector (allowing the user to vary the dilution ratios to achieve optimum saturation). A screenshot of the Cambustion PC interface program is shown in Figure 3.19.

3.7 In-cylinder gas sampling valve system

A fairly high resolution gas sampling system to analyse engine in-cylinder gas composition would help enhance our understanding of in-cylinder processes that lead to the formation of pollutant emissions, especially when using future 'green' fuels. This section describes in detail, the development of a novel in-cylinder gas sampling system consisting of an intermittent, timed, high-speed, electromagnetically actuated, poppet-type sampling valve and a heated dilution tunnel. The sampling valve was extensively bench-tested for repeatability and durability, and to calibrate the valve at optimum operating conditions.

The in-cylinder sampling system (the sampling valve and the dilution tunnel) described in this section was developed to make the extraction and analysis of engine in-cylinder gas samples more efficient and accurate. In previous work done by investigators (Kittelsohn et al. 1988; Zhao et al. 1996; Nowak et al. 2008), the engine in-cylinder gas sample was collected in a bag, requiring a significant volume of sample to be collected (approx. 10 litres) so as to achieve steady readings from typical gas analysers. Since the volume of sample extracted from the cylinder every engine cycle is relatively small (approx. 4-6 cm³)(Zhao et al. 1996), filling a bag with sufficient volume can take considerable time. Furthermore, in the time interval between filling up a bag and analysing the collected gas sample, the sample cools down to room temperature, causing condensation of high boiling point species in the sample. In the current design described in this thesis, the gas sample was kept

at about 200°C from the point at which the sample was extracted from the cylinder to point at which the sample entered the analysers. The dilution tunnel system also allows gas composition analysis data to be obtained faster than with the use of a bag, as no buffer time is needed to collect the gas sample and the gas sample flows directly from the sampling valve to the analysers.

3.7.1 Sampling valve tip

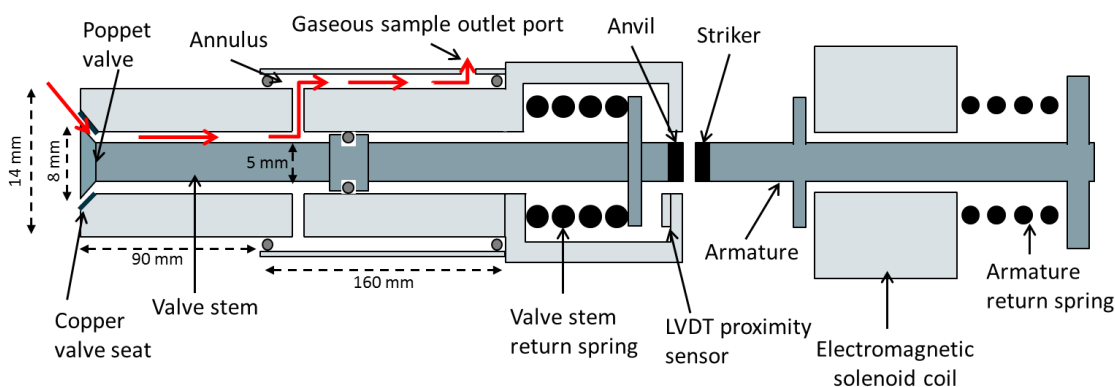


Figure 3.20: Simplified diagram of the in-cylinder sampling valve showing the gas flow from within the cylinder to the sample outlet port

Gas sampling valves can be broadly categorised in terms of the type of valve tip used. The most commonly used type of valve openings are the outward opening poppet-type valve and the inward opening needle-type valves. The gas sampling valve used in the present study has a poppet-type opening at the valve tip. In a poppet-type valve, the poppet is firmly seated in its seat due to the force provided by a pre-compressed return spring, with the in-cylinder gas pressure acting on the valve face providing an additional force and improving the seal at the valve inlet. An actuation mechanism pushes open the poppet valve, allowing gas to flow from the cylinder into the valve. Conversely, needle-type valves use the in-cylinder gas

pressure to push the valve open against the return spring force (Zhao & Ladommatos 2001); the force provided by the return spring must be sufficient to keep the needle-valve firmly shut against the high pressures of the combustion chamber. Both valves possess relative advantage and disadvantage; crevices in the sampling valve are avoidable in poppet-type valves as they can be machined flush with the combustion chamber surface, something which is not possible entirely in a needle-type valve (Zhao et al. 1996). However, needle-type valves have smaller tip diameters (Bennethum et al. 1975; Ozasa et al. 1991; Kato et al. 1997) compared to poppet-type valves (Withrow et al. 1930; Zhao et al. 1996), an advantage where access to the combustion chamber is difficult. A smaller tip diameter is also less likely to interfere with the gas flow inside the combustion chamber.

3.7.2 Valve actuation system

In a poppet-type valve, the actuation force required to open the valve must be sufficient to counter, and overcome the in-cylinder gas pressure and the compression force of the return spring. Most early examples of in-cylinder sampling valves were mechanically actuated by linkages using pushrods and rockers, driven by the engine crankshaft or camshaft (Lovell et al. 1927; Withrow et al. 1930; Egerton et al. 1935; Donahue & Kent 1950; Taylor & Rogowski 1954). Hydraulic actuation systems were also utilised in several investigations (LoRusso et al. 1980; LoRusso et al. 1984; Duggal et al. 1978; Zvonow 1968; Bäcker et al. 1997) as they are relatively space efficient, can provide forces sufficient to open the valve, are precisely controllable

and have a short response time (between 0.8 to 2 ms). In particular, the work done by LoRusso et al. (1980;1984) using the electro-hydraulic gas sampling valve led to new insight regarding unburned hydrocarbon emissions from the quench layer of cylinder walls in SI engines. However, the setup of hydraulic actuation systems tends to be more complicated than other actuation methods (Zhao & Ladommatos 2001).

An electromagnetic actuation mechanism was employed in the gas sampling valve presented in this study. In an electromagnetically actuated poppet-type sampling valve (Figure 3.20), as soon as current is supplied to the electromagnet solenoid, the magnetic flux build up in the solenoid causes the armature to move, thereby opening the valve. In order to ensure a very short opening interval of the sampling valve, a large electromagnetic traction force and high armature acceleration are required. The traction force can be increased by increasing the thickness of the armature allowing it to build up a greater amount of magnetic flux; however, this increases the weight of the armature and therefore lowers armature acceleration (Seilly 1981). Kajima & Kawamura (1995) investigated this trade-off and established that the magnetic flux does not have time to penetrate deeply due to the transient operation of the electromagnet and, therefore, the armature thickness could be reduced without significantly affecting the performance of the solenoid. For the sampling valve design described in this study, the centre volume of the

armature was bored out to carry the hardened end of the armature shaft. To assist the rapid build-up of magnetic flux and provide a faster valve response, investigators have suggested reducing the number of winding turns on the electromagnet coil to reduce self-inductance (Kajima & Kawamura 1995) and slitting the armature to minimize eddy currents (Ohdachi et al. 1991). However, these techniques were not used in the current design, as the armature also acted as the actuating shaft and slitting it would have introduced further design complications. Ohdachi et al. (1991) reported a considerable improvement in armature acceleration with increasing voltage supplied to the electromagnet, attributable to significantly increased initial flux accumulation in the armature. It should be noted, however, that the maximum voltage that can be supplied to the electromagnet is limited by the dielectric strength of the winding insulation, magnetic saturation and overheating of the coil (Zhao & Ladommatos 2001). For the design described in this study, since the electromagnet was switched on for a much smaller period than it was 'off' ('on' period was $\approx 10\%$ of 'on+off' period), it was possible to supply voltages considerably higher (up to 100 V) than the continuous voltage rating of the coil (24V).

While an electromagnet actuation system can be controlled with great flexibility, the response of typical electromagnets is slow (Zhao & Ladommatos 2001), as time is required for the build-up of magnetic flux in the coil. To overcome this issue, the

sampling valve design described in this study was based on the ‘percussion’ principle, where the armature is not rigidly joined to the valve stem (Figure 3.20), as first described by Yates (1988) and successfully implemented by several other investigators (Egerton et al. 1935; Whitehouse et al. 1977; Zhao et al. 1996). In the current design a small gap, of about 3-4 mm, existed between the striker of the armature and the anvil of the valve stem (Figure 3.20). When switched on, the electromagnet caused the armature to accelerate and travel at high speed towards the valve stem and impact the stem, imparting a large enough force to open the poppet valve very briefly. The compressive force of the return spring shut the valve after the impact and a second armature spring returned the armature and striker back to the initial position. An important characteristic of the percussion type sampling valve is that because the valve has to be open for only a very brief period of the engine cycle, the electromagnet can be switched on well before the valve is required to be opened, so that a sufficient amount of flux can build up in the electromagnet. The armature-striker can travel across the gap gaining speed, and building up a substantial amount of kinetic energy, before striking the valve stem. Therefore a strong compressive force of the return spring can be overcome by a relatively small electromagnet size, improving acceleration of the valve stem (Zhao & Ladommatos 2001).

An important design consideration in the ‘percussion’ system is to ensure that the armature return spring (Figure 3.20) should be able to rapidly withdraw the armature away from the valve stem and anvil. This is so as to prevent collision between the anvil and the striker which could delay the poppet valve closing. Zhao et al. (1996) discussed this in great detail and concluded that subsequent collisions were difficult to avoid due to the following reasons. First, the natural frequency of valve return spring is greater than the armature return spring. Values of 35 Hz for the valve return spring and 10 Hz for the armature return spring were calculated for the sampling valve described in this study. This is because the valve return spring constant has to be quite large to ensure proper sealing at the seat. Secondly, the armature spring constant has to be kept low so as not to significantly impede the momentum being gained by the armature as it moves to strike open the valve. For the sampling valve in the present study, high-speed imaging was performed to monitor the collisions between the armature-striker and the anvil of valve stem. It was observed that, even though the anvil collided with the striker during valve closure, the striker was pushed out of the way by the valve stem due to the high in-cylinder pressures acting on the face of the valve and thus it did not appear to obstruct the closure of the poppet valve significantly.

For the current design, extensive bench tests were conducted with the sampling valve using valve stem springs of various stiffnesses, with a wide range of voltages

and voltage durations being applied to the electromagnet. A number of valve parameters such as the maximum valve lift, the valve open duration and the flow rate through the valve opening were monitored. Figure 3.21 shows the valve lift duration and gas flow rate through the valve when the sampling valve was operated at a frequency of 10 Hz (representative of 1200 rpm engine speed, with every successive engine cycle being sampled), with a constant air pressure of 40 bar being applied to the valve face.

3.7.3 Construction materials

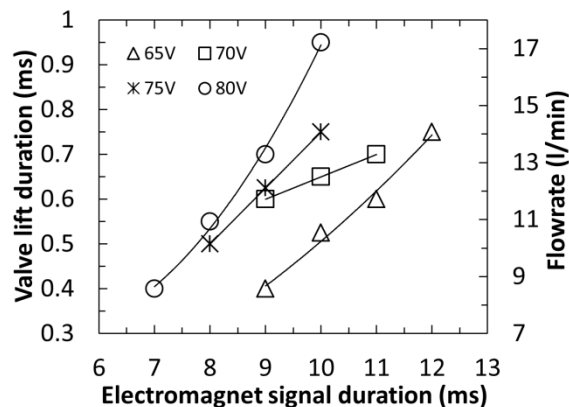


Figure 3.21: Valve lift duration and gas flow rate through the valve of the gas sampling valve at 10Hz operating frequency and 40 bar air pressure on the valve face

The outer body of the sampling valve tip, including the annulus casing, and the striker were manufactured from stainless steel (grade 304) (also utilized in several previous investigations (Duggal et al. 1978; Matsui et al. 1979; Zhao et al. 1996)) due to its generally non-corrosive properties, and high oxidation and thermal resistance (Zhao & Ladommatos 2001). The valve poppet was machined from silver-steel while copper was used to form the valve seat. Repeated impacts by the silver-

steel poppet onto a square-edged copper seat allowed the poppet to hammer a bespoke seat matched to the poppet, thereby forming a good seal, as also observed by Zhao et al. (1996). The hot in-cylinder temperatures of a running engine (800–2000 K) assisted this process through thermal softening of the copper seat, with subsequent work-hardening of the copper seat resulting in a durable surface. The housing of the LVDT (linear variable differential transformer) proximity sensor was made out of a polymer material so as to isolate the sensor from any interfering signals from the electromagnet voltage.

3.7.4 Installation of the sampling valve in the engine head

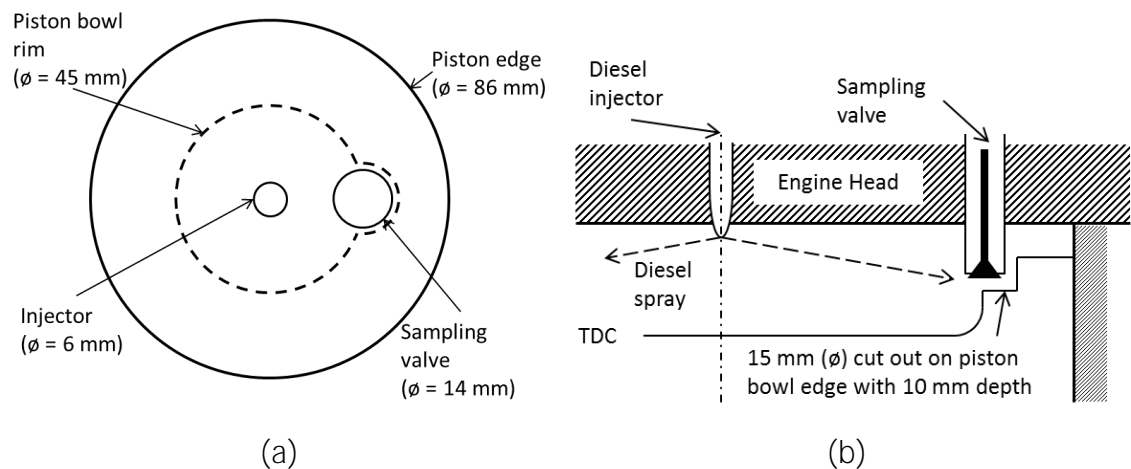


Figure 3.22: Schematic showing (a) plan view and (b) cross-sectional side view of the relative locations of the injector, the sampling valve at maximum in-cylinder penetration and the piston at TDC

The sampling valve was installed in the engine head in place of one of the two inlet valves. The inlet valve was replaced with a dummy valve with a thread on the inner hollow surface; the sampling valve was screwed into this thread of the dummy valve.

An additional set of cursory tests were performed whereby the centrally located diesel fuel injector was rotated in order to move the diesel fuel spray relative to the sampling valve position and investigate the transport delay in the diesel fuel hydrocarbons reaching the sampling valve. It was hoped that these tests would give a preliminary idea of the charge motion inside the combustion chamber; however, it was observed that the hydrocarbons reached the sampling valve at the same time, irrespective of the position of the diesel fuel spray relative to the valve. It is therefore speculatively suggested that the swirl rate has decreased significantly due to the removal of one of the intake valves. It could be expected that a reduction in swirl might create asymmetrical charge motion inside the combustion chamber, leading to reduced combustion efficiency and increased unburned hydrocarbon and particulate emissions. However, a reduction in peak hydrocarbon concentration was observed with increasing distance between the spray and the valve, suggesting dispersion of the diesel spray to have taken place despite the reduction in swirl rates.

The sampling valve tip penetration into the combustion chamber could be varied from 0 mm (flush with the engine head) to a maximum penetration of 9 mm. To prevent the sampling valve from hitting the piston crown, at the sampling valve's maximum penetration, a small part of the piston at the edge of the bowl was cut out. Figure 3.22 shows the relative positions of the piston bowl cut-out, the diesel

injector and the sampling valve inside the engine head with respect to the piston position at TDC.

3.7.5 Shape and volume of an engine in-cylinder gas sample

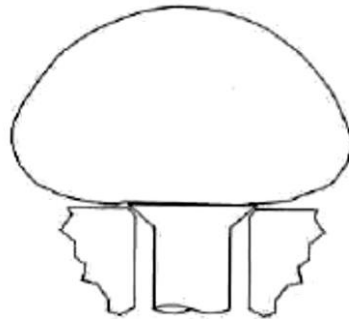


Figure 3.23: Actual sample volume shape at inlet of a poppet-type sampling valve (Zhao & Ladommatos 2001)

The shape and volume of the in-cylinder gas sampling region are important factors that determine the spatial resolution of the sampling valve. Through their investigations on gas sampling valves, Zhao & Ladommatos (2001) concluded that, although theoretically at the inlet of a poppet-type sampling valve, the gas sample could attain a roughly spherical shape, due to distortion as a result of fluid friction at the chamber wall and the presence of a boundary layer, the gas sampling region tends towards a hemispherical shape as shown in Figure 3.23.

Weiss & Keck (1981) carried out a two-dimensional numerical analysis on the hemispherical shape of a gas sample volume around the inlet of a poppet-type sampling valve, which was extended by Zhao & Ladommatos (2001) to three-dimensional hemispherical shapes. The volume of a sample shape attaining a

roughly hemispherical shape, $\Delta V_{C,H}$, and assuming axial symmetry about the axes of the hemisphere, is approximately given by,

$$\Delta V_{C,H} = \frac{P_o T_c}{P_c T_o} V_o \frac{60n}{N} \quad (3.12)$$

where

V_o = volume flow rate from sample valve at atmospheric pressure P_o and temperature T_o

N = engine revolutions per minute

n = number of engine revolutions per cycle (2 for four-stroke and 1 for two-stroke engine)

T_c = engine cylinder gas temperature

P_c = engine cylinder gas pressure

Sampling timing (CAD ATDC)	Duration of sampling window (CAD) [msec]	Cylinder gas pressure (bar)	Cylinder gas temp. (K)	Sample flow rate at atmos. P and T (cm ³ /sec)	Sample volume/cycle at atmos. P and T (cm ³ /cycle)	Sample volume/cycle at cylinder P and T (cm ³ /cycle)
10	6 [0.83]	64	1250	67	6.7	0.44
25	10 [1.4]	33	1200	33	3.3	0.40
40	15 [2.1]	16	1000	17	1.7	0.35

Table 3.2: Estimates of the gas sample flow rates and volumes for different sampling conditions at an engine speed of 1200 rpm

Table 3.2 shows the three sampling windows in the engine cycle at which gas samples were extracted from the engine and the corresponding engine operating conditions. The above equation (Equation 3.4) was used to calculate the approximate values of the volume of the gas sampling regions and the flow rates through the valve at various operating conditions for the sampling valve reported here (Table 3.2). It can be seen from Table 3.2 that the volume occupied by the

gas sample per cycle at cylinder conditions does not vary as significantly as the gas sample volume per cycle at atmospheric conditions. This is because at relatively lower cylinder pressures, both the mass flow rate and density of the sample decreases which results in a less pronounced change in sample volume at in-cylinder conditions.

Based on the work done by Zhao & Ladommatos (2001), an indicative value of the boundary layer thickness, δ , can be estimated from,

$$\delta = (\nu \times t_v)^{1/2} \quad (3.13)$$

where ' ν ', the kinematic viscosity of the cylinder gas within the boundary layer, can be assumed to have a value of $3.5 \times 10^{-4} \text{ m}^2/\text{s}$ (Zhao & Ladommatos 2001) and an average value of 1.5 ms (from Table 3.2) can be used for the sampling period, t_v . Hence an approximate value of 0.72 mm is evaluated for the boundary layer thickness. As per the analysis on cylinder gas sample volumes performed by Zhao & Ladommatos (2001), sample volumes between $0.35 - 0.44 \text{ cm}^3$ (from Table 3.2) should extend to a maximum distance of more than 5 mm from the valve inlet (at in-cylinder conditions), which is well beyond the calculated boundary layer thickness. It is important that the sample collected extends beyond the boundary layer thickness so as to ensure that the gas sample collected is from the reaction zone. The gas sample being extracted from the cylinder should also not have an excessively large volume to ensure minimum interference with the progress of combustion and pollutants formation (Zhao et al. 1996). With regards to experimental setup being discussed in this study, a gas sample of volume 0.4 cm^3 represents about 1.5% of the combustion chamber volume at TDC for the 0.5

litre/cylinder compression-ignition engine used in this study, which reduces to negligible levels as a percentage as the expansion stroke progresses.

3.7.6 Dilution tunnel

The in-cylinder gas samples extracted by the sampling valve were passed to a heated dilution tunnel, also designed and built in-house. Figure 3.24 shows, in schematic form, the gas flows in and out of the dilution tunnel. The purpose of the heated dilution tunnel was to buffer the gas samples and mix them with heated nitrogen gas (at 180°C, using a 750 W in-line heater) to increase the volume of the sample sufficiently for measurement by the gaseous emission analyser rack (Horiba MEXA-9100 HEGR incorporating the CO, CO₂, NO_x and THC analysers). The flow rate of nitrogen gas was controlled and measured using a mass flow meter (MASSVIEW MV-306) and the gas entered the tunnel through several small holes of diameter 1 mm each to increase turbulence and promote mixing of the gas sample with the nitrogen gas. The dilution tunnel was maintained at a temperature of 200°C using six PID controlled band heaters (each with a power rating of 105 W), in order to prevent condensation of low boiling point species in the gas sample. Electromagnetic solenoid valves were placed at various access points of the tunnel and could be remotely controlled using a computer interface developed in the NI LabVIEW environment (Figure 3.25), controlling the various gas flows in and out of the tunnel.

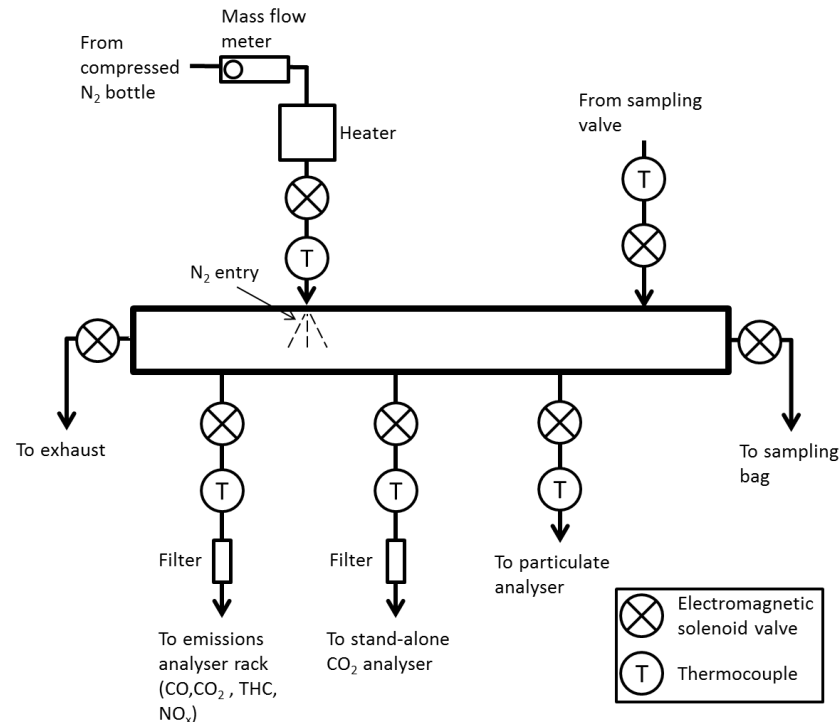


Figure 3.24: Schematic of the heated dilution tunnel with the various gas access points (Length of tunnel – 950 mm, Diameter of tunnel – 28 mm)

The mass ratio of the undiluted to the diluted in-cylinder gas sample was calculated by means of measured molar concentrations of CO₂ in the undiluted and diluted gas sample. These two levels of CO₂ were measured using the following procedure. The undiluted gas sample was first fed into a stand-alone CO₂ analyser, which required much lower flow rates of sample. The N₂ supply to the tunnel was then switched on so as to dilute the in-cylinder gas sample stream, and the diluted gas sample stream was then passed to the emissions analyser rack (Horiba MEXA-9100 HEGR) to obtain the in-cylinder gas composition, including the diluted CO₂ measurement.

The particulate spectrometer (DMS500) was supplied with the gas samples via another access port in the dilution tunnel (Figure 3.24), without the need for

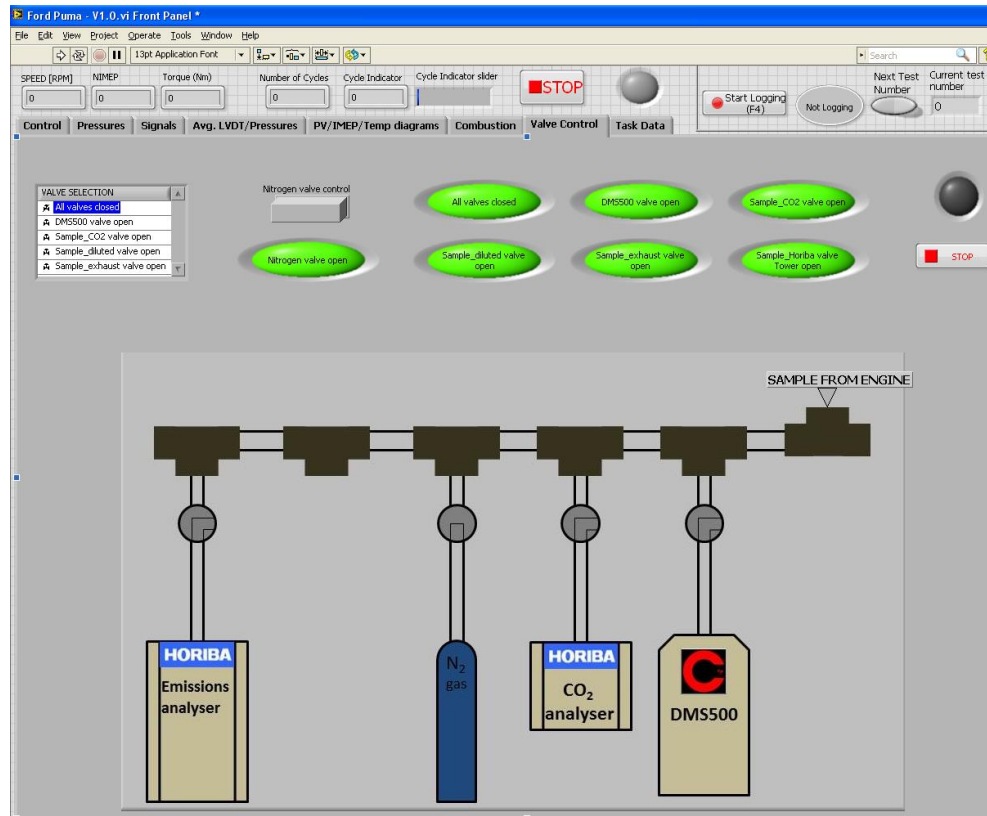


Figure 3.25: Screenshot of the NI LabVIEW program to control solenoid valves installed on dilution tunnel

dilution (the N_2 supply to the tunnel was switched off) as the particulate analyser featured an in-built dilution system.

3.7.7 Control and monitoring system for the sampling valve

The timing and opening duration of the in-cylinder sampling valve was controlled via a National Instruments (NI) data acquisition (DAQ) card with analogue signal output capabilities (NI PCIe-6323, as described in Section 3.6.2), utilising a custom-made NI LabVIEW software control and acquisition program. The trigger output signal to the electromagnet was referenced to the engine crankshaft encoder (which provided synchronisation pulses to the DAQ card at a resolution of 0.2 CAD) so that the sampling valve could be opened at any desired crank angle within the

engine cycle. At the appropriate, preselected crank angle, the trigger signal was sent from the DAQ card to a fast-acting relay circuit which switched on current from an adjustable power supply (0-120 V DC) to the sampling valve electromagnet. The trigger signal to the electromagnet was switched on for a preselected time duration (defined in CAD) after which the power to the electromagnet ceased.

The poppet valve lift (of order 0-0.3 mm) was monitored with a sensitive LVDT proximity sensor (Kaman 1U1), installed so as to sense the displacement of the stem of the sampling valve (Figure 3.20). The signal from the proximity sensor was received by the DAQ card and referenced with the crankshaft encoder so as to continuously monitor the valve motion in real-time. Figure 3.26 shows a typical valve lift trace obtained from the proximity sensor. It was assumed that the poppet valve opened when the lift was greater than 0.05 mm with the software detecting and displaying the CAD values at which the valve lift trace rose above 0.05 mm and fell below this level again. The difference between these two CAD values gave the valve opening duration and the average of the two CAD values was taken to be the sampling timing (as shown in Table 3.2) in CAD in the engine cycle. The valve lift trace along with the relevant CAD values was refreshed every engine cycle. Figure 3.27 shows a simplified flow diagram of the control and monitoring system of the electromagnetic sampling valve.

It is important to note that the poppet valve did not open instantaneously on supply of voltage to the electromagnet. A finite period of time was required for sufficient build-up of electromagnetic flux in the electromagnet coil of the sampling valve to overcome the opposing self-inductance of the electromagnet and the mechanical inertia of the moving parts of the valve (armature and valve stem). For closure of the poppet valve a small finite period of time was again required for the flux to collapse against the opposing self-inductance of the electromagnet. It was therefore necessary to switch on and switch off the power to the electromagnet several crank angle degrees ahead of the timing at which the poppet valve was physically required to start opening and closing respectively, as shown in Figure 3.26. Similar observations have been made by several other investigators (Zhao & Ladommatos 2001; Nowak et al. 2008). The time delay required between the commencement of power supply to the electromagnet and the physical movement of the valve depends on several factors, such as the engine cylinder pressure and can be difficult to predict. Therefore it was necessary to have a fast and independent (of the valve actuation system) valve motion monitoring system, such as the LVDT system described above, which can sense the physical movement of the valve and display it in real-time to the valve operator.

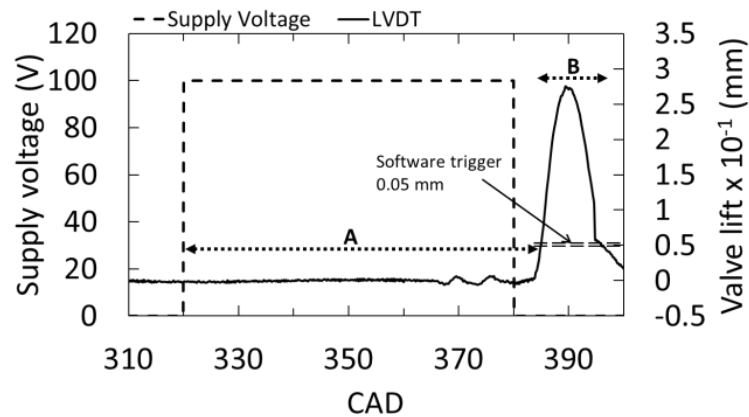


Figure 3.26: Crank angle resolved supply voltage and valve lift trace. A – poppet valve opening time delay, B – valve sampling duration

In order to decrease variability in the valve opening and closing instants (CAD) between consecutive engine cycles, the poppet valve was opened once every three engine cycles, instead of opening it every engine cycle (a technique known as skip-cycle sampling (Zhao & Ladommatos 2001)). Table 3.3 shows that opening the valve once every three engine cycles instead of every engine cycle reduced the standard deviation of the valve opening instant (CAD) by almost 60%. It was speculated that the O-rings in the moving parts of the sampling valve did not have sufficient time to decompress fully between engine cycles, when opening the valve on every combustion cycle, leading to inconsistent valve operation from one engine cycle to the next.

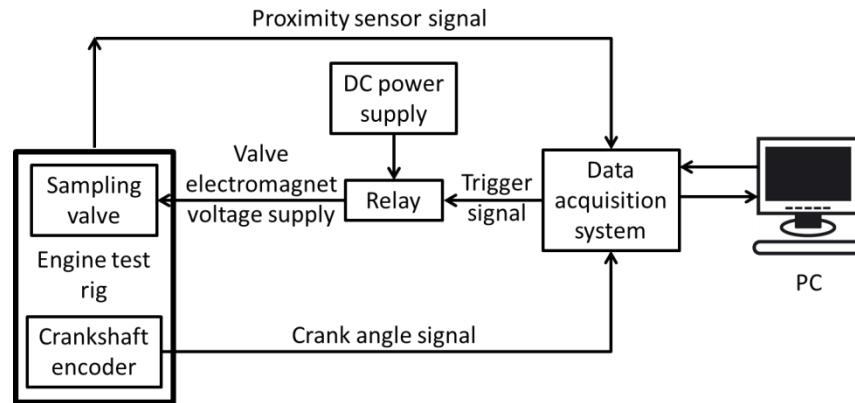


Figure 3.27: Control and monitoring system of the sampling valve

Engine speed (rpm)	Valve opened once per 'n' cycles	Valve opening instant (CAD)	Valve opening st.dev. (CAD)	Valve closing instant (CAD)	Valve closing st.dev. (CAD)
1200	1	338	± 2.03	345	± 2.07
1200	2	341	± 1.71	348	± 1.74
1200	3	342	± 0.85	347	± 0.86

Table 3.3: Standard deviation (st.dev.) in the valve opening and closing instants (CAD) at different valve operating parameters

3.7.8 Verification of dilution ratio results with sample bag

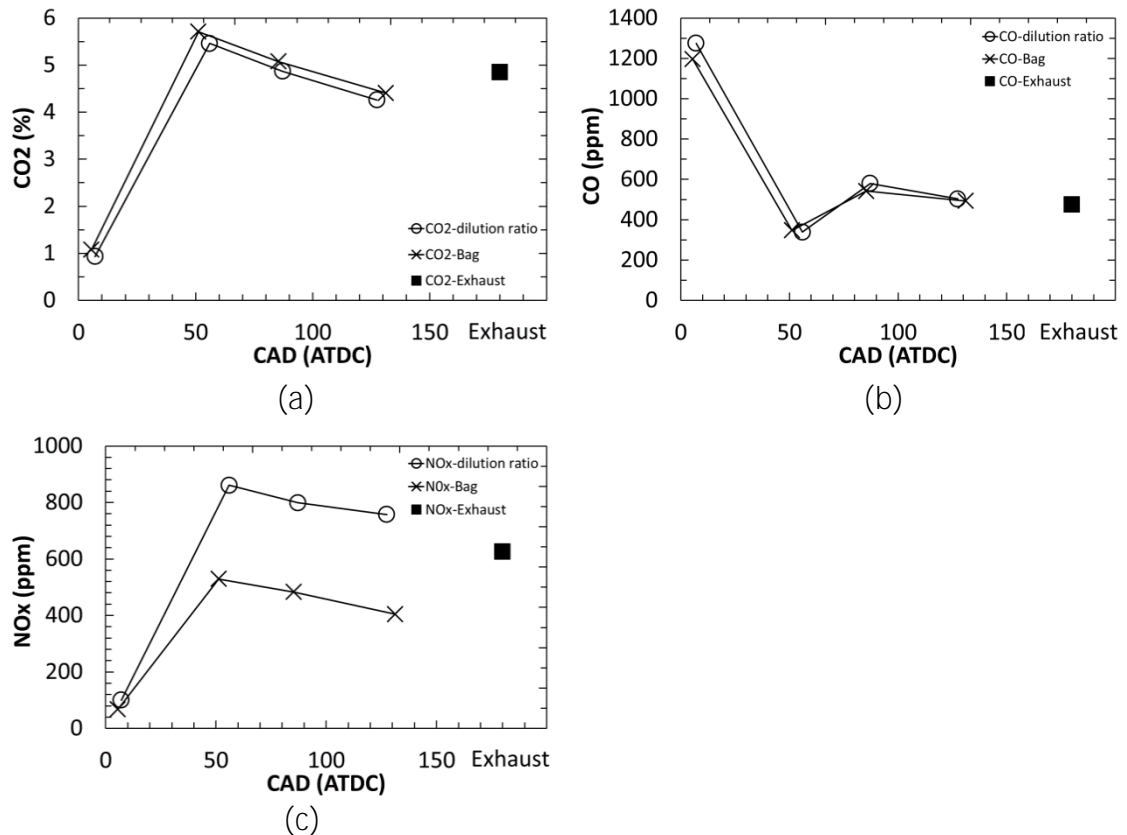


Figure 3.28: Comparison of in-cylinder gas sample composition obtained using the dilution tunnel and sample bag, as well as exhaust emissions for (a) CO₂, (b) CO and (c) NO_x

In order to verify the accuracy of the calculated diluted-to-undiluted gas sample mass ratio (as described in Section 3.7.6), the undiluted in-cylinder gas samples were separately collected in a PTFE sample bag, which was then connected to the emissions analysers for direct measurement of sample gas composition. This was performed at four different crank angle instants in the engine cycle and Figure 3.28 shows the results for the CO₂, CO and NO_x concentrations from these 2 methods at discrete CAD; the figure also shows the emission levels measured in the engine exhaust gas. Figure 3.28 shows that at each of the four different sampling instants (CAD), the in-cylinder CO₂ and CO levels obtained using the nitrogen dilution

method are very similar to those in the undiluted in-cylinder gas collected in the sample bag. Moreover, both the CO₂ and CO levels in the gas sample extracted at about 130 CAD ATDC (well into the expansion stroke and just before the opening of the exhaust valve) are very similar to CO₂ and CO emission levels measured directly in the exhaust gas of the engine. However, when comparing the NO_x levels obtained using the nitrogen dilution method to those in the gas collected in the sample bag, except for gas samples collected at 10 CAD ATDC, there seems to be an offset in the two values, with the NO_x levels in the gas collected in the sample bag being consistently lower (Figure 3.28). It was speculated that this may be due to some of the NO_x dissolving and reacting with water vapour in the sample bag during the interval between filling up the bag with sufficient sample and measuring the bag composition. Some additional cursory tests were performed whereby the bag filled with the gas sample was left for different lengths of time prior to measuring NO_x, and it was observed that NO_x levels decreased with increasing lengths of time prior to analysis.

3.8 High pressure low volume fuel system (HPLVFS)

One of the objectives at the beginning of this research project was to investigate the in-cylinder combustion of alternative, low-emission, 'future' liquid fuels with the insight provided by the gas sampling system. In some instances, these potential prototype fuels were not readily available from commercial chemical suppliers, and had to be specially synthesised. This increased the costs of these types of liquid fuels, and since several litres are required to fill a conventional common-rail fuel system, purchasing these fuels in sufficiently large quantities was not considered to be economically viable. Furthermore, some of these liquid fuels possessed physical properties which were not compatible with the common rail fuel system, such as low lubricity which can be detrimental for the fuel pump or cause erosion of the elastomers in the fuel system. Emptying the fuel system between tests, when changing fuels, would also have entailed wasting large quantities of fuel. These problems were initially encountered by Schönborn (2009) who developed a special low volume fuel delivery system, the design of which was further innovated by (Hellier 2013). Therefore, to be able to test these potential liquid fuels, a special fuel delivery system was designed for this project. However, after the system had been designed and manufactured, the direction of the project changed to focus more on gaseous fuel mixtures, and thus this fuel delivery system was not utilised in this project. It was decided to include the current section as a means of guidance for the design of high pressure fuel delivery systems.

The concept of the special fuel delivery system was to utilise the conventional common rail fuel system to pressurise diesel fuel, which would then act as a hydraulic fluid and create pressure in the test fuel (as shown in Figure 3.29). The design consisted of a stainless steel cylindrical vessel with capped ends and a free moving piston, which divided the vessel into two chambers. One chamber was connected directly to the high pressure fuel pump and common rail setup and was filled with high pressure diesel fuel from the common rail, while the other chamber was filled with test fuel and was connected to the diesel engine fuel injector. The diesel fuel was pressurised to a precise level using the Emtronix control system, and the PRV and pressure transducer mounted on the common rail (Section 3.2). Since the piston was entirely free moving, the diesel fuel pressure was communicated to the test fuel via the piston, and therefore, the test fuel could be injected into the engine at the same pressure as the selected common rail pressure. O-rings installed on the free piston ensured no mixing of fuel between the two chambers took place. The Emtronix system could also be used to control the timing and duration of the test fuel injection event, thus allowing complete control of all the injection parameters (as would be when using the conventional fuel injection system), but at the same time bypassing the need for the test fuel to flow through the conventional fuel injection system. The primary innovation in the low volume fuel system by Hellier (2013) was the introduction of a second free moving piston in the cylinder.

This allowed complete separation of the diesel fuel and test fuel circuits, even when changing fuels between tests, when the piston on the test fuel side could be completely ejected from the system for cleaning without breaking into the diesel fuel circuit.

The maximum volume of test fuel that could be filled in the special fuel system developed by Schönborn (2009) and Hellier (2013) was 100 ml and 250 ml, respectively. It was realized that when conducting in-cylinder investigations, relatively large volumes of fuel would be required so as to prevent frequent engine stops during experiments to refill the fuel system. Additionally, in the previous design by Hellier (2013), port holes were machined along the path of piston movement (in the wall of the central cylinder) to allow the passage of compressed air and fuel in and out of the pressure vessel. A disadvantage of these port holes was that the piston O-rings extruded into these holes as they travelled past them under high pressure, causing considerable abrasions to the O-rings. Keeping these issues in mind, a high pressure fuel system was designed and commissioned which could accommodate up to 1000 ml (1 litre) of test fuel and deliver up to 2000 bar injection pressure. A detailed description of the design procedure and of various features of the high pressure low volume fuel system (HPLVFS) is presented in the following paragraphs with reference to the schematic of the HPLVFS system shown

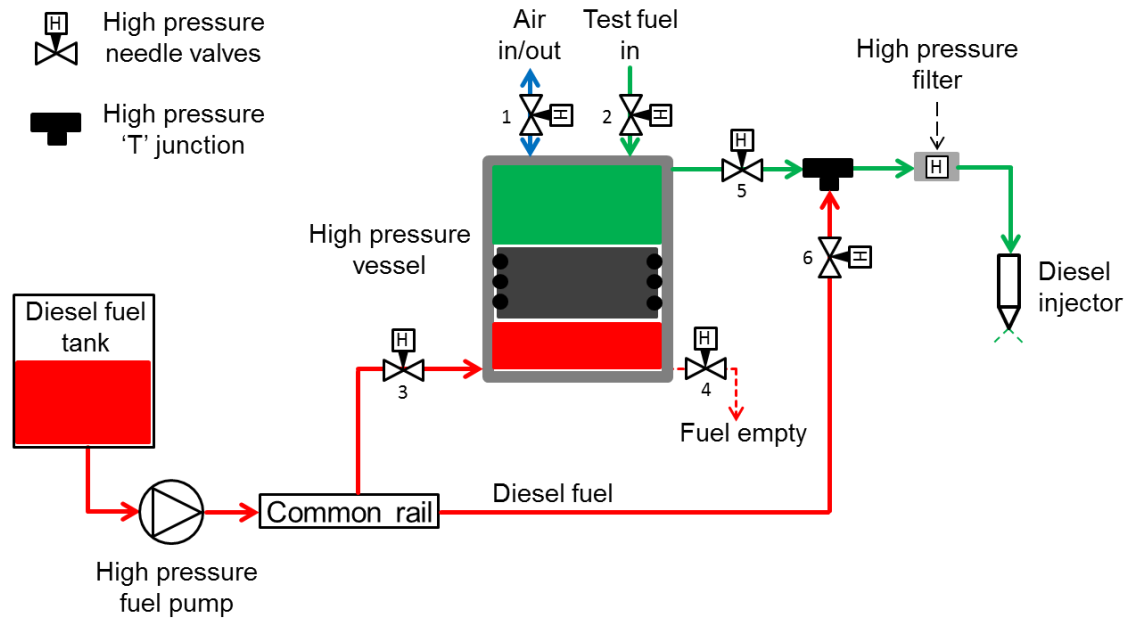


Figure 3.29: Schematic showing fuel flow in the high pressure low volume fuel system

in Figure 3.29 and a cross sectional view of the assembled fuel system shown in

Figure 3.30.

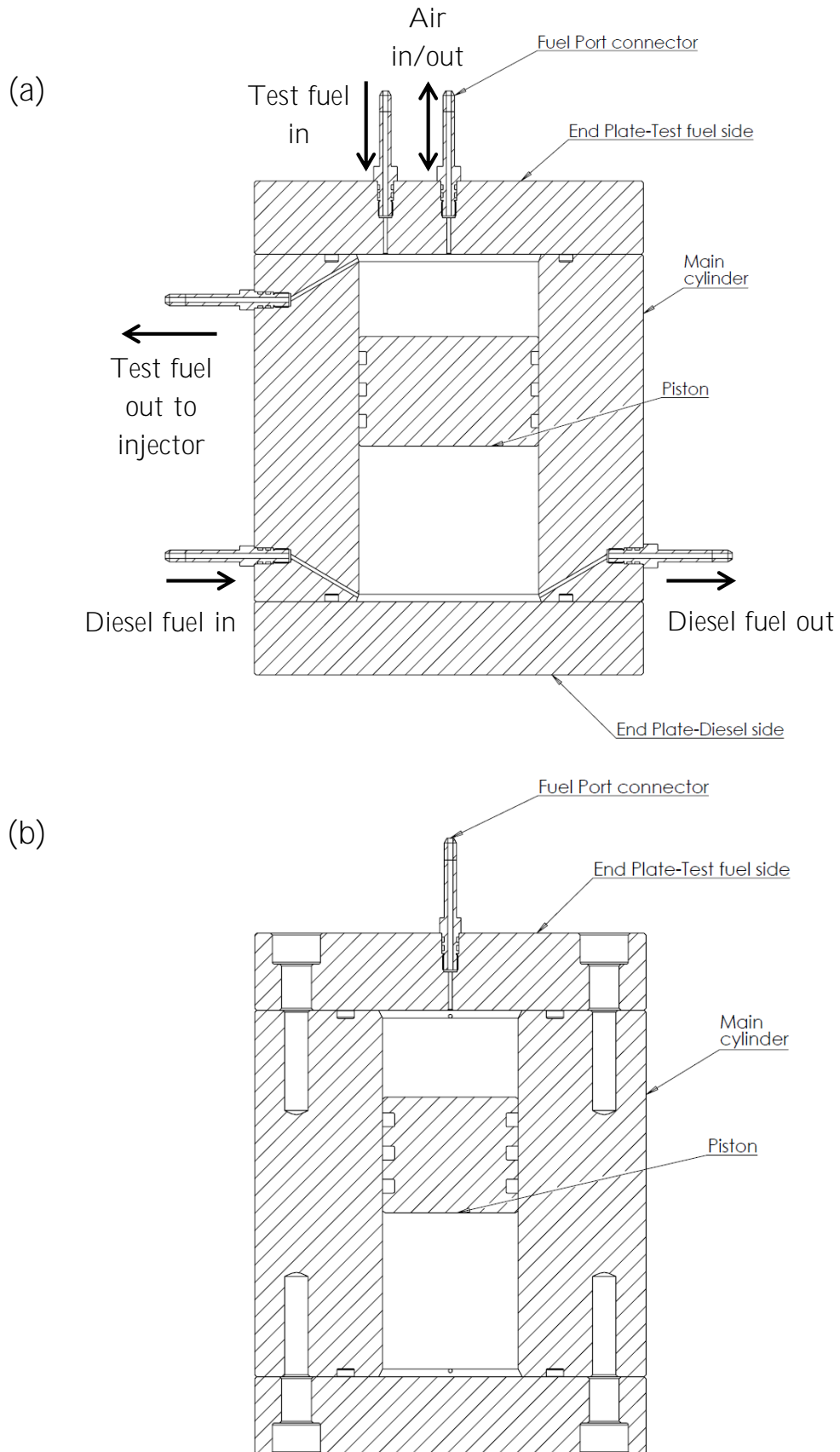


Figure 3.30: Cross-sectional (a) front view and (b) side view of the assembly of the high pressure fuel system

The main cylinder (Figure 3.30) of the fuel system was designed in accordance with British Standard 5500 (BS 5500-2012) to be able to withstand hoop stresses generated by a radial pressure of 2000 bar at a temperature of 150°C or higher. The wall thickness of the cylinder, ' e_c ', was determined using the following equation,

$$e_c = \frac{\textit{Radial pressure} \times \textit{cylinder bore diameter}}{(2 \times \textit{nominal design stress}) - \textit{Radial pressure}} \quad (3.14)$$

and,

Nominal design stress

$$= \frac{\textit{Tensile strength for stainless steel (Grade 316)}}{\textit{safety factor (= 2.5)}} \quad (3.15)$$

The maximum hoop stress acting on the bore of the main cylinder was calculated using Equation 3.8, and was found to be considerably lower than the nominal design stress,

$$\textit{Maximum hoop stress} = \frac{\textit{Radial pressure} \times \textit{cylinder bore diameter}}{\textit{wall thickness} (e_c)} \quad (3.16)$$

The main cylinder was closed off at both sides using end plates (Figure 3.30), the thickness of which was calculated using Equation 3.9 obtained from BS 5500-2012. As can be seen from Figure 3.30, the end plate on the test fuel side has two narrow openings (2 mm diameter) for the flow of test fuel and air. These had to be taken into account when calculating the thickness of the end plates (e_P).

$$e_p = C \times \text{cylinder bore diameter} \times \left(\frac{\text{Radial pressure}}{\text{Nominal design stress}} \right)^{1/2} \times Y_2 \quad (3.17)$$

where,

$C = 0.41$ (from BS5500-2012),

$Y_2 =$ parameters for end plates with openings, calculated using,

$$Y_2 = \left(\frac{\text{Cylinder bore diameter}}{\text{Cylinder bore diameter} - \text{Opening diameter}} \right)^{1/2} \quad (3.18)$$

The end plates were secured to the main cylinder using fourteen M16 outer nominal diameter bolts as can be seen in the side view in Figure 3.30 (b). The bolts used were of Grade 12.9 as they exhibit much higher tensile strengths (1220 MPa) compared to bolts of lower grades (Grade 8.8 – 800 MPa). To select the bolt diameter and the number of bolts, calculations were carried out taking into account the force exerted on the end plate the internal cylinder pressure, the proof load capability of the bolts and the total area of contact between the bolt and cylinder threads. The area of contact between the roots of the threads had to be sufficient to be able to withstand the maximum internal cylinder pressure of vessel.

Viton O-rings were utilised to seal against high pressures in the vessel. O-rings were installed on the piston to prevent fuels from the two sides (diesel and test fuel) from mixing. Three equidistance O-rings were used on the piston to prevent the occurrence of scoring due to skewing of the piston. O-rings were also placed in between the cylinder and the end caps to stop leakages and to enable build up of

pressure inside the vessel. The O-rings were selected and their housings designed based on the recommendations provided by British Standards (BS 3601-1 and 3601-2). The design of the housings varied based on whether the O-rings were installed axially or radially, and whether they were used in static or dynamics applications. The O-ring used between the cylinder and the end plate is an example of an axial static application, while the O-rings on the piston were radially installed and under dynamic conditions. The British Standards defined recommended ranges for certain parameters of the O-rings and their housings to avoid any detrimental effects on the sealing performance. These included: the degree of stretch of the nominal inside diameter of the O-ring when it is installed in its housing, the reduction in the cross-sectional area of the O-ring due to it being stretched and flattened in its housing when in use, and the maximum groove fill of the O-ring to allow for thermal expansion, volume swell due to O-ring fluid exposure and tolerance effects. Additionally, care had to be taken that the edges of groove of the housing were rounded off and lead-in chamfers made to eliminate possible sources of O-ring damage and seal failure.

Machined into the test fuel side end plate and the walls of the main cylinder were five ports that allowed the passage of fuel and air in and out of the system, as can be seen in Figure 3.30. The holes in the wall of the main cylinder were drilled at an angle in such a way that they opened up on the chamfered edges at the two ends

of the bore of the cylinder (Figure 3.30 (a)). The holes were not placed along the inner wall of the cylinder bore in order to avoid the piston O-rings from extruding into these holes and getting abraded during normal operation. Custom designed port connectors (Figure 3.31 (a)) were used to seal these ports by using two O-rings radially stretched around the circumference at one end of the connector, held in place by a depth of thread; the O-rings sealed by compressing against the inner wall of the port chambers (Figure 3.30). The external end of the port connectors was designed to interface directly with high pressure needle valves (Autoclave 30VM4071). A special two part high pressure filter housing (Figure 3.31 (b)) was also designed and installed between the pressure vessel test fuel outlet port and the fuel injector to prevent any damage occurring to the fuel injector by debris (Figure 3.29). The filter housing was designed to operate at pressures of up to 2000 bar and housed a sintered steel filter element; a filter element with a pore size of 1 μm was used with the fuel system. An O-ring stretched around the circumference of the filter element, and compressed by the filter housing, ensured that all the test fuel was directed through the filter. The filter housing was also sealed against internal pressure by two radially installed O-rings, held in place by a depth of thread and compressed between the two parts of the filter housing (Figure 3.31 (b)). The inlet and outlet of the filter housing were high pressure diesel connections (BS ISO 2974:2005) which communicated with the high pressure valve (at the inlet) and fuel

injector (at the outlet). All the connecting pipes were made out of stainless steel, and were rated to withstand pressures of up to 2000 bar. The test fuel end cap additionally had a pressure transducer installed which was connected to the test fuel chamber via a 1.5 mm diameter hole. Preliminary tests were done to compare the pressure in test fuel chamber to the common-rail pressure, and a good agreement, of within 5 bar, was observed between the two pressures.

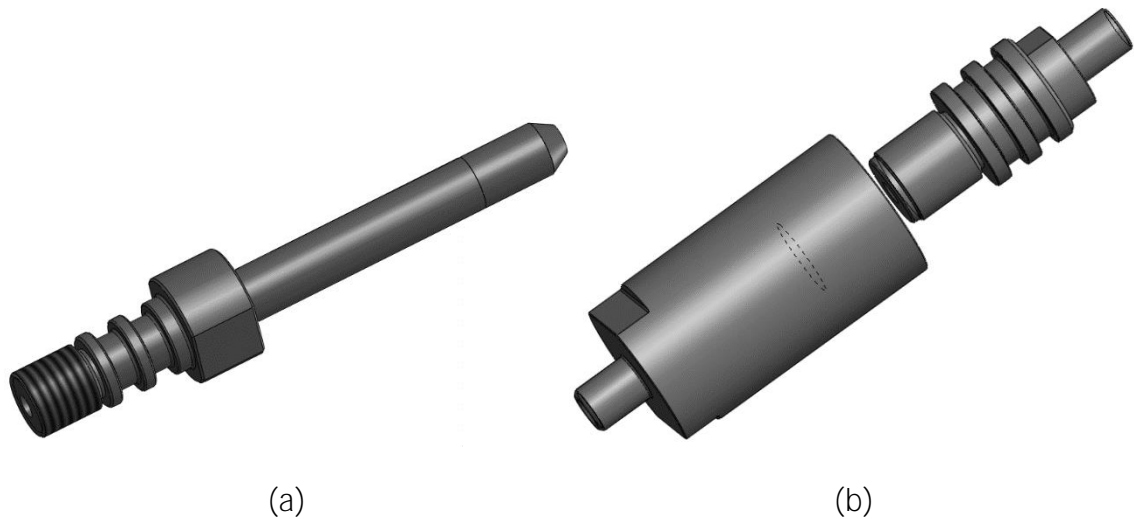


Figure 3.31: Isometric view of (a) custom designed port connectors and (b) two-part high pressure in-line fuel filter housing

At the start of a typical experiment, the piston would be pressed hard against the end cap on the diesel fuel side (Figure 3.30), while the chamber on the other side (the top chamber) would be filled with test fuel. In order to assist the high pressure diesel fuel from the common rail to push the piston and generate pressure in the test fuel, the edge of piston was chamfered. This allowed a small gap between the chamfered edges on the cylinder and the piston, which the pressurised diesel fuel could initially fill and thereby force the piston upwards, towards the test fuel side.

At the end of the experiment, when the test fuel chamber was empty, the piston ended being pressed against the cap on the test fuel side (Figure 3.30). If the same test fuel had to be refilled in the cylinder for the next set of experiments (without needing to clean the pressure vessel), the piston was pushed back down by feeding compressed gas (air or N₂) via high pressure valve (HPV) 1 (Figure 3.29) into the pressure vessel. The test fuel was then introduced into the test fuel chamber via HPV 2, and any gas in the cylinder displaced through HPV 1. However, if a different test fuel had to be used, then it was necessary to clean the cylinder and replace O-rings to prevent any cross-contamination between fuels. For this purpose a special cap was manufactured, which was used in conjunction with spacers of different thicknesses, to allow the piston to be removed to different extents from the main cylinder, depending on whether only the top O-ring needed to be replaced or the entire piston had to be removed (Figure 3.32). If at the end of the test, only the top O-ring had to be replaced, the test fuel side end cap was removed, and replaced by the special end cap which had a hollow inside for the piston to occupy. A metal spacer and a nylon spacer were placed in the hollow; the nylon spacer was used to attenuate the impact between the metal piston and the metal spacer, and avoid denting the piston. Pressurised diesel fuel was used to partially push the piston into the special end cap until it made contact with the spacers, as can be seen in Figure 3.32 (a). The top of the piston could then be cleaned and the top

piston O-ring and the O-ring between the cylinder and the end cap could be replaced. Compressed gas (air or N₂) was then used to push the piston back down, and the diesel fuel in the bottom chamber emptied via HPV 4 (Figure 3.29). However, if the piston had to be entirely taken out of the main cylinder, then the metal spacer was removed and the piston pushed into the end cap, as shown in Figure 3.32 (b). As can be seen in Figure 3.29, a high pressure ‘T’ junction was placed just before the in-line filter which allowed the option of bypassing the high pressure fuel system (by closing HPVs 3 and 5, and opening HPV 6), and feeding the injector directly with diesel fuel from the common rail. Additionally, by closing HPV 3 and opening HPVs 4, 5 and 6, the test fuel chamber could be filled with diesel fuel in order to flush the test fuel circuit at the end of an experiment, in effect ‘resetting’ the system between experiments.

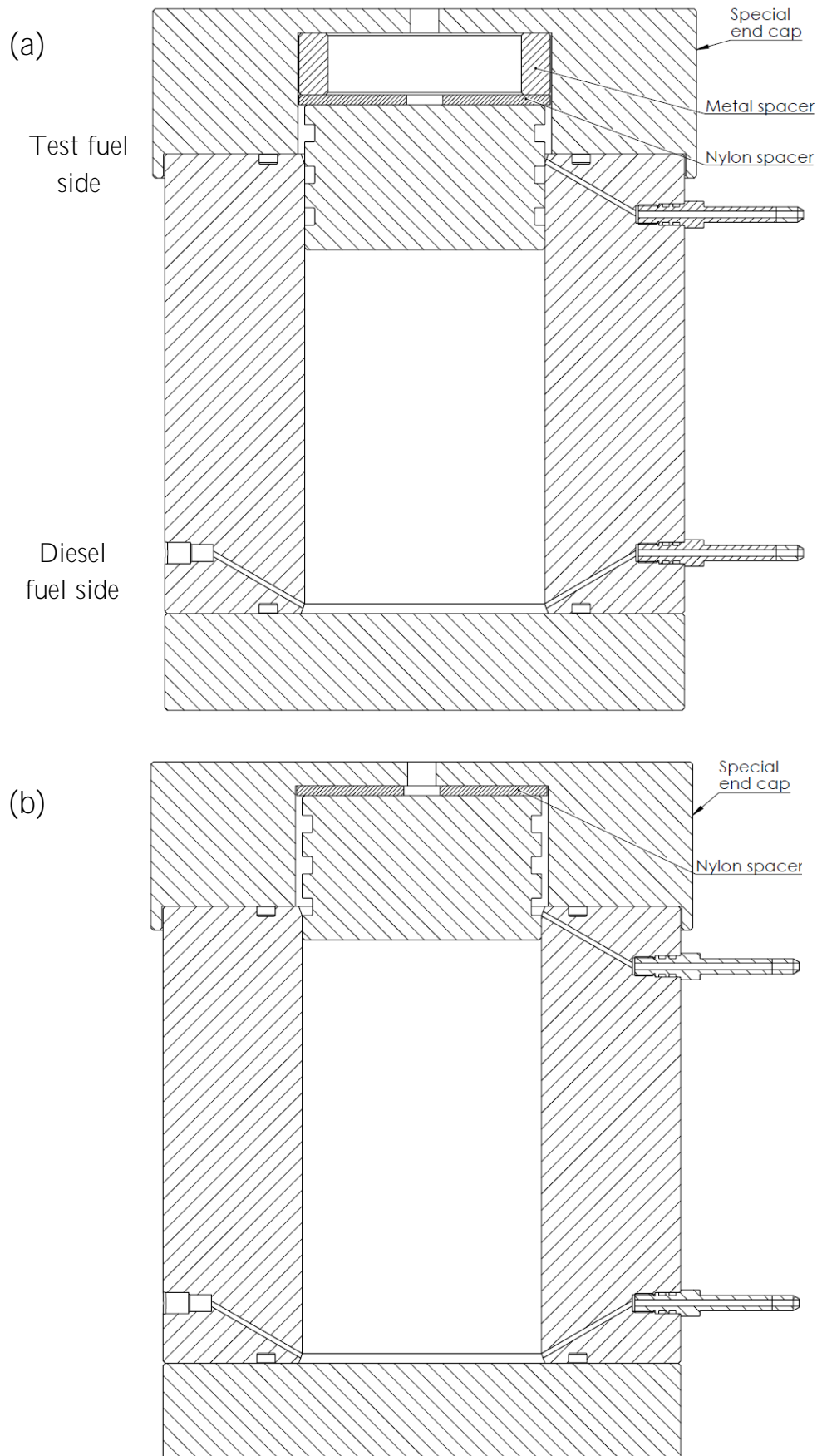


Figure 3.32: Cross-sectional view of the fuel system with the special cap showing (a) piston position with the top O-ring exposed and (b) piston completely removed from the main cylinder

4 Effect of hydrogen-diesel fuel co-combustion on exhaust emissions with verification using an in-cylinder gas sampling technique

This chapter presents an experimental investigation on the effects of co-combustion of diesel fuel with hydrogen (H_2) on exhaust emissions; H_2 addition in the engine ranged from low levels to predominantly H_2 combustion, with the function of diesel injection being only to ignite the H_2 . The tests were performed at fixed diesel injection periods, with H_2 added to vary the engine load between 0 and 6 bar IMEP. For all experiments, the H_2 was injected into the engine inlet manifold to be aspirated with the intake air. In a complimentary set of experiments, nitrogen gas was added to the engine intake air (instead of hydrogen) so as to isolate the effects of diluting the intake charge (reducing the amount of combustible oxygen). The chapter also reports a series of experiments conducted using the in-cylinder

sampling system so as to analyse the burning gases in the engine cylinder at different instants during the combustion cycle.

4.1 Experimental procedure

The experiments discussed in this chapter were conducted on the single cylinder engine utilising the common rail fuel injection system for diesel fuel injection and the gas mass flow controller system for delivering metered quantities of hydrogen (H_2) to the engine. These systems have been described in detail in Chapter 3 of this thesis. All the experiments were carried out at a constant engine speed of 1200 rpm, common rail fuel injection pressure of 900 bar and a diesel fuel injection timing of 10 CAD BTDC. The diesel fuel used for all tests was of fossil origin, with zero fatty acid methyl ester (FAME) content, cetane number of 53.2 and carbon to hydrogen ratio of 6.32:1 by mass. Compressed hydrogen gas of purity 99.995% was obtained from a commercial gas supplier (BOC).

4.1.1 Experimental set 1: Exhaust emission tests

The test procedure followed for these experiments consisted of fixing the diesel fuel injection period (i.e. fixing the flow rate of diesel fuel supplied to the engine) while gradually increasing the H_2 supplied to the engine so as to increase the engine load (power output), at constant engine speed.

The above procedure was repeated for a range of fixed diesel fuel injection periods, as shown in Table 4.1. Figure 4.1 shows the energy supplied to the single cylinder engine from H_2 as a percentage of the total energy supplied to the engine (energy

from H₂ plus diesel fuel) and the concentration of H₂ in the intake air, at various engine loads and fixed diesel injection periods.

Diesel fuel injection period (μs)	Diesel fuel flow per engine cycle ($\times 10^{-3}$ ml/engine cycle)	Diesel fuel-air equivalence ratio (ϕ_D)	Engine load with no H ₂ addition (bar IMEP)	H ₂ flow rate injected in inlet manifold ($\times 10^{-3}$ l/engine cycle)	H ₂ -air equivalence ratio (ϕ_{H_2})
250	1.58	0.08	0.00	0 to 31.3	0 to 0.40
325	2.94	0.20	1.50	0 to 25	0 to 0.31
350	3.93	0.23	2.20	0 to 21.3	0 to 0.26
400	5.30	0.29	3.25	0 to 17.5	0 to 0.21

Table 4.1: Test parameters used in the exhaust emission experiments

IMEP (bar)	1	1.5	2	3	3.5	4	4.5	5	5.5	6
Diesel fuel injection period (μs)	316	331	344	388	413	438	462	486	513	542

Table 4.2: Diesel fuel only engine loads (IMEP) and the corresponding diesel fuel injection periods (μs)

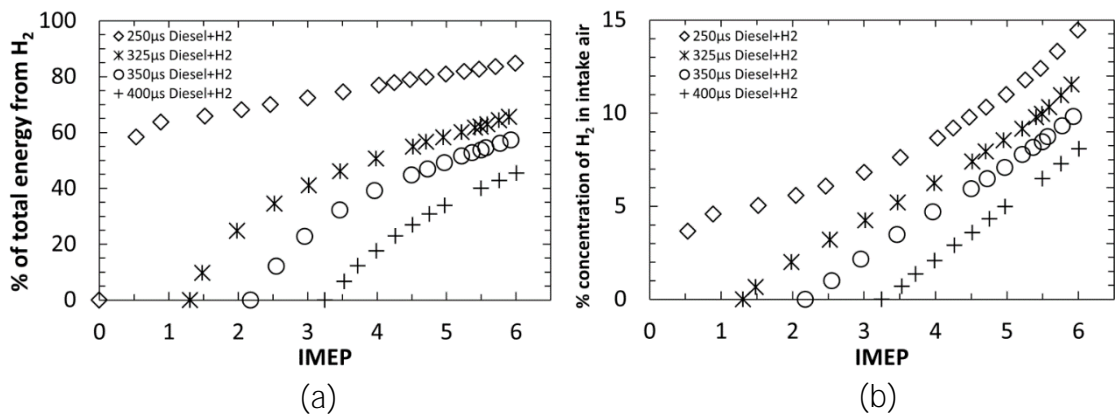


Figure 4.1: (a) Percentage energy from H₂ and (b) concentration of H₂ in the intake air at various engine loads and fixed diesel injection periods

In the above set of tests, the minimum diesel fuel injection period used was 250 μs . With this injection period and no H_2 addition, no heat release could be discerned from the analysis of in-cylinder gas pressure. It is suggested that this may be attributable to diesel fuel-air mixture overleaning and thus unable to sustain a flame front and be more prone to quenching by cooler areas of the in-cylinder charge. Therefore, 250 μs was taken to be the minimum diesel fuel injection period (at an injection pressure of 900 bar), as below this injection duration no discernible exhaust THC emissions could be observed, suggesting that injector opening was insufficient for delivery of diesel fuel. Nevertheless, it was observed that 250 μs diesel fuel injection period was sufficient to ignite the aspirated H_2 -air mixture at all engine loads up to 6 bar IMEP.

An additional series of control tests were carried out using diesel fuel only (without any H_2), with the diesel fuel injection period varied so that the engine load changed between 0 and 6 bar IMEP. Table 4.2 shows the diesel fuel only engine loads (IMEP) and the corresponding diesel fuel flow rates.

4.1.2 Experimental set 2: In-cylinder gas sampling tests

A further set of experiments was carried out using the in-cylinder gas sampling valve; the diesel injection period was fixed at 325 μs for all the tests and H_2 was added to increase the engine load. With the diesel fuel injection period of 325 μs and no H_2 addition, an engine load of 1.5 bar IMEP was obtained. Additionally, from the exhaust NO_x measurement results, it could be seen that negligible levels

of NO_x are obtained at an engine load of 1.5 bar IMEP. Therefore, for the in-cylinder sampling tests, it could be assumed that any observed NO_x could be primarily attributed to the presence of added H₂. Meanwhile, an engine load of 1.5 bar IMEP indicated that sufficient diesel fuel was being delivered at this diesel injection duration for the development of heat release from diesel only combustion, and that spatial differences in the in-cylinder charge attributable to the presence of diesel sprays could likely be observed during in-cylinder sampling.

During these tests, gas samples were extracted from the engine cylinder at two distinctly different locations, relative to one of the six injector nozzle diesel fuel sprays. Figure 4.2 shows the two sampling arrangements with respect to the injector sprays. The first location was a region of high diesel fuel concentration within the core of the diesel fuel spray, while the second location was an area of relatively low diesel fuel concentration between two spray cones. Since the absolute location of the sampling valve in the engine head was fixed, the change in the sampling arrangement, relative to the diesel fuel sprays, was achieved through rotation of the centrally-located injector. The locations of higher and lower diesel fuel concentration were experimentally determined by rotating the diesel fuel injector in small steps and measuring the in-cylinder gas composition (in particular levels of unburned hydrocarbons) at each injector rotation.

For each of the two relative sampling arrangements shown in Figure 4.2, gas samples were extracted at three sampling windows in the engine cycle: (a) the premixed stage of combustion (10 CAD ATDC); (b) the early diffusion combustion stage (25 CAD ATDC); and (c) the late burning stage (40 CAD ATDC). Table 4.3 lists the timings and the durations, within the engine cycle, of the three sampling windows.

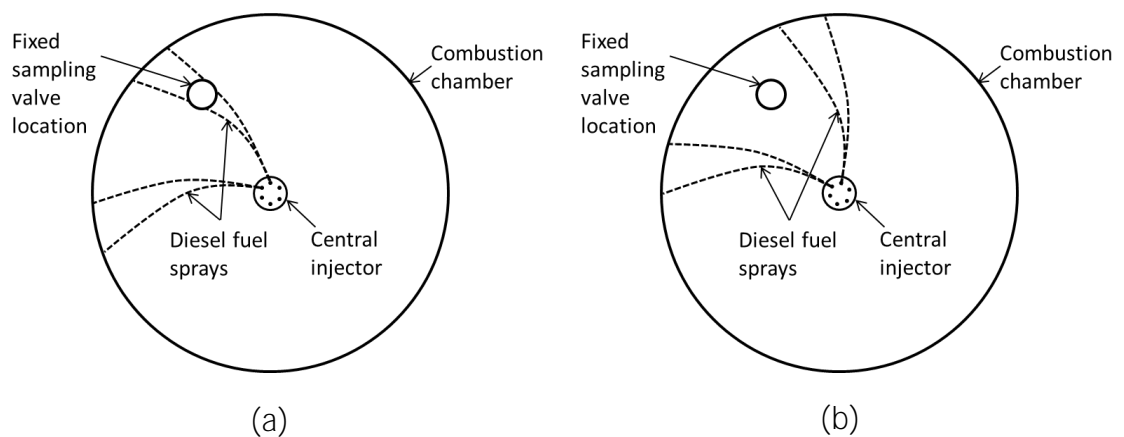


Figure 4.2: Schematic showing (a) sampling arrangement one and (b) sampling arrangement two relative to the diesel fuel sprays; changes to the position of the spray relative to the valve location was achieved by rotating the fuel injector

Sampling instant (middle of sampling window) (CAD ATDC)	Duration of sampling window (CAD)	Diesel fuel injection period (μs)
10	6	325
25	10	325
40	15	325

Table 4.3: Gaseous sample extraction time CAD ATDC during the engine cycle and the corresponding sampling window in CAD

4.2 Results and Discussion

4.2.1 Combustion characteristics

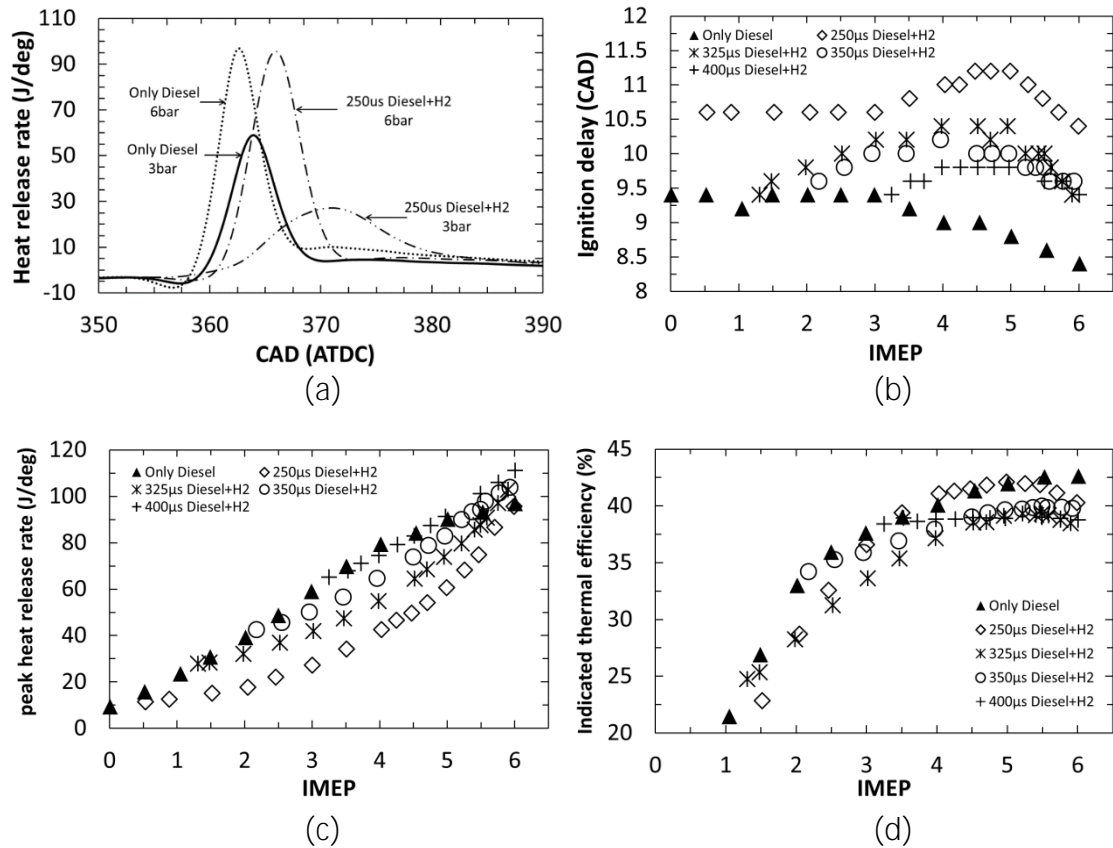


Figure 4.3: (a) Heat release rate curves and combustion characteristics (b) duration of ignition delay, (c) apparent net peak heat release rates (J/deg) and (d) indicated thermal efficiency of the engine at various engine loads and H₂-diesel fuel proportions

Figure 4.3 (a) shows the heat release rate curves at two engine loads, 3 and 6 bar IMEP, for both diesel only combustion and H₂-diesel fuel co-combustion with maximum H₂ concentration in the intake air (therefore at minimum diesel fuel condition). At a lower load of 3 bar IMEP, it can be observed from Figure 4.3 (a) that the duration of combustion increases significantly in the case of H₂-diesel fuel co-combustion relative to diesel fuel only combustion. At 3 bar IMEP, the in-cylinder H₂-air mixture is weaker than stoichiometric ($\phi_{H_2} = 0.18$), and it suggested that this may result in the slower flame propagation speeds than the maximum

speeds achievable during stoichiometric combustion. In contrast, with diesel fuel only ignition, an appreciable amount of diesel fuel-air mixture is already prepared during the delay period, and combusts rapidly, and close to TDC, following ignition, giving rise to higher rates of heat release (Heywood 1988; Hellier et al. 2011). It can be seen from Figure 4.3 (a) that at a higher load of 6 bar IMEP, where the in-cylinder H₂-air mixture is relatively close to stoichiometric ($\phi_{H_2} = 0.40$), both the duration of combustion and the peak rate of heat release (pHRR) for H₂-diesel fuel co-combustion are comparable to diesel fuel only combustion.

Figure 4.3 (b) shows the effect of H₂ addition on the ignition delay at various fixed diesel fuel injection periods. The tests were conducted at fixed diesel fuel flow rates into the engine and the amount of aspirated H₂ into the engine was increased to increase the engine load. Throughout this study, ignition delay is defined as the duration in CAD between the start of diesel fuel injection (SOI) and the start of combustion (SOC); SOI is taken to be the time (in CAD) at which the injector actuation current signal is sent, and SOC is taken as the time (in CAD) at which the first detectable incidence of heat release occurs from fuel burning. It can be seen from Figure 4.3 (b) that the addition of H₂ results in a general trend of increasing ignition delay, which reaches a peak and subsequently decreases with further H₂ addition. The increase in ignition delay could be attributed to the reduction in oxygen (O₂) concentration in the intake charge, as intake air O₂ is displaced by H₂ aspirated into the engine inlet manifold. The reduction in O₂ availability in the

intake charge is expected to have led to a decrease in the rates of low temperature fuel reaction kinetics, that produce reactive radical species and escalate temperatures, thus delaying autoignition (Heywood 1988; Westbrook 2000; Andree & Pachernegg 1969). It is tentatively suggested that a further driver of the increased ignition delay with increasing H_2 addition may be an inhibiting influence of H_2 on the oxidation of diesel fuel. Figure 4.3 (b) shows the ignition delay trend reversing at higher engine loads (beyond 4.5 bar IMEP), with the ignition delay decreasing with further addition of H_2 . This trend reversal is believed to be due to, firstly, the elevated in-cylinder temperatures arising from higher engine loads which improve mixing rates of the injected liquid fuel; and secondly, as the H_2 -air mixture ratio increases towards the stoichiometric level, the higher residual gas temperatures speed up the ignition reactions.

Figure 4.3 (c) shows the effect of increasing H_2 addition, at various fixed diesel fuel injection periods, on the pHRR; the figure shows a general increase in the apparent peak heat release rates with increasing H_2 addition. For comparison purposes, Figure 4.3 (c) also shows the pHRR when the engine load is increased without any H_2 addition, that is, by merely increasing the amount of diesel fuel injected. It can be observed in Figure 4.3 (c) that the peak heat release rates for H_2 -diesel fuel mixtures are generally lower than those for diesel fuel only. In addition to the discussion presented for Figure 4.3 (a), the retardation in the ignition delay (Figure 4.3 (b)) may also contribute to the reduction in pHRR with H_2 -diesel fuel co-

combustion relative to diesel fuel only combustion. As the duration of ignition delay increases the pHRR occurs further away from TDC, into the expansion stroke and this could be expected to result in higher energy losses through heat transfer.

Figure 4.3 (d) shows the indicated thermal efficiency of the engine at various fixed diesel fuel injection periods and engine loads. The indicated thermal efficiency was calculated as the ratio of the power output from the engine to the combined energy input from both diesel fuel and hydrogen. Comparing the indicated thermal efficiencies of diesel fuel only and H₂-diesel fuel mixtures, a small drop in the thermal efficiency is observed when H₂ is supplied to the engine. It is believed that the decrease in thermal efficiency with the addition of H₂, contrary to reports in the literature (Masood et al. 2007; Christodoulou & Megaritis 2013), could be due to some of the aspirated H₂ not burning in the engine cylinder and persisting into the exhaust (Gatts et al. 2010). As the amount of H₂ leaving the engine unburned was not measured, it was therefore not considered when calculating the indicated thermal efficiency (Figure 4.3 (d)), and is possible that the contradictory decrease in thermal efficiency may not have been observed had H₂ persisting into the exhaust been accounted for.

4.2.2 Gaseous emissions of CO, THC and CO₂

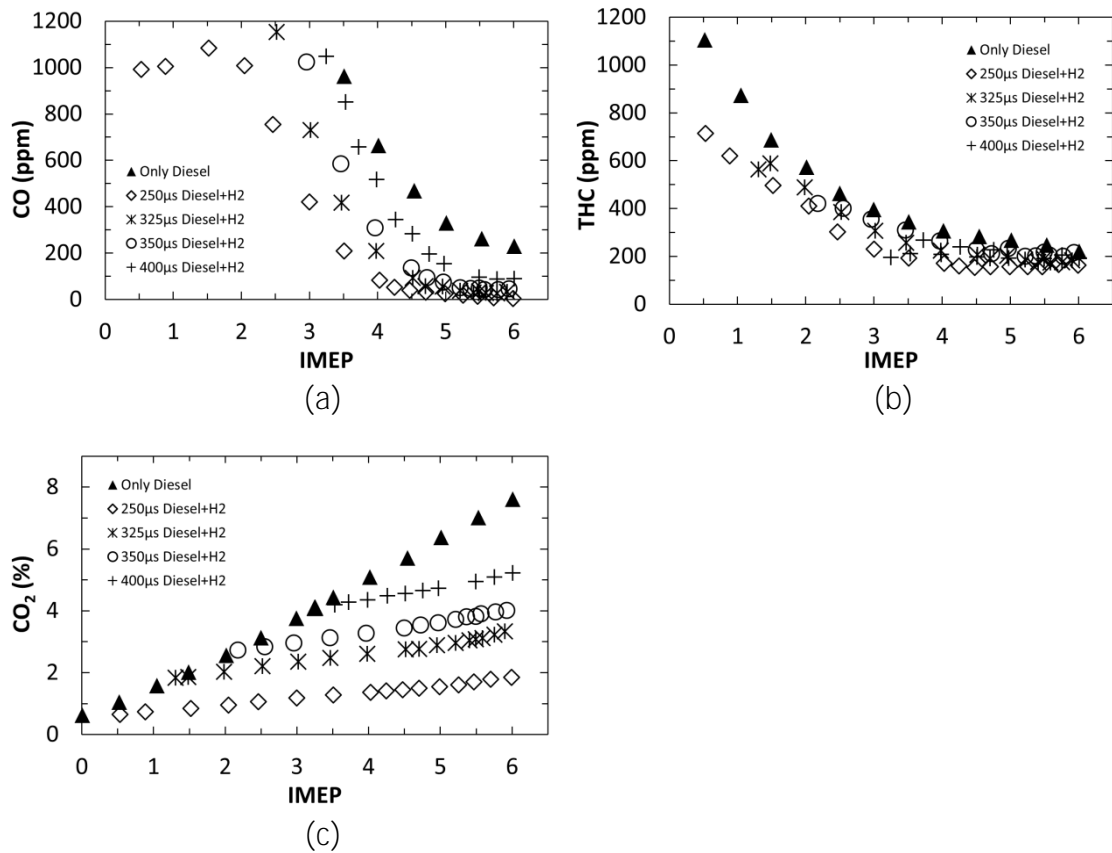


Figure 4.4: Variation in exhaust emissions of (a) carbon monoxide (CO), (b) unburned total hydrocarbons (THC) and (c) carbon dioxide (CO₂) at various engine loads and H₂-diesel fuel proportions

Figure 4.4 (a), (b) and (c) show the effect of H₂ addition, at various fixed diesel fuel injection periods, on the concentrations of CO, THC and CO₂ in the exhaust gas stream respectively. The H₂-diesel fuel co-combustion tests were conducted at fixed diesel fuel flow rates into the engine and the amount of aspirated H₂ into the engine was increased to increase the engine load (IMEP). First, considering CO and THC (Figure 4.4 (a) and (b)), the concentrations of both these gases are high at low engine loads, but then rapidly decrease as the engine load (and level of H₂ addition) rises. At low loads, it is suggested that excessive dilution of diesel fuel at

the spray fringes, combined with lower in-cylinder gas temperatures, results in a diesel fuel-air mixtures which are leaner than their combustion limit, and fuel that is either unreacted or only partially oxidized. As the displacement of intake air by H_2 increases, and thereby the engine load rises, the diesel fuel-air mixture progressively strengthens towards stoichiometric levels, which when combined with high H_2 combustion temperatures, results in higher in-cylinder gas temperatures and more complete combustion.

Interestingly, Figure 4.4 (c) shows a gradual increase in the amount of CO_2 in the exhaust with an increasing amount of hydrogen addition, despite the fact that carbon flow rate to the combustion chamber is fixed (diesel fuel injection duration in μs is fixed). The addition of H_2 in the intake manifold displaces some of the intake air, therefore reducing the flow rate of air through the engine. The H_2 aspirated with the intake air is oxidized to water vapour in the exhaust, which is condensed by the emissions analyser rack prior to measurement of CO_2 in the exhaust gas, therefore reducing the flow rate of exhaust gas. Since the carbon flow rate to the engine is fixed, the amount of CO_2 produced by the diesel fuel could be expected to remain consistent. Therefore, it is suggested that the observed increase in the concentration of CO_2 in the exhaust gas (Figure 4.4(c)) is a consequence of the reduced exhaust flow rate. A secondary, although less significant, possible reason for the increase in CO_2 emissions could potentially be a slight increase in the combustion efficiency of diesel fuel as H_2 addition increases, as an effect of increasing

in-cylinder gas temperatures (as suggested by the higher pHRR with H₂ addition observed in Figure 4.3 (c)). There is some evidence for this in the results in Figure 4.4 (a) and (b) which show a decrease in exhaust gas carbon monoxide and unburned hydrocarbon emissions respectively, with the addition of H₂.

Figure 4.4 (b) also shows that the concentrations of the unburned hydrocarbon exhaust emissions, at different H₂-diesel mixtures, tend to converge at 6 bar IMEP, suggesting almost complete oxidation of all the available hydrocarbon fuel. The remaining hydrocarbons which persist to the exhaust could be originating from a number of sources; crevices in the piston and rings, desorbed off the thin oil layer covering the cylinder walls or from the vaporization of fuel from the injector nozzle sac volume late in the engine cycle (Heywood 1988).

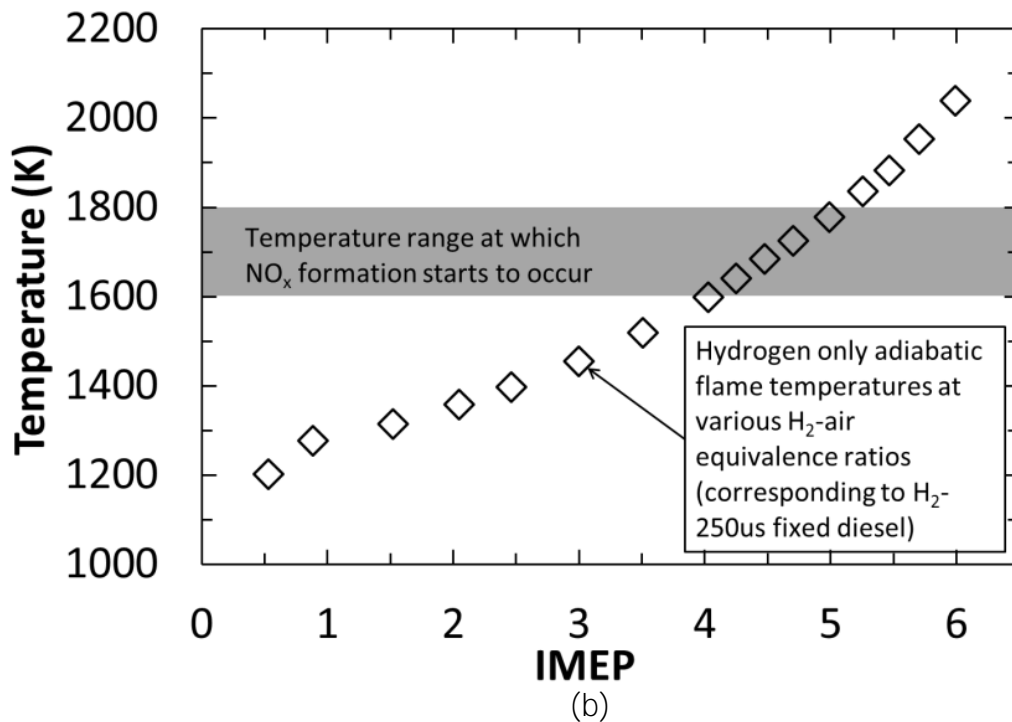
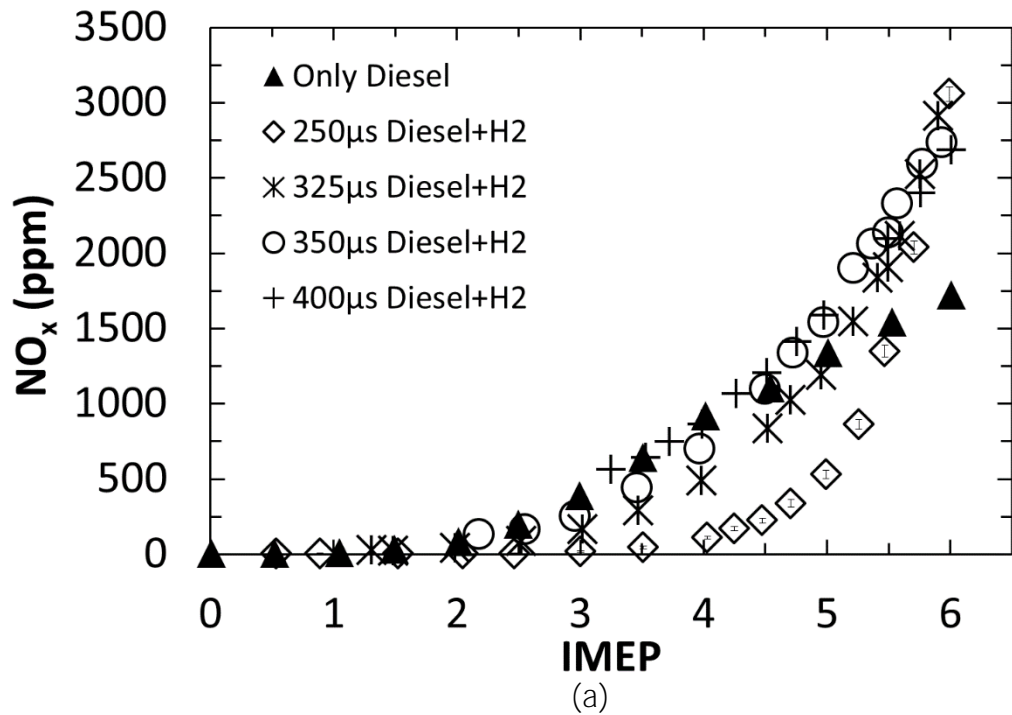
4.2.3 NO_x emissions

Figure 4.5: Variation in (a) exhaust emissions of nitrogen oxides (NO_x) and (b) adiabatic flame temperatures at various engine loads and H₂-diesel fuel proportions. The temperatures were calculated using GASEQ software at an initial pressure of 40 bar and initial temperature of 600 K

Figure 4.5 (a) shows the concentration of NO_x (collective concentrations of NO and NO_2) in the engine exhaust with increasing amounts of H_2 supplied to the engine (at various fixed diesel fuel injection periods. Figure 4.5 (a) shows that when the diesel fuel was limited to the bare minimum ($250 \mu\text{s}$), just sufficient to pilot-ignite the hydrogen, then at low engine loads of up to 4 bar IMEP, very little NO_x (around 20 ppm) was formed. The exhaust NO_x levels, however, increased rapidly when the engine load rose beyond 4 bar IMEP (Figure 4.5 (a)). This suggests that at lower engine loads below 4 bar IMEP, the H_2 -air mixture was far too lean for NO_x to form, with the resulting combustion temperatures from H_2 combustion remaining below the temperatures which promote rapid thermal NO_x formation. At engine loads above 4 bar IMEP, the H_2 concentration in the intake air became sufficient for the in-cylinder gas temperatures to reach a level at which the kinetically controlled NO_x formation rates accelerated significantly, resulting in substantial exhaust emissions of NO_x (Figure 4.5 (a)).

Figure 4.5 (b) helps explain the test results presented in Figure 4.5 (a). In general, the principal reactions governing the oxidation of molecular nitrogen to NO_x initiate at temperatures ranging between 1600 K and 1800 K (Heywood 1988) as shown in Figure 4.5 (b). Figure 4.5 (b) shows that with the level of addition of H_2 present between 1 and 4 bar IMEP, the H_2 -air mixture was still too lean and the hydrogen adiabatic flame temperature was below that needed for significant quantities of NO_x to be produced. It can be seen that only when levels of H_2 addition reached those

required to produce an engine load of greater than 4 bar IMEP, was the H₂ adiabatic flame temperature sufficient for NO_x production (Figure 4.5 (b)), coinciding with the sharp increase in NO_x emissions observed in Figure 4.5 (a).

An additional observation from Figure 4.5 (a) is that diesel fuel was also a significant source of NO_x formation. This is related to the fact that combustion of diesel sprays can be expected to always occur at close-to-stoichiometric conditions at the fuel spray fringes with resultant local temperatures high enough for NO_x formation (Dec 1997). At higher loads of 5.5 bar IMEP and above, and with diesel fuel injection duration of 250 μs, it is apparent that NO_x emissions produced during H₂-diesel fuel co-combustion increase above the level of NO_x observed in the case of diesel fuel only combustion. It is suggested that this may be attributable to higher in-cylinder gas temperatures in the case of combined H₂-diesel fuel co-combustion than in diesel only combustion, resulting in higher rates of NO_x formation.

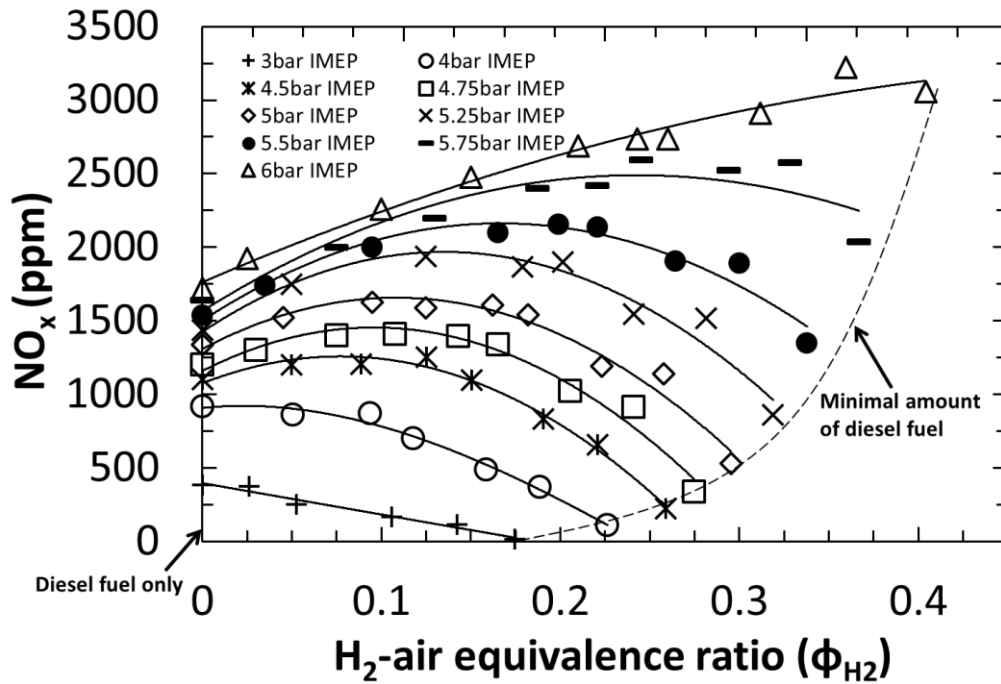


Figure 4.6: Exhaust emissions of nitrogen oxides (NO_x) at constant engine loads and variable H_2 -air equivalence ratio (ϕ_{H_2})

To further explain the effect of H_2 -air mixture stoichiometry on NO_x emissions, the data in Figure 4.5 (b) has been re-plotted in Figure 4.6. Each curve on Figure 4.6 corresponds to a constant engine load (IMEP) and shows the variations in exhaust NO_x emissions when a constant engine load is obtained at different combinations of H_2 -air mixture ratios by the substitution of diesel fuel with H_2 .

Referring to Figure 4.6, consider first the NO_x emissions at a lower constant engine load of 4 bar IMEP. Figure 4.6 shows that at 4 bar IMEP, an increase in the H_2 -air equivalence ratio (ϕ_{H_2}) resulted in reduced NO_x emissions. This is a particularly interesting result and can be explained as follows. At 4 bar IMEP, the H_2 -air equivalence ratio is too lean to produce NO_x (Figure 4.5 (a) and (b)). The bulk of NO_x emissions come from diesel fuel combustion. The diesel fuel injected into the combustion chamber of the diesel engine used in this study can always be expected

to produce significant quantities of NO_x , because spray combustion takes place around the spray fringe where the diesel fuel-air equivalence ratio is at about stoichiometric value. Therefore, the gradual substitution of diesel fuel by H_2 (at constant engine loads of less than or equal to 4 bar IMEP) resulted in the gradual reduction of NO_x exhaust emissions.

At a higher engine load of 6 bar IMEP, a different picture emerges (Figure 4.6). The substitution of diesel fuel by H_2 does not result in a reduction in NO_x but, instead, in a monotonic increase in NO_x . At this engine load, the amount of diesel fuel injected is relatively large and H_2 addition has no effect in reducing NO_x , despite the fact that diesel fuel is being substituted by H_2 . It appears that at these higher loads, H_2 enhances the production of NO_x by further raising the temperatures in the diesel fuel spray combustion zones. As the substitution of diesel fuel with H_2 increases at a constant engine load of 6 bar IMEP, the amount of H_2 needed to sustain the 6 bar IMEP becomes high (ϕ_{H_2} reaches 0.4), which raises the in-cylinder gas temperature above the thermal NO_x production temperature (Figure 4.5 (b)).

Considering now a relatively intermediate engine load of 5 bar IMEP, Figure 4.6 shows that, NO_x first increases with the substitution of diesel fuel by H_2 , but then as H_2 substitution becomes higher, NO_x levels begin to fall. A likely explanation for this observation can be the following. At low H_2 substitution levels, the diesel fuel combustion provides numerous ignition sites and the bulk of the energy release. Therefore NO_x production would be dominated by the diesel fuel burning at near-

stoichiometric local sites and the H_2 providing, locally, additional synergetic heat release and temperature rise, resulting in extra NO_x formation. With the progressive removal of diesel fuel and substitution with H_2 there comes a point when the amount of diesel fuel removed is large enough for the high rate of NO_x production from diesel fuel to be curtailed. At the same time, NO_x production from H_2 is not significant, because at intermediate engine loads the H_2 -air equivalence ratio is still not sufficiently high for commensurate NO_x production, at the same levels that was produced by the diesel fuel that the H_2 substituted. Hence a drop in exhaust NO_x emissions is observed (Figure 4.6).

4.2.4 Nitrogen dilution experiments

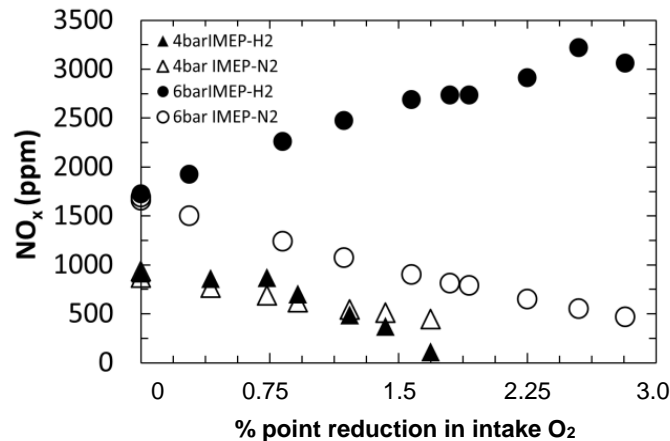


Figure 4.7: Exhaust emissions of NO_x at constant engine loads and varying percentage reduction in intake O_2 due to the aspirated H_2 or N_2 (assuming 21% O_2 in ambient air).

For all the experiments presented in this chapter the H_2 was aspirated into the engine inlet manifold, thus displacing some of the intake air with hydrogen. While the H_2 takes part in the combustion process and releases energy which in turn raises the local gas temperatures in the engine cylinder and thereby, increases NO_x

formation rates, the H_2 also has an additional effect of diluting the local amount of air, and the decreasing oxygen availability could be expected to reduce NO_x . This effect of H_2 addition to reduce NO_x may partially offset the increased NO_x production due to higher in-cylinder temperatures brought about as a result of H_2 combustion. In an effort to separate and quantify the dilution effect of H_2 on NO_x levels, the intake air was displaced by nitrogen (rather than H_2) to displace the same amount of O_2 from the intake air as when using H_2 in the intake. The nitrogen (N_2) dilution tests were conducted at two constant engine loads, 4 bar and 6 bar IMEP and plotted against the reduction in intake O_2 as shown in Figure 4.7. It can be seen from that at the low engine load of 4 bar IMEP, a similar effect of H_2 and N_2 addition is observed, with NO_x levels decreasing with increasing levels of either gas (or reduction in intake O_2). It implies that both gases act just as diluents, by reducing the amount of O_2 and, thereby, reducing NO_x formation from the diesel fuel spray. This result is consistent with previous results presented in this study which showed that at an engine load of 4 bar IMEP, the H_2 -air mixture is too lean to result in the necessary temperature rise for production of significant levels of NO_x . However, it must be noted that with increasing H_2 addition, the diesel fuel flow rate has to be reduced in order to maintain a constant engine load, while the same is not done in the case of N_2 addition. Since diesel fuel can be expected to produce significant NO_x at these engine loads (as can be seen in Figure 4.5 (a)), it

is difficult to discern whether the reduction in NO_x emissions is due to the reduction in diesel fuel or the diesel fuel being replaced by a lean H_2 -air mixture.

It can be seen from Figure 4.7 that at 6 bar IMEP, the addition of N_2 causes an appreciable reduction in the NO_x produced from the diesel fuel spray due to dilution effects. However, with H_2 addition at the constant load of 6 bar IMEP, the combustion of H_2 produces significantly high temperatures which result in not only in offsetting the dilution effect (or reduction in intake O_2) on NO_x production, but also cause a monotonic rise in NO_x as the H_2 -air equivalence ratio is gradually increased by means of substitution of diesel fuel with hydrogen.

4.2.5 Particulate emissions

Figure 4.8 shows the exhaust emissions of total particulate mass at various fixed diesel fuel injection periods and engine loads. The change in engine load was achieved by varying the amount of H₂ addition, while keeping the diesel fuel supplied to the engine fixed. At a fixed diesel fuel injection period, it can be seen that increasing H₂ addition results in a decrease in PM emissions up to 5.5 bar IMEP. At a low fixed diesel fuel injection period, such as 250 μs, particulate emissions drop to negligible levels as H₂ is introduced into the engine. Increasing engine loads beyond 5.5 bar IMEP results in a small increase in emissions of PM (Figure 4.8). The introduction of H₂ in the intake charge can be expected to have resulted in two competing effects on PM formation. Firstly, it can be expected that the reduction in O₂ availability due to the displacement of intake air with H₂

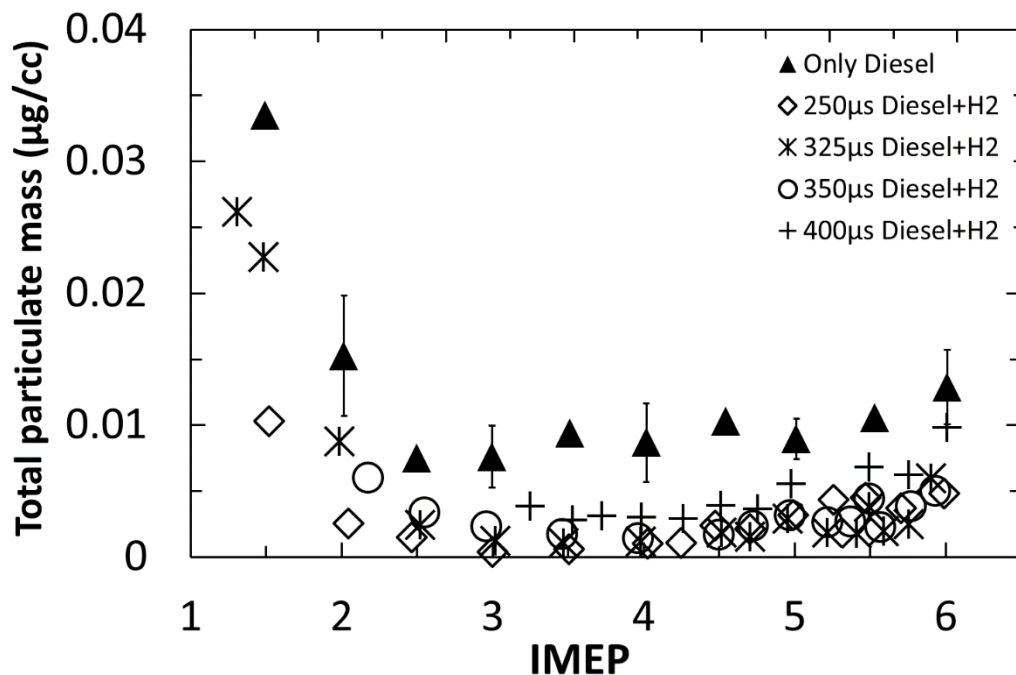


Figure 4.8: Variation in exhaust emissions of total particulate mass ($\mu\text{g}/\text{cc}$) at various engine loads and H₂-diesel fuel proportions

accelerated particle formation via rising pyrolysis rates and, secondly, the high temperatures resulting from H₂ combustion led to a counteracting increase in the rate of thermal soot oxidation. Particulates are mostly formed in the fuel rich, and highly oxygen deficient, core regions of the diesel fuel spray, within the spray flame envelope, when the fuel vapour comes in contact with the hot burned gases (Heywood 1988; Ning et al. 1991). Oxidation of these particulates occurs with the continuous breakdown of the spray due to intense turbulence levels and mixing with air, when PM oxidizes to form gaseous products such as CO and CO₂. The eventual level of PM emissions in the exhaust depends on the balance between these two competing effects, formation and oxidation. Figure 4.8 suggests that the enhanced oxidation process prevails over increased pyrolysis rates when H₂ supply to the engine is increased, resulting in an overall reduction in PM emissions at fixed diesel fuel injection periods.

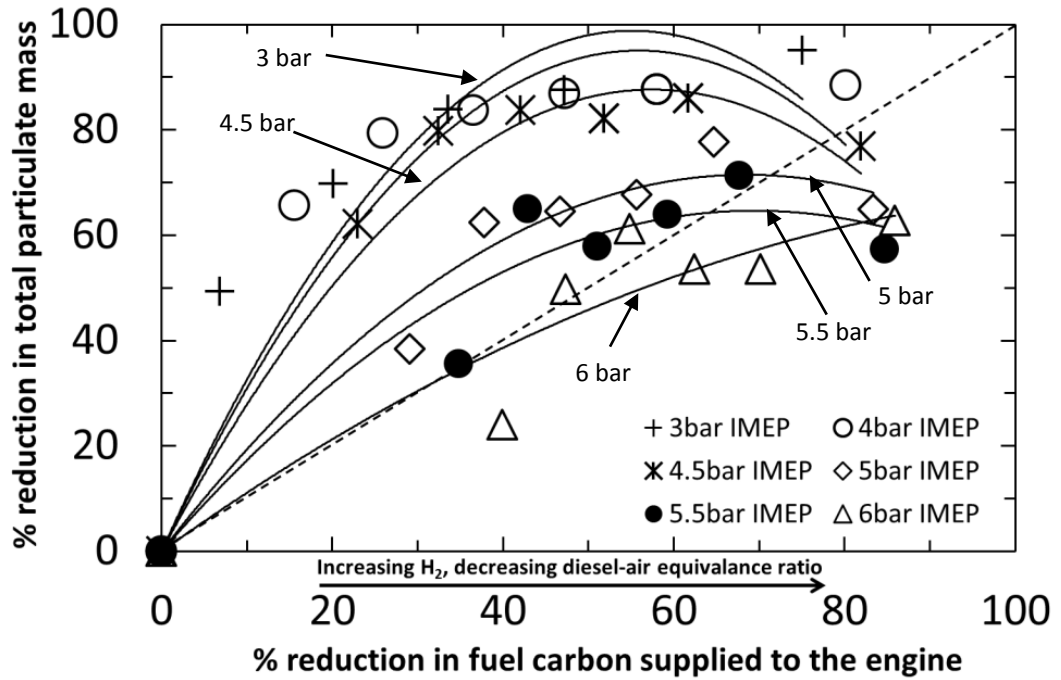


Figure 4.9: Comparison of the percentage reduction in total particulate mass with percentage reduction in the carbon content of the combustible mixture at constant engine loads

Figure 4.9 shows the percentage reduction in the total particulate mass plotted against the percentage reduction in fuel carbon supplied to the engine, at constant engine loads. The reduction in fuel carbon was achieved by lowering the amount of diesel injected and the loss in engine power was restored by adding H_2 in order to maintain a constant engine load. The percentage reductions in both particulates and fuel carbon were calculated against the values obtained with the engine operating on only diesel fuel (no H_2 addition). The 1:1 dashed diagonal line in Figure 4.9 represents equivalent reductions in both PM emissions and fuel carbon supplied to the engine.

For engine loads below 4 bar IMEP, Figure 4.9 shows the reductions in PM emissions to lie in the top half of the graph (above the 1:1 dashed line), implying a

beneficial effect of H₂ addition on PM reduction beyond simple fuel carbon displacement. For example, at a constant engine load 3 bar IMEP, a 10% reduction in fuel carbon causes up to 50% reduction in particulate matter. Therefore, as previously discussed, it could be suggested that an increase in H₂-air stoichiometry (or a decrease in diesel fuel) promotes soot oxidation, or reduces initial soot formation, and at low engine loads these effects are more important than any increase in soot formation due to O₂ reduction. At the higher engine load of 5 bar IMEP, Figure 4.9 shows that the effect of H₂ substitution for diesel fuel results in a net reduction in PM, but this effect is less than that at the lower load of 3 bar IMEP.

At the maximum load tested of 6 bar IMEP (Figure 4.9), the reductions in particulate mass lie almost entirely in the bottom half of the graph (below the 1:1 dashed line). This suggests that the addition of H₂ results in only a small reduction in PM, with this reduction being smaller than the reduction in PM that could be expected from merely the drop in fuel carbon supplied to the engine. One possible explanation for this is, at higher engine loads (6 bar IMEP or above) the air displaced due to the addition of substantial quantities of H₂ to the engine severely affects the oxygen availability for PM oxidation, despite the increase in in-cylinder temperatures arising from higher H₂-air equivalence ratios.

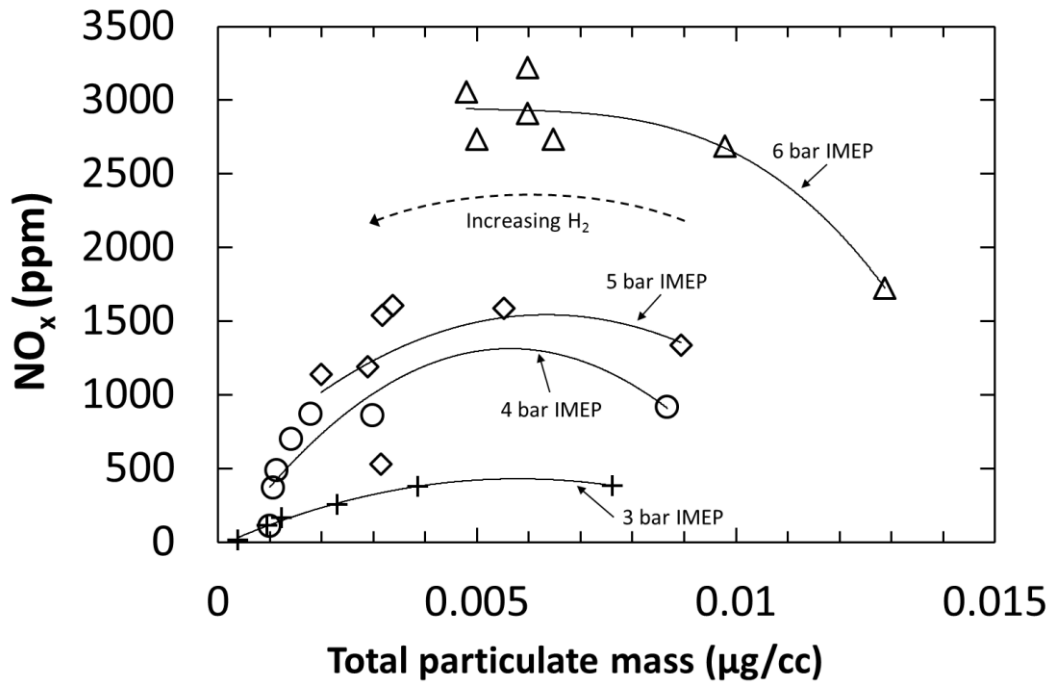


Figure 4.10: Exhaust NO_x emissions against PM emissions at constant engine loads with varying proportions of H₂ and diesel fuel.

Figure 4.10 shows the exhaust NO_x emissions plotted against exhaust PM emissions at constant engine loads. The amount of diesel fuel and H₂ being supplied to the engine was varied to maintain a constant engine load, and the increase in total particulate mass emissions represents an increasing amount of diesel fuel (hence decreasing H₂) being supplied to the engine.

At engines loads of 3, 4 and 5 bar IMEP a reduction in both NO_x and particulate exhaust emissions is observed when diesel fuel is replaced by H₂. The reduction in particulates is expected since the carbon containing diesel fuel is being replaced by H₂. The reduction in NO_x emissions could be due to diesel fuel (which typically burns at near stoichiometric conditions) being replaced by a much leaner H₂-air mixture which results in relatively lower gas temperatures on combustion. At an engine load of 6 bar IMEP (Figure 4.10), a trade-off is observed whereby NO_x

emissions increase when a reduction in particulates is obtained. As discussed earlier, this could be because at an engine load of 6 bar IMEP, a sufficient quantity of diesel fuel exists inside the cylinder (despite some of it being displaced by H_2), and any H_2 combustion that occurs provides additional energy to the on-going in-cylinder reactions, thereby raising gas temperatures and hence the levels of exhaust NO_x .

4.2.6 In-cylinder gas sample analysis

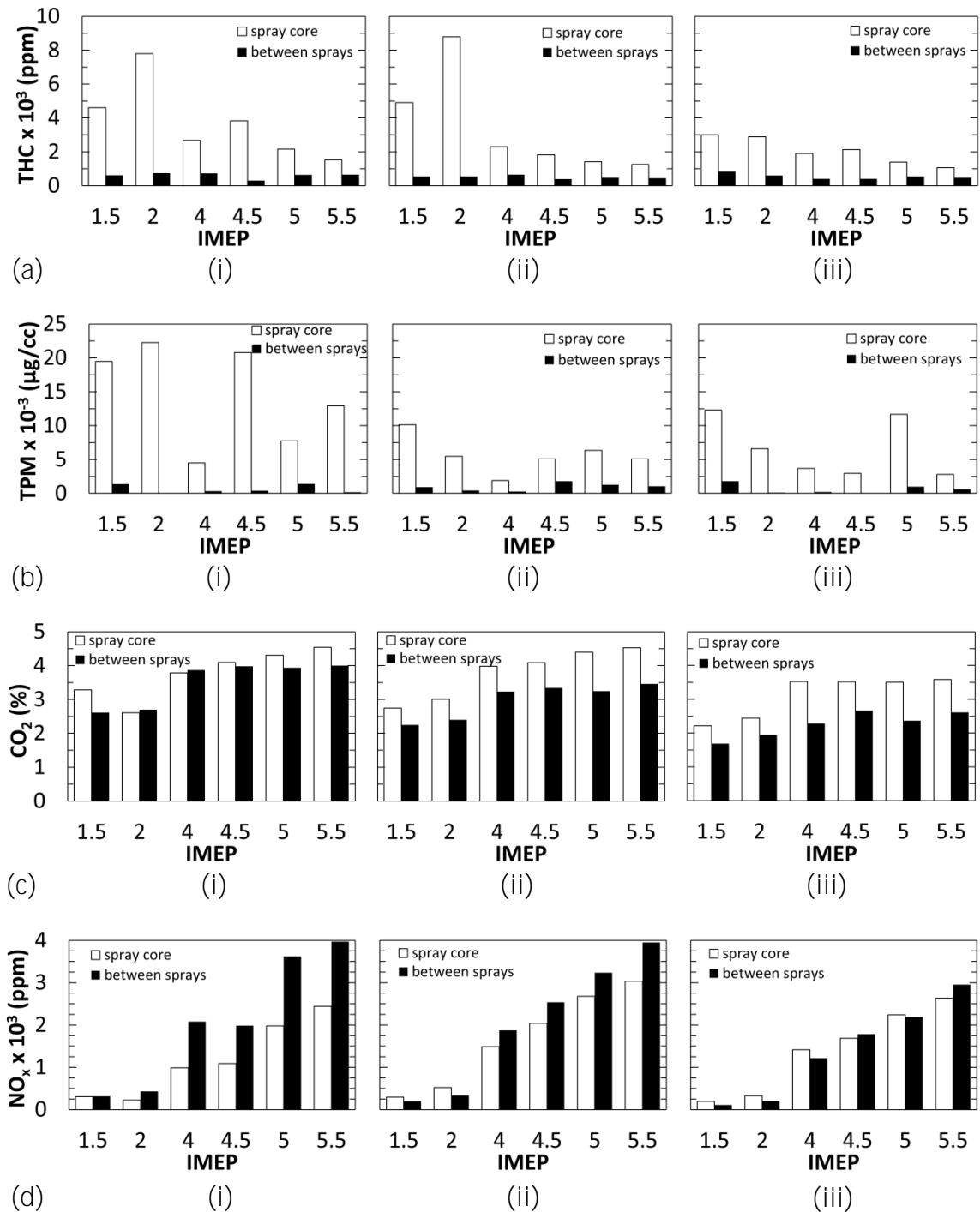


Figure 4.11: Measurement of (a) in-cylinder unburned total hydrocarbon (THC) concentration, (b) total particulate mass (TPM), (c) carbon dioxide (CO₂) concentration and (d) nitrogen oxide (NO_x) concentration in gas samples collected at (i) 10 CAD, (ii) 25 CAD and (iii) 40 CAD ATDC at fixed diesel with increasing amounts of H₂ and variable engine loads (engine speed 1200 rpm) with two sampling arrangements (Figure 4.2)

This section of the chapter presents the results of in-cylinder gas sampling with the two sampling arrangements (in the spray core and between two sprays), as discussed in Section 4.1.2.

Figure 4.11 (a) and (b) show, respectively, the concentrations of unburned total hydrocarbons and particulate matter in gas samples at various engine loads extracted from the engine cylinder at 10, 25 and 40 CAD ATDC of the combustion cycle with the two in-cylinder sampling arrangements relative to the diesel fuel sprays (Figure 4.2). The tests were conducted at a fixed diesel injection period of 325 μs (corresponding to an engine load of 1.5 bar IMEP) and the increase in engine load was achieved by adding H_2 to the intake charge. Therefore, in Figure 4.11 the in-cylinder sample concentration at 1.5 bar IMEP represent that due to diesel fuel only engine operation, and that of H_2 -diesel co-combustion for all loads above 1.5 bar IMEP. Figure 4.11 (a) and (b) show that the concentrations of total hydrocarbons and particulate matter when sampling within the fuel spray were higher, at all engine loads, compared to the results obtained when sampling between two fuel sprays. In the fuel dense core of the diesel spray, local average equivalence ratios are rich, due to lack of air entrainment, especially during the initial stages of combustion, and thereby generate high particulate concentrations. The region in between two individual diesel sprays contains relatively low amounts of fuel vapour that have been swept around by the swirling air flow, and hence is characterized by leaner diesel fuel equivalence ratios, leading to more complete combustion and

lower THC and PM concentrations. These observations are in agreement with similar gas sampling studies undertaken so as to map out fuel distribution in diesel engine cylinders (Nightingale 1975; Bennethum et al. 1975; Rhee et al. 1978).

It can also be observed from Figure 4.11 (a) and (b) that the concentrations of THC and PM, respectively, generally decreased as combustion proceeded; this can possibly be attributed to the enhanced mixing of diesel fuel and air as spray was broken up and came into contact with hot unburned gases, resulting in more complete diesel fuel oxidation. The only exception to this is seen at an engine load of 2 bar IMEP, whereby an increase in THC concentration is observed. It is speculated that this increase is due to the introduction of H_2 with the intake air which reduces the O_2 availability for diesel combustion, resulting in the diesel flame front quenching faster and causing an increase in unburnt THC levels.

The generally decreasing levels of THC and PM emissions with increasing engine load (IMEP), observed at the three sampling instants (Figure 4.11 (a) and (b)), are in agreement with the measurements of exhaust gas composition discussed in Section 4.2.2. H_2 addition is expected to have potentially increased diesel combustion efficiency by raising the in-cylinder gas temperatures, thereby promoting the rate of thermal soot oxidation.

Figure 4.11 (c) shows the molar fraction of CO_2 in gas samples at various engine loads extracted from the engine cylinder at 10, 25 and 40 CAD ATDC of the combustion cycle with the two in-cylinder sampling arrangements relative to the

diesel fuel sprays (Figure 4.2). At 10 CAD ATDC, at all the engine loads, the CO₂ concentrations were quite similar between the two sampling arrangements. As combustion progressed, the CO₂ concentrations in spray core remained fairly high, whereas a reduction was observed in the CO₂ levels in the gas samples obtained from the region between two sprays. At 40 CAD ATDC, the CO₂ concentrations with both the sampling arrangements fell as the burned gas products became further diluted with the unreacted intake air from within the piston bowl as the expansion stroke progresses.

As with the exhaust CO₂ emissions (Figure 4.4 (c)), the CO₂ concentrations in the in-cylinder gas samples, at all sampling instants, gradually increased with increasing H₂ addition (increasing IMEP) (Figure 4.11 (c)), the reasons for which have been discussed in detail in Section 4.2.2.

Figure 4.11 (d) shows the NO_x concentrations in gas samples at various engine loads extracted from the engine cylinder at 10, 25 and 40 CAD ATDC of the combustion cycle with the two in-cylinder sampling arrangements relative to the diesel fuel sprays (Figure 4.2). At 10 and 25 CAD ATDC and at all engine loads, NO_x concentrations were higher between the two sprays, as compared to those in the spray core. Comparing the NO_x concentrations between 10 and 25 CAD ATDC, an increase was seen in NO_x in the spray core, while, between the two sprays, NO_x remained quite similar at both sampling instants (10 and 25 CAD ATDC). At a later stage of the engine cycle, at 40 CAD ATDC, the NO_x concentrations with

both sampling arrangements were of similar magnitude. However, with both sampling arrangements, NO_x concentrations at 40 CAD ATDC were lower compared to those at 25 CAD ATDC.

Spatial and temporal distribution of in-cylinder NO_x and CO_2

From the in-cylinder sampling results presented in Figure 4.11, and notwithstanding that some relative movement of the diesel spray between the three sampling times could be expected due to the effects of in-cylinder swirl, the following further discussion is made. Air is entrained into the diesel fuel vapour at the periphery of the dense diesel fuel spray core by the swirling motion of the air; this, combined with the turbulent environment inside the chamber, results in the mixing and dilution of fuel vapour in the intake charge, especially in the regions between the individual sprays, where there is a higher initial concentration of the air and hydrogen intake mixture (Dec 1997). As mentioned previously, it can be expected that autoignition first occurs at these close-to-stoichiometric diesel fuel vapour-air pockets around the fuel sprays and results in the rapid burning of both the premixed diesel vapour and H_2 -air mixtures around the diesel fuel ignition sites. As suggested in Section 4.2.3, H_2 combustion provides additional energy to diesel fuel combustion, and NO_x production initiates when the combined temperatures from H_2 -diesel fuel co-combustion exceed that required for thermal NO_x formation. Considering the difference in the concentrations of NO_x with the two sampling arrangements at 10 CAD ATDC (Figure 4.11 (d)(i)), the region in between two

sprays (arrangement two) could be expected to have a higher H₂-air concentration resulting in higher gas temperatures and, therefore, higher NO_x formation rates. On the other hand, the lower NO_x concentrations in the spray core (at 10 CAD ATDC) could be attributable to the relatively low concentration of air in the fuel rich core of the diesel fuel spray, resulting in lower combustion temperatures and, hence, reduced NO_x formation. Furthermore, some of the energy released in this fuel rich region can be expected to have been absorbed for fuel pyrolysis (Heywood 1988), resulting in lower gas temperatures, and hence, reduced NO_x formation rates.

Considering the increase in NO_x concentrations between 10 and 25 CAD ATDC (Figure 4.11 (d)), in the spray core, the rich diesel spray core can be expected to have broken up as combustion progresses, with the H₂-air mixture being rapidly entrained into the disintegrated diesel fuel spray. It can be expected that the combined fuel mixture will burn at sufficiently high temperatures to increase NO_x formation rates as combustion progressed from 10 to 25 CAD ATDC. This is further reinforced by the appreciable CO₂ concentrations observed in the spray core at 25 CAD ATDC, suggesting considerable combustion of carbon-containing fuel occurring at that location (Figure 4.11 (c)).

Considering now the region between the two sprays, the following observations can be made:

- NO_x concentration showed no significant change, between 10 and 25 CAD ATDC (Figure 4.11 (d)), as the engine expansion stroke had commenced and

the mixing of the post-combustion gases with excess air could be expected to have frozen the NO_x formation reactions (Stone 2012).

- A decrease in CO_2 concentrations, obtained from the region in between the spray, was observed from 10 to 25 CAD ATDC (Figure 4.11 (c)). For example, at 4 bar IMEP, CO_2 concentrations, between the sprays, decreased from about 4% to 3% as combustion progressed from 10 to 25 CAD ATDC. This could be attributable to the mixing of CO_2 with excess air, resulting in a reduction in the CO_2 concentration measured in the sampled in-cylinder gas.
- At 40 CAD ATDC, CO_2 (Figure 4.11 (c)) and NO_x (Figure 4.11 (d)) concentrations in the extracted sample were quite similar with both sampling arrangements. This may be expected, as at later stages of combustion the effects of air swirl and reverse squish flow (Heywood 1988; Zhao et al. 1996) promote the redistribution of in-cylinder gaseous composition, creating near homogenous conditions in the cylinder.

4.3 Conclusions

- An increase in the duration of ignition delay was observed at intermediate engine loads with H₂ addition, which could be attributed to the decreasing O₂ concentration in the intake charge. This reduction in O₂ availability can be expected to lead to a reduction in the rate of low temperature fuel reaction kinetics, delaying autoignition. At high engine loads, the ignition delay period was observed to have reduced in duration, as elevated in-cylinder temperatures improved the evaporation and subsequent mixing of the injected fuel with air.
- An increase in CO₂ emissions (both exhaust and in-cylinder) with H₂ addition was observed despite fixed fuel carbon flow rate into the combustion chamber (diesel fuel injection period was fixed). The displacement of intake air by H₂ and the subsequent oxidation of H₂ to water vapour reduced the exhaust flow rate, since the water vapour is condensed by the analysers prior to CO₂ measurement. Except for a small increase in diesel combustion efficiency (as seen by the decrease in exhaust gas carbon monoxide and unburned hydrocarbon emissions), the CO₂ produced by the diesel fuel is expected to be unchanged and the CO₂ concentration in the exhaust can be expected to rise, as a consequence of the reduced exhaust flow rate.
- NO_x emissions (both exhaust and in-cylinder) were observed to increase very rapidly with the addition of H₂ but only when the combined temperatures

resulting from H₂-diesel fuel co-combustion exceeded the threshold temperature for NO_x formation temperatures.

- At fixed diesel fuel injection periods and engine loads below 5.5 bar IMEP, a reduction in the overall PM emissions was observed with H₂ addition, as soot burnout by thermal oxidation offset the effects of soot formation via pyrolysis. At higher engine loads, the effect of dilution of intake O₂ due to displacement by H₂ becomes the primary influence on particulate matter generation and a small rise in PM emissions was observed.
- At low engine loads, the addition of H₂ promoted soot burnout due to elevated temperatures and higher oxidation rates; at intermediate engine loads, the effects of soot formation and oxidation counterbalanced each other; and at high engine loads, the excessive displacement of intake O₂ by H₂ led to slightly increased rates of soot formation.
- From in-cylinder gas sampling results it was observed that at early stages of combustion (10 CAD ATDC), NO_x concentrations within the diesel fuel spray were lower than those measured in between two individual fuel sprays. This could be attributed to a higher concentration of H₂-air mixture burning in between the sprays, combined with the combustion of significant amounts of diesel fuel vapour occurring between the sprays. This is expected to have resulted in high temperatures in this region (between the sprays) and,

therefore, higher NO_x formation rates in comparison to the NO_x formation rates within the spray, where a deficiency of air existed.

5 Influence of methane-hydrogen mixtures on combustion and emission characteristics, and in-cylinder gas composition

The complimentary properties of methane (CH_4) and hydrogen (H_2) were discussed in detail in Chapter 2 and have been summarised here. While CH_4 is a relatively stable molecule with a significantly higher ignition energy requirement, H_2 has a flame speed about six to eight times greater than that of CH_4 resulting in smaller time intervals between fuel ignition and peak heat release rates (Karim 2003; Klell et al. 2012). CH_4 operated engines suffer from increased cycle to cycle variation and occasional flame failure, while combustion anomalies such as backfire and knock are normally associated with H_2 burning (Akansu et al. 2007; Demuynck et al. 2009; Verhelst et al. 2010; Diéguez et al. 2014). The use of CH_4 - H_2 mixtures has the potential of utilising the properties of the individual gases in a beneficial manner, for example widening the flammability limits to allow stable engine operation under

lean conditions, which can lead to low temperature combustion and hence reduced NO_x formation.

The chapter presents an experimental investigation of co-combusting methane-hydrogen mixtures with diesel fuel, carried out on the direct injection compression ignition engine. The tests were performed with two different pilot diesel fuel flow rates, with the engine being supplied with different quantities methane-hydrogen mixtures (of various proportions) to vary the engine load between 0 and 7 bar IMEP. In addition, engine in-cylinder gas samples were collected with two distinct sampling arrangements and at various instants during the engine cycle, to measure species concentrations in the cylinder.

5.1 Experimental procedure

The experiments discussed in this chapter were conducted on the single cylinder engine utilising the common rail fuel injection system for diesel fuel injection and the gas mass flow controller system for delivering metered quantities of methane (CH_4) and hydrogen (H_2) to the engine. These systems have been described in detail in Chapter 3 of this thesis. All the experiments were carried out at a constant engine speed of 1200 rpm, common rail fuel injection pressure of 900 bar and a diesel fuel injection timing of 10 CAD BTDC. The diesel fuel used for all tests was of fossil origin, with zero fatty acid methyl ester (FAME) content, cetane number of 53.2 and carbon to hydrogen ratio of 6.32:1 by mass. Compressed methane gas

and compressed hydrogen gas of purity 99.5% and 99.995%, respectively, were obtained from a commercial gas supplier (BOC).

5.1.1 Experimental set 1: Exhaust emission tests (using CH₄-H₂ mixtures)

The adopted test procedure consisted of fixing the flow rate of diesel fuel supplied to the engine (pilot diesel fuel flow rate), while gradually increasing the amount of CH₄-H₂ mixture being delivered to the engine so as to increase the engine load (that is, power output measured in bar IMEP, at constant engine speed). The diesel fuel flow rate was kept fixed by maintaining a constant engine load, henceforth referred to as the pilot diesel fuel IMEP. Two series of tests were conducted and during the first series the pilot diesel fuel flow rate was kept fixed to achieve an engine load of 0 bar IMEP from diesel fuel only (that is, without any CH₄ or H₂ being supplied to the engine). For a pilot diesel fuel only IMEP of 0 bar, no heat release could be discerned from the analysis of in-cylinder gas pressure. Therefore the diesel flow rate, equivalent to a pilot diesel IMEP of 0 bar, was taken to be minimum flow rate below which no spray emerges from the diesel injector nozzle. Nevertheless, it was observed that the diesel flow rate equivalent to a pilot diesel IMEP of 0 bar was sufficient to ignite the aspirated CH₄-H₂-air mixture at all engine loads up to 7 bar IMEP. During the second series of tests, the diesel fuel flow rate was again kept fixed, but this time to develop an engine load of 1.5 bar IMEP without any CH₄ or H₂ addition.

For each of the two pilot diesel fuel IMEPs, the above procedure was repeated for a variety of CH₄-H₂ mixture ratios, ranging from 20% CH₄:80% H₂ (v/v) to 80% CH₄:20% H₂ (v/v), as can be seen in Table 5.1; for each of the mixtures the flow rate was gradually increased to increase the engine load (with the diesel fuel flow kept fixed, as mentioned above). Figure 5.1 (a) and (b) show the energy supplied to the engine from the H₂ as a function of the total energy supplied to the engine (that is, energy from the CH₄-H₂ mixture plus diesel), for the two pilot diesel fuel IMEPs of 0 bar and 1.5 bar, at various engine loads and CH₄-H₂ mixture ratios. Table 5.2 lists the properties of diesel fuel, methane and hydrogen used in these experiments.

An additional series of baseline (control) tests were carried out, for comparison, using diesel fuel only (without any CH₄ or H₂), with the diesel fuel injection period (and hence the diesel fuel flow rate delivered to the engine) gradually increased so that the engine load increased from 0 to 7 bar IMEP.

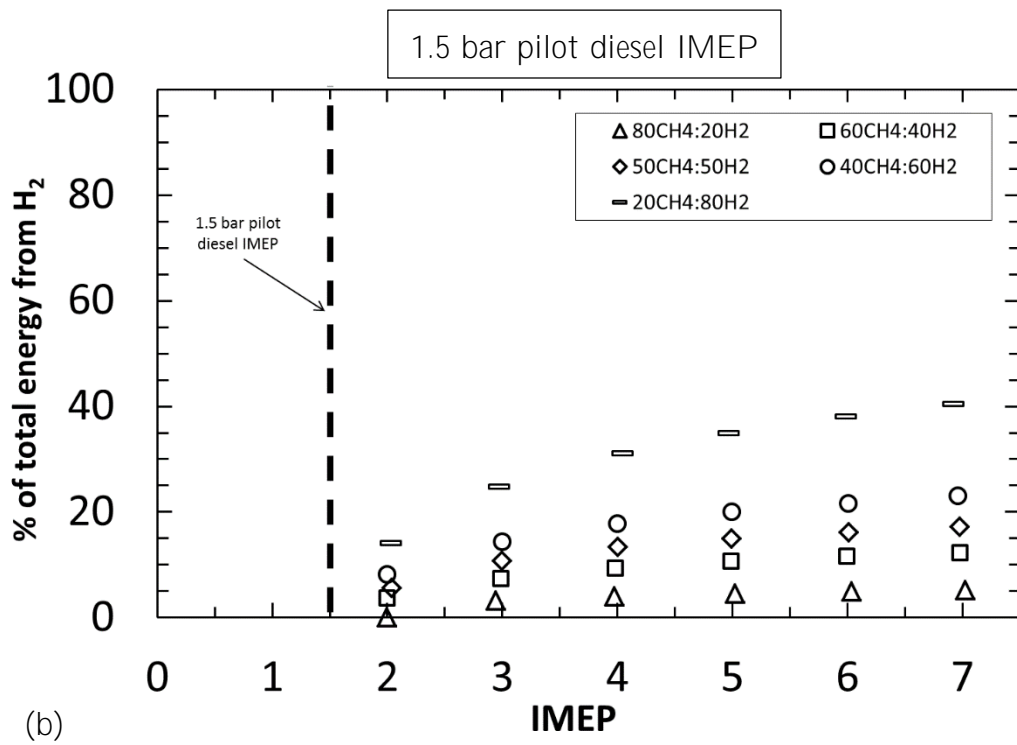
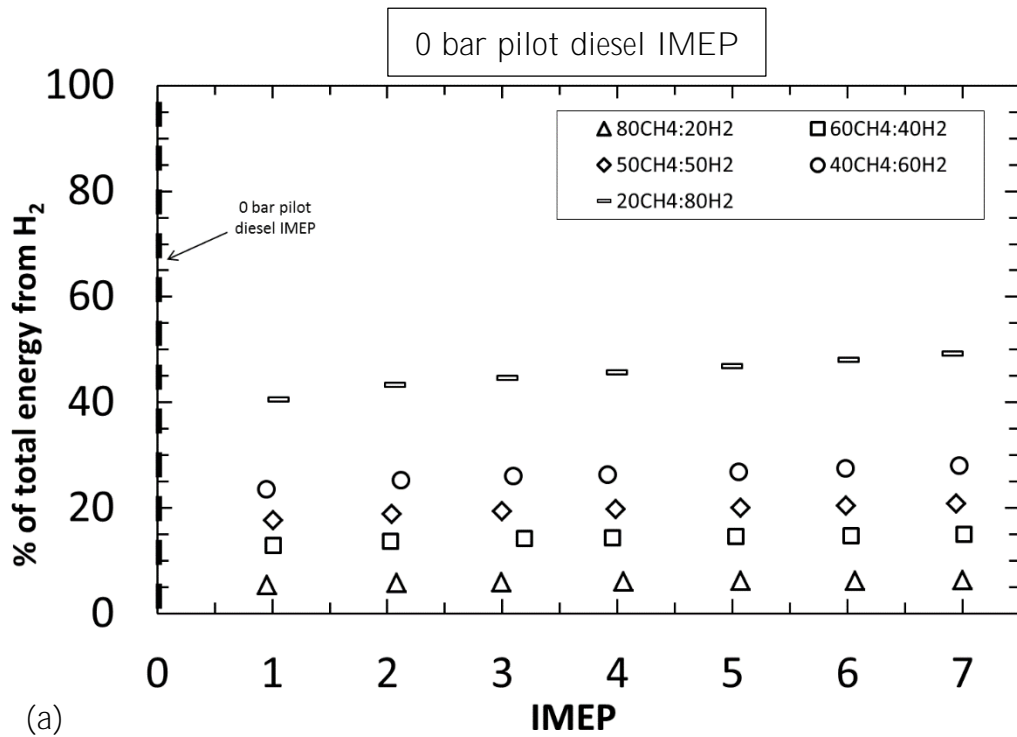


Figure 5.1: Percentage energy from H_2 for (a) 0 bar and (b) 1.5 bar pilot diesel fuel IMEP, at various engine loads (IMEP) and CH_4 - H_2 mixture ratios

Pilot diesel (bar IMEP)	Diesel fuel flow rate (ml/min)	CH ₄ :H ₂ ratio (v/v)	CH ₄ flow rate (l/min)	H ₂ flow rate (l/min)	CH ₄ -air equivalence ratio (ϕ_{CH_4})	H ₂ -air equivalence ratio (ϕ_{H_2})	IMEP (bar)
0	1.40	80:20	4.8 - 12.1	1.2 - 3.0	0.19 - 0.50	0.01 - 0.03	0 - 7
		60:40	4.2 - 10.8	2.7 - 7.2	0.16 - 0.45	0.03 - 0.07	
		50:50	3.7 - 9.8	3.7 - 9.8	0.15 - 0.40	0.03 - 0.09	
		40:60	3.2 - 9.0	4.8 - 13.5	0.13 - 0.38	0.04 - 0.13	
		20:80	2.0 - 6.0	7.8 - 24.2	0.08 - 0.26	0.07 - 0.24	
1.5	3.65	80:20	1.6 - 10.2	0.0 - 2.1	0.06 - 0.41	0.000 - 0.02	1.5 - 7
		60:40	1.0 - 8.9	0.6 - 6.0	0.04 - 0.36	0.005 - 0.06	
		50:50	1.0 - 8.5	1.0 - 8.5	0.04 - 0.35	0.009 - 0.08	
		40:60	1.0 - 7.6	1.5 - 11.4	0.04 - 0.31	0.010 - 0.10	
		20:80	0.6 - 5.0	2.5 - 20.0	0.02 - 0.21	0.022 - 0.20	

Table 5.1: Test parameter matrix for the exhaust emission experiments

Property	Diesel fuel	Hydrogen	Methane
Density (kg/m ³)	831.9	0.0838	0.66
Lower heating value (MJ/kg)	43.14	120	50
Laminar flame speed (cm/s)	5-80	230	42
Flammability range (% v/v in air)	0.6-7.5	4 - 76	4.4 - 15

Table 5.2: Properties of diesel fuel, hydrogen and methane at 1 atm and 300 K (Karim 2003; Saravanan & Nagarajan 2008a; Chong & Hochgreb 2011)

5.1.2 Experimental set 2: In-cylinder gas sampling tests (using CH₄-H₂ mixtures)

A further set of experiments was carried out utilising the in-cylinder gas sampling system on the single cylinder engine; the pilot diesel fuel flow rate was fixed so as to provide an engine load of 1.5 bar IMEP. At an engine load of 1.5 bar IMEP, and with no CH₄ or H₂ addition, only negligible levels of NO_x were measured in the exhaust gases. Therefore, when the CH₄-H₂ mixture was added in the course of the in-cylinder sampling experiments, it could be assumed that any observed NO_x could be primarily attributed to the presence of the CH₄ and H₂. Meanwhile, an engine load of 1.5 bar IMEP indicated that sufficient diesel fuel was being supplied to the engine for the development of measurable heat release from diesel only combustion, and that any spatial differences in the in-cylinder charge attributable to the variation in diesel fuel spray stoichiometry could likely be observed during in-cylinder sampling.

The tests were conducted at a constant engine load of 4 bar IMEP, with the increase in engine load from the pilot diesel IMEP of 1.5 bar (to 4 bar IMEP) achieved by supplying the necessary amount of CH₄-H₂ mixture to the engine. Two CH₄-H₂ mixture ratios of 20% CH₄: 80% H₂ (v/v) and 80% CH₄: 20% H₂ (v/v) were utilised so as to provide a significant contrast between the in-cylinder gas composition obtained from the two series of experiments.

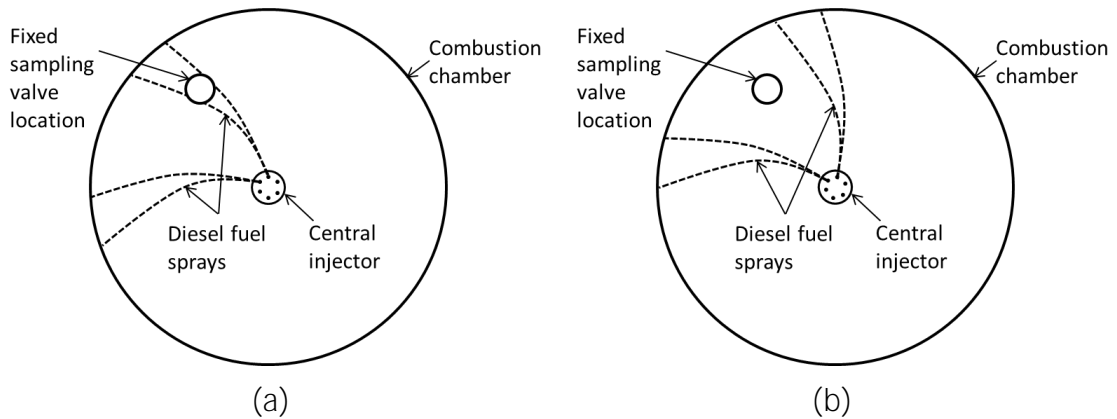


Figure 5.2: Schematic showing (a) sampling arrangement one and (b) sampling arrangement two relative to the diesel fuel sprays; changes to the position of the spray relative to the valve location was achieved by rotating the fuel injector

During these tests, gas samples were extracted from the engine cylinder at two distinctly different locations, relative to one of the six injector nozzle diesel fuel sprays. Figure 5.2 shows the two relative sampling arrangements with respect to the injector sprays. The first location, relative to the spray, was a region of high diesel fuel concentration within the core of the diesel fuel spray, while the second location, relative to the spray, was an area of relatively low diesel fuel concentration between two spray cones. Since the absolute location of the sampling valve in the engine head was fixed, the change in the sampling arrangement, relative to the diesel fuel sprays, was achieved through rotation of the centrally-located injector. The locations of relatively high and low diesel fuel concentration were experimentally determined by rotating the diesel fuel injector in small steps and measuring the in-cylinder gas composition (in particular the levels of unburned hydrocarbons) at each injector rotation. This methodology allowed approximate

spray core boundaries to be sketched, as by means of broken lines shown in Figure 5.2.

For each of the two relative sampling arrangements shown in Figure 5.2, gas samples were extracted at a number of sampling windows in the engine cycle, from 20 CAD BTDC to 100 CAD ATDC in incremental crank angle steps ranging between 10 and 20 CAD. This allowed in-cylinder gas samples to be obtained at various stages of the combustion cycle, from before diesel fuel injection and through the ignition delay period, the premixed burn stage and the early and late diffusion burn stage. At each sampling crank angle window, a voltage of 100 V was applied to the solenoid; this voltage is larger compared to the voltages used during the sampling valve bench tests (described in Chapter 3), as in the engine the in-cylinder gas pressures reached much higher values (60-70 bar) than the pressures that could be applied on the sampling valve face during the bench tests (maximum 40 bar).

5.1.3 Experimental set 3: In-cylinder gas sampling tests (using CH₄)

An additional set of in-cylinder gas sampling tests were conducted whereby only CH₄ was supplied to the engine to increase the engine load above the pilot diesel IMEP of 1.5 bar, up to an engine load of 5.5 bar IMEP. These tests were carried out to understand the effect of co-combustion of CH₄ and diesel fuel on the in-cylinder gas composition, without the influence of H₂ as a third combustible component.

Again, as explained Section 4.1.2, gas samples were collected from two distinct regions of diesel fuel concentration, relative to the injector nozzle diesel fuel sprays (Figure 5.2). For each of the two relative sampling arrangements, gas samples were extracted at three sampling windows in the engine cycle: (a) during the premixed stage of combustion (at 10 CAD ATDC); (b) during the early diffusion combustion stage (at 25 CAD ATDC); and (c) during the late burning stage (at 40 CAD ATDC). Table 5.3 lists the sampling valve crank angle timings and the sampling durations, within the engine cycle. It can be seen from Table 5.3 that the duration of the sampling window increases as the engine cycle progresses, in response to decaying in-cylinder gas pressure. Post combustion, the in-cylinder gas pressure decreases quite rapidly, and so does the flow rate through the valve sampling valve opening (if the sampling duration were to be kept constant). Hence, in order to obtain a sufficient volume of gas sample (for the analysers) the valve had to be kept open for a longer duration.

Sampling timing (middle of sampling window) (CAD ATDC)	Duration of sampling window (CAD)
10	6
25	10
40	15

Table 5.3: In-cylinder gas sample extraction timings in CAD ATDC during the engine cycle and the corresponding sampling windows in CAD

5.2 Results and discussion

5.2.1 Combustion characteristics

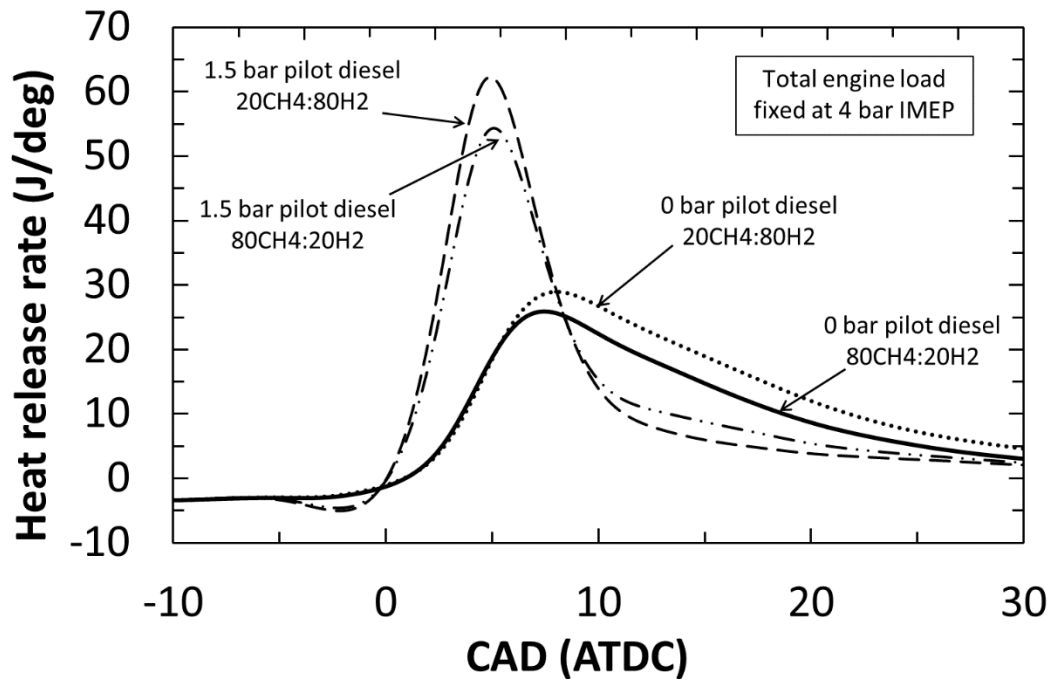


Figure 5.3: Heat release rate curves for a fixed engine load of 4 bar IMEP, for the two pilot diesel fuel IMEPs of 0 and 1.5 bar and two CH₄-H₂ mixture proportions

Figure 5.3 shows the heat release rate curves for the two pilot diesel fuel IMEPs of 0 bar and 1.5 bar and supplying the engine with two different CH₄-H₂ mixture ratios of 20% CH₄: 80% H₂ (v/v) and 80% CH₄: 20% H₂ (v/v) to achieve the required total engine load of 4 bar IMEP (that is, including the pilot diesel fuel IMEP). Comparing the heat release rate curves at the two pilot diesel IMEP conditions (0 bar and 1.5 bar), it can be seen that the rate of increase of heat release post ignition is considerably faster in the case of 1.5 bar pilot diesel fuel IMEP, leading to higher peak heat release rates closer to engine TDC. This is because at the higher pilot diesel IMEP of 1.5 bar, significantly more diesel is injected into the combustion chamber (Table 5.2), and hence an appreciable amount of diesel fuel-air mixture is

already premixed and prepared during the delay period, and combusts rapidly once ignition has occurred (Heywood 1988). It can also be speculated that the larger volume of pilot diesel fuel being injected (as compared to 0 bar pilot diesel fuel IMEP) increases the number of ignition sites available for CH₄ and H₂ combustion, which along with diesel fuel combustion results in a larger proportion of energy being released closer to TDC, and hence higher peak heat release rates. On the other hand, for a pilot diesel IMEP of 0 bar, the in-cylinder CH₄-H₂-air mixtures are considerably weaker than stoichiometric ($\phi_{\text{H}_2} = 0.02$ and $\phi_{\text{CH}_4} = 0.35$ at 80CH₄:20H₂ at a total engine load of 4 bar IMEP), which may result in flame propagation speeds being slower than the maximum propagation speeds achievable with stoichiometric combustion, resulting in slower rates of release of energy, lower peak heat release rates occurring further away from TDC and relatively longer durations of combustion (Figure 5.3).

Now considering the heat release rate curves for the two different CH₄-H₂ mixture proportions at the same pilot diesel IMEP of 1.5 bar, the peak heat release rate for a mixture ratio of 20CH₄:80H₂ is higher as compared to that for 80CH₄:20H₂, despite the ignition delay period being similar in both cases (Figure 5.3). This could be attributed to the higher adiabatic flame temperatures of H₂ as compared to CH₄ (Karim 2003; Klell et al. 2012), leading to greater release of energy from combustion, when the in-cylinder mixture contains a higher proportion of H₂. Furthermore, a higher heat release rate can be observed for 80CH₄:20H₂ during the diffusion burning

stage in Figure 5.3 (after 10 CAD ATDC), which could be because of significant quantities of CH_4 burning later during the cycle due to the lower flame propagation speeds of CH_4 as compared to H_2 (Karim 2003). Similar comparisons could also be made for the heat release rate curves for the two CH_4 - H_2 mixture proportions at the pilot diesel IMEP of 0 bar (Figure 5.3).

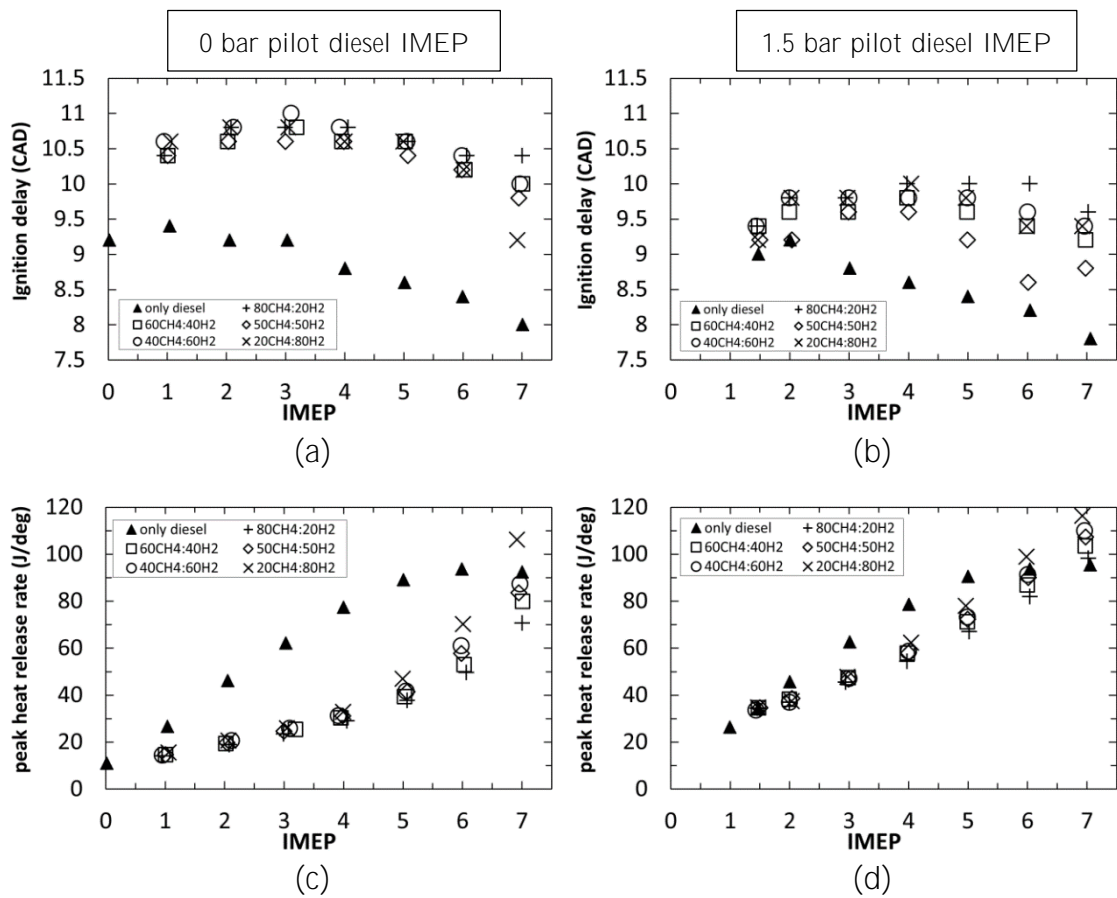


Figure 5.4: Combustion characteristics (a) and (b) duration of ignition delay, and (c) and (d) peak heat release rates for the two pilot diesel fuel IMEPs of 0 and 1.5 bar, and at various engine loads and CH_4 - H_2 mixture proportions

Figure 5.4 shows the ignition delay period and the peak heat release rates for the two pilot diesel fuel IMEPs of 0 bar and 1.5 bar, at a variety of engine loads and CH_4 - H_2 mixture proportions. For comparison purposes, Figure 5.4 also shows the ignition delay and peak heat release rates when the engine load is increased without

any CH₄ or H₂ addition, that is, by merely increasing the amount of diesel fuel injected. Ignition delay is defined here as the duration in CAD between the start of diesel fuel injection (SOI) and the start of combustion (SOC). SOI is taken to be the time when the actuation signal is sent to the injector, whereas the SOC is defined as the first incidence of detectable heat release following autoignition of the diesel fuel. The increase in IMEP, above the pilot diesel fuel IMEP, is achieved by delivering increasing amounts of CH₄-H₂ mixtures to the engine. The most apparent feature in Figure 5.4 is the considerably longer ignition delay with CH₄-H₂ mixtures as compared to diesel only fuelling. It could be speculated that at low temperature ignition conditions, the CH₄ and H₂ remain intact and do not participate chemically in the ignition process; in fact, they might hamper the process by diluting the intake O₂ and hindering oxidation reactions that lead to ignition.

For a pilot diesel fuel IMEP of 0 bar, the ignition delay period at the various engine loads is quite similar between the different CH₄-H₂ mixtures, with the only exception being at 7 bar IMEP where the ignition delay period decreases as the proportion of H₂ in the CH₄-H₂ mixture increases. For a pilot diesel IMEP of 1.5 bar, differences in the ignition delay period between the various CH₄-H₂ mixtures can be observed above an engine load of 4 bar IMEP, whereby the ignition delay period initially decreases as the mixture proportion changes from 80CH₄:20H₂ to 50CH₄:50H₂, but then subsequently increases as the CH₄ is further substituted by H₂ (Figure 5.4).

For both the pilot diesel IMEPs, it can be seen from Figure 5.4 that for each CH₄-H₂ mixture, there is a general trend of an initial increase and then a subsequent decrease in ignition delay as the amount CH₄-H₂ mixture being supplied is increased (moving from left to right). Similar trends in ignition delay were also observed with H₂-diesel fuel mixtures, and have been discussed in great detail in Chapter 5 and also in a publication led by the author (Talibi et al. 2014). The peak heat release rates for each of the pilot diesel IMEPs, at all engine loads and CH₄-H₂ mixture proportions are quite similar except for the peak heat release rates for the 20CH₄:80H₂ mixture ratio at 0 bar pilot diesel IMEP, which shows an almost exponential increase in peak heat release rates at engine loads above 4 bar IMEP. The increasing proportion of H₂ in the in-cylinder gas mixture results in smaller ignition delay periods and higher gas temperatures achieved post combustion.

5.2.2 CO₂, CO and unburned THC exhaust gas emissions

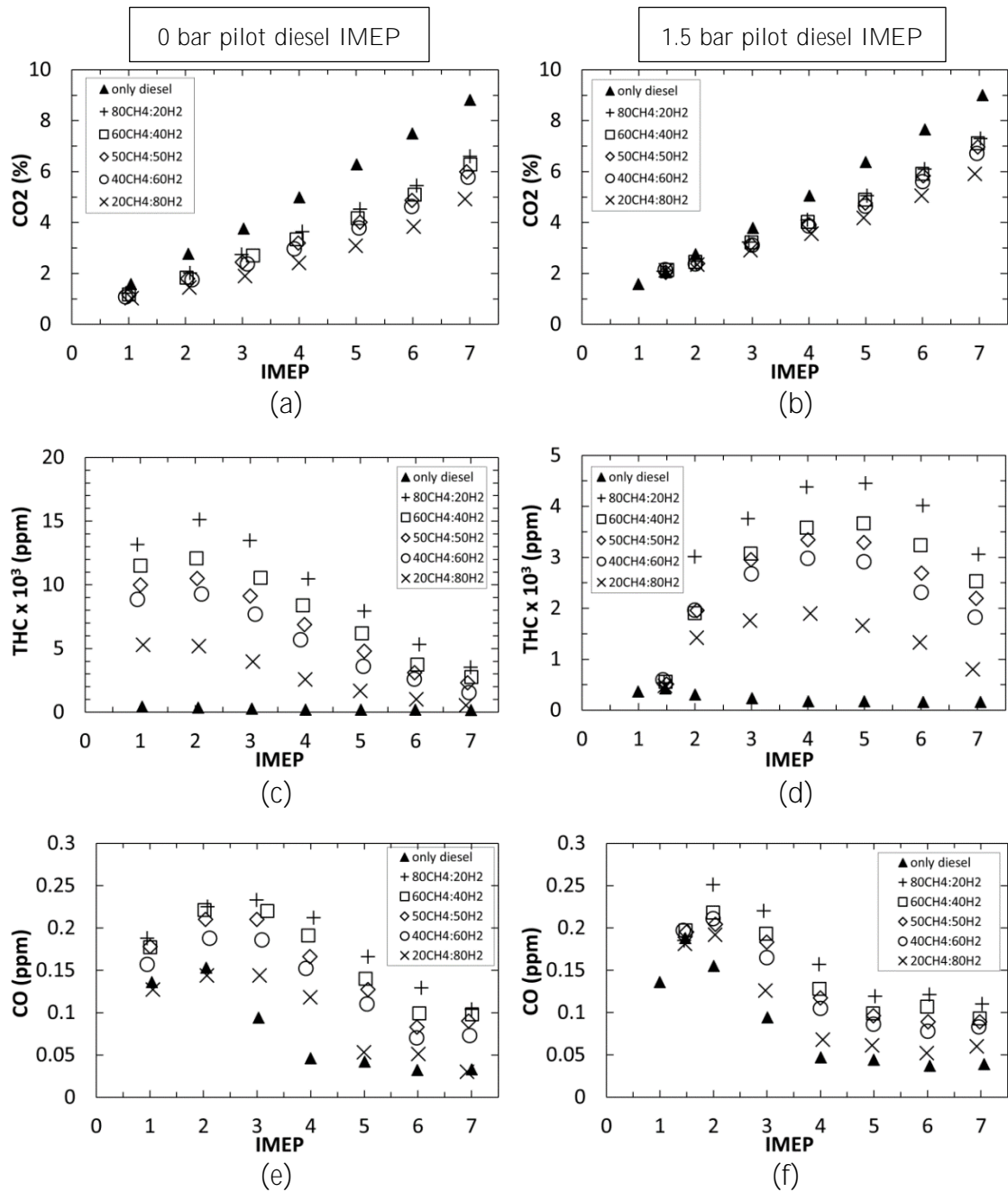


Figure 5.5: Variation in the exhaust emissions of (a) carbon dioxide (CO₂), (b) unburned total hydrocarbons (THC) and (c) carbon monoxide (CO) for the two pilot diesel fuel IMEPs, at various engine loads and CH₄-H₂ mixture proportions

Figure 5.5 shows the gaseous exhaust emissions of CO₂, unburned total hydrocarbons (THC) and CO for the two pilot diesel fuel IMEPs of 0 bar and 1.5 bar, at various engine loads and CH₄-H₂ mixture proportions. For both pilot diesel

IMEPs and at all CH₄-H₂ mixture proportions, an almost linear increase in CO₂ emissions is observed as the amount of CH₄-H₂ mixture being supplied to the engine is increased in order to increase the engine load. Comparing CO₂ emissions between different CH₄-H₂ mixture proportions, as expected, the CH₄-H₂ mixtures with a higher proportion of H₂ produce relatively less CO₂ from combustion. Figure 5.5 also shows the exhaust emissions of CO₂, unburned THC and CO when the engine load is increased without any CH₄ or H₂ addition, that is, by merely increasing the amount of diesel fuel injected. It is important to note from Figure 5.5 that at all engine loads, the CO₂ emissions when combusting CH₄-H₂ mixtures (along with the pilot diesel fuel) are considerably lower compared to when burning only diesel fuel to develop the same engine load. This is due to CH₄ having a lower carbon to hydrogen ratio as compared to diesel fuel, and hence resulting in lower CO₂ emissions.

Now considering the unburned THC and CO emissions for both pilot diesel IMEPs of 0 bar and 1.5 bar, it can be seen from Figure 5.5, that for each CH₄-H₂ mixture there is a general trend of an initial increase in THC and CO emissions followed by a subsequent decrease, as the engine load is increased (by increasing the CH₄-H₂ mixture supply to the engine). The initial increase in unburned THC and CO emissions at low engine loads of below 4 bar IMEP (the term 'low' is used relative to the range of engine loads tested) could most likely be attributed to increased quenching of the CH₄ flame front due to lower in-cylinder temperatures. At such

low load conditions, the in-cylinder CH_4 -air and H_2 -air mixture stoichiometry is quite lean, and the generated flame front is not able to sustain itself to consume all the aspirated CH_4 , resulting in either unburned or partially oxidized hydrocarbons (mainly CH_4) passing into the exhaust. As the engine load is increased by aspirating a greater volume of CH_4 - H_2 mixture, the in-cylinder CH_4 -air mixture progresses towards stoichiometric conditions, the residual in-cylinder gas temperatures increase, resulting in improved CH_4 oxidation and, therefore, lower unburned THC and CO emissions. As expected, at each engine load, unburned THC and CO emissions decrease as the proportion of H_2 in the aspirated CH_4 - H_2 mixture increases.

5.2.3 NO_x exhaust gas emissions

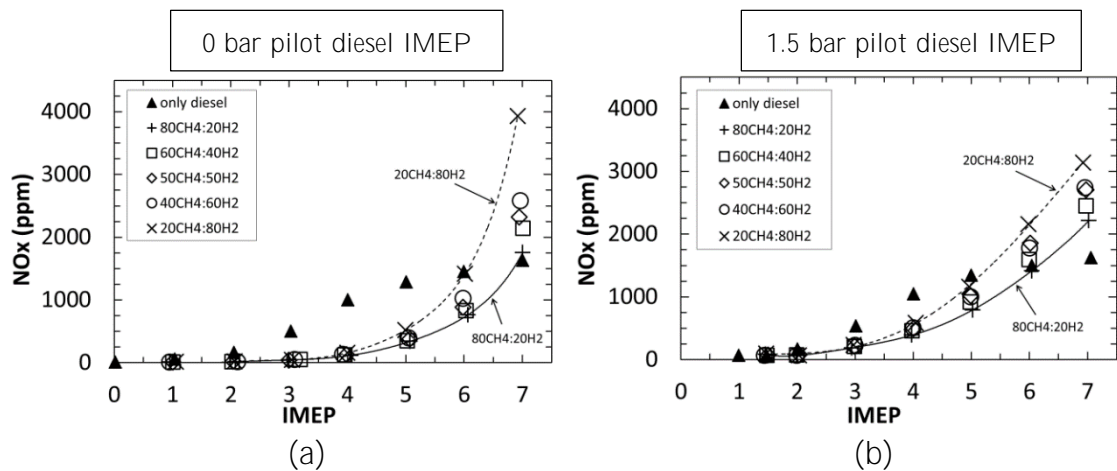


Figure 5.6: Variation in the exhaust emissions of oxides of nitrogen (NO_x) for the two pilot diesel fuel IMEPs, at various engine loads and CH_4 - H_2 mixture proportions

Figure 5.6 shows the gaseous exhaust emissions of NO_x for the two pilot diesel fuel IMEPs of 0 bar and 1.5 bar, at various engine loads and CH_4 - H_2 mixture proportions. Considering the tests carried out with a pilot diesel fuel IMEP of 0 bar, it can be seen from Figure 5.6 that at low engine loads, below 4 bar IMEP, NO_x emission

levels are quite low (< 100 ppm). However, above 4 bar IMEP, NO_x levels in the exhaust gas rise quite steeply with increasing engine load. These results are comparable to the NO_x exhaust emission results obtained with H_2 -diesel fuel co-combustion (as described in Chapter 5), and therefore can be explained in a similar manner. At engine loads lower than 4 bar IMEP, the temperatures resulting from the combustion of the very lean in-cylinder CH_4 -air and H_2 -air mixtures ($\phi_{\text{H}_2} = 0.02$ and $\phi_{\text{CH}_4} = 0.35$ at $80\text{CH}_4:20\text{H}_2$ at an engine load of 4 bar IMEP) are below the threshold temperatures (1600K - 1800K) which promote rapid thermal NO_x formation. However, as the CH_4 - H_2 mixture being supplied to the engine is increased, to increase the engine load above 4 bar IMEP, the in-cylinder mixture concentration becomes sufficient for the post combustion gas temperatures to go above the level at which NO_x formation rates accelerate significantly. This exponential increase in NO_x production rates is expected with as the in-cylinder CH_4/H_2 -air mixture progresses towards stoichiometric conditions, and is consistent the extended Zeldovich NO_x formation mechanism (discussed in Chapter 2) (Miller & Bowman 1989). Comparing the NO_x emissions from the $20\text{CH}_4:80\text{H}_2$ and $80\text{CH}_4:20\text{H}_2$ mixtures, it can be observed from Figure 5.6 that NO_x emission levels rise more rapidly when the mixture has a higher proportion of H_2 . As expected, this is due to H_2 exhibiting a shorter ignition delay and combusting closer to TDC resulting in higher gas temperatures (Figure 5.3), and hence increased thermal NO_x formation rates.

Now considering NO_x emissions for a pilot diesel fuel IMEP of 1.5 bar (Figure 5.6), similar trends to those described in the paragraph above can be observed with increasing engine loads and with different $\text{CH}_4\text{-H}_2$ mixtures. However, the NO_x emissions start increasing rapidly above 3 bar IMEP, as compared to the 4 bar IMEP threshold observed with a pilot diesel fuel IMEP of 0 bar. This can be attributed to the higher amount of diesel fuel being injected into the combustion chamber to achieve a pilot diesel fuel IMEP of 1.5 bar. Diesel fuel combustion can be expected to always occur, at the local level in the engine cylinder, at near stoichiometric conditions with resultant local temperatures sufficient for NO_x formation (Dec 1997). Therefore, the temperatures resulting from the combined $\text{CH}_4\text{-H}_2\text{-diesel}$ fuel combustion are likely to reach the threshold for accelerated thermal NO_x formation at a lower load of 3 bar IMEP.

Figure 5.6 also shows the NO_x exhaust emissions when the engine load is increased without any CH_4 or H_2 addition, that is, by merely increasing the amount of diesel fuel injected. It can be observed that although the NO_x levels do increase with increasing engine load when only diesel fuel is used, the rise in NO_x levels is not as rapid as observed in the case of $\text{CH}_4\text{-H}_2$ mixture combustion. As explained above, diesel combustion occurs at close-to-stoichiometric conditions, whereas the aspirated $\text{CH}_4/\text{H}_2\text{-air}$ mixtures are considerably below stoichiometric levels. Hence, as the supply of $\text{CH}_4\text{-H}_2$ mixture to the engine is increased (that is, the in-cylinder mixture proceeds towards stoichiometric conditions), it is likely that the increase

in temperatures is much more significant than that obtained just with increasing diesel fuel, resulting in the rapid increase in NO_x emissions.

5.2.4 Particulate exhaust emissions

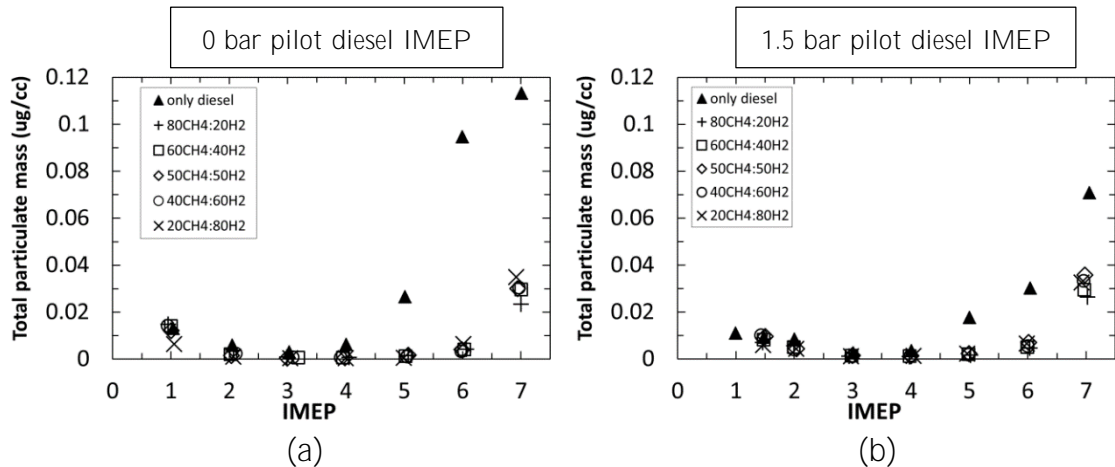


Figure 5.7: Exhaust emissions of total particulate mass for the two pilot diesel fuel IMEPs, at various engine loads and $\text{CH}_4\text{-H}_2$ mixture proportions

Figure 5.7 shows the exhaust emissions of total particulate mass (PM) for the two pilot diesel fuel IMEPs of 0 bar and 1.5 bar, at various engine loads and $\text{CH}_4\text{-H}_2$ mixture proportions. It can be observed that for both the pilot diesel IMEPs and for all $\text{CH}_4\text{-H}_2$ mixture proportions, the level of PM emissions does not increase with increasing engine load (achieved by increasing the $\text{CH}_4\text{-H}_2$ mixture supply) up to 6 bar IMEP, beyond which a rapid increase in PM emissions is seen. As discussed in the case of PM emissions from H_2 -diesel fuel co-combustion (Chapter 5), the introduction of CH_4 and H_2 in the cylinder is likely to have two competing effects on PM formation, increased oxidation rates and increased pyrolysis rates. It is possible that for engine loads above 6 bar IMEP, the displacement of intake air by

CH₄ and H₂ leads to sufficient reduction in O₂ availability for hydrocarbon combustion, resulting in increased pyrolysis rates.

Figure 5.7 also shows the total particulate mass (PM) emissions when the engine load is increased without any CH₄ or H₂ addition, that is, by merely increasing the amount of diesel fuel injected. It is interesting to note that at higher engine loads ('higher' relative to the range of engine loads tested) of 5, 6 and 7 bar IMEP, the PM emissions from diesel only engine operation are significantly higher as compared to pilot diesel fuel-CH₄-H₂ combustion. This is in part due to replacing the diesel fuel with 'zero' carbon H₂, but also shows that CH₄ is less likely to form particulates as compared to diesel fuel. This could potentially be attributed to the aspirated CH₄ being well mixed with the intake air, while the injected diesel fuel spray contains fuel-rich, oxygen deficient core region where a majority of the particulates originate from (Dec 1997).

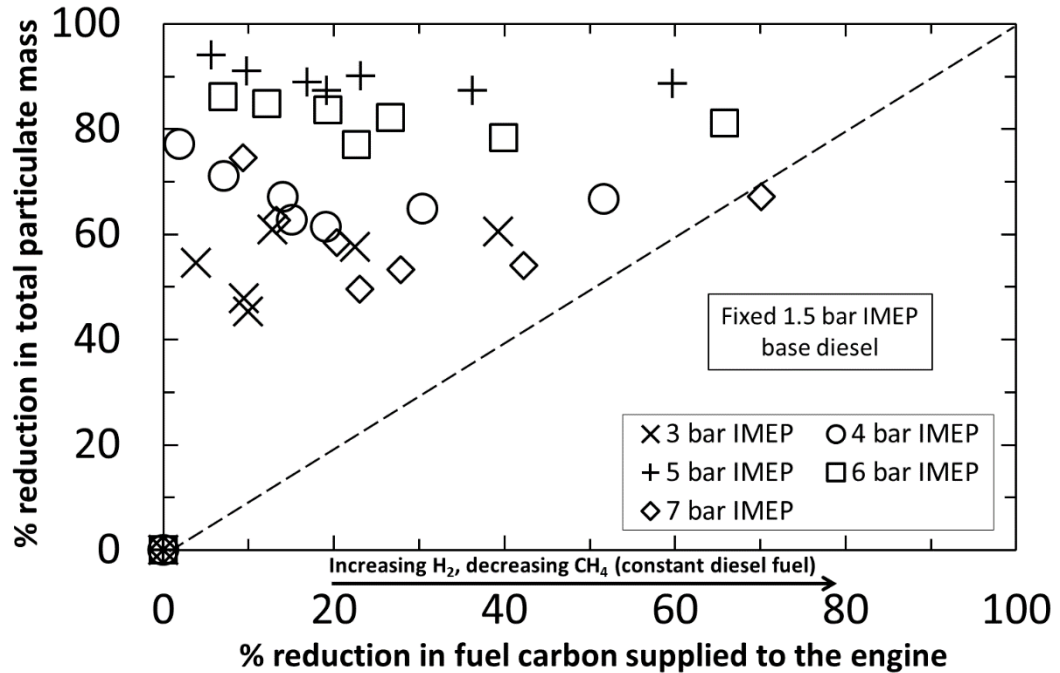


Figure 5.8: Comparison of percentage reduction in total particulate mass with percentage reduction in the carbon content of the combustible mixture at constant engine loads and for a fixed pilot diesel fuel IMEP of 1.5 bar.

Figure 5.8 shows the percentage reduction in the total particulate mass plotted against the percentage reduction in fuel carbon supplied to the engine, at constant engine loads and for a fixed pilot diesel fuel IMEP of 1.5 bar. The reduction in fuel carbon was achieved by lowering the proportion of CH₄ and increasing the proportion of H₂ in the aspirated CH₄-H₂ mixture in order to maintain a constant engine load. The percentage reductions in both particulates and fuel carbon were calculated against the values obtained with the engine operating on only diesel fuel (no CH₄ or H₂ addition). The 1:1 dashed diagonal line in Figure 5.8 represents equivalent reductions in both PM emissions and fuel carbon supplied to the engine. For all engine loads shown in Figure 5.8, the reductions in PM emissions lie in the top half of the graph (above the 1:1 dashed line), implying a beneficial effect of

replacing diesel fuel with CH₄-H₂ mixture on PM reduction beyond simple fuel carbon displacement. For example at a constant engine load 4 bar IMEP, a 20% reduction in fuel carbon causes up to 60% reduction in particulate matter. As previously discussed, this is possibly due to premixed CH₄ having a lower tendency of forming particulates as compared to the injected diesel fuel (which will always have regions of rich stoichiometry). Now comparing the reduction in PM emissions between different engine loads, an increase in the percentage reduction in PM emissions can be observed from Figure 5.8 as the engine load increases from 3 bar to 5 bar IMEP. However, as the engine load is further increased to 7 bar IMEP, the percentage reduction in PM emissions decreases. It should be remembered here that all the tests were conducted at a fixed diesel fuel flow into the engine (equivalent to pilot diesel fuel IMEP of 1.5 bar), and any increase in engine load was achieved by increasing the amount of CH₄-H₂ mixture being aspirated into the engine (hence displacing intake air). It is likely that the increase in the supply of CH₄-H₂ mixture to the engine (to increase the engine load up to 5 bar IMEP) resulted in higher in-cylinder gas temperatures, leading to higher carbon oxidation rates and lower PM emissions. However, as the amount of aspirated CH₄-H₂ mixture is further increased (to increase the engine load above 5 bar IMEP), the effect of O₂ unavailability for PM oxidation becomes more important than the increase in in-cylinder temperatures arising from higher CH₄/H₂-air equivalence ratios.

It can also be observed from Figure 5.8, that at each constant engine load, as the amount of CH₄ being supplied to the engine is decreased, and concurrently the supply of H₂ is increased (moving from left to right on Figure 5.8), a significant change in the reduction in PM emissions is not observed. This observation lends some credence to the earlier speculation that the reduction in PM emissions is primarily due to replacing diesel fuel with CH₄-H₂ mixtures.

5.2.5 In-cylinder gas sample composition (using CH₄ only - Experimental set 3)

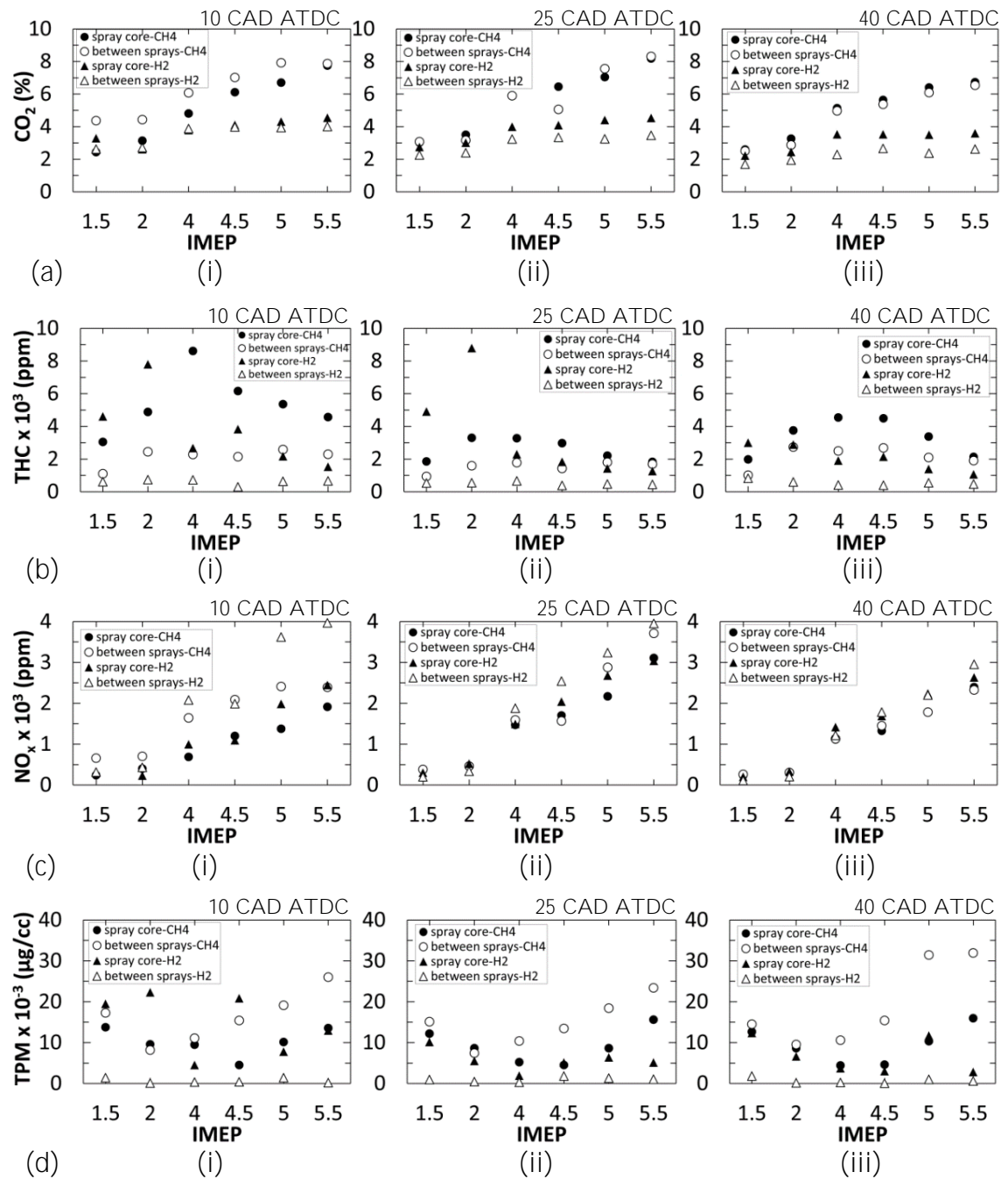


Figure 5.9: Measurement of in-cylinder (a) carbon dioxide (CO₂) concentration, (b) unburned total hydrocarbon (THC) concentration, (c) nitrogen oxide (NO_x) concentration and (d) total particulate mass (PM) in gas samples collected at (i) 10 CAD, (ii) 25 CAD and (iii) 40 CAD ATDC at fixed pilot diesel fuel IMEP of 1.5 bar with increasing amounts of H₂ or CH₄ and variable engine loads with two sampling arrangements (Figure 5.2)

Figure 5.9 shows the in-cylinder concentrations of CO₂, unburned THC, NO_x and PM at various engine loads, with the increase in engine load above a pilot diesel IMEP of 1.5 bar achieved by supplying the engine with CH₄. For comparison purposes, in-cylinder concentrations obtained using H₂ instead of CH₄, and following the same experimental methodology, have also been included.

Figure 5.9 (a) shows the CO₂ concentration in gas samples at various engine loads extracted from the engine cylinder at 10, 25 and 40 CAD ATDC during the combustion cycle, with the two in-cylinder sampling arrangements (firstly, within and, secondly, between the diesel sprays as shown in Figure 5.2). The tests were conducted at a fixed diesel fuel flow rate and the increase in engine load was achieved by adding either H₂ or CH₄ to the intake charge. First, considering the addition of H₂, at 10 CAD ATDC the CO₂ concentrations were similar with the two sampling arrangements (Figure 5.2) and at all the engine loads. As combustion progressed (that is, from 10 to 25 CAD ATDC), the CO₂ concentrations within the spray remained fairly high, whereas the CO₂ levels in the gas samples obtained from between two sprays were relatively lower (Figure 5.9 (a-ii)). Interestingly, the CO₂ concentrations showed a gradual increase with increasing amount of H₂ addition (Figure 5.9 (a)), despite the fact that carbon flow rate to the combustion chamber was fixed. This is most noticeable in the gas samples collected from the spray core at 25 CAD ATDC and could be due to the following reasons:

- The addition of H_2 in the intake manifold displaces some of the intake air, therefore reducing the flow rate of air through the engine.
- Additionally, the H_2 aspirated with the intake air is oxidized to water vapour in the engine, which is condensed by the emissions analyser system (Horiba emissions analyser rack) prior to measurement of CO_2 in the gas sample, therefore reducing the total amount of exhaust gas. Since the carbon flow rate to the engine is fixed, the amount of CO_2 produced by the diesel fuel could be expected to remain consistent. Therefore, it is suggested that the observed increase in the concentration of CO_2 in the in-cylinder gas sample (Figure 5.9 (a)) is a consequence of the reduced total flow rate of the exhaust gas.
- A secondary, although less significant, possible reason for the increase in CO_2 emissions could be a slight increase in the combustion efficiency of diesel fuel as H_2 addition increases, as an effect of increasing in-cylinder gas temperatures.

Considering now the addition of CH_4 (Figure 5.9 (a)), the CO_2 concentrations in the gas samples obtained from within the spray core and between the two sprays were very similar at all three sampling windows (10, 25 and 40 CAD ATDC) except at some engine loads at 10 CAD ATDC where the CO_2 levels between sprays were slightly higher. Now, comparing the CO_2 levels obtained with CH_4 with those obtained with H_2 , the CO_2 concentrations with CH_4 were significantly higher than those obtained from H_2 . Since the diesel fuel flow into the engine is fixed, this difference in CO_2 is due to the carbon in CH_4 oxidizing to form CO_2 , whereas H_2 is

being a carbon-free fuel does not produce any CO_2 . At 40 CAD ATDC, the CO_2 concentrations with the two sampling arrangements (Figure 5.2) and for both H_2 and CH_4 , decreased as the post-combustion gas products became diluted with unreacted air inside the combustion chamber.

Figure 5.9 (b) shows the concentrations of unburned total hydrocarbons in gas samples at various engine loads, extracted from the engine cylinder at 10, 25 and 40 CAD ATDC of the combustion cycle with the two in-cylinder sampling arrangements (Figure 5.2). Figure 5.9 (b) shows that, in the case of both H_2 and CH_4 addition, the concentrations of total hydrocarbons when sampling within the fuel spray were higher, at all engine loads, compared to the results obtained from co-combustion of either gaseous fuel (H_2 or CH_4), when sampling between two fuel sprays. In the fuel-dense core of the diesel spray, local average equivalence ratios are rich, due to limited air entrainment, especially during the initial stages of combustion (at 10 CAD ATDC in Figure 5.9 (b)), and thereby high THC concentrations are generated. The region in between two individual diesel sprays contains relatively low amounts of fuel vapour that have been swept around by the swirling air flow; hence this region is characterised by leaner diesel fuel equivalence ratios, leading to more complete combustion and lower THC concentrations. These observations are in agreement with similar gas sampling studies undertaken by other researchers who mapped out fuel distribution in diesel engine cylinders (Nightingale 1975; Bennethum et al. 1975; Rhee et al. 1978). It can also be observed

from Figure 5.9 (b) that the concentrations of THC, in the case of both H₂ and CH₄, decreased as combustion proceeded (i.e. from 10 to 25 CAD ATDC); this can be attributed to the enhanced mixing and consumption of diesel fuel, as the fuel spray was broken up and encountered hot unburned gases, resulting in higher rates of diesel fuel oxidation and lower unburned THC levels.

Comparing the THC concentrations in gas samples obtained from H₂-diesel fuel and CH₄-diesel fuel co-combustion (Figure 5.9 (b)), the THC levels are considerably higher in the gas samples from CH₄-diesel fuel co-combustion, most likely due to significant quantities of the CH₄ remaining unreacted in the combustion chamber and persisting in the extracted in-cylinder gas sample. This is most noticeable at lower engine loads between 2 and 4 bar IMEP in Figure 5.9 (b), at all three sampling windows, and is likely to be attributable to low equivalence ratios (lean mixtures), and thereby increased quenching of the propagating CH₄ flame front as a result of lower in-cylinder temperatures. As the engine load increased with the addition of CH₄ and the in-cylinder CH₄-air mixture progressed towards stoichiometric conditions, global in-cylinder temperatures increased resulting in improved hydrocarbon oxidation and, therefore, lower THC levels. A similar, albeit less significant, effect can also be seen with the decreasing levels of THC concentration when sampling within the spray core when H₂ is progressively added to the intake charge (Figure 5.9 (b)).

Figure 5.9 (c) shows the NO_x concentrations in the gas samples extracted from the engine cylinder at 10, 25 and 40 CAD ATDC during the combustion process, at various engine loads, with the two in-cylinder sampling arrangements relative to the diesel fuel sprays (Figure 5.2). In the case of both H_2 and CH_4 , at 10 and 25 CAD ATDC and at all engine loads, NO_x concentrations were higher between the two sprays, as compared to those in the spray core. This may be due to local in-cylinder temperatures being higher between the two sprays relative to the temperatures within the spray core (where O_2 availability for combustion is limited), resulting in a higher rate of production of thermal NO_x in the region between diesel fuel sprays, as observed by Talibi et al. (2014) and explained in the following paragraph.

It can be expected that auto-ignition first occurs at the close-to-stoichiometric diesel fuel vapour-air pockets formed by the entrainment of diesel fuel vapour in the swirling motion of the air, especially in the regions between individual sprays (Dec 1997). A near-homogenous mixture of intake charge (H_2 -air or CH_4 -air mixture) can also be expected to exist in the region between the individual diesel fuel sprays, and the combustion of premixed diesel vapour results in the ignition of the H_2 -air/ CH_4 -air mixture that is present around the diesel fuel ignition sites. It is possible that the temperature increase resulting from the combustion of H_2 / CH_4 provides additional energy to the diesel flame temperature and accelerates NO_x production. Therefore the existence of the near-homogenous mixture of H_2 -air or CH_4 -air in the

region between the two sprays can result in higher gas temperatures and, therefore, higher NO_x formation rates (Figure 5.9 (c)). On the other hand, the lower NO_x concentrations in the spray core (especially at 10 CAD ATDC) could be attributable to the relatively low concentration of air in the fuel rich core of the diesel fuel spray, resulting in reduced combustion rates and temperatures and, hence, lower NO_x formation.

Comparing the NO_x concentrations at the sampling timings of 10 and 25 CAD ATDC, for both H_2 and CH_4 (Figure 5.9 (c)), an increase was observed in NO_x levels in the spray core, while, between the two sprays, the NO_x concentration remained at quite a similar level at both these sampling timings (10 and 25 CAD ATDC). The increase in NO_x concentrations between 10 and 25 CAD ATDC in the spray core (Figure 5.9 (c)) could be attributed to the rich diesel spray core having broken up, as combustion progressed, and rapidly entraining the intake charge (H_2 -air or CH_4 -air mixture). The combined diesel fuel- H_2 (or CH_4) mixture at 25 CAD BTDC is expected to have burned at higher temperatures relative to those at 10 CAD, thereby raising NO_x formation rates.

Comparing the NO_x concentrations between H_2 -diesel fuel and CH_4 -diesel fuel co-combustion, it can be seen from Figure 5.9 (c) at 10 and 25 CAD ATDC, that the NO_x levels in the in-cylinder gas samples obtained from H_2 combustion were considerably higher than those from CH_4 combustion. This can be attributed to the higher in-cylinder gas temperatures reached when burning H_2 , as the adiabatic

flame temperature of H_2 is higher than that of CH_4 , thereby resulting in higher NO_x formation rates. At later stages of combustion, i.e. 40 CAD ATDC, it is believed that the effects of air swirl and reverse squish flow (Heywood 1988; Zhao et al. 1996) promoted the redistribution of in-cylinder gaseous composition towards near homogenous conditions in the engine cylinder, and therefore similar NO_x concentrations between the four test conditions (Figure 5.9 (c)).

Figure 5.9 (d) shows the concentration of particulate matter in in-cylinder gas samples, at various engine loads at 10, 25 and 40 CAD ATDC during combustion, with the two in-cylinder sampling arrangements (Figure 5.2). Considering, first, the effect of H_2 addition on PM concentration, the PM levels in the gas samples extracted from within the fuel spray were higher, at all engine loads, compared to those obtained from between the two fuel sprays. As discussed previously in the case of THC concentrations (Figure 5.9 (b)), this could be attributed to the higher fuel pyrolysis and soot formation rates in the oxygen-lacking, fuel-rich core of the diesel spray. Interestingly, the trend is reversed when considering the effect of CH_4 addition on PM concentration. PM levels were significantly higher in the region between the two diesel fuel sprays relative to within the fuel spray itself, as can be seen in Figure 5.9 (d), at all engine loads and all three sampling timings. It is suggested that this could be attributable to CH_4 producing significant quantities of particulates, in addition to the particulates formed solely from diesel fuel. The region between the two diesel fuel sprays can be expected to have a higher

concentration of CH₄-air mixture than in the diesel fuel-rich spray core, resulting in higher gas temperatures, and higher pyrolysis rates, in the region between the two sprays. Within the spray core, concentration of the CH₄-air mixture is relatively low, resulting in lower temperatures and possibly reduced pyrolysis and soot formation rates. Therefore, it is tentatively suggested that a greater abundance of H₂-air or CH₄-air mixture between the two diesel fuel sprays causes higher local temperatures and pyrolysis rates than in the spray core itself, where the levels of H₂-air or CH₄-air mixture are relatively low. There is some evidence for this in the higher concentration of thermal NO_x present between the sprays (as shown in Figure 5.9 (c)), which is indicative of higher gas temperatures between sprays relative to within the spray. Alternatively, it could also be tentatively suggested that the presence of CH₄ in the diesel fuel spray core tends to displace O₂, thereby reducing diesel fuel combustion and lowering temperatures, and resulting in lower pyrolysis reaction rates in the spray core region.

5.2.6 In-cylinder gas sample composition (using CH₄-H₂ mixtures)

Figure 5.10 shows the CO₂ concentration in gas samples extracted from the engine

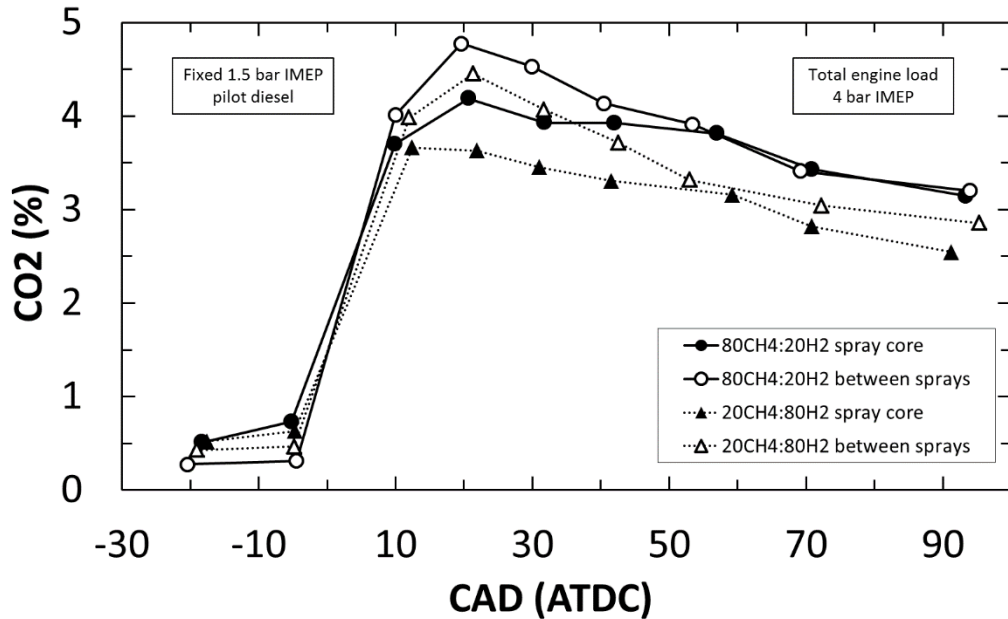


Figure 5.10: Measurement of carbon dioxide (CO₂) concentration in in-cylinder gas samples collected between -20 and 100 CAD ATDC with two sampling arrangements (Figure 5.2), at a fixed pilot diesel fuel IMEP of 1.5 bar, two different CH₄-H₂ mixture proportions and an overall engine load of 4 bar IMEP

cylinder at various CAD degrees ranging between -20 CAD and 100 CAD ATDC, with the two sampling arrangements (Figure 5.2). The amount of diesel fuel being injected into the cylinder was kept fixed (equivalent to 1.5 bar pilot diesel IMEP), and the overall engine load of 4 bar IMEP achieved by aspirating the necessary amount of CH₄-H₂ mixture with the intake air. At -20 CAD ATDC, the CO₂ concentration is quite similar at the four test conditions; this is expected, since at this time in the engine cycle no diesel fuel has been injected in to the cylinder, nor has combustion taken place. Furthermore, the CO₂ concentration at -20 CAD ATDC reflects the composition of the residual combustion gases trapped in the cylinder from the preceding engine cycle. After diesel fuel injection (at -10 CAD

ATDC) and subsequent ignition (at about 0 CAD ATDC) takes place, the in-cylinder CO_2 concentration is observed to rise sharply. First, comparing the in-cylinder CO_2 concentration (post ignition, at about 20 CAD ATDC), between the two different $\text{CH}_4\text{-H}_2$ mixture proportions used, it can be seen from Figure 5.10 that mixtures with a higher proportion of CH_4 (than H_2) yield a higher amount of CO_2 . Now, comparing the post ignition in-cylinder CO_2 concentration between the two sampling arrangements, it can be observed that, for both $\text{CH}_4\text{-H}_2$ mixtures, the CO_2 concentration is higher between the sprays than in the spray core. These results are in line with the previous results obtained using CH_4 -diesel fuel co-combustion whereby a higher in-cylinder CO_2 concentration was observed between the sprays as compared to within the spray core (Section 5.2.5). Therefore, considering the differences in the CO_2 concentrations, the region in between two diesel fuel sprays could be expected to have a higher concentration of CH_4 -air mixture which burns to form CO_2 . In contrast, the lower CO_2 concentration within the diesel spray core region could be attributed to the lack of air entrainment in the fuel spray, especially during the initial stages of combustion. Furthermore, the difference in the in-cylinder CO_2 concentrations could just be due to the relative amounts of carbon in the injected diesel fuel (to achieve a pilot diesel IMEP of 1.5 bar) and in the aspirated CH_4 . Beyond 20 CAD ATDC, the CO_2 concentration at the four test conditions slowly decreases as the expansion stroke progress and the burned gas

products become further diluted with the unreacted intake air that moves from within the piston bowl to the region above the piston.

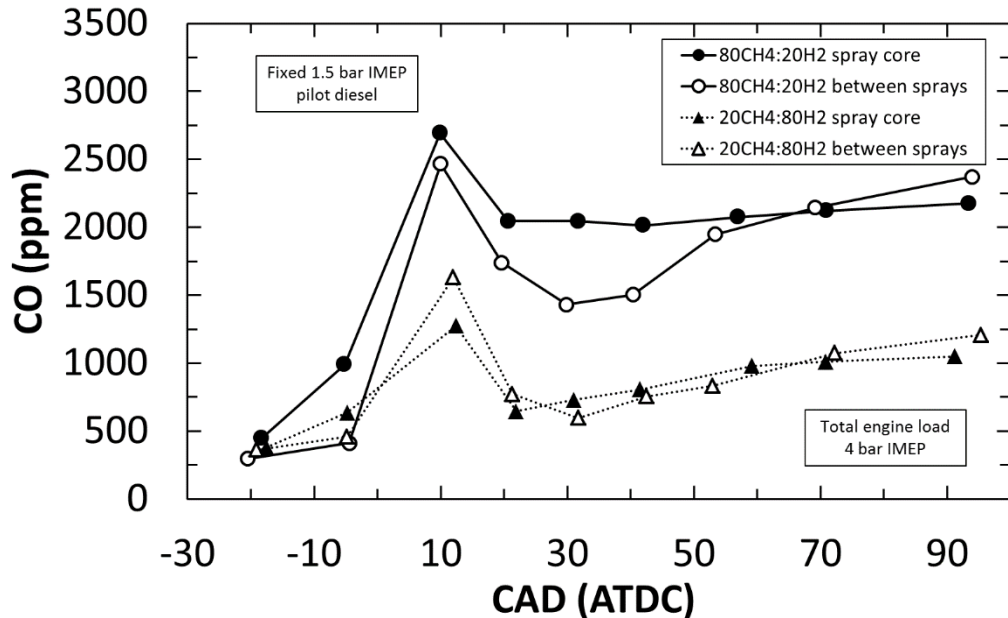


Figure 5.11: Measurement of carbon monoxide (CO) concentration in in-cylinder gas samples collected between -20 and 100 CAD ATDC with two sampling arrangements (Figure 5.2), at a fixed pilot diesel fuel IMEP of 1.5 bar, two different CH₄-H₂ mixture proportions and an overall engine load of 4 bar IMEP

Figure 5.11 shows the CO concentration in gas samples extracted from the engine cylinder at various CAD degrees ranging between -20 CAD and 100 CAD ATDC, for the two CH₄-H₂ mixture proportions and with the two sampling arrangements (Figure 5.2). The in-cylinder CO concentration increases significantly following ignition at about 0 CAD ATDC, as the burning process initiates and carbon oxidation begins. Peak CO levels are reached at about 10 CAD ATDC and, as expected, the CO concentration is higher when the aspirated CH₄-H₂ mixture contains a higher proportion of CH₄. The CO concentration is then observed to decrease sharply between 10 and 20 CAD ATDC, which is consistent with the

increase in the in-cylinder CO_2 concentration between 10 and 20 CAD ATDC (Figure 5.10), as the CO oxidises to form CO_2 . Comparing the peak CO levels (at 10 CAD ATDC) between the two sampling arrangements, it can be observed that the CO concentration is higher within the spray core when the aspirated $\text{CH}_4:\text{H}_2$ mixture has a higher proportion of CH_4 . In contrast, when the $\text{CH}_4:\text{H}_2$ mixture being supplied to the engine has a higher proportion of H_2 , the CO concentration is lower within in the spray core.

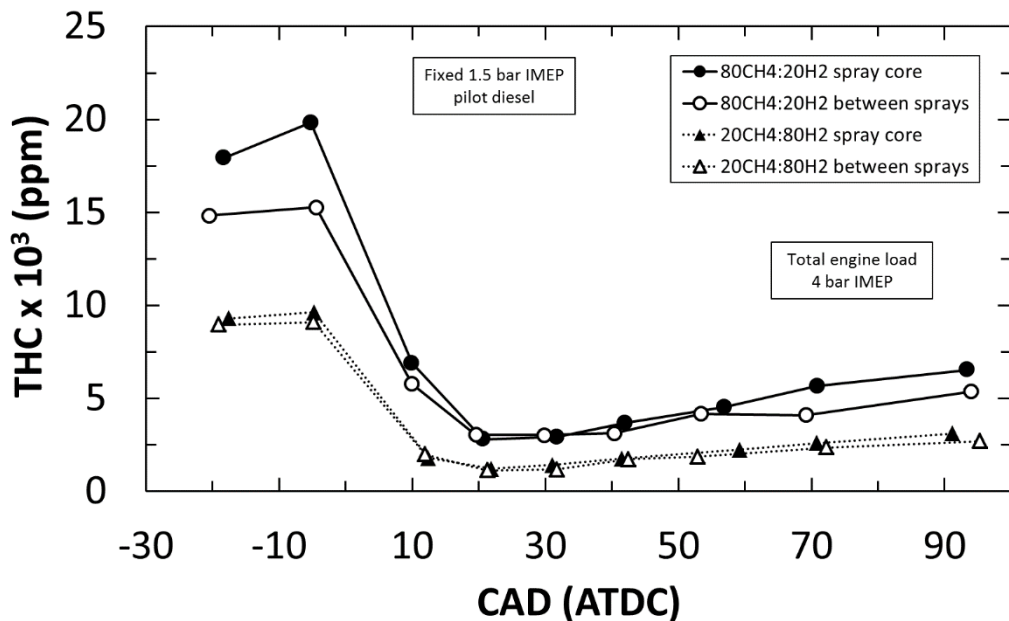


Figure 5.12: Measurement of unburned hydrocarbon (THC) concentration in in-cylinder gas samples collected between -20 and 100 CAD ATDC with two sampling arrangements (Figure 5.2), at a fixed pilot diesel fuel IMEP of 1.5 bar, two different $\text{CH}_4\text{-H}_2$ mixture proportions and an overall engine load of 4 bar IMEP

Figure 5.12 shows the unburned THC concentration in gas samples extracted from the engine cylinder at various CAD degrees ranging between -20 CAD and 100 CAD ATDC, for the two $\text{CH}_4\text{-H}_2$ mixture proportions and with the two sampling arrangements (Figure 5.2). At -20 CAD ATDC, prior to diesel fuel injection, the in-cylinder THC concentration is higher for a $80\text{CH}_4:20\text{H}_2$ mixture as compared to

a 20CH₄:80H₂ mixture, due to higher proportion of CH₄ in the aspirated mixture. A slight anomaly is observed in the results for 80CH₄:20H₂ at -20 CAD ATDC, whereby a higher THC concentration is observed in the region of the diesel fuel spray core even before diesel injection occurs. This could be due to diesel fuel persisting in the spray core region from the previous cycle, but a similar result is not observed in the case of 20CH₄:80H₂ mixture. Following ignition at about 0 CAD ATDC, a sharp decrease in THC concentration is observed (up to 20 CAD ATDC) as the diesel fuel and CH₄ are consumed. However, a higher concentration of unburned THC is maintained for mixture of 80CH₄:20H₂ beyond 20 CAD ATDC.

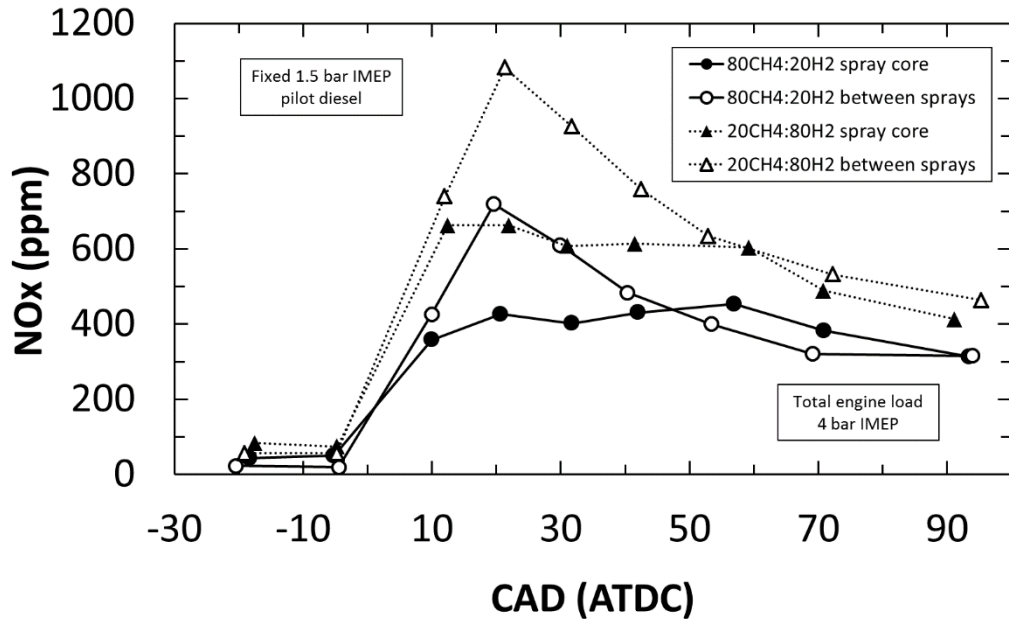


Figure 5.13: Measurement of oxides of nitrogen (NO_x) concentration in in-cylinder gas samples collected between -20 and 100 CAD ATDC with two sampling arrangements (Figure 5.2), at a fixed pilot diesel fuel IMEP of 1.5 bar, two different $\text{CH}_4\text{-H}_2$ mixture proportions and an overall engine load of 4 bar IMEP

Figure 5.13 shows the NO_x concentration in gas samples extracted from the engine cylinder at various CAD degrees ranging between -20 CAD and 100 CAD ATDC, for the two $\text{CH}_4\text{-H}_2$ mixture proportions and with the two sampling arrangements (Figure 5.2). Following ignition at about 0 CAD ATDC, NO_x concentrations are observed to increase and reach peak values at about 20 CAD ATDC. Comparing the in-cylinder NO_x concentration between the two $\text{CH}_4\text{-H}_2$ mixtures with both the sampling arrangements, it can be observed that NO_x levels are higher when H_2 is present in a greater proportion in the aspirated $\text{CH}_4\text{-H}_2$ mixture. As previously discussed, H_2 exhibits a shorter ignition delay, combusting closer to TDC and resulting in higher gas temperatures reached inside the cylinder. Since NO_x formation is primarily a thermal process (Zeldovich et al. 1947; Bowman 1973;

Miller & Bowman 1989), higher in-cylinder gas temperatures can be expected to result in higher NO_x formation rates.

Now, comparing the NO_x concentration between the two sampling arrangements (within the diesel fuel spray core and between two sprays) at 20 CAD ATDC, it can be observed from Figure 5.13, for both $\text{CH}_4\text{-H}_2$ mixture proportions, that NO_x levels are higher in the region between the two sprays as compared to within the spray core. These results are consistent with the in-cylinder NO_x concentration results obtained from H_2 -diesel fuel and CH_4 -diesel fuel co-combustion experiments conducted previously by the author (Section 5.2.5). During the initial stages of combustion, the entrainment of air into the diesel fuel spray cone due to the turbulent swirling motion inside the cylinder results in the mixing of the fuel vapour at the periphery of the spray with the intake charge, especially in the region between the individual sprays (Gatts et al. 2010). As mentioned previously, it is expected that autoignition first occurs at these near stoichiometric diesel fuel vapour-air pockets around the fuel sprays (Dec 1997) and results in the rapid burning of both premixed diesel vapour and the CH_4/H_2 -air mixtures (which occur in a higher concentration between fuel sprays as compared to within the spray core during these initial stages of combustion) around the diesel fuel ignition sites. It is suggested that the temperature rise from the combined diesel fuel- $\text{CH}_4\text{-H}_2$ combustion exceeds the threshold for accelerated thermal NO_x formation, resulting in high NO_x levels in the region between two individual sprays. On the other hand,

the lower NO_x concentration in the spray core (at about 20 CAD ATDC) could possibly be attributed to the relatively low concentration of entrained air into the diesel fuel rich spray core during the initial stages of combustion (prior to complete spray break up), resulting in lower post-combustion temperatures and hence, reduced NO_x formation. Additionally, some of the energy released in this fuel rich region may be expected to have been absorbed for fuel pyrolysis (Heywood 1988), possibly leading to lower gas temperatures and NO_x formation rates.

5.3 Conclusions

- The use of CH₄-H₂ mixtures in internal combustion engines has the potential to combine the many complimentary properties of the individual gases in order to yield beneficial effects on engine combustion and emission characteristics.
- For same CH₄-H₂ mixture proportion and engine load, shorter ignition delay periods and higher peak heat release rates closer to the engine TDC position were observed with a higher amount of pilot diesel fuel flow rate. Increasing the proportion of H₂ in the CH₄-H₂ mixture reduced the ignition delay period and increased peak heat release rates, but only at high engine loads above 6 bar IMEP.
- At all engine loads, exhaust CO₂ emissions were considerably lower when operating the engine on CH₄-H₂ mixtures relative to diesel fuel only engine operation, attributable to the lower carbon to hydrogen ratio of CH₄ compared to diesel fuel.
- For all CH₄-H₂ mixtures tested, the exhaust CO and unburned THC emissions were observed to be considerably high below 4 bar IMEP due to low temperature quenching effects. Above 4 bar IMEP, the increased in-cylinder temperatures enabled improved CO and hydrocarbon oxidation rates and hence, decreased CO and unburned THC emissions.

- For both fixed pilot diesel fuel IMEPs of 0 bar and 1.5 bar, NO_x emissions were observed to increase rapidly with increasing engine load, but only when the in-cylinder temperatures due to combined diesel fuel and $\text{CH}_4\text{-H}_2$ mixture combustion exceeded the threshold for NO_x formation temperatures.
- Significant reductions in PM emissions were observed when diesel fuel was replaced with $\text{CH}_4\text{-H}_2$ mixtures. For a fixed pilot diesel IMEP, the magnitude of PM reduction increased when the engine load was increased up to 5 bar IMEP (by increasing the supply of $\text{CH}_4\text{-H}_2$ mixture). Increasing the engine load above 5 bar IMEP, significantly lowered the magnitude of PM reduction, attributable to excessive displacement of intake O_2 by the $\text{CH}_4\text{-H}_2$ mixture.
- At 10 and 25 CAD ATDC, the in-cylinder NO_x concentrations in the region between the two diesel fuel sprays were higher than those within the fuel spray, in the case of both H_2 -diesel fuel and CH_4 -diesel fuel co-combustion. This could be attributed to a higher concentration of intake charge (H_2 -air or CH_4 -air mixture) burning between the sprays, leading to higher gas temperatures in this region relative to the fuel rich spray core.
- In the case of H_2 -diesel fuel co-combustion, the in-cylinder PM levels were higher in the diesel fuel spray as compared to between two sprays, most probably due to higher pyrolysis rates in the oxygen-lacking, fuel-rich core of the diesel fuel spray, and greater availability of air (and hence O_2) in the region between sprays for oxidation of soot precursors. Conversely, in the case

of CH₄-diesel fuel co-combustion, the in-cylinder PM levels were significantly higher between the two diesel fuel sprays relative to within the fuel spray. This was attributed to CH₄ contributing significant quantities of particulates (unlike H₂) to the total PM concentration produced from the CH₄-diesel fuel mixture in between two sprays aided by higher temperatures in this region.

- The in-cylinder gas composition results obtained from CH₄-H₂ mixtures were consistent with previous in-cylinder studies conducted by the author using only H₂ or CH₄. Higher NO_x levels were observed when the H₂ was present in a higher proportion in the aspirated CH₄-H₂ mixture. Comparing the NO_x levels obtained with the two sampling arrangements, the NO_x concentration was higher in the region between the sprays as compared to within the spray core. This was attributed to higher temperatures reached post ignition, in the region between two individual fuel sprays due to presence of a higher concentration of CH₄-H₂ mixture in that region (as compared to within the spray core).

6 Experimental investigation on the combustion and exhaust emission characteristics, and in-cylinder gas composition, of hydrogen enriched biogas mixtures in a diesel engine

This chapter presents the experiments conducted with a variety of CH₄-CO₂ and CH₄-CO₂-H₂ mixtures to investigate their combustion and emission characteristics in a diesel engine. While the CH₄-CO₂ mixtures represented typical biogas mixture compositions, CH₄-CO₂-H₂ mixtures were tested to determine whether the thermal energy absorbing effects of the inert CO₂ in biogas on combustion could be countered by H₂. Additionally, tests were conducted to analyse the in-cylinder gas composition when combusting CH₄-CO₂ and CH₄-CO₂-H₂ mixtures, with two different in-cylinder sampling arrangements relative to the diesel fuel sprays. Finally, some exhaust emission tests were also conducted with real biogas samples

obtained from a commercial anaerobic digester, which utilised animal manure as organic waste to produce biogas.

6.1 Experimental procedure

The experiments discussed in this chapter were conducted on the single cylinder engine utilising the common rail fuel injection system for diesel fuel injection and the gas mass flow controller system for delivering metered quantities of methane (CH_4), carbon dioxide (CO_2) and hydrogen (H_2) to the engine. These systems have been described in detail in Chapter 3 of this thesis. All the experiments were carried out at a constant engine speed of 1200 rpm, common rail fuel injection pressure of 900 bar and a diesel fuel injection timing of 10 CAD BTDC. The diesel fuel used for all tests was of fossil origin, with zero fatty acid methyl ester (FAME) content, cetane number of 53.2 and carbon to hydrogen ratio of 6.32:1 by mass. Compressed CH_4 gas of purity 99.5%, and compressed H_2 and compressed CO_2 gases, each of purity 99.995%, were obtained from a commercial gas supplier (BOC).

6.1.1 Experimental set 1: Exhaust emission tests (using CH_4 - CO_2 - H_2 mixtures)

The test procedure followed for these set of tests consisted of fixing the flow rate of diesel fuel supplied to the engine (pilot diesel flow rate), while gradually increasing the amount of CH_4 - CO_2 - H_2 mixture being delivered to the engine so as to increase the engine load (power output measured in bar IMEP), at constant engine speed. The fossil diesel fuel was primarily used for the purpose of igniting

the gaseous $\text{CH}_4\text{-CO}_2\text{-H}_2$ mixture, while the purpose of the gaseous fuel mixture was to deliver engine power output. The diesel fuel flow rate was kept fixed by maintaining a constant engine load, henceforth referred to as the pilot diesel fuel IMEP. Two series of tests were conducted with two different pilot diesel fuel flow rates which were sufficient to develop engine loads of 0 bar and 1.5 bar, respectively. For a pilot diesel fuel only IMEP of 0 bar, no heat release could be discerned from the analysis of in-cylinder gas pressure. Therefore the diesel flow rate, equivalent to a pilot diesel fuel IMEP of 0 bar, was taken to be minimum flow rate for which spray was just emerging from the diesel fuel injector nozzle, and was not only sufficient to ignite in the engine cylinder but also cause ignition of the aspirated $\text{CH}_4\text{-CO}_2\text{-H}_2$ mixture at all engine loads up to 7 bar IMEP.

For each of the two pilot diesel IMEPs, the above procedure was repeated for different $\text{CH}_4\text{-CO}_2$ and $\text{CH}_4\text{-CO}_2\text{-H}_2$ mixtures (henceforth, collectively termed as $\text{CH}_4\text{-CO}_2\text{-H}_2$ mixtures), which have been detailed in Table 6.1. The two different mixture proportions tested, 60 CH_4 :40 CO_2 (v/v) and 80 CH_4 :20 CO_2 (v/v), represent typical biogas qualities: biogas which has been obtained directly from anaerobic digesters and biogas which has undergone post-production CO_2 scrubbing, respectively. H_2 was added to the $\text{CH}_4\text{-CO}_2$ mixture in two different proportions, 5% and 15% v/v; at a 5% H_2 addition level, the in-cylinder H_2 -air stoichiometry would be too lean to produce a significant change in temperature upon H_2 combustion. Hence, at this level of H_2 addition, any apparent effect of H_2 would

either be due to substitution or chemical synergy with the CH₄-CO₂ mixture. For all H₂ addition levels, the relative proportions of CH₄ and CO₂ were maintained. Table 6.1 also shows the percentage ratio of each of the gases in the mixtures being used in these experiments. Table 6.2 shows the important properties of the fuels and gases utilised in these experiments. Figure 6.1 (a) and (b) shows the energy supplied to the engine from the different CH₄-CO₂-H₂ mixtures as a function of the total energy supplied to the engine (energy from the CH₄-CO₂-H₂ mixtures plus diesel), for the two pilot diesel fuel IMEPs of 0 bar and 1.5 bar.

An additional series of baseline (control) tests were carried out, for comparison, using diesel fuel only (without any CH₄-CO₂-H₂ mixture addition), with the diesel fuel injection period (and hence the diesel fuel flow rate delivered to the engine) gradually increased so that the engine load increased from 0 to 7 bar IMEP.

Pilot diesel (bar IMEP)	Diesel fuel flow rate (ml/min)	Aspirated mixture ratio (v/v)	CH ₄ :CO ₂ :H ₂ ratio (v/v)	CH ₄ flow rate (l/min)	CO ₂ flow rate (l/min)	H ₂ flow rate (l/min)	IMEP (bar)
0	1.40	60CH ₄ :40CO ₂	60:40:0	8.5 - 13.7	5.7 - 9.1	0	0 - 7
		60CH ₄ :40CO ₂ + 5% H ₂	57:38:5	8.1 - 13.1	5.4 - 8.8	0.7 - 1.2	
		60CH ₄ :40CO ₂ + 15% H ₂	51:34:15	7.2 - 12.2	4.8 - 8.1	2.1 - 3.6	
		80CH ₄ :20CO ₂	80:20:0	8.0 - 13.0	2.0 - 3.3	0	
		80CH ₄ :20CO ₂ + 5% H ₂	76:19:5	7.6 - 12.6	1.9 - 3.2	0.5 - 0.8	
		80CH ₄ :20CO ₂ + 15% H ₂	68:17:15	7.1 - 12.2	1.8 - 3.0	1.6 - 2.7	
1.5	3.65	60CH ₄ :40CO ₂	60:40:0	1.6 - 11.1	1.1 - 7.4	0	1.5 - 7
		60CH ₄ :40CO ₂ + 5% H ₂	57:38:5	1.7 - 10.5	1.1 - 7.0	0.5 - 0.9	
		60CH ₄ :40CO ₂ + 15% H ₂	51:34:15	1.6 - 10.0	1.1 - 6.6	0.5 - 2.9	
		80CH ₄ :20CO ₂	80:20:0	4.0 - 10.2	1.0 - 2.5	0	
		80CH ₄ :20CO ₂ + 5% H ₂	76:19:5	6.1 - 10.6	1.5 - 2.7	0.4 - 0.7	
		80CH ₄ :20CO ₂ + 15% H ₂	68:17:15	4.1 - 9.3	1.0 - 2.5	0.9 - 2.2	

Table 6.1: Test parameter matrix for the exhaust emission experiments

Property	Lower heating value (MJ/kg)	Density (kg/m ³)
Diesel fuel	43.14	831.9
Methane (CH ₄)	50	0.66
Carbon dioxide (CO ₂)	-	1.91
Hydrogen (H ₂)	120	0.0838

Table 6.2: Important properties of diesel fuel, CH₄, CO₂ and H₂ at 1 atm and 300 K (Karim 2003; Saravanan & Nagarajan 2008a)

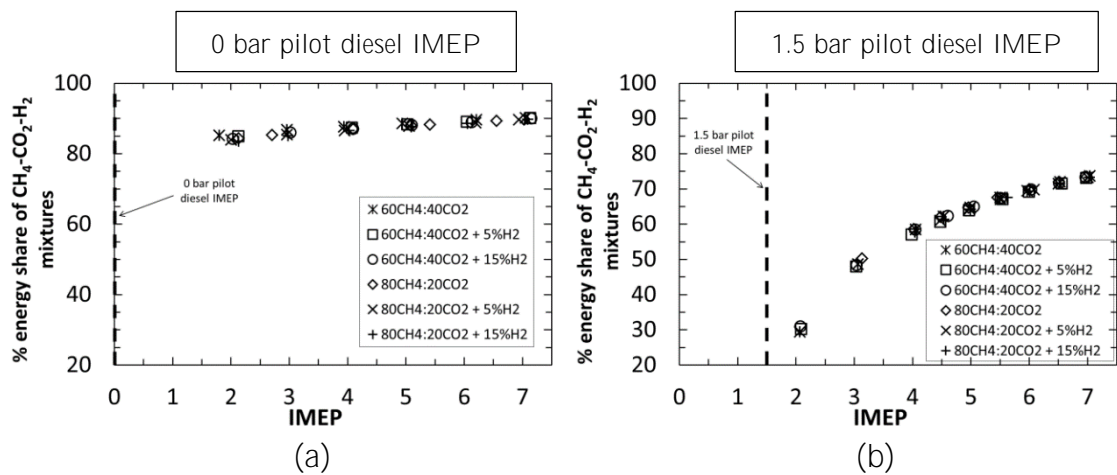


Figure 6.1: Percentage energy supplied to the engine from the different CH₄-CO₂ and CH₄-CO₂-H₂ mixtures for (a) 0 bar and (b) 1.5 bar pilot diesel IMEP, at various engine loads (IMEP)

6.1.2 Experimental set 2: In-cylinder gas sampling tests (using CH₄-CO₂-H₂ mixtures)

A further set of experiments was carried out utilising the in-cylinder gas sampling system on the single cylinder engine; for the in-cylinder sampling experiments the diesel fuel flow rate was fixed so as to provide a constant pilot diesel fuel IMEP of 1.5 bar. At an engine load of 1.5 bar IMEP, and with no CH₄, CO₂ or H₂ addition, only negligible levels of NO_x were measured in the exhaust gases. Therefore, in the course of the in-cylinder sampling experiments, it could be assumed that any observed NO_x could be primarily attributed to the presence of CH₄-CO₂-H₂ mixtures

generating NO_x on their own account or in synergy with the diesel fuel. Meanwhile, an engine load of 1.5 bar IMEP indicated that sufficient diesel fuel was being supplied to the engine for the development of measurable heat release from diesel only combustion.

The tests were conducted at engine loads of 3, 4, 5 and 5.5 bar IMEP by supplying the necessary amount of $\text{CH}_4\text{-CO}_2\text{-H}_2$ mixture to the engine to increase the engine load beyond the pilot diesel fuel IMEP of 1.5 bar. Two $\text{CH}_4\text{-CO}_2\text{-H}_2$ mixtures of 60 CH_4 :40 CO_2 (v/v) and 60 CH_4 :40 CO_2 + 15% H_2 (v/v) were used to investigate the effect of adding H_2 to $\text{CH}_4\text{-CO}_2$ mixtures, on the in-cylinder gas composition.

During these tests, gas samples were extracted from the engine cylinder at two distinctly different locations, relative to one of the six injector nozzle diesel fuel sprays. Figure 6.2 shows the two relative sampling arrangements with respect to the injector sprays. The first location, relative to the spray, was a region of high diesel fuel concentration within the core of the diesel fuel spray, while the second location, relative to the spray, was an area of relatively low diesel fuel concentration between two spray cones. Since the absolute location of the sampling valve in the engine head was fixed, the change in the sampling arrangement, relative to the diesel fuel sprays, was achieved through rotation of the centrally-located injector. The locations of relatively high and low diesel fuel concentration were experimentally determined by rotating the diesel fuel injector in small steps and measuring the in-cylinder gas composition (in particular the levels of unburned

hydrocarbons) at each injector rotation. This methodology allowed approximate spray core boundaries to be sketched, as by means of broken lines shown in Figure 6.2.

For each of the two relative sampling arrangements, gas samples were extracted at three sampling windows in the engine cycle: (a) during the premixed stage of combustion (at 10 CAD ATDC); (b) during the early diffusion combustion stage (at 25 CAD ATDC); and (c) during the late burning stage (at 40 CAD ATDC). Table 6.3 lists the sampling valve crank angle timings and the sampling durations, within the engine cycle. It can be seen from Table 6.3 that the duration of the sampling window increases as the engine cycle progresses, in response to decaying in-cylinder gas pressure. Post combustion, the in-cylinder gas pressure decreases quite rapidly, and so does the flow rate through the valve sampling valve opening (if the sampling duration were to be kept constant). Hence, in order to obtain a sufficient volume of gas sample (for the analysers) the valve had to be kept open for a longer duration. At each sampling crank angle window, a voltage of 100 V was applied to the solenoid; this voltage is larger compared to the voltages used during the sampling valve bench tests (described in Chapter 3), as in the engine the in-cylinder gas pressures reached much higher values (60-70 bar) than the pressures that could be applied on the sampling valve face during the bench tests (maximum 40 bar).

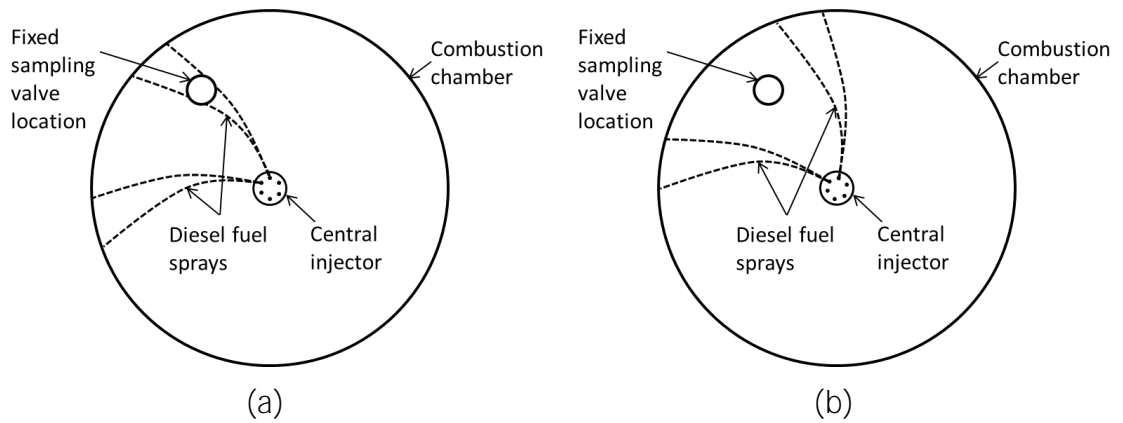


Figure 6.2: Schematic showing (a) sampling arrangement one and (b) sampling arrangement two relative to the diesel fuel sprays; changes to the position of the spray relative to the valve location was achieved by rotating the fuel injector

Sampling timing (middle of sampling window) (CAD ATDC)	Duration of sampling window (CAD)
10	6
25	10
40	15

Table 6.3: In-cylinder gas sample extraction timings in CAD ATDC during the engine cycle and the corresponding sampling windows in CAD

6.1.3 Experimental set 3: Exhaust emissions from real biogas

An additional set of tests were carried out using real biogas samples obtained from an anaerobic digester manufactured by Sistema Biobolsa (Biobolsa 2015). The pre-fabricated biodigester is a continuous flow reactor designed for small and medium sized farms, and converts organic waste, such as animal manure, into biogas (Figure 6.3).

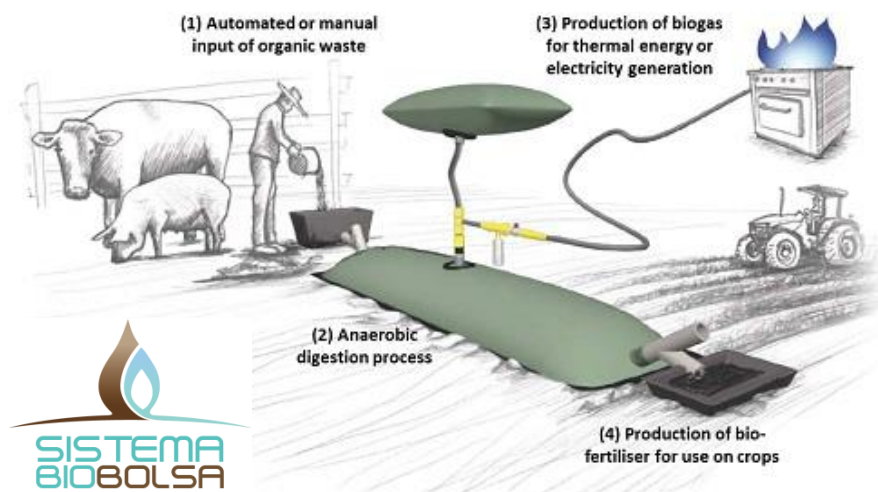


Figure 6.3: Schematic of the Sistema Biobolsa biodigester system, including feed stocks and use of outputs (Biobolsa 2015).

Two different samples of real biogas were tested with measured proportions of $54\text{CH}_4:40.5\text{CO}_2$ and $48\text{CH}_4:29\text{CO}_2$, with the balance assumed to be made up of inert components (Table 6.4). The biogas was collected in Tedlar bags, and delivered to the engine via a positive displacement gas pump, at a constant flow rate of 4.6 l/min (which was the maximum achievable with the available gas pump). The engine load was varied by changing the diesel fuel injection period (and hence the diesel fuel flow rate delivered to the engine) to vary the engine load between 3 and 7 bar IMEP. The exhaust emissions from the biogas-diesel fuel combustion were

compared with diesel fuel only combustion at the same engine loads, to determine any effect of displacing diesel fuel by biogas on exhaust emissions.

Sample name	CH ₄ :CO ₂ * mixture ratio (v/v)	Biogas flow rate (l/min)	Diesel fuel flow rate (ml/min)	Engine load (bar IMEP)
Biogas 1	54CH ₄ :40.5CO ₂	4.6	6.5 - 12.7	3 - 7
Biogas 2	48CH ₄ :29CO ₂	4.6	6.7 - 12.6	4 - 7

Table 6.4: Test parameter matrix for biogas-diesel fuel co-combustion tests (*the balance was assumed to be made up of inert components)

6.2 Results and discussion

6.2.1 Combustion characteristics

Figure 6.4 shows the heat release rate curves for a pilot diesel fuel IMEP of 0 bar

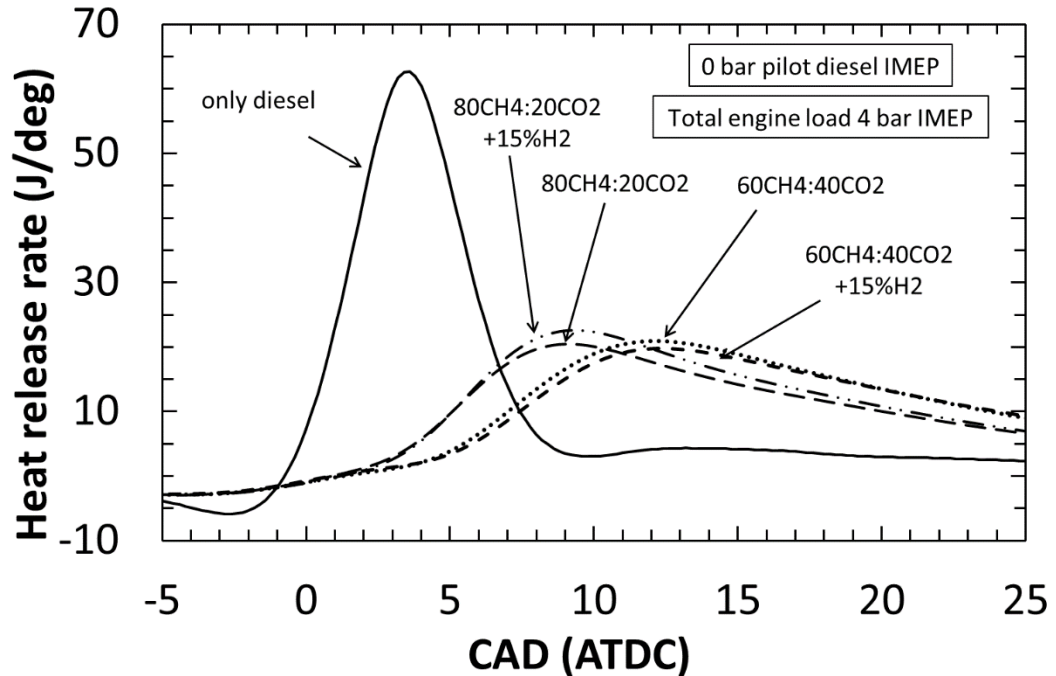


Figure 6.4: Heat release rate curves for an engine load of 4 bar IMEP, for a pilot diesel fuel IMEP of 0 bar and various CH₄-CO₂-H₂ mixture proportions (v/v)

and supplying the engine with different CH₄-CO₂-H₂ mixtures, to achieve the required engine load of 4 bar IMEP. The graph also shows the heat release rate curve at the same engine load of 4 bar IMEP when the engine is operating on only diesel fuel. First, comparing the heat release rate curve of diesel only engine operation with that of diesel fuel pilot ignited CH₄-CO₂-H₂ mixtures, it can be observed that the rate of increase of heat release post ignition is considerably faster in the case of only diesel, resulting in higher peak heat release rates closer to engine TDC. For diesel only combustion, an appreciable amount of diesel fuel-air mixture, prepared during the ignition delay period, is available for combustion and burns at diesel fuel stoichiometric flame propagation speeds. On the other hand, for a pilot

diesel IMEP of 0 bar, the in-cylinder CH₄-CO₂-H₂ mixtures are significantly leaner ($\phi_{\text{H}_2} = 0.018$ and $\phi_{\text{CH}_4} = 0.36$ for 80CH₄:20CO₂ + 15% H₂ mixture at a total engine load of 4 bar IMEP), and hence the developed multiple flame fronts travel at considerably lower velocities than achievable with stoichiometric combustion. This results in slower rates of release of energy, lower peak heat release rates occurring further away from TDC and relatively longer combustion durations (Figure 6.4). Another interesting point to note is that for diesel only combustion, the two distinct stages of premixed combustion and diffusion controlled burning can be clearly distinguished from the heat release rate curve, whereas in the case of CH₄-CO₂-H₂ mixture combustion, the heat release curve appears as a prolonged premixed stage (that is, there is an obscure diffusion burning stage). This is because the aspirated CH₄-CO₂-H₂ mixture can be assumed to be mixed almost homogeneously with the intake air, and burns gradually with multiple flame propagation fronts which have been pilot ignited by the diesel fuel.

Now, considering the heat release rate curves for the two CH₄-CO₂ mixtures shown in Figure 6.4, it can be seen that the rate of increase of heat release is higher for the 80CH₄:20CO₂ mixture, as compared to the 60CH₄:40CO₂ mixture, resulting in slightly higher peak heat release rates, considerably closer to engine TDC. CO₂ acts as an inert gas in the combustion chamber, absorbing energy from the combustion flame and severely curtailing burning velocities (Bari 1996). Therefore, the effect of CO₂ of slowing down the rate of combustion is more apparent in aspirated mixtures

with a higher proportion of CO_2 ($60\text{CH}_4:40\text{CO}_2$). The inclusion of 15% H_2 in each of the $\text{CH}_4\text{-CO}_2$ mixtures tends to increase the peak heat release rate somewhat, which can be attributed to the H_2 burning at a higher flame temperatures as compared to CH_4 .

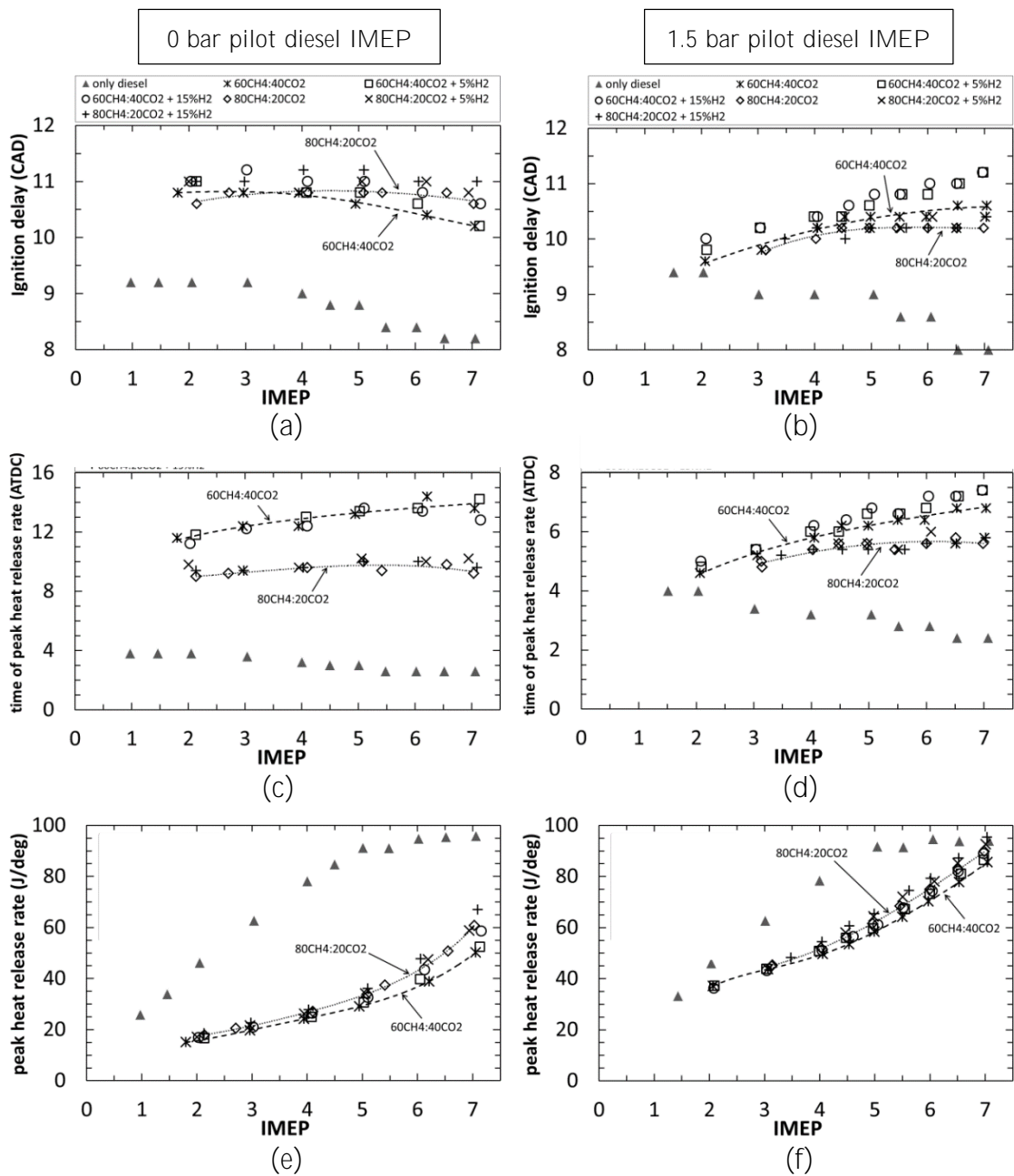


Figure 6.5: Combustion characteristics for the two pilot diesel fuel IMEPs of 0 and 1.5 bar, at various engine loads and $\text{CH}_4\text{-CO}_2\text{-H}_2$ mixture proportions: (a) and (b) duration of ignition delay; (c) and (d) time of peak heat release rate; (e) and (f) peak heat release rates

Figure 6.5 shows the ignition delay period, time of peak heat release and the peak heat release rates for the two pilot diesel fuel IMEPs of 0 bar and 1.5 bar, at a variety of engine loads and CH₄-CO₂-H₂ mixture proportions. For comparison purposes, Figure 6.5 also shows the ignition delay, time of peak heat release and peak heat release rates when the engine load was increased without any CH₄, CO₂ or H₂ addition, that is, by merely increasing the amount of diesel fuel injected. Ignition delay is defined here as the duration in CAD between the start of diesel fuel injection (SOI) and the start of combustion (SOC). SOI is taken to be the time when the actuation signal is sent to the injector, whereas the SOC is defined as the first incidence of detectable heat release following autoignition of the diesel fuel. It is important to reiterate here that the increase in IMEP, above the pilot diesel fuel IMEP, is achieved by delivering increasing amounts of CH₄-CO₂-H₂ mixtures to the engine.

Firstly, it can be observed in Figure 6.5 that the ignition delay period for both pilot diesel fuel IMEPs of 0 bar and 1.5 bar, and at all engine loads, is significantly higher for CH₄-CO₂-H₂ mixture combustion as compared to diesel only combustion. This can be explained, in general, by the reduction in local O₂ availability due to displacement by the aspirated CH₄-CO₂-H₂ mixtures. Additionally, this difference in the ignition delay period could be attributed to diesel fuel burning at close to stoichiometric conditions, while the aspirated CH₄-CO₂-H₂ mixture being significantly below stoichiometric levels. Secondly, comparing the ignition delay

period between the two pilot diesel fuel IMEPs, it can be seen from Figure 6.5 that the ignition delay period is generally smaller for the higher quantity of pilot diesel fuel (that is, for 1.5 bar pilot diesel IMEP), due to the presence of larger number of diesel ignition sites and multiple flame propagation fronts, which promote CH₄-CO₂-H₂ mixture ignition. Thirdly, considering the two annotated CH₄-CO₂ mixtures in Figure 6.5 (a) and (b), it can be observed, for a pilot diesel IMEP of 1.5 bar, that the ignition delay period is higher for the 60CH₄:40CO₂ mixture, as compared to 80CH₄:20CO₂ mixture, which could be attributed to the inert CO₂ interfering with the low temperature fuel breakdown molecular dynamics and chemical reactions by absorbing heat energy. These breakdown reactions are responsible for producing reactive radical species and escalating reaction rates and temperatures, leading to autoignition. However, for a pilot diesel IMEP of 0 bar, the trend is reversed with the 60CH₄:40CO₂ mixture exhibiting smaller ignition delay periods above 4 bar IMEP engine load, as compared to the 80CH₄:20CO₂ mixture. Finally, considering the effect on ignition delay period of adding H₂ to the two CH₄-CO₂ mixtures, it can be seen from Figure 6.5 that the ignition delay increases only for the 15% H₂ inclusion case, for both pilot diesel fuel IMEP conditions. The increase in ignition delay for low H₂ addition levels was also observed in the case of H₂-diesel fuel co-combustion (Chapter 5) and was attributed to the reduction in the O₂ concentration of the intake charge, as the intake air was displaced by the aspirated H₂. For the current case of CH₄-CO₂-H₂ mixtures, the H₂ that was included in the

CH₄-CO₂ mixture displaced some of the CH₄. Since the calorific value per unit volume of H₂ is lower than that of CH₄ (Table 6.2), a higher amount of H₂ is needed as compared to CH₄ to achieve the same engine load. Therefore, it follows that the H₂ displaced a relatively higher amount of O₂ as compared to CH₄ resulting in an increase in ignition delay.

From Figure 6.5 (c) and (d), it can be observed that the difference in the time of peak heat release rate (tPHRR) between 60CH₄:40CO₂ and 80CH₄:20CO₂ mixtures, at both pilot diesel IMEPs, is significantly more than the difference in the ignition delay period. As discussed earlier for Figure 6.4, the higher proportion of inert CO₂ in the 60CH₄:40CO₂ mixture reduces in-cylinder gas temperatures, thereby decreasing flame propagation velocities and prolonging the time taken to achieve peak heat release rates.

Figure 6.5 (e) and (f) shows that the peak heat release rates are lower for CH₄-CO₂-H₂ mixture combustion as compared to diesel only combustion, at both pilot diesel IMEPs and at all engine loads. This could be in part due to the in-cylinder CH₄-air and H₂-air mixtures being well below stoichiometric levels, and in part due to the energy absorbing effect of the inert CO₂. The only exception to this are the peak heat release rates for CH₄-CO₂-H₂ mixtures at an engine load of 7 bar IMEP for a pilot diesel IMEP of 1.5 bar, which are comparable to diesel only peak heat release rates at the same engine load (Figure 6.5 (f)). It can also be seen for both pilot diesel IMEPs, as the quantity of the supplied CH₄-CO₂-H₂ mixtures is increased (to

increase engine load), the peak heat release rate increases. This is due to the in-cylinder CH_4 -air and H_2 -air mixtures progressing towards stoichiometric conditions and hence burning with higher flame temperatures upon combustion.

6.2.2 CO_2 , CO and unburned THC exhaust gas emissions

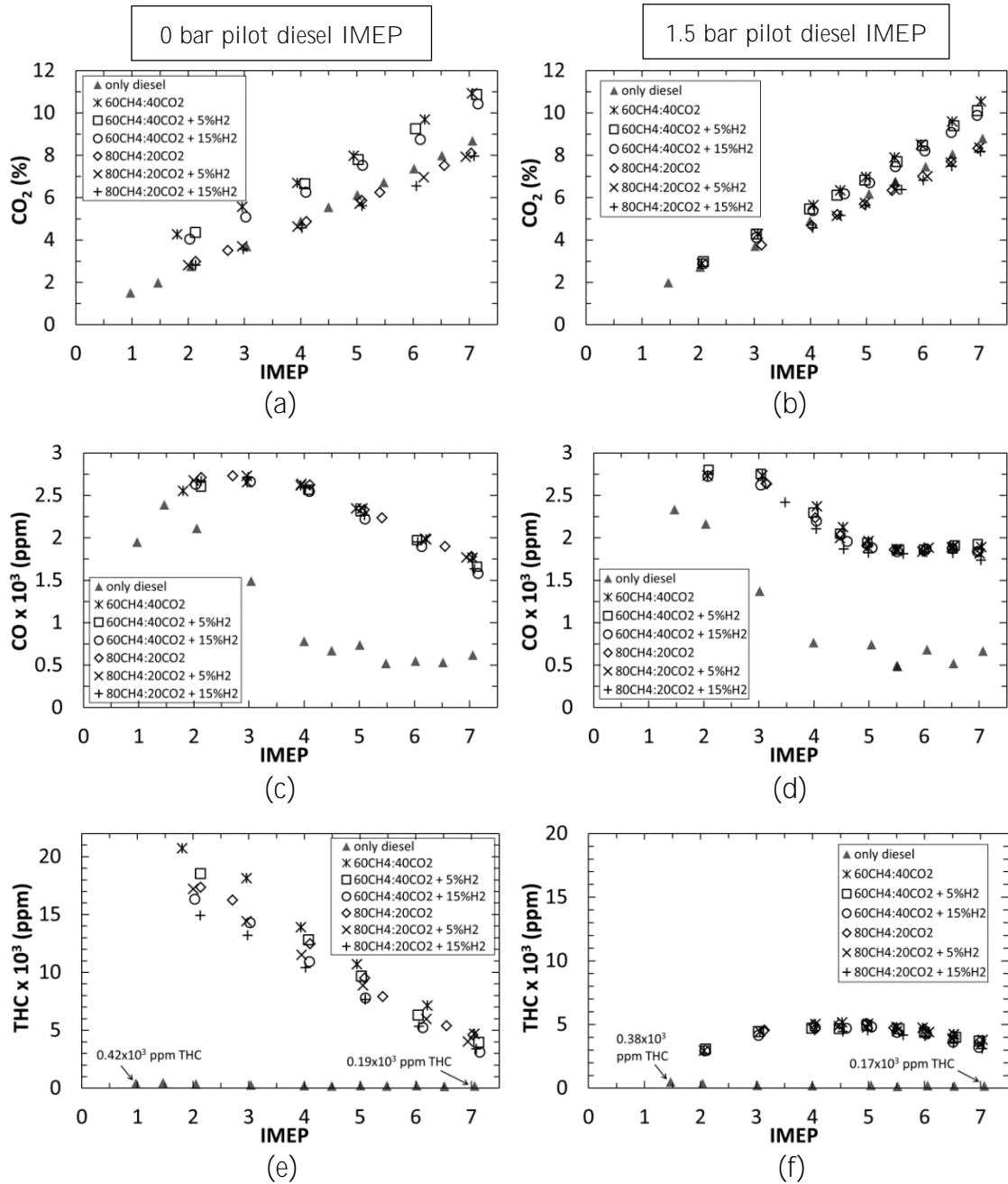


Figure 6.6: Variation in the exhaust emissions of (a) carbon dioxide (CO_2), (b) carbon monoxide (CO) and (c) unburned total hydrocarbons (THC) for the two pilot diesel fuel IMEPs, at various engine loads and CH_4 - CO_2 - H_2 mixture proportions

Figure 6.6 shows the gaseous exhaust emissions of CO₂, CO and unburned total hydrocarbons (THC) for the two pilot diesel fuel IMEPs of 0 bar and 1.5 bar, at various engine loads and CH₄-CO₂-H₂ mixture proportions. For both pilot diesel fuel IMEPs and all CH₄-CO₂-H₂ mixtures, an almost linear increase in CO₂ emissions is observed as the quantity of the supplied CH₄-CO₂-H₂ mixture to the engine is increased in order to increase the engine load. Comparing the CO₂ emissions between the two CH₄-CO₂ mixtures, for both pilot diesel fuel IMEPs the CO₂ emissions from the 60CH₄:40CO₂ mixture are higher due to the larger proportion of CO₂ in the aspirated mixture. It can also be observed from Figure 6.6 (a) and (b) that CO₂ emissions from diesel only combustion are similar to CO₂ emissions from the 80CH₄:20CO₂ mixture, and significantly lower than those from the 60CH₄:40CO₂ mixture. Since the typical composition of biogas produced in anaerobic digesters is about 60CH₄:40CO₂, post-production scrubbing of the biogas reduces an adverse effect of biogas combustion on CO₂ emissions. Common methods of biogas scrubbing include pressurised water scrubbing, pressure swing adsorption and amine absorption among others and have been described in detail in Chapter 2 of this thesis (Patterson et al. 2011; Yang, Ge, et al. 2014; Yang, Wang, et al. 2014). A slight reduction in CO₂ emissions is observed, at both pilot diesel IMEPs and at all engine loads, when H₂ is included in the CH₄-CO₂ mixtures due to the H₂ displacing some of both CH₄ and CO₂.

The CO emissions (Figure 6.6 (c) and (d)) from the CH₄-CO₂-H₂ mixtures are generally higher than the CO emissions from diesel only combustion, which could potentially be in part due to partial oxidation of the aspirated CH₄ and in part due to dissociation of some of the aspirated CO₂. The CO emissions are observed to decrease with increasing engine load for both pilot diesel IMEPs. As the engine load is increased by aspirating a greater volume of CH₄-CO₂-H₂ mixture, the in-cylinder CH₄-air and H₂-air mixtures progress towards stoichiometric conditions, resulting in higher post-combustion in-cylinder gas temperatures, improved CH₄ oxidation and, therefore, lower CO emissions. No significant differences are seen between the CO emissions from the different CH₄-CO₂-H₂ mixtures, leading the speculation that CO emissions are exclusively engine load (and hence in-cylinder gas temperature) dependent.

Similar to CO emissions, the unburned THC emissions (Figure 6.6 (e) and (f)) from the CH₄-CO₂-H₂ mixtures are generally higher than those from diesel only combustion, and in the case of pilot diesel fuel IMEP of 0 bar the unburned THC emissions decrease with increasing engine load. As discussed in the paragraph above, a large percentage of the aspirated CH₄ remains unburned in the cylinder and passes into exhaust, however, the percentage of unburned CH₄ decreases with increasing engine load (as can be observed in (Figure 6.6 (e))). A closer comparison of the unburned THC emissions (Figure 6.6 (e) and (f)) shows that the THC levels, at all engine loads, for a pilot diesel fuel IMEP of 0 bar are substantially higher as

compared to 1.5 bar pilot diesel fuel IMEP, while the CO emissions (Figure 6.6 (c) and (d)) show similar levels for both pilot diesel fuel flow rates. Taken together, the unburned THC and CO emission results provide a strong indication that the pilot diesel fuel IMEP of 0 bar is barely sufficient to provide reliable ignition of the aspirated gaseous fuel mixtures, especially when these mixtures are lean.

6.2.3 NO_x exhaust gas emissions

Figure 6.7 shows the gaseous exhaust emissions of NO_x for the two pilot diesel fuel

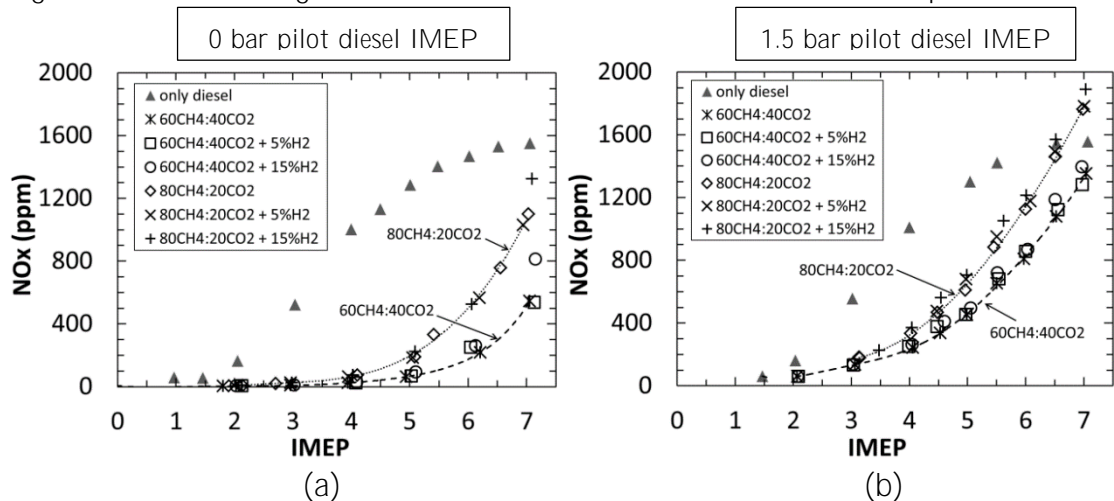


Figure 6.7: Variation in the exhaust emissions of oxides of nitrogen (NO_x) for the two pilot diesel fuel IMEPs, at various engine loads and CH₄-CO₂-H₂ mixture proportions

IMEPs of 0 bar and 1.5 bar, at various engine loads and CH₄-CO₂-H₂ mixture proportions. First, considering the NO_x emissions from CH₄-CO₂-H₂ mixtures with a pilot diesel fuel IMEP of 0 bar, the minimum quantity of fuel required to pilot ignite the aspirated CH₄-CO₂-H₂ mixtures, it can be observed from Figure 6.7 (a) that, at engine loads below 4 bar IMEP, NO_x emission levels are fairly low (< 100 ppm). However, as the engine load increases above 4 bar IMEP, NO_x emissions undergo an almost exponential increase. These trends in NO_x emissions are quite

similar to those obtained with H₂-diesel fuel co-combustion (as described in Chapter 5), and therefore can be explained likewise. At engine loads lower than 4 bar IMEP, the temperatures resulting from the combustion of the very lean in-cylinder CH₄-air and H₂-air mixtures ($\phi_{\text{H}_2} = 0.018$ and $\phi_{\text{CH}_4} = 0.36$ for 80CH₄:20CO₂+15% H₂ mixture at an engine load of 4 bar IMEP) are below the threshold temperatures which promote rapid thermal NO_x formation. However, as the CH₄-CO₂-H₂ mixture being supplied to the engine is increased, to increase the engine load above 4 bar IMEP, the in-cylinder mixture concentration becomes sufficiently rich for the post combustion gas temperatures to go above the level at which NO_x formation rates accelerate significantly. This exponential increase in NO_x production rates with increasing temperatures is expected according to the extended Zeldovich mechanism (discussed in Chapter 2) (Miller & Bowman 1989). Similar trends in NO_x emissions with increasing engine load can also be seen from Figure 6.7 (b), however, an exponential rise in NO_x emissions occurs above 2 bar IMEP, as compared to the 4 bar IMEP threshold observed with a pilot diesel IMEP of 0 bar. This is likely due to a higher quantity of diesel fuel being injected into the combustion chamber to achieve a pilot diesel IMEP of 1.5 bar. Diesel fuel combustion can be expected to always occur at near stoichiometric conditions with resultant local temperatures sufficient for NO_x formation (Dec 1997). Therefore, the temperatures resulting from the combined combustion of CH₄-CO₂-H₂ mixtures and diesel fuel are likely to reach the threshold for accelerated thermal NO_x formation at a lower load of 2 bar IMEP.

Additionally, it could be suggested that at a pilot diesel IMEP of 0 bar, there was a significantly higher amount of unburned CH_4 and CO_2 in the cylinder resulting in lower temperatures, and hence, lower NO_x emissions, especially at low engine loads.

Comparing NO_x emissions between the two CH_4 - CO_2 mixtures for both pilot diesel IMEPs, it can be observed from Figure 6.7 that NO_x emissions increase more rapidly for the 80 CO_2 :20 CO_2 mixture, as compared to for the 60 CH_4 :40 CO_2 mixture. This is expected, as the mixture with the higher proportion of CO_2 would tend to decrease in-cylinder temperatures to a greater degree, hence slowing down NO_x formation rates. The peak heat release rates, which can be expected to be indicative of in-cylinder gas temperatures, are similarly lower in the case of the 60 CH_4 :40 CO_2 mixture, as compared to the 80 CO_2 :20 CO_2 mixture (Figure 6.5 (e) and (f)).

The inclusion of H_2 in the CH_4 - CO_2 mixtures does not appear to have a significant effect on NO_x emissions, except at the highest tested engine load condition of 7 bar IMEP. For example, at 7 bar IMEP (total engine load) and for a pilot diesel IMEP of 0 bar, the addition of 15% H_2 (v/v) to the 60 CH_4 :40 CO_2 mixture increases NO_x emissions by almost 50%. This sharp increase in NO_x emissions at 7 bar IMEP can be attributed to the flame temperatures of the 60 CH_4 :40 CO_2 + 15% H_2 mixture being considerably higher than those of the 60 CH_4 :40 CO_2 mixture.

Figure 6.7 also shows the NO_x exhaust emissions when the engine load is increased without any CH_4 - CO_2 - H_2 mixture addition, that is, by merely increasing the amount

of diesel fuel injected. It is important to note that the NO_x emissions from CH_4 - CO_2 - H_2 mixture combustion, at all engine loads, are lower than those from diesel only combustion. The only exception to this is for the pilot diesel IMEP of 1.5 bar, 80 CH_4 :20 CO_2 + 15% H_2 condition at an engine load of 7 bar IMEP (Figure 6.7 (b)). The lower NO_x emissions are due to the lean burn capability of biogas, which allows low temperature combustion, and hence reduced NO_x formation rates, while still maintain diesel fuel comparable efficiencies (Yoon & Lee 2011; Bora et al. 2014). In contrast, for diesel only fuelling (that is no CH_4 - CO_2 - H_2 mixture addition) the burning zone is naturally located where the diesel fuel-air mixture is approximately near stoichiometric, which results in high flame temperatures and high NO_x production rates.

6.2.4 Particulate exhaust emissions

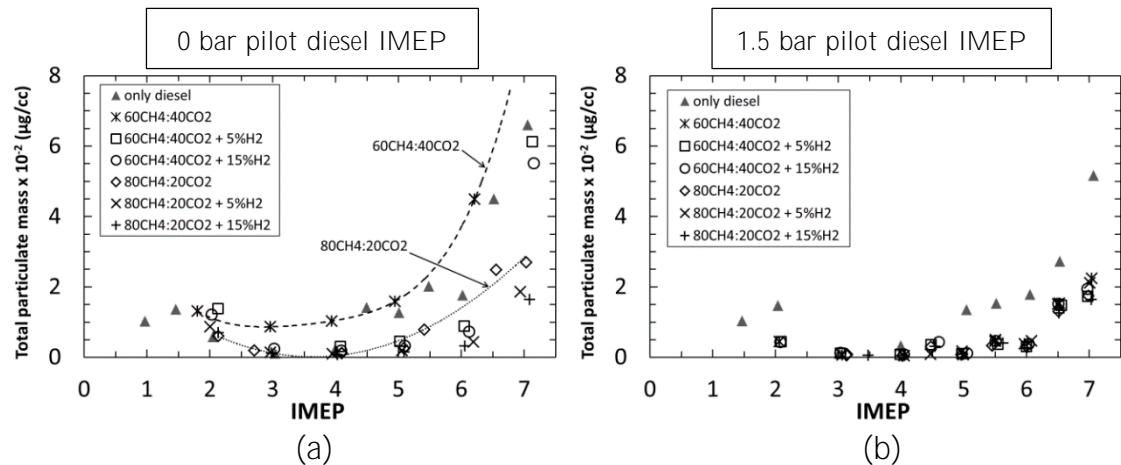


Figure 6.8: Exhaust emissions of total particulate mass for the two pilot diesel fuel IMEPs, at various engine loads and CH₄-CO₂-H₂ mixture proportions

Figure 6.8 shows the exhaust emissions of total particulate mass (PM) for the two pilot diesel fuel IMEPs of 0 bar and 1.5 bar, at various engine loads and CH₄-CO₂-H₂ mixture proportions. It can be observed that PM emissions increase sharply above engine loads for 5 bar IMEP (for 0 bar pilot diesel fuel IMEP) and 6 bar IMEP (for 1.5 bar pilot diesel fuel IMEP). This rapid increase in PM emissions can also be seen to occur with diesel fuel only combustion (Figure 6.8) and can be attributed to the natural reduction in the air available for combustion as the engine load increases beyond about 5 bar IMEP, and towards the highest tested load condition of 7 bar IMEP. It should be noted that the increase in in-cylinder gas temperatures with increasing engine loads can be expected to enhance oxidation rates. However, Figure 6.8 suggests that at engine loads above 5 bar IMEP, increased pyrolysis rates prevail over enhanced oxidation rates, resulting in a net increase in PM emissions. Additionally, Figure 6.8 shows lower PM emissions with

the CH₄-CO₂-H₂ mixture as compared to diesel fuel only combustion, which can be attributed to the reduction in carbon flow rate being supplied to the engine from the CH₄-CO₂-H₂ mixture, as compared to diesel fuel, for a given engine load.

It can also be observed from Figure 6.8 (a), for a pilot diesel IMEP of 0 bar, that PM emission levels for the 60CH₄:40CO₂ mixture are significantly higher as compared to the 80CH₄:20CO₂ mixture. It appears that the higher proportion of inert CO₂ in the 60CH₄:40CO₂ mixture results in greater in-cylinder gas temperature reductions (due to heat energy absorption), leading to reduced soot oxidation rates and higher PM emissions. The inclusion of H₂ to the 60CH₄:40CO₂ mixture produces significant reductions in PM emissions, which could be attributed to two factors: the displacement of some of the CH₄ and CO₂ by H₂, and higher post-combustion gas temperatures (and hence, increased soot oxidation rates) from CH₄-CO₂-H₂ mixtures, as compared to CH₄-CO₂ mixtures.

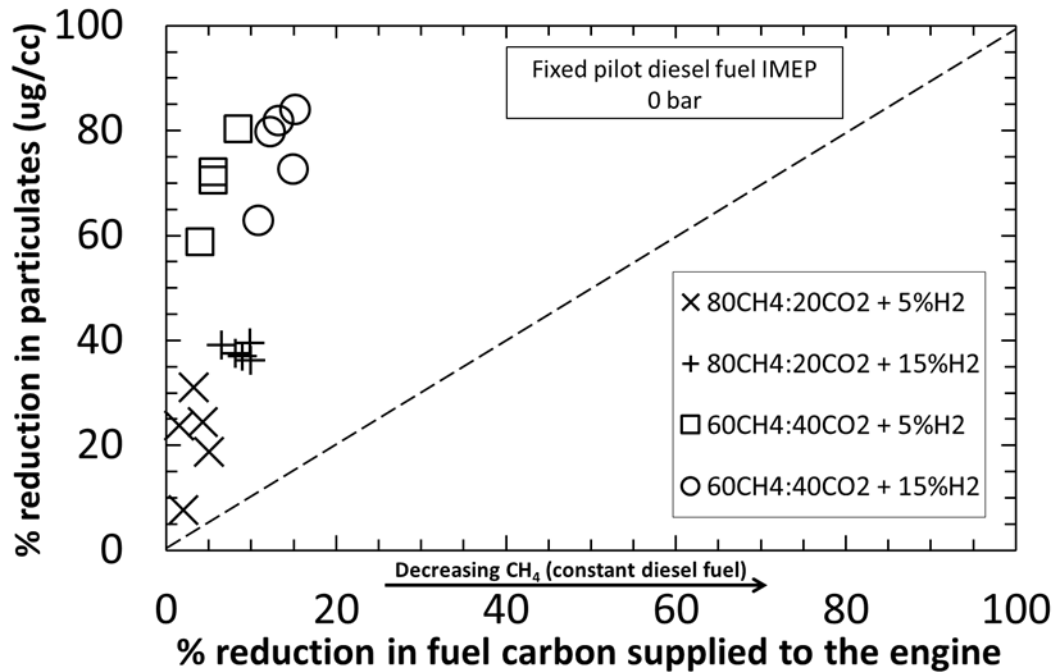


Figure 6.9: Comparison of percentage reduction in total particulate mass with percentage reduction in the CH_4 content (fuel carbon) of the combustible mixture at constant engine loads and for a fixed pilot diesel IMEP of 0 bar.

Figure 6.9 shows the percentage reduction in the total particulate mass plotted against percentage reduction in fuel carbon supplied to the engine, for a fixed pilot diesel IMEP of 0 bar and various CH_4 - CO_2 - H_2 mixtures. The reduction in fuel carbon was achieved by lowering the proportion of CH_4 and increasing the proportion of H_2 in the aspirated CH_4 - CO_2 - H_2 mixture, while the relative proportions of the three gases were maintained. The purpose of the graph is to determine whether reducing the proportion of CH_4 and CO_2 and increasing the proportion of H_2 in the aspirated mixture has an effect on the reduction in exhaust particulate emissions. The percentage reduction in both particulates and fuel carbon for the $80\text{CH}_4:20\text{CO}_2 + 5\%/15\% \text{H}_2$ mixture were calculated against the values obtained with the engine operating only on the $80\text{CH}_4:20\text{CO}_2$ mixture (without any

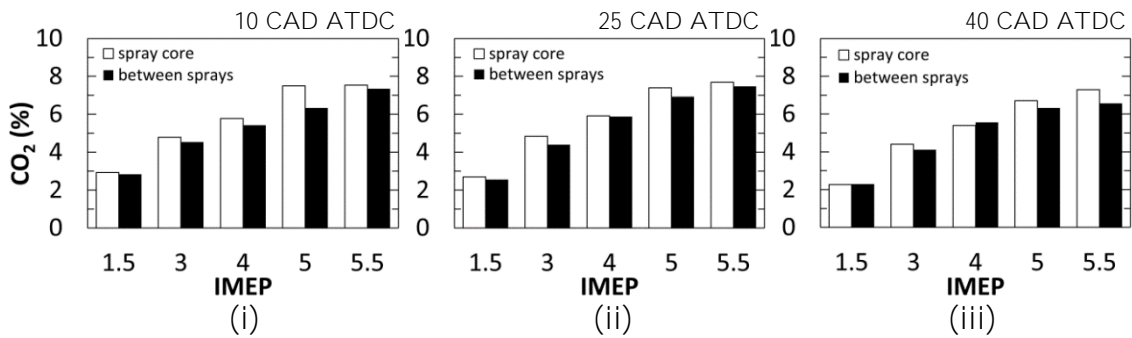
H₂). The percentage reductions for the 60CH₄:40CO₂ mixture were also calculated in a similar manner. The 1:1 dashed diagonal line in Figure 6.9 represents equal reductions in both PM emissions and fuel carbon supplied to the engine.

For all the CH₄-CO₂-H₂ mixtures shown in Figure 6.9, the reductions in PM emissions lie in the top half of the graph (above the 1:1 dashed line), implying a beneficial effect of replacing some of the CH₄ (and CO₂) with H₂ on PM reduction, beyond simple fuel carbon displacement. For example for the 60CH₄:40CO₂ + 15% H₂ mixture, a 10% reduction in fuel carbon causes an approximately 60% reduction in particulate matter. As discussed previously, this reduction could be a result of CH₄-CO₂-H₂ mixtures burning at higher flame temperatures compared to only CH₄-CO₂ mixtures, resulting in increased soot oxidation rates.

Figure 6.9 also shows that the reduction in particulates for the 60CH₄:40CO₂ mixture is considerably greater as compared to the 80CH₄:20CO₂ mixture, despite the percentage reductions in fuel carbon being quite similar for the two mixture types. A possible explanation for this observation is that the 60CH₄:40CO₂ mixture lowers the spray core and flame temperatures to a greater extent as compared to the 80CH₄:20CO₂ mixture (due to higher amount of CO₂ being supplied for a given engine load). This results in a reduction in the diesel fuel pyrolysis rates, leading to a reduction in PM formation rates.

6.2.5 In-cylinder gas sample composition

(a) 60CH₄:40CO₂



(b) 60CH₄:40CO₂ + 15%

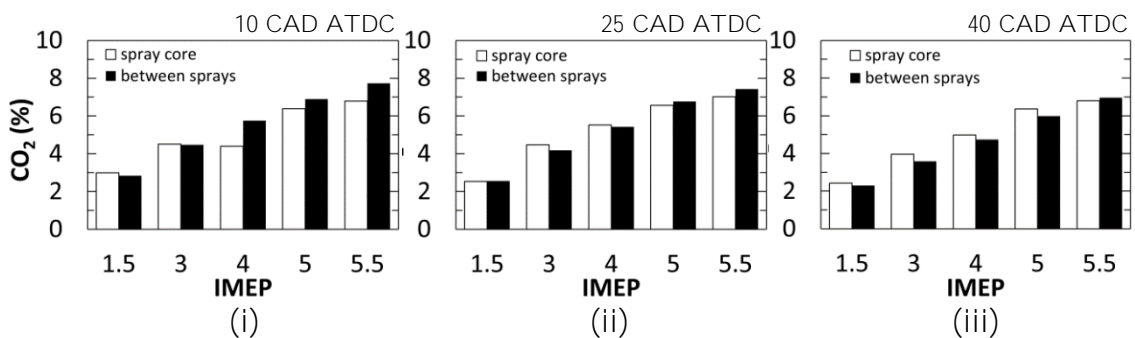


Figure 6.10: Measurement of in-cylinder carbon dioxide (CO₂) concentration for (a) 60CH₄:40CO₂ and (b) 60CH₄:40CO₂ + 15% H₂ mixtures in gas samples collected at (i) 10 CAD, (ii) 25 CAD and (iii) 40 CAD ATDC at a fixed pilot diesel fuel IMEP of 1.5 bar with increasing amounts of CH₄-CO₂-H₂ mixtures and variable engine loads with two sampling arrangements (Figure 6.2)

Figure 6.10 shows the CO₂ concentration in gas samples at various engine loads extracted from the engine cylinder at 10, 25 and 40 CAD ATDC (sampling windows) of the combustion cycle with the two in-cylinder sampling arrangements relative to the diesel fuel sprays (Figure 6.2). The tests were conducted for fixed pilot diesel fuel IMEP of 1.5 bar and the increase in engine load achieved by increasing the supply of the CH₄-CO₂-H₂ mixture (as applicable) to the engine. First, considering the gas samples collected when burning the 60CH₄:40CO₂ mixture, it can be observed that the CO₂ concentrations are quite similar for the two sampling

arrangements, at all the three sampling windows. This can be attributed to comparable quantities of CO_2 occurring in the region of the spray core and between the two sprays. In the spray core region, CO_2 is produced by diesel fuel combustion, and aspirated CO_2 is also present in the intake air mixture that entrains into the diesel fuel spray. The region between the two sprays contains a higher concentration of the aspirated $\text{CH}_4\text{-CO}_2\text{-H}_2$ mixture, and hence a higher quantity of CO_2 as compared to the spray core region; additionally, CO_2 is also produced from the combustion of CH_4 in the region between two sprays.

The inclusion of 15% H_2 (v/v) to the 60 CH_4 :40 CO_2 mixture does not appear to have a significant effect on the in-cylinder CO_2 concentration, except for a slight increase in CO_2 levels in the region between the two sprays especially at 10 CAD and 25 CAD ATDC. This is most likely due to the increase hydrocarbon oxidation rates as a result of increased flame temperatures for the $\text{CH}_4\text{-CO}_2\text{-H}_2$ mixture (as compared to the $\text{CH}_4\text{-CO}_2$ mixture).

The concentration of CO_2 is observed to fall, for both the $\text{CH}_4\text{-CO}_2\text{-H}_2$ mixtures (Figure 6.10 (a) and (b)) as the combustion cycle progresses from 10 CAD to 40 CAD ATDC; this is expected to be a result of the burned gas products becoming diluted with the unreacted in-cylinder air.

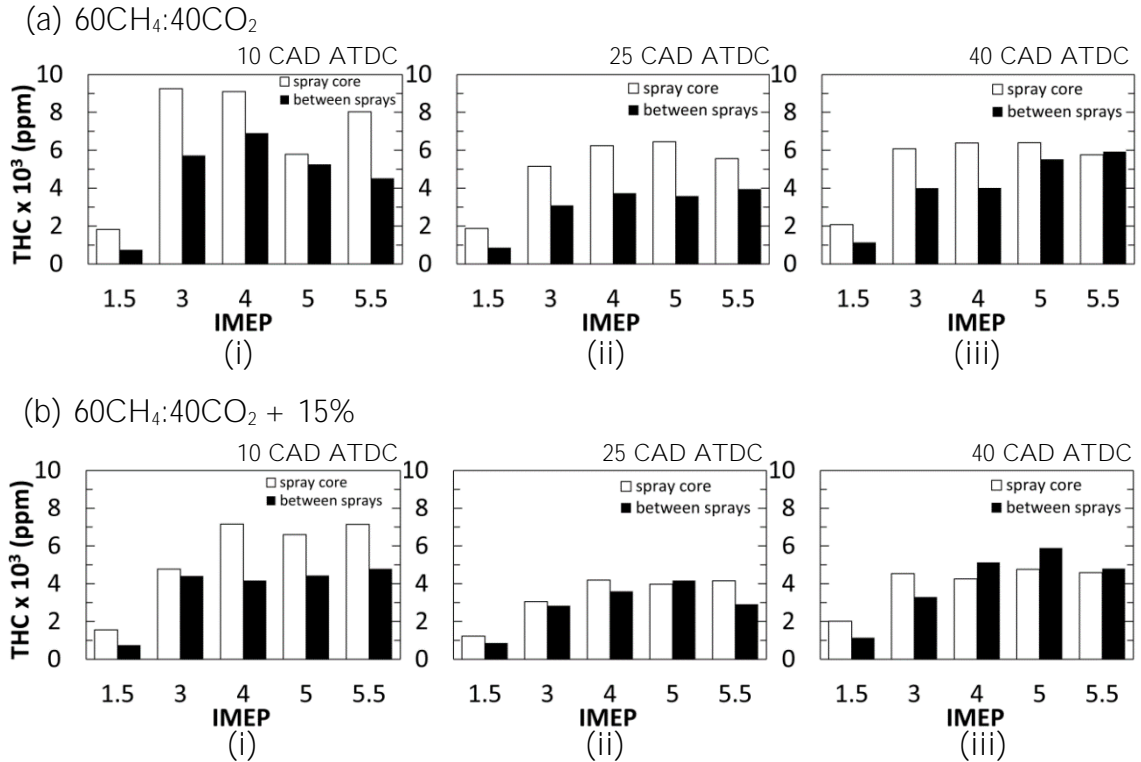


Figure 6.11: Measurement of in-cylinder unburned total hydrocarbon (THC) concentration for (a) 60CH₄:40CO₂ and (b) 60CH₄:40CO₂ + 15% H₂ mixtures in gas samples collected at (i) 10 CAD, (ii) 25 CAD and (iii) 40 CAD ATDC at a fixed pilot diesel fuel IMEP of 1.5 bar with increasing amounts of CH₄-CO₂-H₂ mixtures and variable engine loads with two sampling arrangements (Figure 6.2)

Figure 6.11 shows the unburned THC concentration in gas samples at various engine loads extracted from the engine cylinder at 10, 25 and 40 CAD ATDC (sampling windows) of the combustion cycle with the two in-cylinder sampling arrangements relative to the diesel fuel sprays (Figure 6.2). For both mixtures, 60CH₄:40CO₂ and 60CH₄:40CO₂ + 15% H₂, it can be observed that the unburned THC concentrations at 10 CAD ATDC, when sampling within the spray core region, were higher as compared to the region between the fuel sprays. At the initial stages of the combustion (10 CAD ATDC), the diesel fuel spray has not fully broken down and combusted, and therefore is an important source for unburned THC. In addition, the intake air mixture that entrains into the diesel fuel contains aspirated

CH₄, which is included in the sample collected from the spray core region. It is thought that the combined THC concentrations from the diesel fuel and CH₄ result in higher unburned THC levels occurring in the spray core region. As the combustion cycle progresses from 10 to 25 CAD ATDC, the unburned THC levels in the spray core region are observed to decrease; the mixing of diesel fuel with air results in higher rates of diesel fuel oxidation, and therefore lowers unburned THC levels.

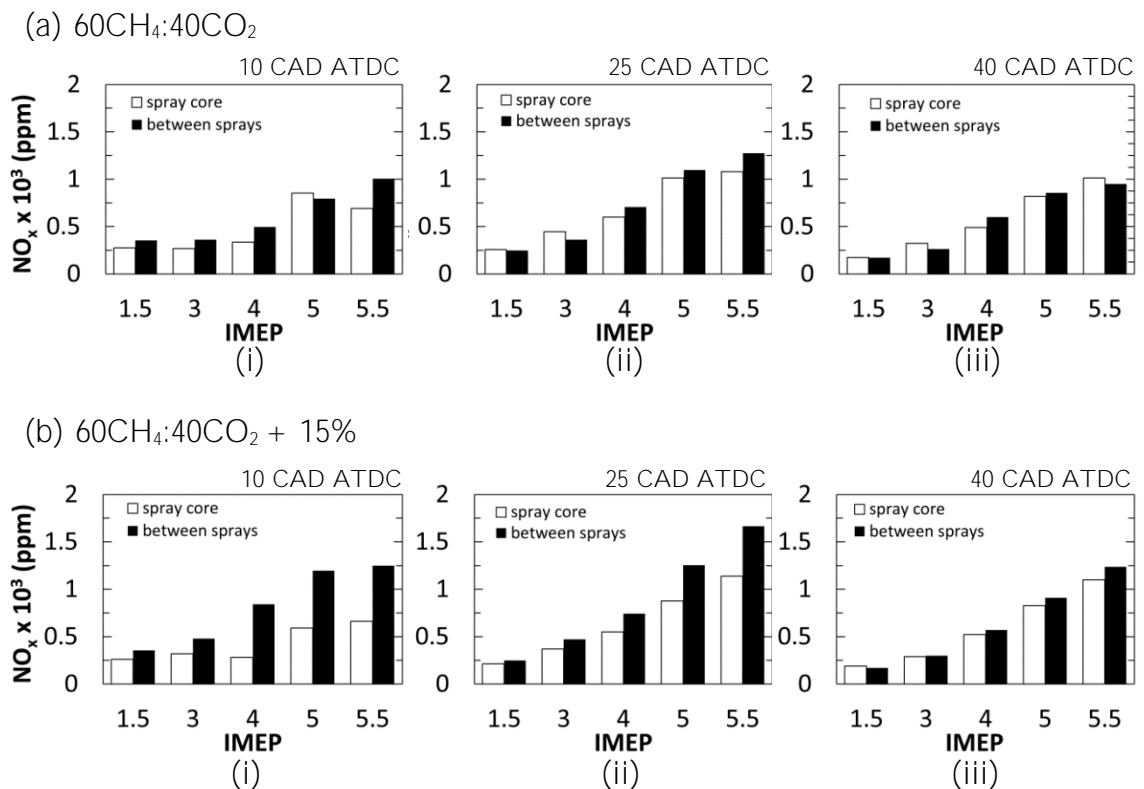


Figure 6.12: Measurement of in-cylinder nitrogen oxide (NO_x) concentration for (a) 60CH₄:40CO₂ and (b) 60CH₄:40CO₂ + 15% H₂ mixtures in gas samples collected at (i) 10 CAD, (ii) 25 CAD and (iii) 40 CAD ATDC at a fixed pilot diesel IMEP of 1.5 bar with increasing amounts of CH₄-CO₂-H₂ mixtures and variable engine loads with two sampling arrangements (Figure 6.2)

Figure 6.12 shows the NO_x concentration in gas samples at various engine loads extracted from the engine cylinder at 10, 25 and 40 CAD ATDC (sampling

windows) of the combustion cycle with the two in-cylinder sampling arrangements relative to the diesel fuel sprays (Figure 6.2). First, considering the gas samples collected from the cylinder at 10 CAD and 25 CAD ATDC, it can be observed that NO_x levels are significantly higher in the region between two sprays for the $60\text{CH}_4:40\text{CO}_2 + 15\% \text{H}_2$ mixture, as compared to the $60\text{CH}_4:40\text{CO}_2$ mixture. As suggested previously when discussing NO_x exhaust emissions, the temperatures resulting from the combined $\text{CH}_4\text{-H}_2\text{-air}$ mixture combustion are expected to be higher as compared to $\text{CH}_4\text{-air}$ combustion, resulting in higher NO_x formation rates. Now comparing the difference in NO_x concentrations between the two sampling arrangements, for the $60\text{CH}_4:40\text{CO}_2 + 15\% \text{H}_2$ mixture, NO_x levels are higher in the region between the two sprays as compared to within the spray core region, especially at 10 CAD and 25 CAD ATDC. The region between the two sprays can be expected to have a higher concentration of the aspirated $\text{CH}_4\text{-CO}_2\text{-H}_2$ mixture resulting in higher post combustion gas temperatures and, therefore, higher NO_x formation rates. On the other hand, the lower NO_x concentrations in the spray core region (at 10 CAD ATDC) could be attributable to the relatively low concentration of air in the fuel rich core of the diesel fuel spray, resulting in lower combustion temperatures and, hence, reduced NO_x formation.

As the combustion cycle progresses to 25 CAD ATDC, NO_x levels are seen to increase in both regions, within spray core and between two sprays. At 25 CAD ATDC, the rich diesel spray core might be expected to have broken up, with the

aspirated intake mixture being rapidly entrained into the disintegrated diesel fuel spray. The combined fuel mixture is expected to have burned at sufficiently high temperatures to increase NO_x formation rates as combustion progressed from 10 to 25 CAD ATDC.

As combustion proceeds beyond 25 CAD ATDC, the expansion of post combustion gases reduces temperatures significantly and NO_x concentrations adjust to lower levels through reversible dissociation reactions. At 40 CAD ATDC, NO_x levels for both the aspirated mixtures decrease relative to NO_x levels at 25 CAD ATDC; additionally, NO_x levels are quite similar for the gas samples collected with the two sampling arrangements (Figure 6.12 (iii)). The decrease in NO_x levels can be attributed to dilution of post combustion gases with the unreacted air, while the homogeneity in NO_x levels might be due to the effects of air swirl and reverse squish flow (Heywood 1988; Zhao et al. 1996), which promote the redistribution of in-cylinder gaseous composition at later stages of combustion (40 CAD ATDC). After 40 CAD ATDC, the in-cylinder gas temperature drops rapidly, 'freezing' the NO_x reaction chemistry.

6.2.6 Exhaust emissions from real biogas

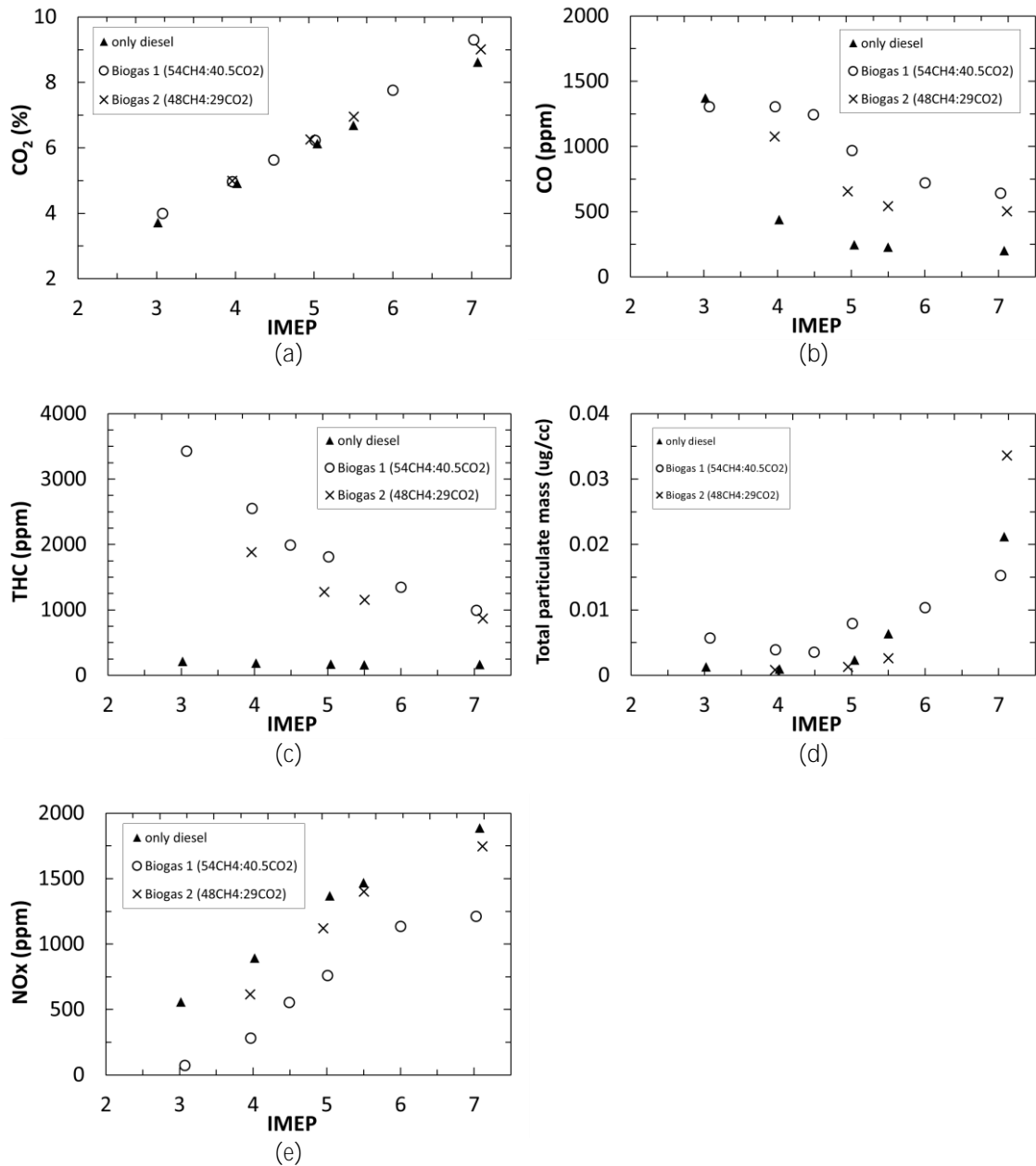


Figure 6.13: Exhaust emissions of (a) CO_2 , (b) CO, (c) unburned THC, (d) particulates and (e) NO_x for two real biogas samples for a fixed flow rate of biogas to the engine and various engine loads. For comparison, the exhaust emissions from diesel fuel only engine operation (no biogas addition) are also shown.

Figure 6.13 shows the exhaust emissions of CO_2 , CO, unburned THC, particulates and NO_x from the combustion of two real biogas samples of different CH_4 - CO_2 compositions at various engine loads. The composition of biogas sample 1 was measured to be $54\text{CH}_4:40.5\text{CO}_2$, while that of biogas sample 2 was measured to be $48\text{CH}_4:29\text{CO}_2$; the balance for both biogas samples was assumed to be made up of inert components. It should be pointed out here that a different test procedure was employed for these tests as compared to that utilised so far in Chapter 6. For these tests with real biogas, the flow rate of the biogas to the engine was kept fixed, and the increase in engine load was achieved by increasing the diesel fuel injection duration period (that is, the diesel fuel flow rate to the engine). For comparison purposes, the exhaust emissions for diesel only combustion (no biogas addition) were also included. Some separate cursory tests were done whereby the real biogas mixtures were simulated by using CH_4 - CO_2 mixtures from compressed gas bottles and fed into the engine at the same flow rate (as the real biogas). These tests showed very similar exhaust emission levels to the emissions obtained using the real biogas, lending some confidence to the assumption that the remaining proportion of the real biogas mixtures (apart from CH_4 and CO_2) is made up of inert components.

It can be observed from Figure 6.13 (a) that the CO_2 emissions from the two different biogas samples are quite similar to diesel only CO_2 emissions, at all loads up to 6 bar IMEP. At an engine load of 7 bar IMEP, the CO_2 emissions from biogas

sample 1 were slightly higher than sample 2, due to sample 1 having a higher proportion of CO_2 . The emissions of CO and unburned THC were generally higher for biogas sample 1 at all engine loads, as compared to both biogas sample 2 and diesel only condition (Figure 6.13 (b) and (c)). This could be attributed to the higher proportion of inert CO_2 in biogas sample 1 which caused a reduction in in-cylinder gas temperatures (by absorbing heat energy), thereby curtailing oxidation rates of both CH_4 and diesel fuel and resulting in increased unburned (not ignited) or partially oxidised hydrocarbon emissions. Similarly, particulate emissions (Figure 6.13 (d)) appeared to be higher for biogas sample 1 at all engine loads up to 5.5 bar IMEP, as compared to both biogas sample 2 and diesel only condition, most likely due to the effect of reduced thermal soot oxidation rates, as previously discussed in the case of CO and unburned THC emissions. Above 5.5 bar IMEP, particulate emissions were observed to increase rapidly for both biogas samples and diesel only combustion, with the sharpest increase occurring for biogas sample 2. The sharp increase in PM emissions at engine loads above 5.5 bar IMEP could be attributed to the natural reduction in air availability for combustion, as the engine load rises and the in-cylinder diesel fuel-air mixture being supplied to the engine becomes richer. Now considering NO_x emissions, it can be observed from Figure 6.13 (e), that NO_x emissions were lowest for biogas sample 1, as compared to both biogas sample 2 and diesel only condition. As mentioned before, the higher proportion of CO_2 in biogas sample 1 tends to lower in-cylinder gas temperatures,

and since NO_x is produced primarily via thermal means in diesel engines (Bowman 1973; Miller & Bowman 1989), a reduction in in-cylinder gas temperatures can be expected to impede NO_x formation rates.

6.3 Conclusions

- The rate of increase of heat release for the $\text{CH}_4\text{-CO}_2\text{-H}_2$ mixtures was considerably slower, as compared to diesel only combustion resulting in lower peak heat release occurring relatively further away from engine TDC.
- For a pilot diesel fuel IMEP of 1.5 bar, the ignition delay period was higher for the 60 CH_4 :40 CO_2 mixture, as compared to 80 CH_4 :20 CO_2 mixture, which could be attributed to the higher proportion of inert CO_2 interfering with low temperature fuel breakdown reactions. This trend appeared to reverse for a pilot diesel IMEP of 0 bar, with the 60 CH_4 :40 CO_2 mixture exhibiting smaller ignition delay periods above 4 bar IMEP engine load, as compared to the 80 CH_4 :20 CO_2 mixture.
- Peak heat release rates were observed to be lower for the 60 CH_4 :40 CO_2 mixture as compared to the 80 CH_4 :20 CO_2 mixture, at both pilot diesel IMEPs and at all engine loads, attributable to the presence of higher proportion of CO_2 in the aspirated mixture.
- Exhaust CO_2 emissions were observed to be higher for the 60 CH_4 :40 CO_2 mixture as compared to diesel only combustion, outlining the need to scrub the biogas post-production to decrease its CO_2 content.

- While no significant differences were seen in the exhaust CO and unburned THC emissions between the different CH₄-CO₂-H₂ mixtures, both CO and unburned THC emissions decreased with increasing engine loads, due to increasing in-cylinder gas temperatures resulting in enhanced thermal oxidation rates.
- For both fixed pilot diesel IMEPs, NO_x emissions were observed to increase rapidly, but only when the in-cylinder temperatures due to combined diesel fuel and CH₄-CO₂-H₂ mixture combustion exceeded the threshold for NO_x formation temperatures. The heat energy absorbing effect of the inert CO₂ resulted in NO_x emission from the 60CH₄:40CO₂ mixture being lower as compared to the 80CH₄:20CO₂ mixture
- Exhaust PM emissions for the 60CH₄:40CO₂ mixture were observed to be considerably greater as compared to both 80CH₄:20CO₂ mixture and diesel only condition. The inclusion of H₂ to 60CH₄:40CO₂ mixture significantly reduced PM emissions, speculated to be due to higher post-combustion gas temperatures.
- In-cylinder unburned THC levels at 10 CAD ATDC were observed to be higher in gas samples collected from within the spray core region, as compared to the region between two sprays. As the cycle progressed from 10 to 25 CAD ATDC and the diesel fuel spray core disintegrated due to air entrainment, the unburned THC levels in the spray core region were observed to decrease.

- In-cylinder NO_x levels were observed to be significantly higher in the region between two sprays for the $60\text{CH}_4:40\text{CO}_2 + 15\% \text{H}_2$ mixture, as compared to the $60\text{CH}_4:40\text{CO}_2$ mixture. This was attributed to the temperatures resulting from the combined $\text{CH}_4\text{-H}_2\text{-air}$ mixture combustion being higher than those achieved by $\text{CH}_4\text{-air}$ combustion, resulting in higher NO_x formation rates.
- Exhaust emissions from real biogas samples were in agreement with the trends obtained with the simulated $\text{CH}_4\text{-CO}_2$ mixtures. The inert CO_2 has a significant effect of reducing in-cylinder gas temperatures which is beneficial for NO_x emissions, but has a detrimental impact on CO , unburned THC and PM emissions (due to reduced thermal oxidation rates).

7 The influence of hydrogen-diesel co-combustion on an EGR applied, intake air boosted CI engine

Global demand for liquid fuels is projected to rise at a rapid pace; however, current and future energy policies are increasingly aiming to reduce CO₂ emissions from the transport sector (Schiermeier 2014). The combustion of fossil fuels releases carbon, in the form of carbon dioxide (CO₂), and there is consensus that the rapid anthropogenic emission of fossil bound carbon is resulting in global climate change. Co-currently, there is growing awareness of the negative impacts of toxic exhaust pollutants from internal combustion engines, such as nitrogen oxides (NO_x) and carbonaceous soot or particulate matter (PM), on the health of urban populations (Pope et al. 2002). The displacement of fossil diesel fuel with hydrogen (H₂) is an attractive proposition for compliance with emissions standards and reduction of harmful pollutants from diesel engines. With a carbon content of zero, co-combustion of H₂ and diesel fuel has potential for a reduction in the levels of both

exhaust gas CO₂ and PM (Karim 2003; Christodoulou & Megaritis 2013; Talibi et al. 2014).

This chapter investigates the effects of increasing the percentage of energy supplied to the engine from H₂ (while reducing that from diesel fuel) on combustion characteristics and emissions production at a range of engine loads (IMEP), simulated EGR levels and intake air boosting combinations. This chapter is complimentary to Chapter 4 which dealt with H₂-diesel fuel co-combustion in a naturally aspirated engine without EGR and intake air boost. It was observed in Chapter 4 that at higher engine loads above 4 bar IMEP NO_x exhaust emissions increased significantly; additionally, the substitution of intake air by H₂ resulted in the reduced O₂ availability for diesel fuel combustion resulting in increased exhaust particulate emissions. The utilisation of EGR allows low temperature combustion to take place hence decreasing NO_x formation rates, while intake air boosting allows additional O₂ to be fed into the engine, potentially mitigating the effect of intake air substitution by H₂ and N₂ (for simulated EGR).

7.1 Experimental procedure

The experiments discussed in this chapter were conducted on the single cylinder engine utilising the common rail fuel injection system for diesel fuel injection and the gas mass flow controller system for delivering hydrogen (H₂) and nitrogen (N₂) to the engine. The N₂ was used to dilute the intake air and reduce the intake O₂ concentration. This allowed EGR-like conditions to be achieved inside the

combustion chamber. Additionally, the intake air supercharger system was deployed on the engine to increase the density of the intake air being supplied to the combustion chamber and allow higher engine loads (IMEPs) to be achieved. These systems have been described in detail in Chapter 3 of this thesis. All the experiments were carried out at a constant engine speed of 1200 rpm, common rail fuel injection pressure of 900 bar and a constant diesel fuel injection timing of 6 CAD BTDC. The diesel fuel used for all tests was of fossil origin with zero fatty acid methyl ester (FAME) content, cetane number of 53.2 and carbon to hydrogen mass ratio of 6.32:1. Compressed H₂ gas of purity 99.995% and compressed N₂ gas of purity 99.5% were obtained from a commercial gas supplier (BOC).

Table 7.1 shows the test conditions used for the combined EGR and intake air boost tests. For each engine load (IMEP) the amount of H₂ and diesel fuel, supplied to maintain a constant engine load, were varied to change the energy contribution of H₂ as a function of the total energy supplied to the engine. The measured volumetric flow rates of N₂ gas and intake air were used to calculate the amount of O₂ reduction (v/v) in the intake air due to the aspirated N₂ gas, while the pressure transducer and thermocouple mounted in the engine intake manifold monitored the intake boost pressure and temperature, respectively. It should also be noted here that when both H₂ and N₂ were being aspirated into the engine, the flowrates of both gases were adjusted so as to keep the reduction in intake O₂ constant. Table 7.1 also shows the corresponding engine power output for each load (IMEP); in

each instance this corresponds to the half-litre single cylinder engine used for all tests, and has not been scaled to represent an equivalent two litre, four cylinder engine. Table 7.2 shows the important properties of the diesel fuel and H₂ gas utilised in these experiments.

Intake air boost pressure (bar)	Intake temperature (°C)	Engine load (bar IMEP)	Indicated engine power (kW)	% points O ₂ reduction (v/v)
1.33	30	8.5	4.25	Only H ₂ (no N ₂)
				1
				2
				3
1.67	30	10	5.00	Only H ₂ (no N ₂)
				1
				2
				3
1.99	30	11.5	5.75	Only H ₂ (no N ₂)
				1
				2
				3

Table 7.1: Combined EGR and intake air boost test operating condition matrix showing different intake air boost/ engine load combinations (and corresponding power developed by the engine in kW) at various EGR ratios and engine speed 1200 rpm.

Property	Diesel fuel	Hydrogen
Density (kg/m ³)	831.9	0.0838
Lower heating value (MJ/kg)	43.14	120

Table 7.2: Properties of diesel fuel and hydrogen at 1 atm and 300 K (Karim 2003; Saravanan & Nagarajan 2008a)

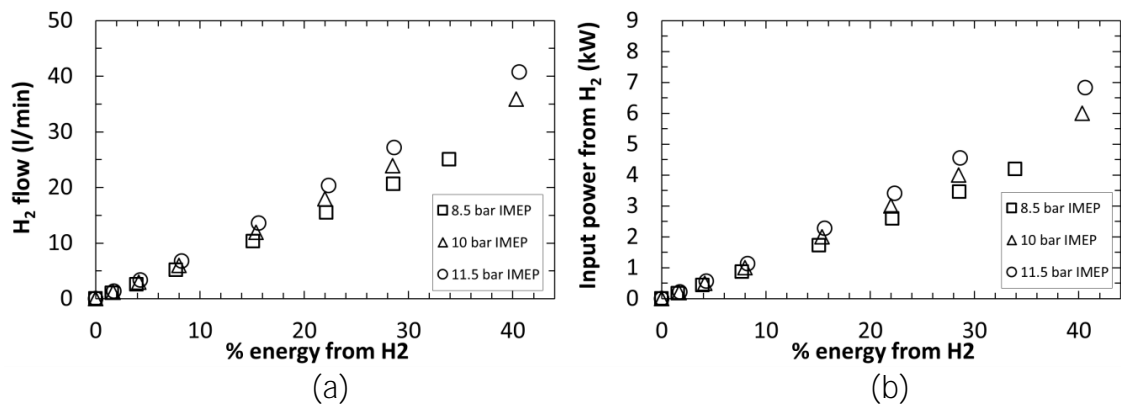


Figure 7.1: H₂ flow rates (l/min) and (b) power content of H₂ (kW) at constant engine loads and varying percentage energy from H₂

Figure 7.1 shows the energy supplied to the single-cylinder research engine from H₂ as a function of the total energy supplied to the engine (energy supplied from H₂ plus the energy supplied from diesel fuel); the corresponding H₂ flow rates and the power content of H₂ supplied to the engine are shown in Figure 7.1 (a) and (b), respectively.

Some preliminary tests were conducted to determine the combustion efficiency of H₂ through measurement of unburned H₂ levels in the exhaust. The level of H₂ in the exhaust was considered to be the H₂ remaining unburned during combustion, as diatomic hydrogen is unlikely to have formed from diesel hydrogen content. The

exhaust gas composition was analysed for H₂ at different engine loads using a gas chromatograph system with a thermal conductivity detector (GC-TCD), and measurements of the H₂ exhaust levels at varying loads corresponded to an average value of 10% of the H₂ supplied to the engine remaining unburned. This value is in good agreement with previous measurements under similar diesel fuel co-combustion operating conditions by Christodoulou & Megaritis (2013). In addition, a smaller amount of aspirated H₂ is expected to have been lost due to blow-by past the piston rings during the compression and early combustion stages.

The experiments presented in this chapter were repeated at a higher engine speed of 2200 rpm, which represents the average typical urban driving speed. Similar trends were observed for all the combustion and emission characteristics, across all the test conditions, as for the lower speed (1200 rpm) tests. Hence, to avoid repetition, the results conducted with an engine speed of 2200 rpm have not been included in this chapter.

Additionally, all exhaust emissions in the following 'Results and Discussion' section have been reported in g/kWh as reporting the results in terms of exhaust concentrations could be confusing due to the increase in exhaust flow rates when the intake air boost pressure is increased.

7.2 Results and Discussion

7.2.1 Combustion characteristics

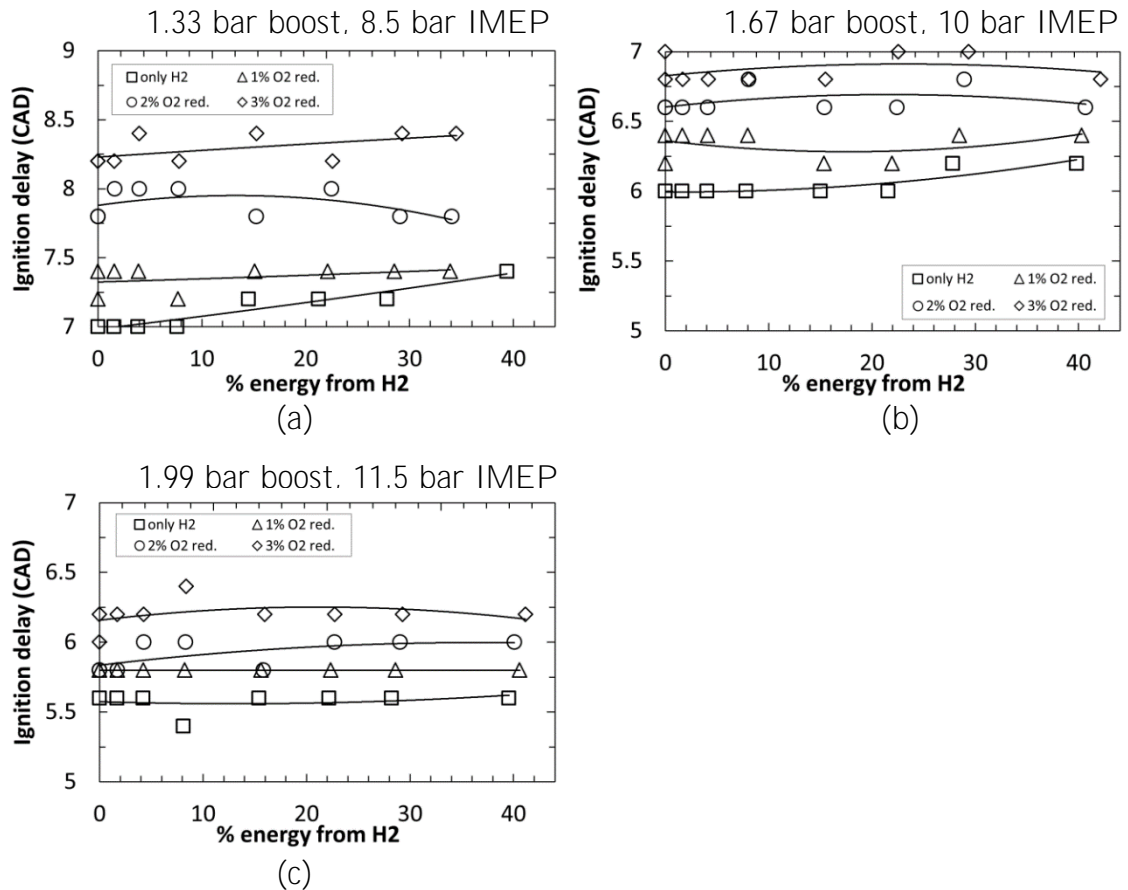


Figure 7.2: Duration of ignition delay for three intake air boost-engine load combinations, at constant percentage reductions in intake O₂ and varying percentage energy from H₂

Figure 7.2 shows the duration of ignition delay for three intake air boost pressure-engine load combinations, at constant percentage reductions in intake O₂ and varying percentage energy from H₂. The duration of ignition delay is defined as the time in crank angle degrees (CAD) between the start of the injection signal supplied to the diesel fuel injector (SOI) and the start of combustion (SOC) as indicated by the first incidence of positive heat release. Figure 7.2 shows that an increase in intake air pressure leads to a decrease in the duration of ignition delay. This is

likely to be the result of the increasing O_2 concentration accelerating the low temperature fuel oxidation rate during the ignition delay period. It can also be seen from Figure 7.2 that for each intake air pressure, increasing the percentage reduction in intake O_2 (that is, decreasing the amount aspirated O_2) increases the duration of ignition delay. As mentioned earlier this could be attributed to the displacement of intake air O_2 with the aspirated N_2 , which reduces the pool of reactive species available for combustion and thus the rates of low temperature diesel fuel breakdown and oxidation reactions, thus delaying SOC. Figure 7.2 also shows that the substitution of diesel fuel with H_2 has little or no effect on the duration of ignition delay. However, it must be noted that since the resolution of the engine crankshaft encoder is 0.2 CAD, any changes in the ignition delay duration within this range can be a result of equipment variability and resolution errors.

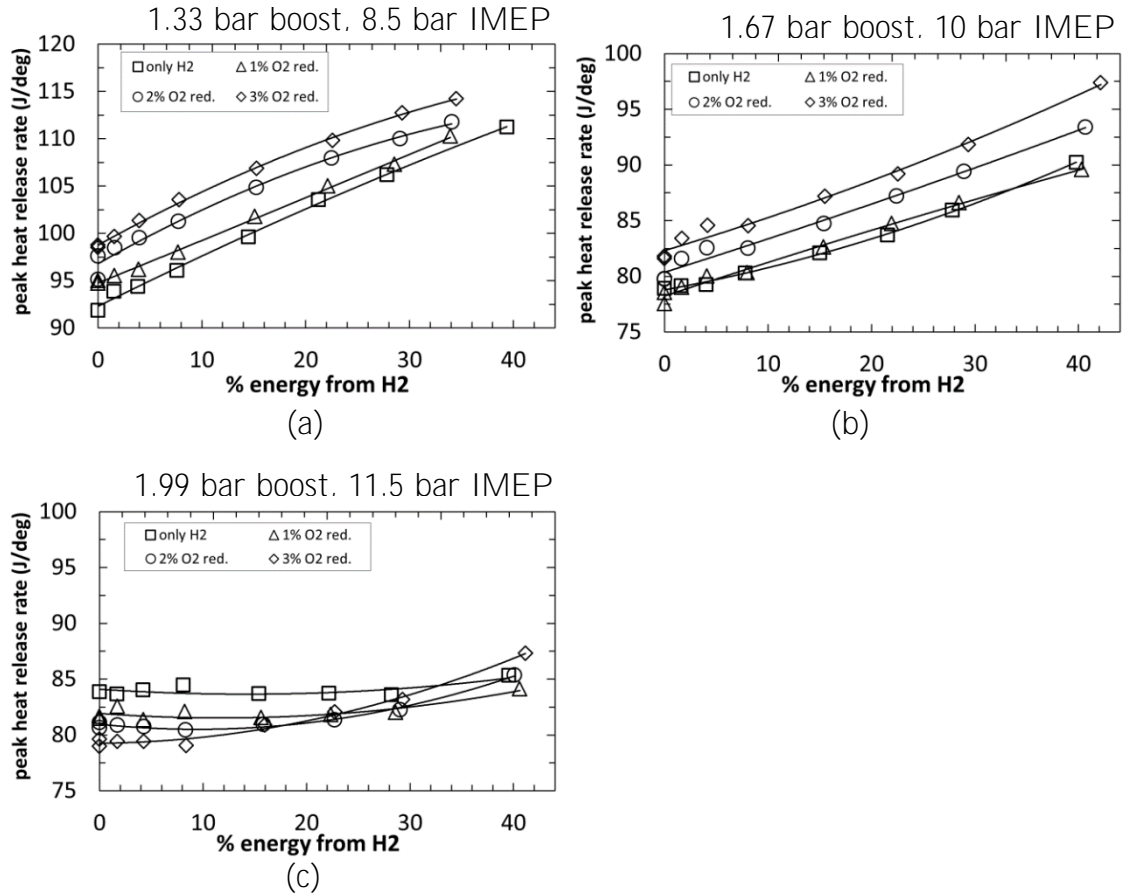


Figure 7.3: Peak heat release rates (J/deg) for three intake air boost-engine load combinations, at constant percentage reductions in intake O₂ and varying percentage energy from H₂

Figure 7.3 shows the apparent net peak heat release rates (pHRR) for three intake air boost pressure-engine load combinations, at constant percentage reductions in intake O₂ and varying percentage energy from H₂. It can be seen from Figure 7.3 that an increase in the intake air pressure leads to a reduction in the magnitude of pHRR; this can be attributed to an increase in the density of the intake air within the combustion chamber, with fuel heat release therefore resulting in lower in-cylinder gas temperatures. Figure 7.3 also shows that at 1.33 bar and 1.67 bar intake air pressures, increasing the percentage reduction in intake O₂ (that is,

decreasing the amount aspirated O_2) results in an increase in the magnitude of pHRR. This is due to an increase in the duration of ignition delay, as observed in Figure 7.2 (a) and (b), which allows more time for the fuel and air to mix, resulting in a greater amount of premixed diesel fuel-air mixture, of appropriate stoichiometry, available to undergo combustion at SOC. Similarly, Figure 7.3 (a) and (b) show an increase in the pHRR as the percentage energy from H_2 is increased. This is expected, as H_2 combusts in a premixed mode providing additional energy to that of the diesel fuel and, furthermore, H_2 burns at higher adiabatic flame temperatures compared to diesel fuel, leading to higher in-cylinder gas temperatures during combustion. However, Figure 7.3 (c) shows no significant effect of either percentage O_2 reduction or H_2 substitution (up to 30% energy from H_2) on the magnitude of pHRR. This can likely be attributed to two factors: Firstly, the change in the duration of ignition delay due to increasing EGR is relatively small. Secondly, the air flow rate at intake air pressure of 1.99 bar is quite high (approx. 980 l/min), which means that even at the highest percentage energy input from H_2 of 41%, the H_2 flow rate is relatively low (40 l/min) resulting in a very lean H_2 -air mixture inside the combustion chamber, and therefore lower flame temperatures during combustion.

7.2.2 Exhaust gas emissions

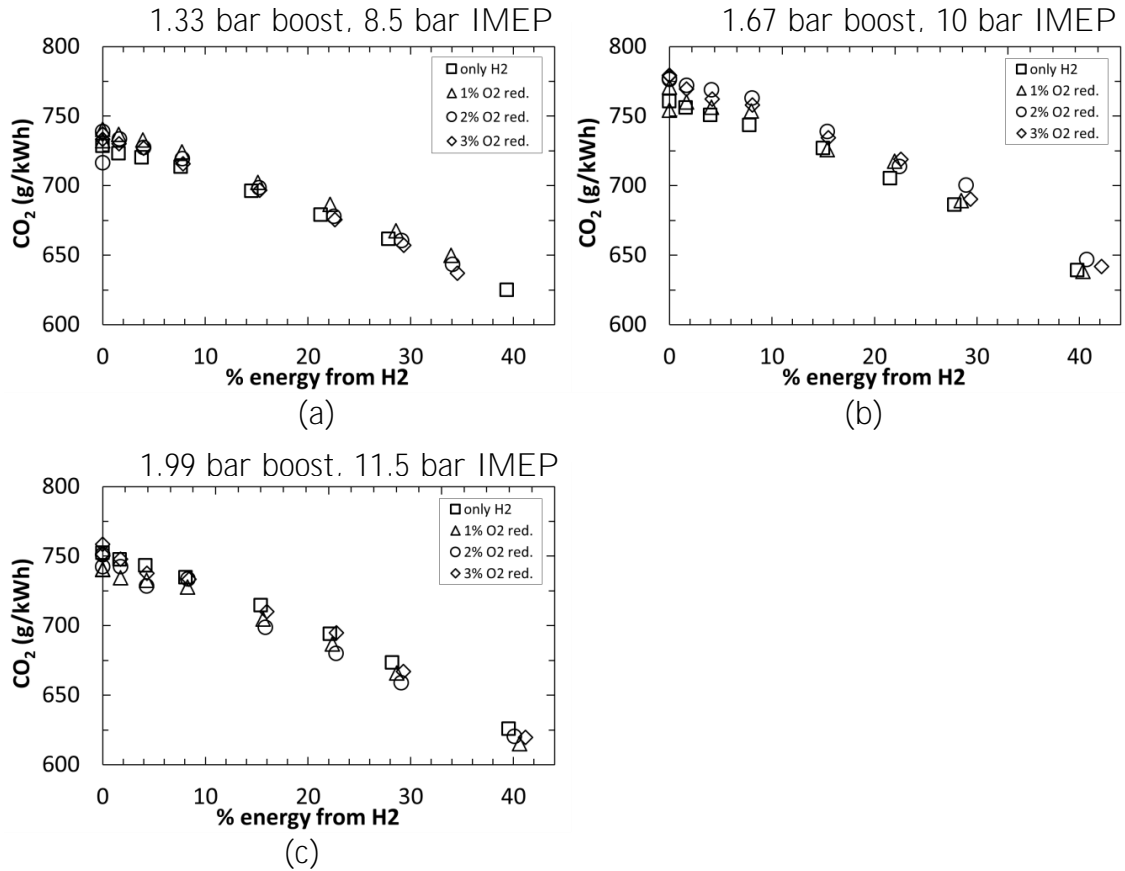


Figure 7.4: Specific emissions of carbon dioxide (CO_2) for three intake air boost-engine load combinations, at constant percentage reductions in intake O_2 and varying percentage energy from H_2

Figure 7.4 shows the specific exhaust gas emissions of carbon dioxide (CO_2) for three intake air boost pressure-engine load combinations, at constant percentage reductions in intake O_2 and varying percentage energy from H_2 . It can be seen from Figure 7.4 that at all three intake air pressure-load combinations, a decrease in the specific emissions of CO_2 is observed as diesel fuel is substituted by H_2 (increase in percentage energy from H_2). This is expected as carbon containing diesel fuel is replaced by H_2 which does not produce CO_2 as a combustion product. No significant effect of changing the intake O_2 concentration (% O_2 reduction) on CO_2 emissions

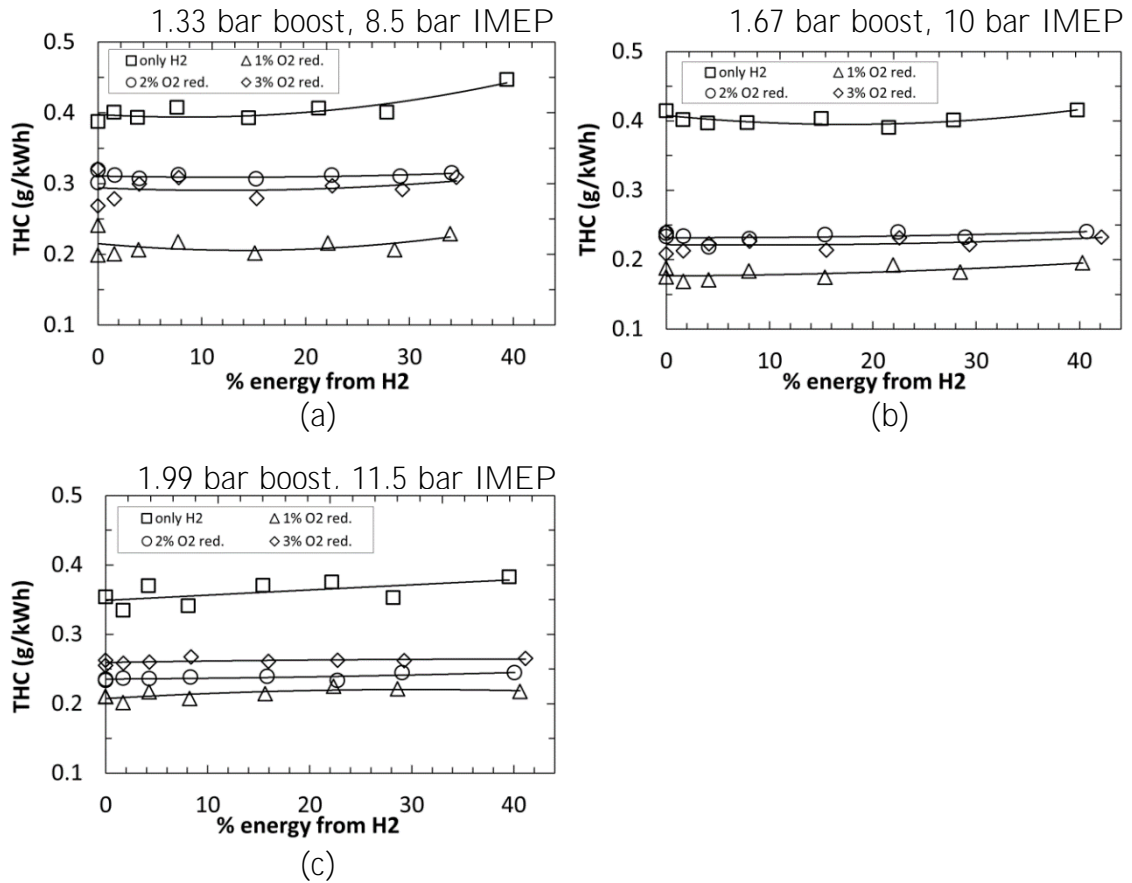


Figure 7.5: Specific emissions of unburned total hydrocarbons (THC) for three intake air boost-engine load combinations, at constant percentage reductions in intake O₂ and varying percentage energy from H₂

is observed except for a slight increase in CO₂ levels at 1.67 bar intake pressure (Figure 7.4 (b)), which corresponds to an increase in ignition delay observed in Figure 7.2 (b).

Figure 7.5 shows the specific exhaust gas emissions of unburned total hydrocarbons (THC) for three intake air boost pressure-engine load combinations, at constant percentage reductions in intake O₂ and varying percentage energy from H₂. It can be seen from Figure 7.5 that at all three intake air boost pressure-engine load combinations, decreasing the intake O₂ concentration (or increasing the % O₂ reduction) up to 1% point results in a decrease in THC emissions, with any further

decrease in intake O_2 leading to an increase in THC emissions. The initial decrease in THC emissions may be a result of the increase in the duration of ignition delay (as observed in Figure 7.2), allowing more time for diesel fuel and air to mix prior to SOC. Further reduction in intake O_2 concentration above 1% (intake O_2 reduction) may severely affect the availability of O_2 for diesel fuel oxidation, prevailing over the influence of increased ignition delay on combustion phasing, and leading to increased THC emissions. Figure 7.5 does not show an apparent effect of displacement of diesel fuel by H_2 on THC emissions. This might be because, at such relatively high engine loads of 8.5 bar IMEP and above, a substantial quantity of diesel fuel (diesel fuel flow rate ≈ 18 ml/min) is being injected in the combustion chamber and the displacement of some of this diesel fuel by H_2 is not sufficient to have a significant effect on unburned THC exhaust emissions.

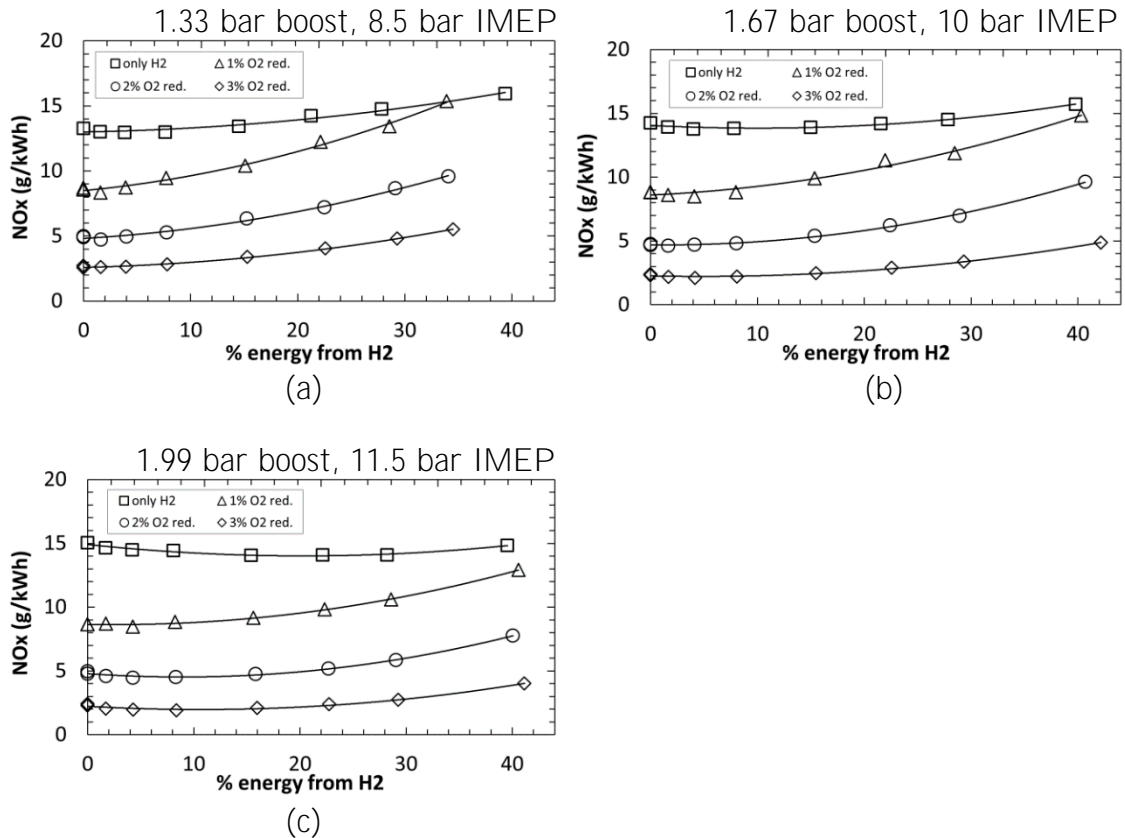


Figure 7.6: Specific emissions of oxides of nitrogen (NO_x) for three intake air boost-engine load combinations, at constant percentage reductions in intake O_2 and varying percentage energy from H_2

Figure 7.6 shows the specific exhaust gas emissions of oxides of nitrogen (NO_x) for three intake air boost pressure-engine load combinations, at constant percentage reductions in intake O_2 and varying percentage energy from H_2 . The effect of reducing intake O_2 on exhaust NO_x emissions is very apparent from Figure 7.6, for example, at 1.67 bar intake air pressure and 8% energy from H_2 , a 67% decrease in NO_x emissions is observed when intake O_2 level is reduced by 1%. This is expected, as the aspirated N_2 displaces the intake O_2 required for fuel oxidation (which reduces local flame temperatures) and for thermal oxidation of N_2 to form NO_x , thus reducing rates of reducing NO_x formation.

A slight decrease in NO_x emissions is observed at low levels of H_2 substitution (< 5% energy from H_2) at all three intake air boost pressures in Figure 7.6. However, any further displacement of diesel fuel results in an increase in exhaust NO_x levels (Figure 7.6). This can be explained by the following: Diesel fuel injected into the combustion chamber of the diesel engine used in this study can always be expected to produce significant quantities of NO_x , because combustion of the spray takes place around the spray fringe where the diesel fuel-air equivalence ratio is at an approximately stoichiometric value. As diesel fuel is progressively removed and replaced by H_2 , this high rate of NO_x production from diesel fuel is curtailed. At the same time, NO_x production from H_2 is not significant, because at such low levels of the H_2 substitution, the H_2 -air equivalence ratio is still not sufficiently high for commensurate NO_x production (or production at the same levels produced by the diesel fuel for which the H_2 had been substituted). Hence a small drop in exhaust NO_x emissions is observed. As the amount of H_2 is increased, it appears that H_2 enhances the production of NO_x by further raising the temperatures in the diesel fuel spray combustion zones. Therefore it seems that the H_2 provides, locally, additional synergetic heat release and temperature rise, resulting in extra NO_x formation, above NO_x emission levels due to diesel fuel alone at a constant EGR level.

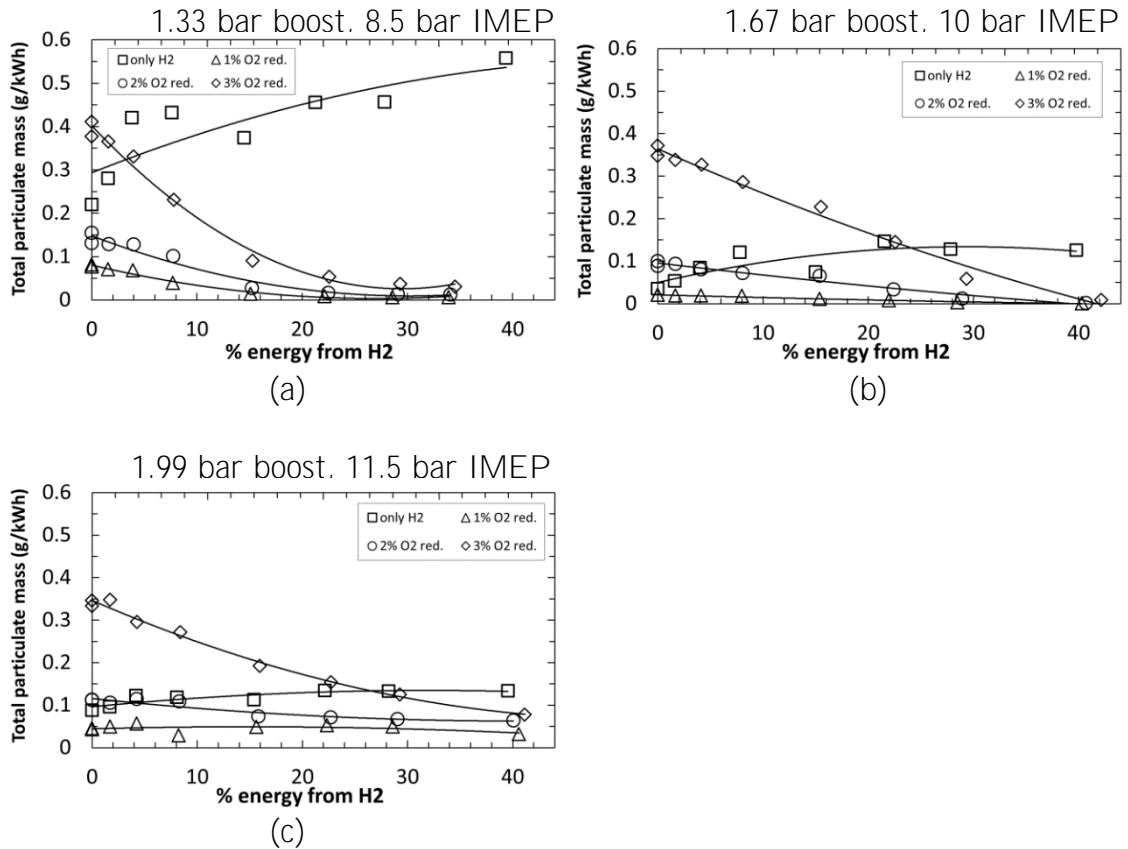


Figure 7.7: Specific emissions of total particulate mass for three intake air boost-engine load combinations, at constant percentage reductions in intake O₂ and varying percentage energy from H₂

Figure 7.7 shows the specific exhaust gas emissions of total particulate mass (TPM) for three intake air boost pressure-engine load combinations, at constant percentage reductions in intake O₂ and varying percentage energy from H₂. It can be seen from Figure 7.7 that at 0% energy from H₂ (that is, with only diesel fuel and no H₂ substitution), a substantial increase in exhaust TPM levels is seen when the intake O₂ concentration is decreased above the 1% level. This is a similar trend to that observed for exhaust THC emissions (Figure 7.5), and is due to the reduction in O₂ availability as a result of displacement of intake air by N₂, resulting in reduced oxidation of soot precursors in the diesel fuel spray and soot particles already

formed. The decrease in TPM levels as the percentage energy from H₂ is increased is a result of replacing diesel fuel with a zero-carbon fuel (H₂). The decrease in TPM levels is most apparent for the highest level of percentage O₂ reduction of 3% at all three intake air boost pressure-engine load combinations, for example at 1.99 bar intake air pressure and 3% intake O₂ reduction, a 50% drop in TPM level is observed at 15% energy from H₂. Significant decreases in TPM levels of similar magnitude also occur at other percentage O₂ reduction levels, for example, at 1.33 bar intake air pressure and 2% intake O₂ reduction, a 75% drop in TPM level is observed at 15% energy from H₂.

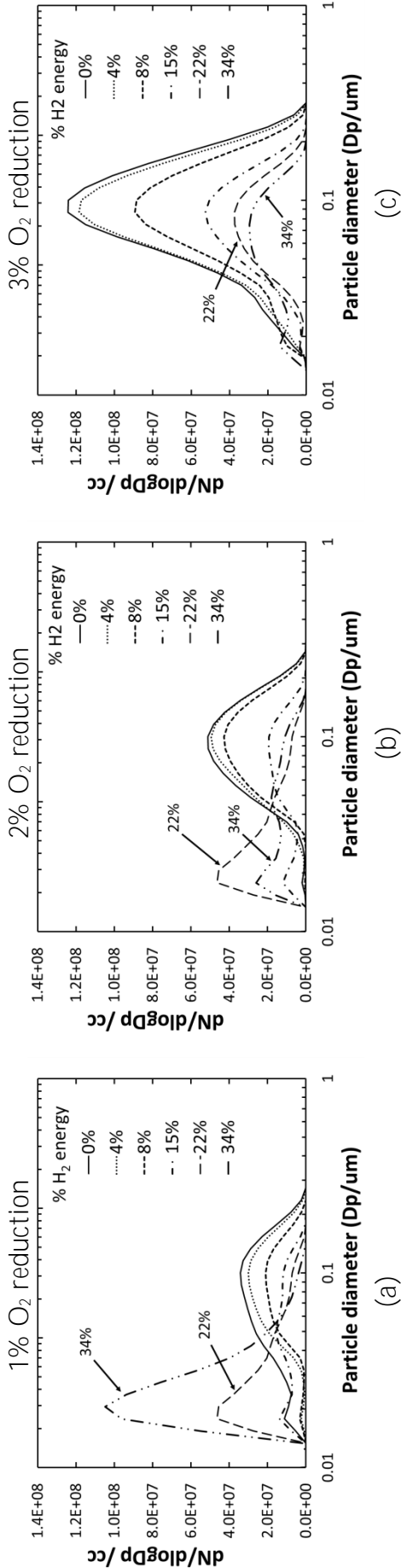


Figure 7.8: Particulate number distribution for 1.33 bar intake air pressure – 8.5 bar IMEP engine load, at various percentage reduction in intake O_2 and varying percentage energy from H_2 .

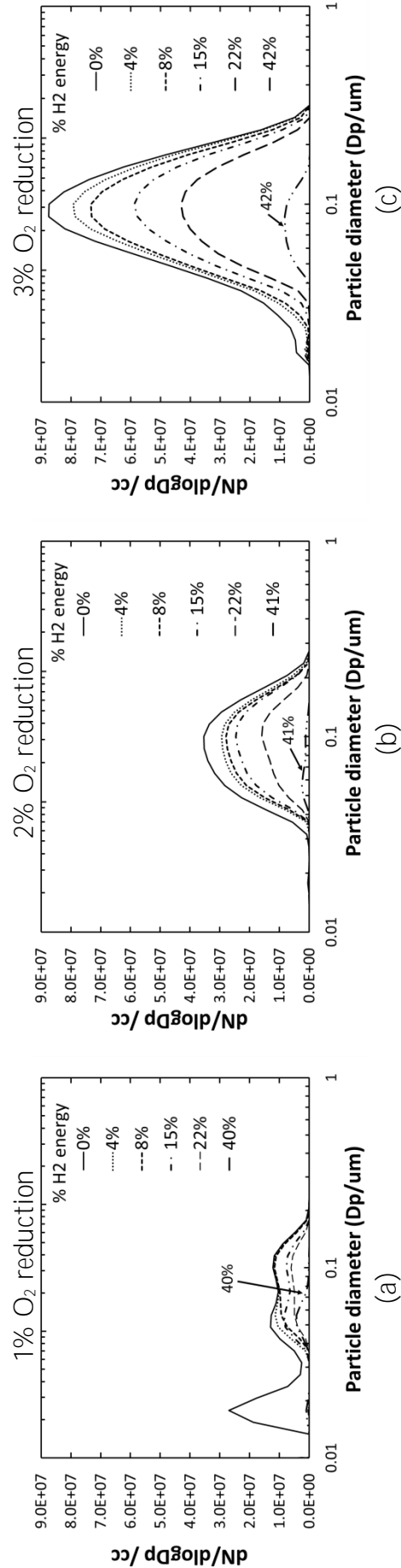


Figure 7.9: Particulate number distribution for 1.67 bar intake air pressure – 10 bar IMEP engine load, at various percentage reduction in intake O_2 and varying percentage energy from H_2 .

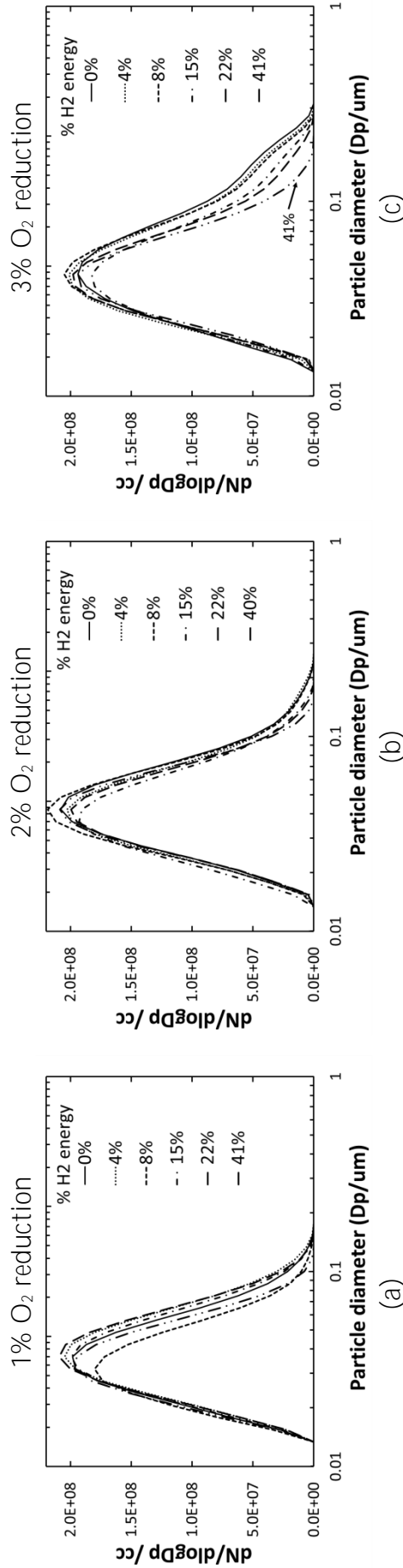


Figure 7.10: Particulate number distribution for 1.99 bar intake air pressure – 11.5 bar IMEP engine load, at various percentage reduction in intake O₂ and varying percentage energy from H₂.

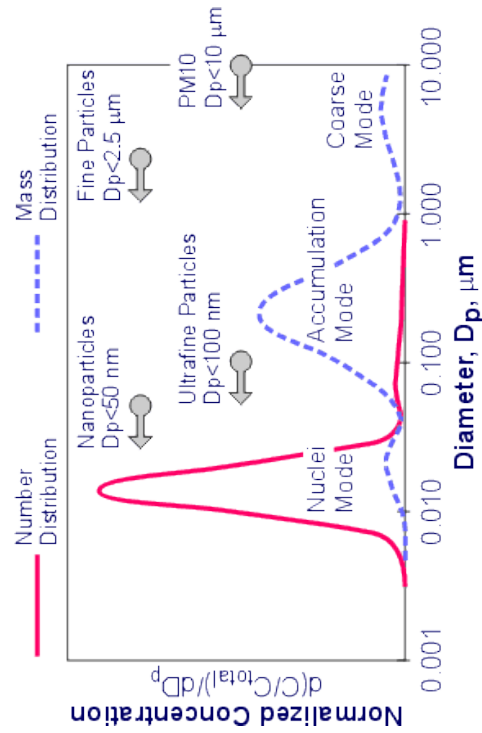


Figure 7.11: Typical size distribution of diesel exhaust particulates (Kittelson et al. 2002)

Figure 7.8, Figure 7.9 and Figure 7.10 show the size distribution of the number of particulates in the engine exhaust gas from tests conducted in this study for three intake air pressure-engine load combinations, respectively, with various percentage reduction in intake O_2 and varying percentage energy from H_2 . Figure 7.11 shows a typical size distribution of diesel engine exhaust particles, both in terms of number of particles and total mass of particles, where particles have been divided into categories based on their diameters. It can be seen from Figure 7.11 that almost all diesel engine particulates have diameters significantly lower than $1 \mu m$ and represent a mix of fine ($D_p < 2.5 \mu m$, PM2.5), ultrafine ($D_p < 0.1 \mu m$) and nanoparticles.

First, considering the effect of decreasing the amount of intake O_2 on the size distribution of the number of particulates, it can be seen from both Figure 7.8 and Figure 7.9 that as the percentage O_2 reduction level is increased, the number of particles tends to increase significantly across the entire range of diameters (0.05 - $0.2 \mu m$). As discussed previously, this increase in the number of particles is due to the increasingly severe unavailability of O_2 (as it is displaced by the aspirated N_2) for diesel fuel combustion, which results in reduced rates of soot oxidation. The effect of decreasing the amount of intake O_2 on the particle distribution is not as evident at the highest intake boost-engine load combination (1.99 bar boost- 11.5 bar IMEP, Figure 7.10), apart from an increase in the number of particles of

diameters ranging between 0.1 μm and 0.2 μm at the 3% O_2 reduction level. Since these particles are on the large end of the particle size spectrum, they account for most the total particulate mass despite being fewer in number. This is the reason for the significant increase in total particulate mass emission observed in Figure 7.7 (c) when the O_2 reduction level is increased to 3%.

Now, considering the effect of H_2 , it can be observed from Figure 7.8 and Figure 7.9, at each percentage O_2 reduction level, that the number of particles (of diameters between 0.05 μm and 0.2 μm) reduces as the percentage energy from H_2 is increased. The reduction primarily occurs for particles of diameters ranging between 0.05 μm and 0.2 μm , which (as can be seen from Figure 7.11), lie in the fine and ultrafine particle size range. The fine and ultrafine particles pose a serious health risk, as they can penetrate deeper into the lungs (as compared to particles in the PM_{10} size range) resulting in an increased risk of lung cancer, and cardiovascular and breathing disorders (Raaschou-Nielsen et al. 2013). Hence, a reduction in the fine and ultrafine particles due to H_2 substitution can potentially be quite beneficial in terms of the health hazards associated with particulates. As the percentage energy from H_2 is increased above 22% in Figure 7.8 (a), a significant increase in particulates of diameter less than 0.02 μm is observed.

At the highest intake boost-engine load combination (1.99 bar boost-11.5 bar IMEP, Figure 7.10), the effect of H_2 is not very distinct except at the 3% O_2 reduction level (Figure 7.10 (c)), where H_2 substitution results in the reduction of particles

with diameters above 0.1 μm . As discussed before, since these large particles make up the majority of the total particulate mass, any reduction in these large particles results in a significant reduction in the total particulate mass (Figure 7.7).

7.2.3 Optimum H₂ operating window based on exhaust gas emissions results

Figure 7.12 shows the specific emissions of NO_x and particulate mass for three intake air boost pressure-engine load combinations, at a constant 1% intake O₂ reduction level and varying percentage energy from H₂. The 1% intake O₂ reduction level was chosen as any further reductions in the intake O₂ concentration result in an increase in exhaust unburned hydrocarbon emissions, which is undesirable. It can be observed from Figure 7.12 that NO_x exhaust emissions increase when the percentage energy from H₂ increases above 10%, however, below the 10% H₂ level NO_x emissions remain stable. Therefore, based on Figure 7.12, it can be suggested that the use of H₂ would be favourable below a level of about 10% energy from H₂ (as shown by the shaded blue region on Figure 7.12), where there is no increase in NO_x emissions. Additionally, the greatest particulate reduction benefit is obtained for the lowest intake air boost pressure-engine load combination (1.33 bar boost, 8.5 bar IMEP), where a 50% reduction in the specific emissions of total particulate mass can be observed at the 10% H₂ energy contribution level (Figure 7.12). Similarly, the blue shaded region in Figure 7.13 shows the benefit of H₂ in terms of CO₂ reduction whereby significant reductions in CO₂ can be obtained without an

increase in NO_x emissions, and this benefit occurs below the 10% H₂ energy contribution level.

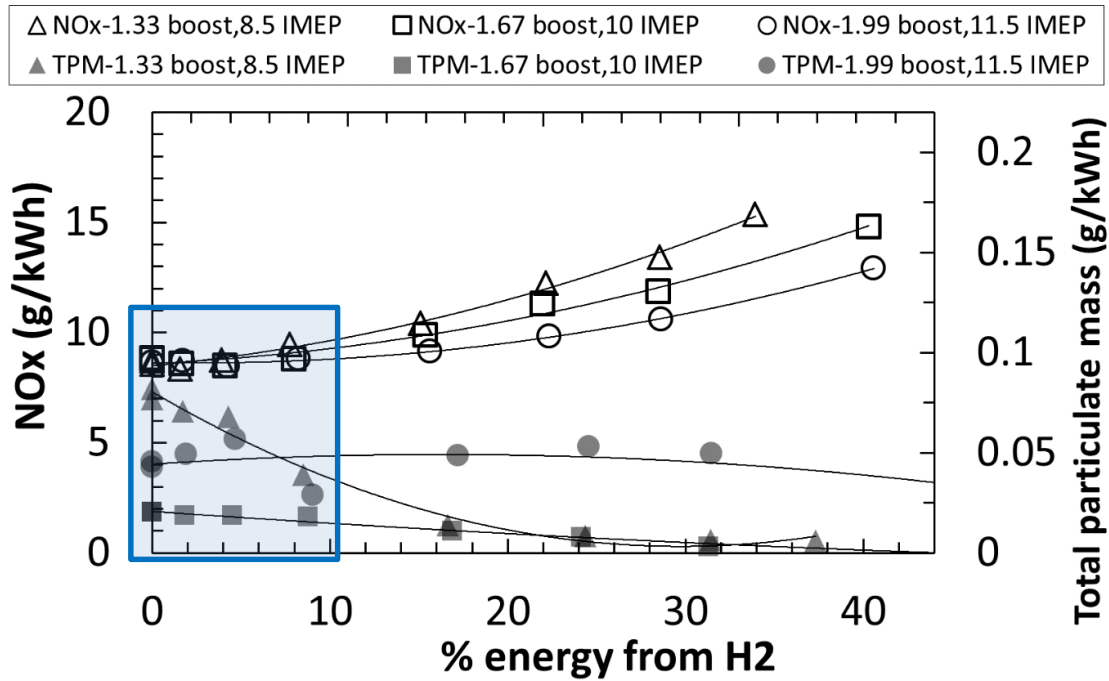


Figure 7.12: Specific emissions of NO_x and total particulate mass (TPM) for constant intake air pressure - engine load combinations and varying % energy from H₂, at an intake O₂ reduction level of 1%.

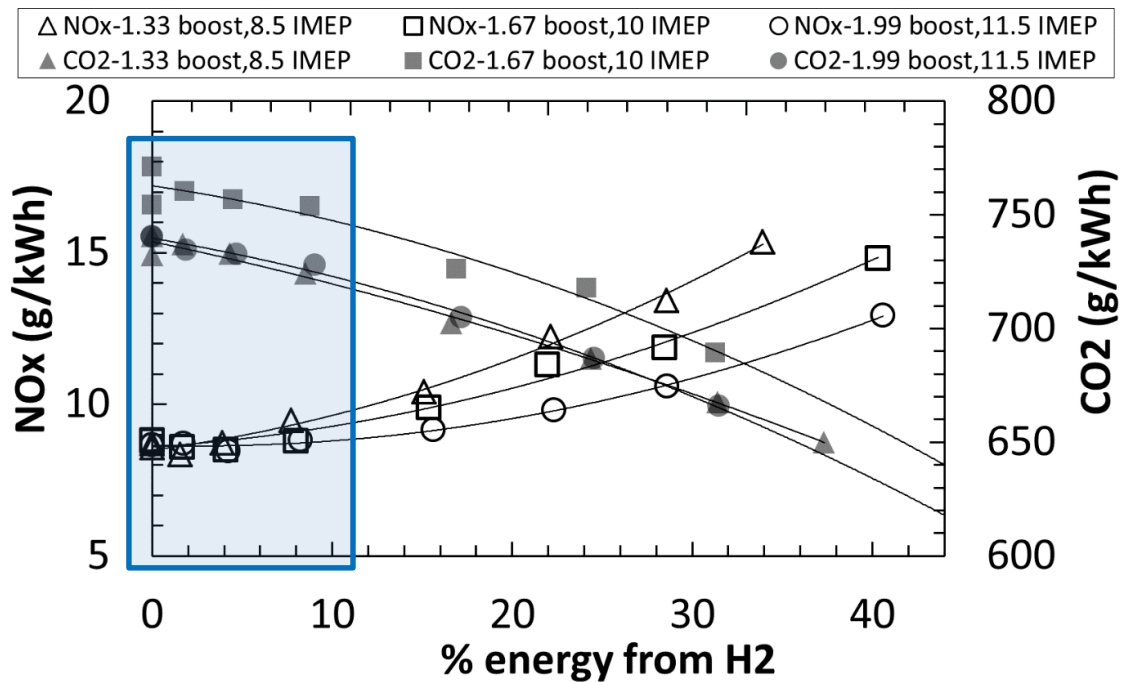


Figure 7.13: Specific emissions of NO_x and CO₂ for constant intake air pressure - engine load combinations and varying % energy from H₂, at an intake O₂ reduction level of 1%.

7.3 Conclusions

- Decreasing the amount of intake O_2 (simulating increasing EGR) being supplied to the engine, increased the duration of ignition delay due to displacement of O_2 by the aspirated N_2 . No significant influence of H_2 on the ignition delay was observed.
- An increase in peak heat release rates was observed as the percentage energy being supplied to the engine from H_2 was increased. This was attributed to the extra heat release during H_2 premixed combustion and higher adiabatic flame temperatures of H_2 relative to diesel fuel.
- The specific emissions of CO_2 reduced with increasing percentage energy from H_2 , due to displacement of carbon containing diesel fuel with H_2 .
- Decreasing intake O_2 concentration above the 1% level resulted in an increase in the unburned hydrocarbon emissions due to O_2 unavailability for diesel fuel oxidation. No influence of H_2 on unburned hydrocarbon emissions was observed.
- Specific emissions of NO_x were observed to increase but only when the energy contribution from H_2 was increased above the 10% level. This increase in NO_x emissions was attributed to H_2 -diesel co-combustion resulting in higher in-cylinder temperatures relative to diesel fuel-only combustion.
- Significant reductions in the total particulate mass were observed with increasing percentage energy from H_2 especially at high percentage O_2

reduction levels. For example, at the 1.33 bar intake air pressure – 8.5 bar IMEP engine load combination, and 2% intake O₂ reduction, a 75% drop in TPM level is observed at 15% energy from H₂.

- A reduction in the number of particles of diameter between 0.05-0.2 μm (in the range of fine and ultrafine particles) was observed with increasing percentage energy from H₂, specifically at the low and mid- intake air boost levels.
- Based on the exhaust emission results, it was suggested that H₂ can have a favourable effect of reducing CO₂ and particulate emissions with no increase in NO_x emissions when the energy contribution from H₂ is below the 10% level, at an EGR equivalent of 1% reduction in intake O₂ concentration for all the intake air boost pressures - engine loads combinations tested in this study.

8 Conclusions and recommendations for future work

The main conclusions of the previous chapters are brought together in the following sections, followed by a global summary of the most important findings of the work conducted in this study. Claims as to the originality of this work are stated and recommendations for future work made.

8.1 Conclusions and summary

8.1.1 Literature review

The following conclusions can be drawn from the review on technical literature presented in Chapter 2:

- Hydrogen (H_2) as a fuel does not produce carbon pollutants from combustion, has a wide flammability limit, high flame speeds and adiabatic flame temperatures, but can suffer from anomalies such as knock and backfiring. A review of literature suggests that the co-combustion of H_2 with diesel fuel has

a varying effect on NO_x emissions. Methane (CH₄) has a narrow flammability limit, low flame propagation velocity, high ignition energy requirement, but excellent anti-knock properties. The use of CH₄-H₂ mixtures in IC engines was identified by various past researchers as having the potential to yield beneficial effects due to the complimentary properties of both the fuel gases.

- A wide variety of timed in-cylinder gas sampling valves have been used by previous investigators in both SI and CI engines to extract and analyse the constituents of in-cylinder gas at various instants of the combustion cycle. The in-cylinder sampling systems have been used in conjunction with gas analysers, electron microscopy and chromatographic techniques, with the in-cylinder gas sample typically collected in a collection bag.

8.1.2 Co-combustion of hydrogen and diesel fuel

From the experimental investigation of H₂-diesel fuel co-combustion carried out on a naturally aspirated diesel engine (Chapter 4), the following conclusions can be drawn:

- NO_x emissions (both exhaust and in-cylinder) were observed to increase very rapidly with the addition of H₂ but only when the combined temperatures resulting from H₂-diesel fuel co-combustion exceeded the threshold temperature for rapid NO_x formation.
- At low engine loads (below 4 bar IMEP), the addition of H₂ promoted soot burnout due to elevated temperatures and higher oxidation rates; at

intermediate engine loads (between 4 and 6 bar IMEP), the effects of soot formation and oxidation counterbalanced each other; and at high engine loads (6 bar IMEP and above), the excessive displacement of intake O_2 by H_2 led to slightly increased rates of soot formation.

- From in-cylinder gas sampling results it was observed that at early stages of combustion (10 CAD ATDC), NO_x concentrations within the diesel fuel spray were lower than those measured in between two individual fuel sprays. This could be attributed to a higher concentration of H_2 -air mixture burning in between the sprays, combined with the combustion of significant amounts of diesel fuel vapour occurring between the sprays. This is expected to have resulted in high temperatures in the region between the sprays and, therefore, higher NO_x formation rates in comparison to the NO_x formation rates within the spray, where a deficiency of the H_2 -air mixture existed.

The following points can be summarised from the study carried out on H_2 -diesel fuel co-combustion in a diesel engine with EGR (simulated by aspirating N_2 and reducing intake O_2) and intake air boost:

- Based on the exhaust emission results, it was proposed that H_2 can have a favourable effect of considerable reductions in CO_2 and particulate emissions with no increase in NO_x emissions when the energy contribution from H_2 is below the 10% level, at an EGR equivalent of 1% reduction in intake O_2

concentration for all the intake air boost pressures - engine load combinations tested in this study.

- A reduction in the number of exhaust particles of diameter between 0.05-0.2 μm (in the range of fine and ultrafine particles) was observed with increasing percentage energy from H_2 , specifically at the low (1.33 bar) and intermediate (1.67 bar) intake air boost levels.

8.1.3 Co-combustion of $\text{CH}_4\text{-H}_2$ mixtures with diesel fuel

Regarding the effect of burning $\text{CH}_4\text{-H}_2$ mixtures (of various proportions) in a diesel engine, the following observation can be made:

- At all the engine loads tested, exhaust CO_2 emissions when burning $\text{CH}_4\text{-H}_2$ mixtures were considerably lower as compared to CO_2 emissions with diesel fuel only operation, attributable to the lower carbon to hydrogen ratio of CH_4 compared to diesel fuel. For all the $\text{CH}_4\text{-H}_2$ mixtures, a sharp increase in exhaust NO_x emissions was observed with increasing engine load but only when the in-cylinder gas temperatures exceeded the threshold for NO_x formation temperatures. Significant reductions in exhaust PM emissions were observed when diesel fuel was replaced by $\text{CH}_4\text{-H}_2$ mixtures, however, lower magnitudes of PM reductions were observed at higher loads (above 5 bar IMEP), due to excessive displacement of intake O_2 by the aspirated $\text{CH}_4\text{-H}_2$ mixture.

- From in-cylinder gas sampling, in the case of H₂-diesel fuel co-combustion, PM levels were higher in the diesel fuel spray as compared to between two sprays, most probably due to higher pyrolysis rates in the oxygen-lacking, fuel-rich core of the diesel fuel spray, and greater availability of air (and hence O₂) in the region between sprays for oxidation of soot precursors. Conversely, in the case of CH₄-diesel fuel co-combustion, PM levels were significantly higher between the two diesel fuel sprays relative to within the fuel spray. This was attributed to CH₄ contributing significant quantities of particulates (unlike H₂) to the total PM concentration produced from the CH₄-diesel fuel mixture in between two sprays aided by higher temperatures in this region.
- The in-cylinder gas composition results obtained from CH₄-H₂ mixtures were consistent with previous in-cylinder studies conducted by the author using only H₂ or CH₄. Higher NO_x levels were observed when the H₂ was present in a higher proportion in the aspirated CH₄-H₂ mixture. Comparing the NO_x levels obtained with the two sampling arrangements, the NO_x concentration was higher in the region between the sprays as compared to within the spray core, attributable to higher gas temperatures occurring in the region between the sprays.

8.1.4 Co-combustion of CH₄-CO₂-H₂ mixtures (simulating H₂ enriched biogas) with diesel fuel

The following main conclusions are presented from the work conducted on combusting CH₄-CO₂-H₂ mixtures (in various proportions) in a diesel engine:

- The thermal energy absorbing effect of the inert CO₂ was evident in the slower increase of heat release, longer ignition delay periods and lower peak heat release rate when using CH₄-CO₂-H₂ mixtures, as compared to diesel fuel only combustion.
- Exhaust CO₂ emissions were observed to be higher for the 60CH₄:40CO₂ mixture as compared to diesel only combustion (and 80CH₄:20CO₂ mixture), indicating the desirability to scrub the biogas post-production to decrease its CO₂ content. In-line with previous results, exhaust NO_x emissions were seen to increase sharply when the in-cylinder temperatures went above NO_x formation levels. Exhaust PM emissions for the 60CH₄:40CO₂ mixture were observed to be considerably greater as compared to both 80CH₄:20CO₂ mixture and diesel only condition. The inclusion of H₂ to 60CH₄:40CO₂ mixture significantly reduced PM emissions, speculated to be due to higher post-combustion gas temperatures.
- In-cylinder NO_x levels were observed to be significantly higher in the region between two sprays for the 60CH₄:40CO₂ + 15% H₂ mixture, as compared to the 60CH₄:40CO₂ mixture. This was attributed to the temperatures resulting

from the combined CH₄-H₂-air mixture combustion being higher than those achieved by CH₄-air combustion, resulting in higher NO_x formation rates.

8.1.5 Summary of conclusions

- A novel in-cylinder gas sampling system was developed which allowed gas samples to be collected from within the combustion chamber of an engine at any selected crank angle in the engine cycle.
- The H₂-diesel fuel co-combustion tests in a naturally aspirated engine provided some useful insights into the effect of H₂ as a thermal energy source providing additional energy and increasing in-cylinder gas temperatures.
- For the H₂-diesel fuel co-combustion tests conducted with intake air boost and simulated EGR, an optimum H₂ operating window was identified where the addition of H₂ had a beneficial effect on exhaust emissions.
- The addition of H₂ to either CH₄ or biogas (CH₄-CO₂) mixtures was seen to reduce ignition delay periods, increase peak heat release rates and reduce PM emissions (beyond simple carbon displacement) due to the higher post-combustion gas temperatures.

The following paragraphs provide a global summary of the conclusions of the thesis, comparing the exhaust emission and in-cylinder gas composition results obtained throughout the course of the project.

Exhaust NO_x emissions are observed to be primarily dependent on the temperature of the post combustion in-cylinder gases and secondarily on the intake O₂

concentration, which concurs with the thermal (Zeldovich) reaction mechanism (Miller & Bowman 1989). Below certain engine loads exhaust NO_x emissions are seen to be quite minimal, which is attributed to the in-cylinder fuel gas-air mixture (with the fuel gas being H_2 and/or CH_4) being far too lean for NO_x to form, with the resulting fuel gas combustion temperatures remaining below the threshold of NO_x formation temperatures (~ 1800 K). The minimal amount of NO_x being produced at these low engine loads can be ascribed to the combustion of the small amount of pilot diesel fuel being injected in the chamber (to ignite the fuel gas), as spray combustion always takes place where the diesel fuel-air equivalence ratio is at near-stoichiometric. As the amount of aspirated fuel gas is increased to increase the engine load (IMEP), the in-cylinder fuel gas concentration in the intake air becomes sufficient for the post combustion in-cylinder gas temperatures to reach a level at which the kinetically controlled NO_x formation rates accelerate significantly, resulting in substantial exhaust emissions of NO_x .

The exhaust PM emissions were observed to be dependent on the two competing factors of soot formation and soot oxidation. The aspiration of fuel gas reduced the intake O_2 concentration resulting in increased pyrolysis (fuel breakdown) rates. On the other hand, the high temperatures resulting from the combustion of the fuel gas led to a counteracting increase in thermal soot oxidation rates. Taking the case of H_2 -diesel fuel co-combustion as an example, it was observed that for engine loads below 4 bar IMEP, H_2 had a beneficial effect on PM reduction beyond simple carbon

fuel displacement (as H_2 was replaced by diesel fuel), which could be attributed to soot oxidation rates prevailing over the competing soot formation rates. At the maximum tested load of 6 bar IMEP, the reduction in PM emissions as a result of H_2 were considerably smaller than that could be expected from the reduction in injected carbon (via diesel fuel) to the engine. It was speculated that this was due to substantial displacement of intake air by the aspirated H_2 , resulting in severe O_2 unavailability for diesel fuel combustion.

A reduction in particulates which lie in the fine and ultrafine particle size range (between $0.05\ \mu\text{m}$ and $0.2\ \mu\text{m}$) was observed with increasing percentage energy contribution by H_2 . A reduction of particulates in this size range is quite beneficial since these particulates pose a serious health risk. They can penetrate deeper into the air passages of the lungs (relative to large particulates) causing an increased risk of lung cancer, and cardiovascular and breathing disorders.

Considering the NO_x concentration in the collected in-cylinder gas samples when co-combusting fuel gases with diesel fuel, it was generally observed that during the initial stages of combustion, that is, at 10 CAD ATDC, NO_x concentration in the region between the sprays was higher as compared to that within the spray core. Auto-ignition is first expected to occur at the near-stoichiometric diesel fuel-air pockets which, at 10 CAD ATDC, are more likely to occur in the region between two sprays, where there is a higher concentration of the fuel gas-air mixture. The gas temperatures resulting from the rapid burning of both premixed diesel fuel and

fuel gas-air mixture are expected to be higher than those required for thermal NO_x formation, resulting in considerable NO_x levels in the region between two sprays. On the other hand, at 10 CAD ATDC, the spray core is yet to break up by air entrainment (hence, combustion temperatures are low), and some of the energy released in this fuel rich region can be expected to be absorbed for fuel pyrolysis. Beyond 10 CAD ATDC, as the expansion stroke progresses, the effects of air swirl and reverse squish flow promote the redistribution of in-cylinder gaseous composition, leading towards homogenous conditions across the cylinder.

8.2 Claims of originality

In the work done by previous investigators on engine in-cylinder sampling, the in-cylinder gas sample was collected in a bag, requiring a significant volume of sample to be collected (approx. 10 litres) so as to achieve steady readings from typical gas analysers. Since the volume of sample extracted from the cylinder every engine cycle is relatively small (approx. 4-6 cm³) (Zhao & Ladommatos 2001), filling a bag with sufficient volume can take considerable time. Furthermore, in the time interval between filling up a bag and analysing the collected gas sample, the sample cools down to room temperature, causing condensation of high boiling point species in the sample. The novel in-cylinder sampling system conceptualised and developed for this work is believed to make the extraction and analysis of engine in-cylinder gas samples considerably more efficient and accurate by drastically reducing the duration between collecting the sample from the engine cylinder and analysing it.

The sampling system was used to study the in-cylinder gas composition, and its effect on the pollutant exhaust emissions, when burning a variety of gaseous fuels (including H_2 , CH_4 , CH_4-H_2 and $CH_4-CO_2-H_2$ mixtures), something which had not been undertaken previously. Through this work, a few new insights into the development of engine in-cylinder species during the combustion process were gained by the author. During the early stages of combustion, an appreciable contrast was observed in the concentration of pollutant species between the two sampling locations considered (between the sprays and within the spray core), while in the later stages of engine cycle, the distinction in species concentration (between the two locations) was considerably less. Furthermore, the combustion of H_2 was observed to primarily have a thermal effect of adding energy to the on-going in-cylinder combustion reactions, rather than a chemical synergetic effect between the H_2 and the diesel fuel. The results obtained from this work will not only complement optical analysis undertaken using in-cylinder laser diagnostic techniques, but also contribute towards the validation of in-cylinder kinetic models based on computational modelling.

To date, this work has resulted in the publication of one peer-reviewed journal paper:

- Talibi et al., “*Effect of hydrogen-diesel fuel co-combustion on exhaust emissions with verification using an in-cylinder gas sampling technique*”, International Journal of Hydrogen Energy, Volume 39, Issue 27, 12 September 2014, Pages 15088-15102, ISSN 0360-3199, <http://dx.doi.org/10.1016/j.ijhydene.2014.07.039>.

8.3 Recommendations for future work

- Injection of fuel gases such as H_2 and/or CH_4 into the chamber: Instead of aspirating the fuel gases (as was done in this work), provision could be made to directly inject the fuel gas into the combustion chamber. This would have the benefit of not displacing some of the intake O_2 hence preventing the increase in particulate formation at high H_2/CH_4 substitution levels. However, the fuel gas might not have enough time to mix homogeneously with the air resulting in stratified combustion.
- Co-combustion of synthesis gas (syngas) with diesel fuel: Syngas is produced through gasification of solid fuel feedstock and usually consists of carbon monoxide, hydrogen, methane, carbon dioxide and nitrogen in various proportions. It would be interesting to observe the effect of carbon monoxide (CO) on the combustion and emission characteristics, as CO can be expected to absorb heat energy and also use oxygen radicals to oxidise to CO_2 .
- Characterization of in-cylinder charge motion: The sampling system can be quite a powerful tool to determine certain parameters such as the rotational speed of the in-cylinder air due to swirl effects. This can help further our understanding of the diesel fuel spray core breakdown and the mixing of fuel and air.

Appendix A

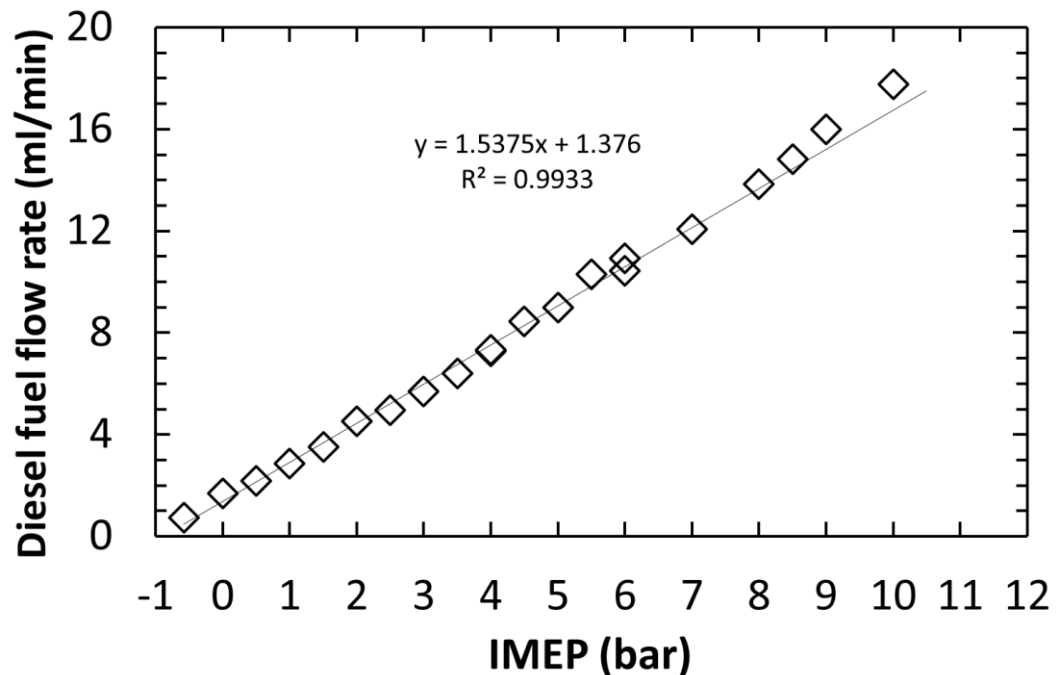


Figure A.1: Diesel fuel flow rate (ml/min) at different engine load (bar IMEP) for a single cylinder, half-litre engine at an engine speed of 1200 rpm

The diesel fuel flow rate through the fuel injector is a measure of the flow of diesel fuel-bound carbon into the engine cylinder, and is important in determining various parameters such as the thermal efficiency of the engine and specific exhaust emissions (in g/kWh). The diesel injector was calibrated so that the volume of diesel fuel injected per engine cycle could be determined from the duration of injection period. The diesel fuel injector calibration was carried out using a burette with which the volumetric flow rate of diesel fuel was determined, at steady state conditions, with different diesel fuel injection duration periods (and therefore at different engine loads, bar IMEP) at an engine speed of 1200 rpm, as can be seen in Figure . The calibration tests were repeated after a couple of months and a good repeatability in the results was observed.

Appendix B

Methods of data analysis

This appendix describes the methods of mathematical analysis carried out on the recorded experimental data in order to extract further information regarding in-cylinder combustion behaviour. In particular, the in-cylinder pressure data was utilised to calculate heat release rates, duration of ignition delay, engine work output and the thermal efficiency of the engine.

Heat release analysis

The in-cylinder pressure data over a range of CAD can be utilised to obtain quantitative information on the progress of combustion which can be useful for further analysis of fuel burning behaviour. This section describes suitable methods of determining the instantaneous in-cylinder volume, rate of heat release (release of fuel chemical energy), duration of ignition delay and global in-cylinder gas temperature.

In-cylinder volume calculation

For all experiments conducted throughout this work, the instantaneous engine cylinder gas pressure was logged as a discrete value at intervals of 0.2 CAD over the entire duration of 720 CAD, of the four stroke engine cycle. In order to be able to further analyse the recorded data, it was necessary to know the cylinder volume (also referred to as the combustion chamber volume) at each interval of recorded

CAD. The total cylinder volume (V) changes with piston position, and can be calculated at a given CAD using (Heywood 1988),

$$V = V_{clear} + [A_{bore}(l_{con} + r_{crank} - \sigma)] \quad (B.1)$$

where V_{clear} is the measured clearance volume, A_{bore} is the cylinder bore area, l_{con} is the length of the connecting rod, r_{crank} is the crank radius and σ is the instantaneous stroke position.

The cylinder bore area (A_{bore}) and instantaneous stroke position (σ) can be determined using,

$$A_{bore} = \frac{\pi D_{bore}^2}{4} \quad (B.2)$$

$$\sigma = a \cos(\theta) + \sqrt{l_{con}^2 - a^2 \sin^2(\theta)} \quad (B.3)$$

where D_{bore} is the cylinder bore diameter and θ is the crank angle with respect to the piston TDC position.

Apparent net heat release rate

A one dimensional and single zone thermodynamic model, developed and evaluated through comprehensive study by previous researchers (Chun & Heywood 1987; Cheung & Heywood 1993), was used to derive the apparent heat release rate from in-cylinder pressure data. The term ‘apparent’ is used since the heat release calculated utilises a number of assumptions including: the cylinder contents are homogenous and regarded as a single phase fluid making no distinction between

the burned and unburned gas regions or the non-uniformity in air-fuel ratio across the cylinder, the combustion process is considered as a separate heat addition process, no mass flow occurs across the system boundaries for the duration of heat release, the process is quasi static, the effect of crevice regions (such as the volume between the cylinder wall and piston) is not taken into consideration.

The net heat release rate (Q_n) is the difference between the gross heat release of fuel during combustion (Q_{ch}) and the heat transfer from the system to the cylinder.

Hence, the net heat release rate (Q_n) at any CAD can be expressed as,

$$\frac{dQ_n}{d\theta} = \frac{dQ_{ch}}{d\theta} - \frac{dQ_{ht}}{d\theta} \quad (\text{B.4})$$

The net heat release rate can be derived from basic principles pertaining to the application of the first law of thermodynamics to cylinder volume, and is thus equal to the sum of the work done on the piston and the rate of change of sensible internal energy of the system (U_s). The sensible changes in energy are due to temperature alone and not an effect of chemical reaction or phase change. Therefore, the expression for the net heat release rate (Q_n) can also be written down as,

$$\frac{dQ_n}{d\theta} = p \frac{dV}{d\theta} + \frac{dU_s}{d\theta} \quad (\text{B.5})$$

where p is the in-cylinder pressure.

Since the contents of the cylinder are assumed to behave as an ideal gas, that is,

$$pV = mRT \quad (\text{B.6})$$

and,

$$dU_s = mc_v dT \quad (\text{B.7})$$

then Equation B.5 can be written as,

$$\frac{dQ_n}{d\theta} = p \frac{dV}{d\theta} + mc_v \frac{dT}{d\theta} \quad (\text{B.8})$$

where m is the mass of the cylinder contents, R is the gas constant and c_v is the specific heat constant for the cylinder contents at a constant volume.

Since m and R are constants, the ideal gas law (Equation B.6) can be used to describe changes in temperature as a function of changes in pressure and volume,

$$\frac{dp}{p} = \frac{dV}{V} + \frac{dT}{T} \quad (\text{B.9})$$

Combining Equations B.8 and B.9 gives the following expression for net heat release rate (Q_n),

$$\frac{dQ_n}{d\theta} = p \left(1 + \frac{c_v}{R}\right) \frac{dV}{d\theta} + V \left(\frac{c_v}{R}\right) \frac{dp}{d\theta} \quad (\text{B.10})$$

Furthermore, the ratio of the specific heat constant at a constant pressure (c_p) to the specific heat constant at a constant volume (c_v) can be defined as,

$$\gamma = \frac{c_p}{c_v} \quad (\text{B.11})$$

Heywood (1988) recommends using a value of $\gamma = 1.35$ for the compression stage and a value of $\gamma = 1.26$ for the expansion stage of the cycle. For the sake of simplicity, an average value of $\gamma = 1.30$ was used for the net heat release rate calculations.

The relationship between the specific heat constants and the gas constant (R) can be expressed as,

$$R = c_p - c_v \quad (\text{B.12})$$

Therefore, substituting Equations B.11 and B.12 in Equation B.10, the following final expression for net heat release rate (Q_n) can be derived, which was used throughout this work to calculate the net heat release rate at a resolution of 0.2 CAD (equivalent to the resolution of the shaft encoder, which provided the time-base signal for logging the data, described in Section 3.6.2),

$$\frac{dQ_n}{d\theta} = \frac{\gamma}{\gamma - 1} p \frac{dV}{d\theta} + \frac{1}{\gamma - 1} V \frac{dp}{d\theta} \quad (\text{B.13})$$

The values for $\frac{dV}{d\theta}$ and $\frac{dp}{d\theta}$ were determined by calculating the difference between the values of volume (V) and pressure (p) at the current (instantaneous) crank angle (n) for which the heat release (Q_n) was calculated, and the values of V and p at the preceding crank angle ($n - 1$).

$$\frac{dV}{d\theta} = \frac{V_n - V_{n-1}}{d\theta} \quad (\text{B.14})$$

$$\frac{dp}{d\theta} = \frac{p_n - p_{n-1}}{d\theta} \quad (\text{B.15})$$

The value of p at each CAD was measured using the in-cylinder pressure transducer, while the value of V was determined using Equation B.1.

Ignition delay

The duration of fuel ignition delay was defined as the interval, in CAD, between the start of diesel fuel injection (SOI) and the start of combustion (SOC); SOI is taken to be the time (in CAD) at which the fuel injector actuation current signal is sent, and SOC is taken as the time (in CAD) at which the first detectable incidence of heat release occurs from fuel burning. The first detectable heat release

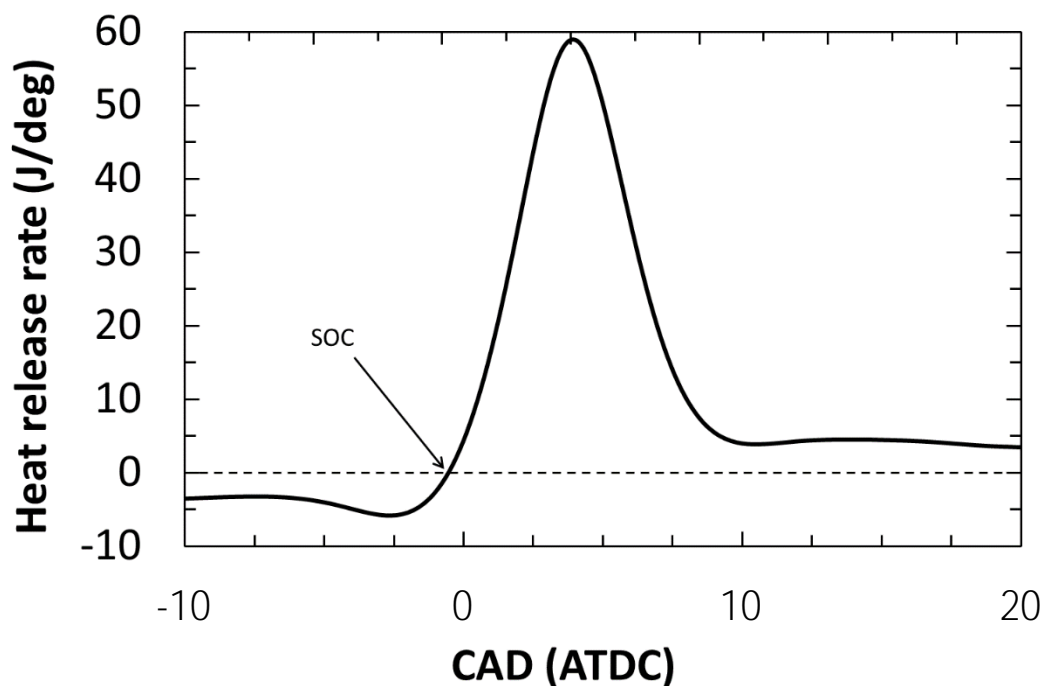


Figure B.1: Typical net heat release rate (J/deg) from diesel fuel combustion, showing the start of combustion (SOC) as the point (in CAD) when the heat release first becomes positive after fuel burning

rate was determined from the trace of net heat release against CAD, as the point where the net heat release rate first becomes positive following fuel injection (Figure B.1).

Cumulative heat release

The cumulative heat release can be used to determine the total value of chemical energy released by the fuel for the duration of fuel combustion. The duration of fuel combustion was defined as the interval between SOC and the first incidence of negative heat release following peak heat release rate. The cumulative heat release (CHR) was found by integrating the heat release rate (determined using Equation B.13) for the entire duration of combustion,

$$CHR = \int_{\theta_{start}}^{\theta_{end}} \frac{dQ_n}{d\theta} d\theta \quad (B.16)$$

Global in-cylinder gas temperature

The global gas temperature within the cylinder, at any crank angle, can be estimated by following similar assumptions of homogeneity and ideal gas behaviour of in-cylinder contents, as outlined for the determination of heat release rate earlier.

The temperature (T) can be calculated using the ideal gas law,

$$T = \frac{pV}{n\bar{R}} \quad (B.17)$$

where n is the number of moles of air and \bar{R} is the universal gas constant.

The number of moles of air was estimated from the measurement of the intake air volumetric flow rate (previously described in Section 3.1) during each cycle. The presence of fuel molecules or combustion products was not taken into account when calculating the total number of moles of the in-cylinder contents. Since compression ignition combustion is typically very lean and the cylinder contents are predominantly air, such an assumption was considered valid.

Air mass flow rate

The positive displacement volumetric flow meter (previously described in Section 3.1) sent an output pulse to the data acquisition system for every 0.01 m³ of air passing through it. The time difference between two consecutive pulses was calculated, and the volumetric flow rate (\dot{V}_{air}), in m³/s, was determined using,

$$\dot{V}_{air} = \frac{0.01}{t_n - t_{n-1}} \quad (\text{B.18})$$

As previously mentioned, the pressure (\dot{p}_{air}) and temperature (T_{air}) of the intake air was measured immediately adjacent to the volumetric flow meter, and the air mass flow rate (\dot{m}_{air}) calculated using,

$$\dot{m}_{air} = \frac{\dot{p}_{air}\dot{V}_{air}}{R_{air}T_{air}} \quad (\text{B.19})$$

where $R_{air} = 287.058 \text{ J/kgK}$

The volume of air lost during the valve overlap period was not included in this calculation as the valve overlap period was determined to be less than 5 CAD

(Schönborn 2009), and therefore, the volume of air lost during this period was assumed to be negligible (relative to the total intake air flow rate).

Indicated mean effective pressure

The indicated mean effective pressure (*IMEP*) defines the work output by the engine and is the ratio of the net indicated displacement work per cycle (W_i) and the swept volume of the engine (V_d),

$$IMEP = \frac{W_i}{V_d} \quad (\text{B.20})$$

The net indicated displacement work per cycle (W_i) can be determined by calculating the integral of the pressure with respect to the cylinder volume over the entire cycle,

$$W_i = \oint p dV \quad (\text{B.21})$$

and taking into account the work done by/on the in-cylinder gas during each piston stroke, the expression for W_i can be expanded to,

$$\begin{aligned} W_i = & - \int (pdV)_{intake} + \int (pdV)_{compression} - \int (pdV)_{expansion} \\ & + \int (pdV)_{exhaust} \end{aligned} \quad (\text{B.22})$$

The swept volume (V_d) can be determined from the cylinder bore area (A_{bore}) and the piston stroke length ($\bar{\sigma}$) using the following,

$$V_d = A_{bore} \bar{\sigma} \quad (\text{B.23})$$

Indicated thermal efficiency

The indicated thermal efficiency of the engine ($n_{thermal}$) was determined from the ratio of the indicated displacement work done per cycle (W_i) to the measured total chemical energy of the fuel(s) that were introduced into the cylinder during each cycle.

$$n_{thermal} = \frac{W_i}{\sum m Q_{LHV}} \quad (B.24)$$

where m is the measured mass of fuel injected and Q_{LHV} is the lower heating value of the fuel. The mass of gaseous fuel(s) that were fed into the intake manifold was measured using the thermal mass flow controllers (Section 3.4), while a calibration curve was used to determine the amount of diesel fuel injected into the cylinder every cycle. The calibration curve was obtained by performing a set of experiments, whereby the volumetric flow rate of diesel fuel injected into the cylinder was measured (using a burette and timer arrangement at room temperature and pressure) at a variety of fuel injection pressures and injector opening durations.

Conversion to specific emissions

For certain experiments involving intake air supercharging, it was necessary to convert the exhaust gas emission values from a volumetric fraction basis (ppm) to specific units of grams of emissions per kilowatt-hour of engine work output (g/kWh). This was done to compensate for the increased intake air flow rate, and hence increased exhaust gas flow rate, due to intake air supercharging, since specific

emissions normalise the emissions values against exhaust gas flow rate. The conversion was done using the numerical method of atomic balances described in considerable detail in Chapter 4 of the PhD thesis of Schönborn (2009).

Determination of sampling valve parameters

The trace from the displacement proximity sensor installed on the sampling valve was used in conjunction with threshold detection software, written in the NI LabVIEW environment, to determine the poppet valve opening and closing instants, the valve opening duration and the maximum valve lift. The details of the monitoring system of the sampling valve have been previously described in Section 3.7.7.

Appendix C

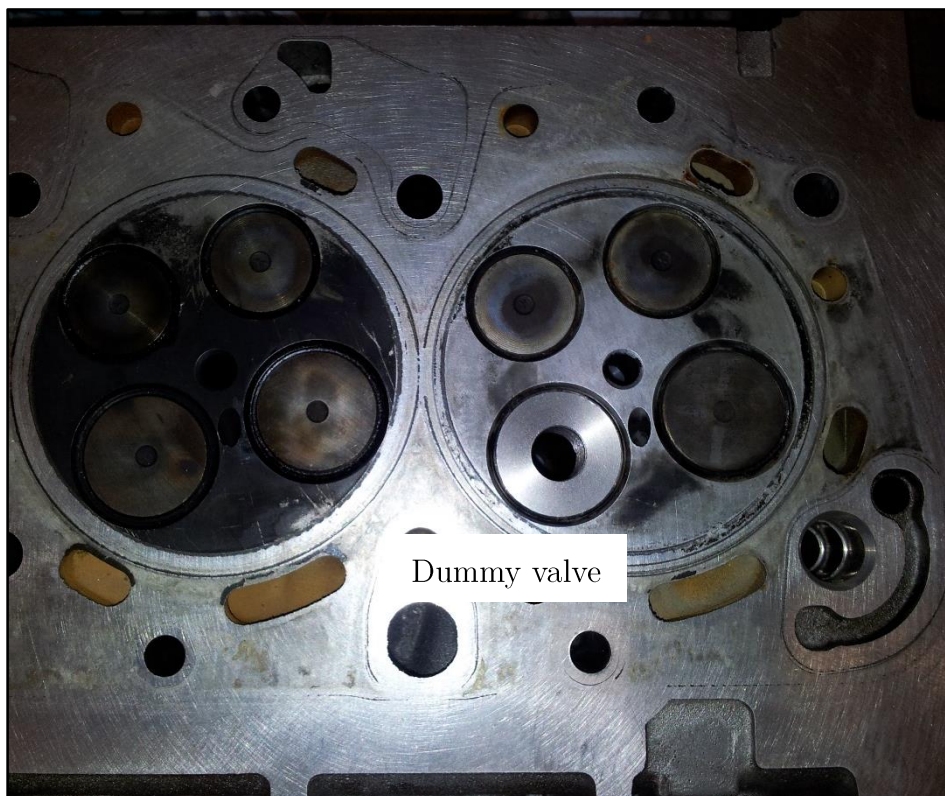


Figure C.1: One of the two intake valves on the 1st cylinder of the engine head replaced by a dummy valve with threaded hole for the sampling valve

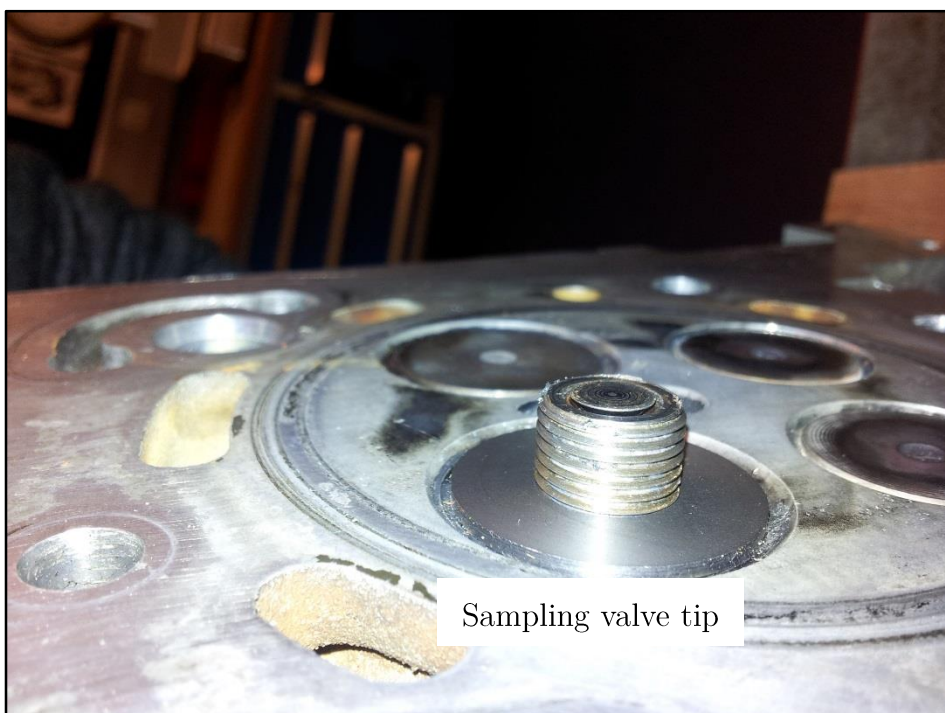


Figure C.2: Tip of the gas sampling valve protruding through the dummy valve in the cylinder head



Figure C.3: A small part at the edge of the piston bowl (of diameter 15 mm and depth 10 mm) was removed to prevent the sampling valve tip from hitting the piston

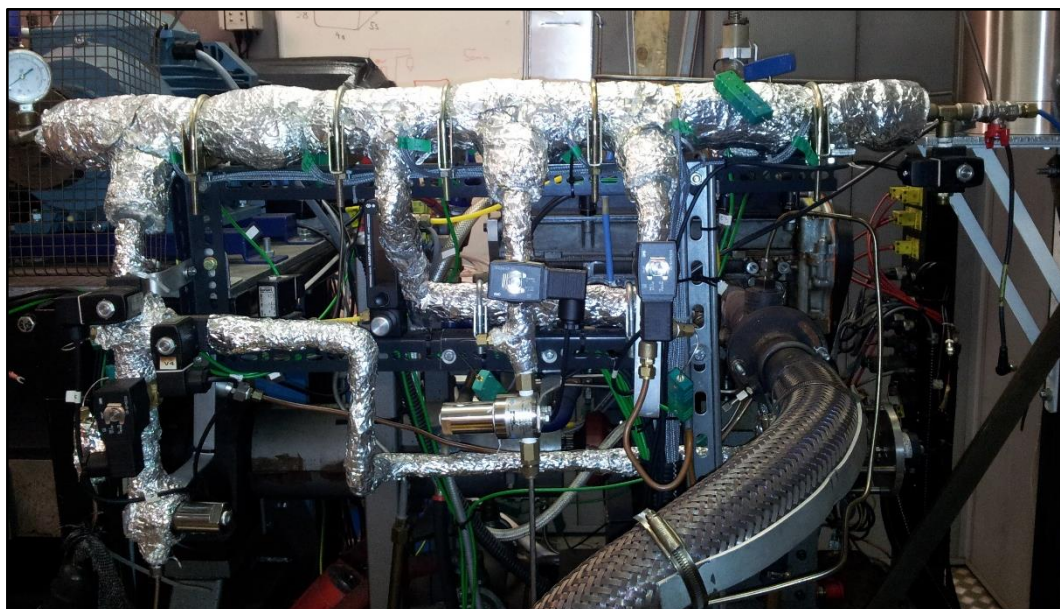


Figure C.4: Heated dilution tunnel (insulated) with various electromagnetic solenoid valves to control gas flows in and out of the tunnel

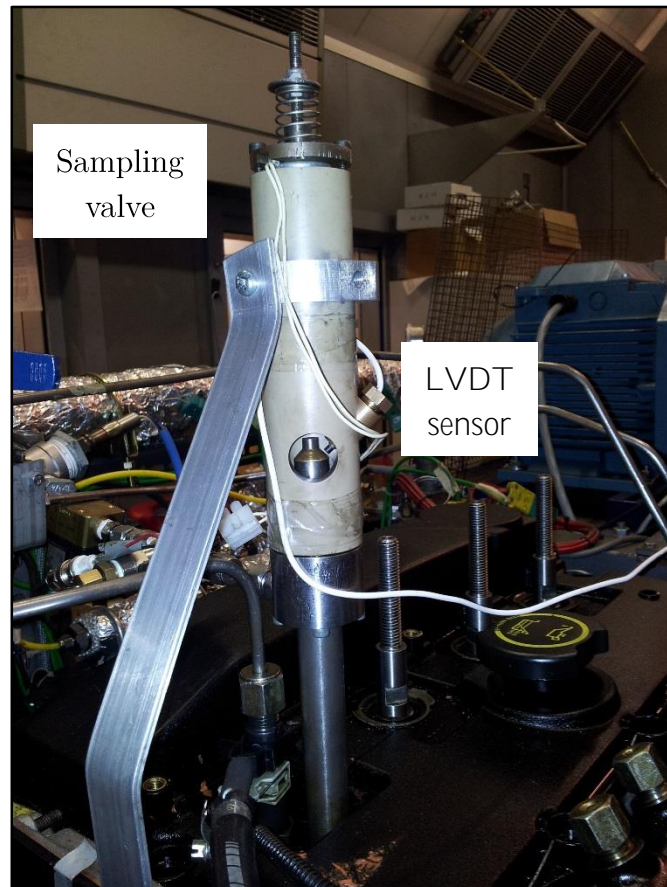


Figure C.5: The gas sampling valve mounted on the engine cylinder head. A bracket was used to reduce the stress on the long valve stem due to engine vibrations



Figure C.6: The amplifier electronics box and power supply for the LVDT proximity sensor mounted on the gas sampling valve

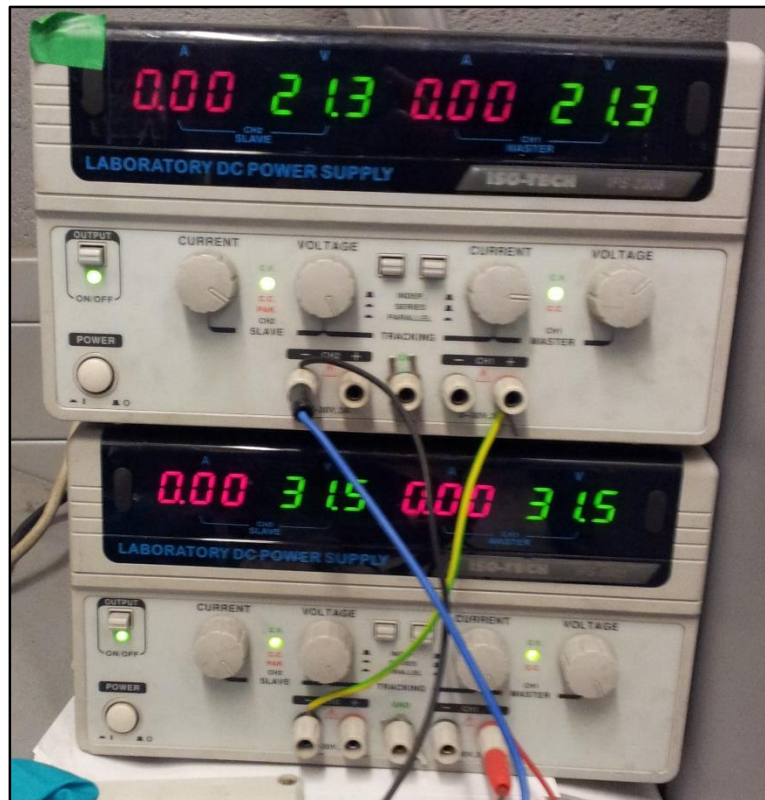


Figure C.7: Adjustable power supply for the electromagnetic actuation system of the gas sampling valve



Figure C.8: Kistler charge amplifier (type 5018) for use in conjunction with the piezoelectric transducer mounted on the engine head to measure in-cylinder gas pressure

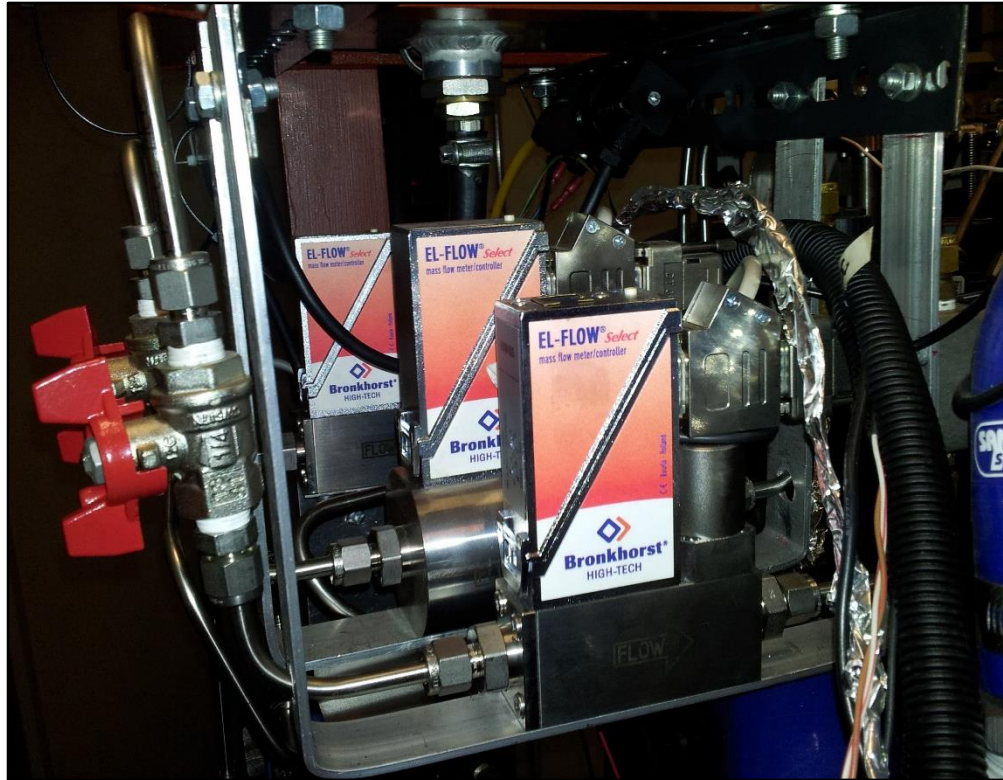


Figure C.9: Bronkhorst EL-Flow thermal mass flow controllers which precisely meter the amount of gas being supplied to the engine

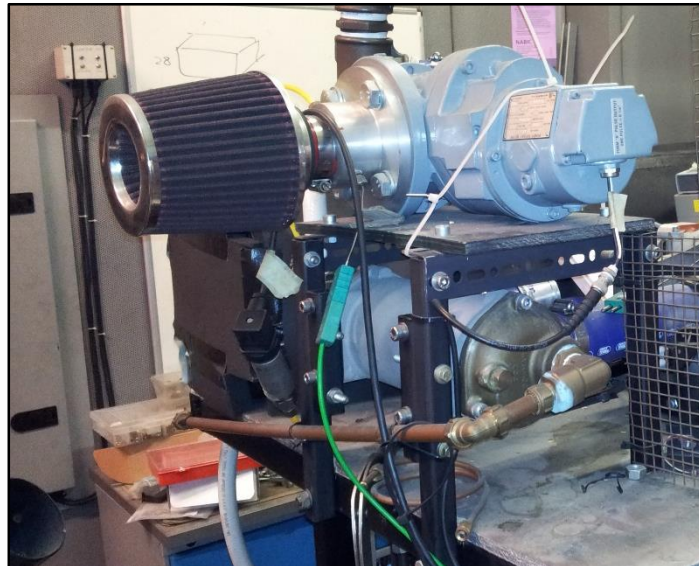


Figure C.10: Positive displacement air flow meter (Romet G65) to measure the volumetric flow rate of intake air being supplied to the engine

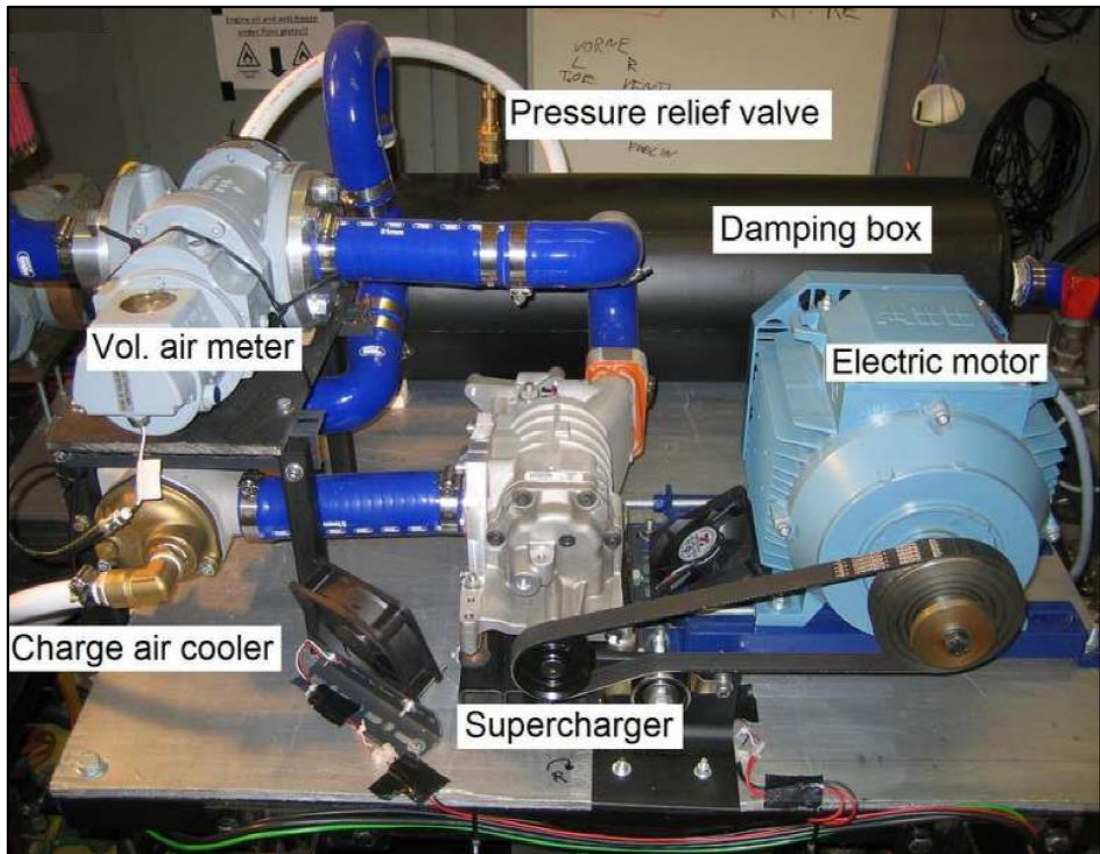


Figure C.11: Intake air boot system including the electric motor, supercharger and charge air cooler (which is a heat exchanger for maintaining intake air temperature)



Figure C.12: Potentiometer controller to control the speed of the electric motor, which drives the supercharger in the intake air boost system

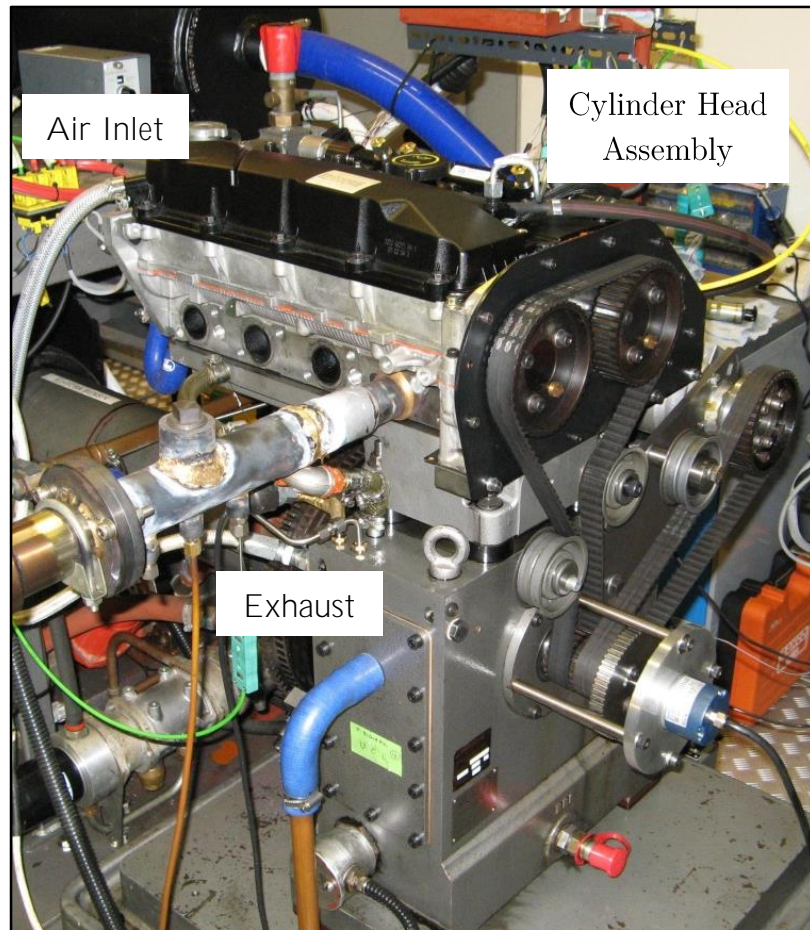


Figure C.13: Single cylinder, compression-ignition engine assembly

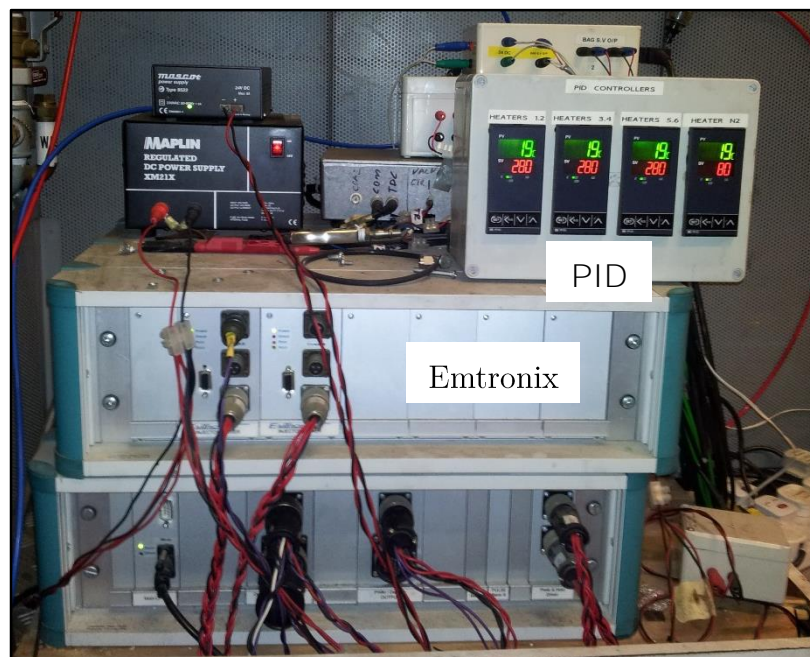


Figure C.14: Emtronix electronic engine control unit and heated tunnel PID control box



Figure C.15: Exhaust gas emissions analyser rack (Horiba MEXA-9100HEGR)



Figure C.16: Particulate spectrometer (Combustion DMS500)



Figure C.17: Engine dynamometer speed, and oil and coolant level and temperature control unit

Appendix D



Petrochem Carless Ltd Head Office - Cedar Court Guildford Road, Fetcham Leatherhead Surrey, KT22 9RX Telephone 44 (0) 1372 360000 Fax 44 (0) 1372 380400 A member of H•C•S Group		 PETROCHEM CARLESS Certificate of Analysis Lot : 10021532 Batch : 13-288M		Petrochem Carless BVBA Orteliuskaai 2-4/Bus 26 2000 Antwerp Belgium Telephone + 323 2059370 Fax + 323 2263126 A member of H•C•S Group	
Customer Name	University College London	Product Name	Carcal RF-06-03 (Marked)		
Customer No	357440	Product Number	47244		
Consignee	University College London	Certificate No	20052368		
Delivery Address	Mechanical Engineering Dept, 4th Floor Roberts Building, Torrington Place, London WC1E	Certificate Date	03/03/2014		
PCL Order Reference	436708	Approval Date	11/12/2013		
Customer Reference	TBC	Approved By:	Nicholas Hielt		
Customer Item Code		Checked by	Stuart Calver		
Customer Description		Approval Status	Released For Sale		
		Spec No	47244 v 11		
Method	Description	Min	Max	Results	Unit
ASTM D4052	Density at 15°C	0.833	0.837	0.8347	g/mL
Appearance					
VISUAL	Marker			PASS	
Distillation					
ASTM D86	I.B.Pt.			202.5	°C
ASTM D86	10 % Recovered at			226.5	°C
ASTM D86	50 % Recovered at	245		268.0	°C
ASTM D86	90 % Recovered at			327.5	°C
ASTM D86	95 % Recovered at	345	350	346.5	°C
ASTM D86	F.B.Pt.		370	350.5	°C
Engine Tests					
ASTM D613	Cetane Number	52.0	54.0	52.8	Units
FIA					
ASTM D1319	Aromatics			19.1	% vol
ASTM D1319	Olefins			4.8	% vol
General Properties					
ASTM D93	Flash Point, Pensky Closed	55		84.5	°C
IP 391	Polycyclic Aromatic Hydrocarbons (PCA)	3.0	6.0	4.9	% mass
ASTM D974	Strong Acid Number		0.02	0	mg KOH/g
ASTM D2274	Oxidation Stability		2.5	0.1	mg/100mL
ASTM D130	Copper Corrosion, 3hrs at 100°C			1A	
ASTM D445	Viscosity at 40°C	2.3	3.3	2.715	mm ² /s
ASTM D5453	Sulphur		10	<1.0	mg/kg
ISO 12156-1	Lubricity at 60°C		400	391	µm
ASTM D4530	Carbon Residue (on 10% Dist. Res)		0.20	<0.1	% m/m
ASTM D482	Ash		0.01	<0.001	% mass
EN 116	Cold Filter Plug Pt.		-5	-16	°C
IP 438	Water Content		200	40	mg/kg
EN 14078	Fatty Acid Methyl Ester (FAME) Content			NONE	% v/v
Printed : 03/03/2014					
This certificate is generated electronically and is therefore valid without a signature					
Page 1					

Figure D.1: Certificate of analysis for the fossil diesel fuel used in the experiments presented in this thesis (page 1 of 2)

Petrochem Carless Ltd Head Office - Cedar Court Guildford Road, Fetcham Leatherhead Surrey, KT22 9RX Telephone 44 (0) 1372 360000 Fax 44 (0) 1372 380400 A member of H•C•S Group		 PETROCHEM CARLESS Certificate of Analysis Lot : 10021532 Batch : 13-288M		Petrochem Carless BVBA Orteliuskaai 2-4/Bus 26 2000 Antwerp Belgium Telephone + 323 2059370 Fax + 323 2263126 A member of H•C•S Group	
Customer Name	University College London	Product Name	Carcal RF-06-03 (Marked)		
Customer No	357440	Product Number	47244		
Consignee	University College London	Certificate No	20052368		
Delivery Address	Mechanical Engineering Dept, 4th Floor Roberts Building, Torrington Place, London WC1E	Certificate Date	03/03/2014		
PCL Order Reference	436708	Approval Date	11/12/2013		
Customer Reference	TBC	Approved By:	Nicholas Hiett		
Customer Item Code		Checked by	Stuart Calver		
Customer Description		Approval Status	Released For Sale		
		Spec No	47244	v	11

Method	Description	Min	Max	Results	Unit
To Be Recorded					
ASTM D2500	Cloud Point			-11	°C
IP 12	Gross Heat of Combustion			45.94	MJ/kg
IP 12	Net Calorific Value			43.18	MJ/kg
IP 12 / CALCULATION	Net Calorific Value			18564	Btu/lb
ELEMENTAL ANALYSIS	Oxygen Content			<0.04	% m/m
ASTM D5291	Carbon Content			86.99	% m/m
ASTM D5291	Hydrogen Content			13.01	% m/m
CALCULATION	Atomic H/C Ratio			1.783	Ratio
CALCULATION	Atomic O/C Ratio			<0.0003	Ratio
CALCULATION	C/H Mass Ratio			6.69	Ratio
IP 391	Aromatics: Total			29.0	% m/m
ASTM D2709	Water & Sediment			0	% vol
CALCULATION	Carbon Weight Fraction			0.8699	Units

Additional Details

Printed : 03/03/2014

This certificate is generated electronically and is therefore valid without a signature

Page 2

Figure D.2: Certificate of analysis for the fossil diesel fuel used in the experiments presented in this thesis (page 2 of 2)

KAMAN INSTRUMENTATION CORPORATION
1500 GARDEN OF THE GODS ROAD
COLORADO SPRINGS, COLORADO 80907
CUSTOMER SERVICE (719) 599-1919

CALIBRATION RECORD

CUSTOMER: Daco Scientific Ltd DATE: 30-Aug-96

CUSTOMER P.O.# k1248/6643 SYSTEM SN: S9620872-01-01
KAMAN SALES ORDER NO: S9620873 SENSOR SN:
SYSTEM MODEL NO. KDM 7200-4sb-spl CHANNEL #:

DISPLACEMENT millimeters	OUTPUT VOLTAGE	LEAST SQUARES FIT VOLTAGE	NON-LINEARITY % FSO
0.00	0.000	0.114	-3.79%
0.30	0.362	0.416	-1.79%
0.60	0.720	0.718	0.07%
0.90	1.062	1.020	1.40%
1.20	1.395	1.322	2.43%
1.50	1.708	1.624	2.80%
1.80	2.004	1.926	2.60%
2.10	2.283	2.228	1.83%
2.40	2.542	2.530	0.40%
2.70	2.782	2.832	-1.66%
3.00	3.005	3.134	-4.29%

SUPPLY VOLTAGE (VOLTS): +/- 15
TARGET MATERIAL: customer pin non-magnetic
TARGET CURVATURE: tapered circular
CABLE LENGTH (FEET): 10
CALIBRATION OFFSET (millimeters): minimal
P/N:
NOTES: log, amp, by-pass

CALIBRATION TECHNICIAN: *Gary Roebel*
GARY ROEBEL

Figure D.3: Calibration certificate for the Kaman 1U1 proximity sensor mounted on the in-cylinder gas sampling valve

Kalibrierschein DRUCK

Calibration Certificate PRESSURE

Type **6056A** Serial No. **1754770**

Kalibriert durch Calibrated by	Datum Date
G. Ratano	17.10.2008

Referenzgeräte Reference Equipment	Typ Type	Serien-Nr. Serial No.
Gebrauchsnorm Working Standard	Kistler 7005-350	492592
Ladungsverstärker Charge Amplifier	Kistler 5017B	1479194
Ladungskalibrator Charge Calibrator	Kistler 5395A	441991

Umgebungstemperatur Ambient Temperature	Relative Feuchte Relative Humidity
°C	%
25	41

Messergebnisse Results of Measurement

Kalibrierter Bereich Calibrated Range	Empfindlichkeit Sensitivity	Linearität Linearity
bar	pC / bar	≤ ± %FSO
0 ... 250 (23°C)	-22,11	0,04
0 ... 150 (23°C)	-22,15	0,03
0 ... 100 (23°C)	-22,17	0,04
0 ... 50 (23°C)	-22,19	0,05
0 ... 250 (200°C)	-21,91	0,03
0 ... 150 (200°C)	-21,95	0,05
0 ... 100 (200°C)	-21,96	0,06
0 ... 50 (200°C)	-22,00	0,05
0 ... 250 (350°C)	-22,22	0,08
0 ... 150 (350°C)	-22,24	0,13
0 ... 100 (350°C)	-22,23	0,18
0 ... 50 (350°C)	-22,19	0,27

Messverfahren **Kontinuierliche Kalibrierung, Vergleichsverfahren**
 Measurement Procedure Continuous Calibration, Comparison Method

Bestätigung Confirmation

Die Geräte halten die Herstellertoleranzen gemäss Spezifikationen der Datenblätter ein. Wir bestätigen, dass das oben identifizierte Gerät nach den vorgeschriebenen Verfahren geprüft wurde. Alle Messmittel sind auf nationale Normale rückverfolgbar. Kistler betreibt die SCS (Swiss Calibration Service) Kalibrierstelle Nr. 049, akkreditiert nach ISO 17025. Das Kistler Qualitätsmanagement System ist nach ISO 9001 zertifiziert.


The equipment meets the manufacturing tolerances according to the specification data sheets. We confirm that the device identified above was tested by the prescribed procedures. All measuring devices are traceable to national standards. The SCS (Swiss Calibration Service) Calibration Laboratory No. 049 is operated by Kistler and accredited per ISO 17025. The Kistler Quality Management System is certified per ISO 9001.

Kistler Instrumente AG
 Eulachstrasse 22 Tel. +41 52 224 11 11 ZKB Winterthur BC 732 IBAN: CH67 0070 0113 2003 7462 8
 PO Box Fax +41 52 224 14 14 Swift: ZKBKCHZZ80A VAT: 229 713
 CH-8408 Wintherthur info@kistler.com Account: 1132-0374.628 ISO 9001 certified

www.kistler.com

Seite page 1 / 1

Figure D.4: Calibration certificate for the Kistler piezoelectric pressure transducer mounted on the cylinder head to measure in-cylinder gas pressure



cewal UK LTD

• Pressure & Temperature Instrumentation & Controls Manufacturer •

Unit 4c Woodhall Business Park Sudbury Suffolk CO10 1WH United Kingdom

Tel: 01787 882038 Fax: 01787 882039 E-mail: info@cewal.co.uk Web: www.cewal.co.uk

POINT TO POINT CALIBRATION CERTIFICATE NO: 14080

TO : MMPI SPECIAL METALS LTD
DUNMOW INDUSTRIAL ESTATE
CHELMSFORD ROAD
GREAT DUNMOW
ESSEX
CM6 1HD

INSTRUMENT SERIAL NO : C05996
OUR JOB NO : 07348


ITEM	QTY	INSTRUMENT DESCRIPTION WITH IDENTIFICATION/REF/PART CODE
1	1	100MM DIAMETER, S/STEEL CASE, BRASS INTERNALS, BOTTOM ENTRY, 3/8" BSP THREAD, 0-40 BAR/PSI DUAL SCALE, GLYCERINE FILLED, CLASS 1

INSTRUMENT READING SCALED BAR	TEST PRESSURE READING RISING BAR	TEST PRESSURE READING FALLING BAR
0	-	-
5	5.2	5.0
10	10.3	10.0
15	15.1	14.9
20	20.1	19.9
25	25.1	24.9
30	30.2	29.9
35	35.2	35.0
40	40.3	-

We certify that the above instrument has been tested to BS EN 837-1: 1998. Accuracy tested to and within $\pm 1.00\%$ FSD limits.
Readings are as shown above.
Instrument tested with: WATER medium
Instrument tested in: VERTICAL position
Laboratory Temperature $20^{\circ}\text{C} \pm 2^{\circ}\text{C}$


Range in bar	CALIBRATION EQUIPMENT USED MARKED WITH "X"						
	-1 / 0 / +1	-1 / 0 / +3	0 - 20	0 - 135	0 - 350	0 - 600 bar	0 - 1000 bar
Transmitter	31564	17118	34181	31566	31567	31568	31569
Display	56418	17118	56414	56415	56416	56417	56419
Used				X			

Calibration equipment above is within its period of calibration and traceable to NPL/National Standards

Signed:  Date: 6 November 2007

July 2006 Issue 2 F16 Registered in England No. 2485646

Figure D.5: Calibration certificate for the damping vessel which is part of the intake air system



Bronkhorst®
HIGH-TECH

CALIBRATION CERTIFICATE

FLUID NO. 1 OF 1

CERTIFICATE NO. BHT177/1495808

Calibration by comparison
Calibration date: 9 Aug 2013

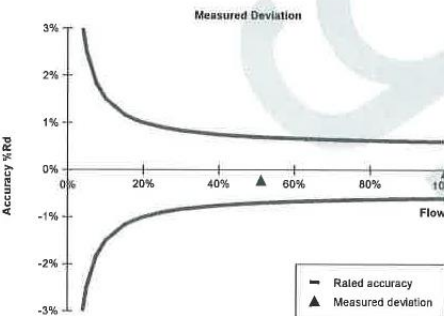
We hereby certify that the instrument mentioned below has been calibrated in accordance with the stated values and conditions. The calibration standards used are traceable to national standards of the Dutch Metrology Institute VSL.

Calibrated instrument		Calibration standard	
Type	Flow controller (D)	Type	Rotor meter
Serial number	M13207670A	Serial number	M0205926H
Model number	F-201AV-70K-AGD-22-V	Certificate no.	NMI/G1S1986
Rated accuracy*	±(0.5%Rd + 0.1%FS)	Uncertainty	±0.3% Rd

Customer conditions		Calibration conditions	
Fluid	H2	Fluid	AiR
Flow	80.00 In/min	Flow	84.58 In/min (equivalent flow)
Pressure	3.0..8.0 bar (g)	Pressure	5.0 bar (a)
Temperature	20.0 °C	Temperature	23.2 °C
		Atm. pressure	1017.5 hPa (a)

Output signal	Customer flow**	Equivalent flow**	Reference flow	Measured deviation*	Measurement uncertainty*
99.99%	79.99 In/min	84.57 In/min	84.61 In/min	-0.05 % Rd	0.4 % Rd
51.31%	41.05 In/min	41.72 In/min	41.82 In/min	-0.22 % Rd	0.4 % Rd
0.00%	0.000 In/min	0.000 In/min	0.000 In/min	-	-

Measured Deviation




Notes

Flow unit In/min is defined at conditions 0.00 °C, 1013.25 hPa (a).

* Rated accuracy, measured deviation and measurement uncertainty are specified under calibration conditions in digital mode.


** The customer flow at customer conditions is converted to equivalent flow at calibration conditions using Bronkhorst High-Tech FLUIDAT® software.

Measurement uncertainties are based upon 95% (k=2) confidence limits. Although the item calibrated meets the specifications and performance at the time of calibration, due to any number of factors, this does not imply continuing conformance to the specifications.

Calibrator	R.Pet.	QC	A.U.
		Date	15 Aug 2013
		Signed	

Multical V1.50
FLUIDAT® V5.73 (Database: 17-03-2003)
Report V1.13

Figure D.6: Thermal mass flow controller 1 calibration certificate for H₂



Bronkhorst®
HIGH-TECH

CALIBRATION CERTIFICATE

FLUID NO. 1 OF 2
CERTIFICATE NO. BHTG18/1618304

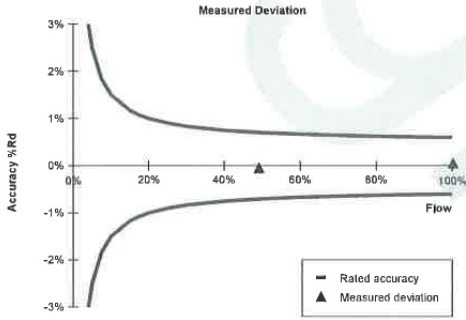
Calibration by comparison
Calibration date: 18 Mar 2014

We hereby certify that the instrument mentioned below has been calibrated in accordance with the stated values and conditions. The calibration standards used are traceable to national standards of the Dutch Metrology Institute VSL.

Calibrated instrument		Calibration standard	
Type	Flow controller (D)	Type	Rotor meter
Serial number	M14201630A	Serial number	80188
Model number	F-202AV-M20-AAD-22-V	Certificate no.	NMI/G12S2734
Rated accuracy*	±(0.5%Rd + 0.1%FS)	Uncertainty	±0.3% Rd

Customer conditions		Calibration conditions	
Fluid	CO2	Fluid	AiR
Flow	150.0 l/min	Flow	200.8 l/min (equivalent flow)
Pressure	5.0..8.0 bar (g)	Pressure	5.0 bar (a)
Temperature	20.0 °C	Temperature	22.7 °C
		Atm. pressure	1011.9 hPa (a)

Output signal	Customer flow** CO2	Equivalent flow** AiR	Reference flow AiR	Measured deviation*	Measurement uncertainty*
100.22%	150.3 l/min	201.3 l/min	201.2 l/min	0.05 % Rd	0.4 % Rd
49.14%	73.71 l/min	100.7 l/min	100.7 l/min	-0.05 % Rd	0.4 % Rd
0.00%	0.000 l/min	0.000 l/min	0.000 l/min	-	-



Measured Deviation

Accuracy %Rd

Flow

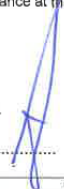
— Rated accuracy
▲ Measured deviation

Notes

Flow unit l/min is defined at conditions 0.00 °C, 1013.25 hPa (a).
 * Rated accuracy, measured deviation and measurement uncertainty are specified under calibration conditions in digital mode.
 ** The customer flow at customer conditions is converted to equivalent flow at calibration conditions using Bronkhorst High-Tech FLUIDAT® software.

Measurement uncertainties are based upon 95% (k=2) confidence limits. Although the item calibrated meets the specifications and performance at the time of calibration, due to any number of factors, this does not imply continuing conformance to the specifications.

Calibrator	R.Mu.	QC	A.F.K.
		Date	19 Mar 2014
		Signed



MultiCal V2.03
FLUIDAT® V5.73 (Database: 05-05-1999)
Report V1.13

Figure D.7: Thermal mass flow controller 2 calibration certificate for CO₂ (page 1 of 2)



 Bronkhorst® HIGH-TECH			
CONVERSION TABLE			
FLUID NO. 2 OF 2			
CERTIFICATE NO. BHTG18/CL9/1618065	Conversion date: 18 Mar 2014		
We hereby certify that the instrument mentioned below has been calibrated in accordance with the stated values and conditions. The calibration standards used are traceable to national standards of the Dutch Metrology Institute VSL.			
Calibrated instrument		Calibration standard	
Type	Flow controller (D)	Type	Rotor meter
Serial number	M14201630A	Serial number	80188
Model number	F-202AV-M20-AAD-22-V	Certificate no.	NMI/G12S2734
Rated accuracy*	±(0.5%Rd + 0.1%FS)	Uncertainty	±0.3% Rd
Customer conditions		Calibration conditions	
Fluid	N2	Fluid	AIR
Flow	150.0 In/min	Flow	150.4 In/min (equivalent flow)
Pressure	5.0..8.0 bar (g)	Pressure	5.0 bar (a)
Temperature	20.0 °C	Temperature	22.7 °C
		Atm. pressure	1012.0 hPa (a)
Calibration and conversion results			
Output signal	Customer flow** N2	Equivalent flow** AIR	
100.00%	150.0 In/min	150.4	In/min
90.00%	135.0 In/min	135.4	In/min
80.00%	120.0 In/min	120.3	In/min
70.00%	105.0 In/min	105.3	In/min
60.00%	90.00 In/min	90.26	In/min
50.00%	75.00 In/min	75.22	In/min
40.00%	60.00 In/min	60.18	In/min
30.00%	45.00 In/min	45.13	In/min
20.00%	30.00 In/min	30.10	In/min
10.00%	15.00 In/min	15.04	In/min
0.00%	0.000 In/min	0.000	In/min
Notes			
Flow unit In/min is defined at conditions 0.00 °C, 1013.25 hPa (a).			
* Rated accuracy, measured deviation and measurement uncertainty are specified under calibration conditions in digital mode.			
** The customer flow at customer conditions is converted to equivalent flow at calibration conditions using Bronkhorst High-Tech FLUIDAT® software.			
Measurement uncertainties are based upon 95% (k=2) confidence limits. Although the item calibrated meets the specifications and performance at the time of calibration, due to any number of factors, this does not imply continuing conformance to the specifications.			
BHTMultiFluidToolCLL V3.50		FLUIDAT® V5.73 (Database: 05-05-1999)	
		Report V1.13	

Figure D.8: Thermal mass flow controller 2 calibration certificate for N₂ (page 2 of 2)



Bronkhorst®
HIGH-TECH

CALIBRATION CERTIFICATE

FLUID NO. 1 OF 1
CERTIFICATE NO. BHT178/1660309

Calibration by comparison
Calibration date: 5 Jun 2014

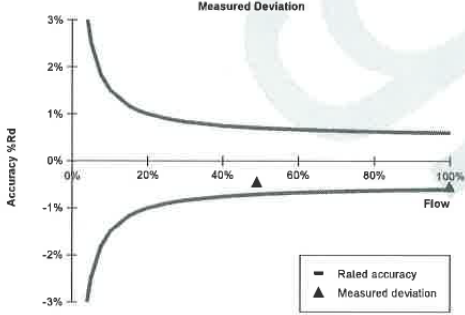
We hereby certify that the instrument mentioned below has been calibrated in accordance with the stated values and conditions. The calibration standards used are traceable to national standards of the Dutch Metrology Institute VSL.

Calibrated instrument		Calibration standard	
Type	Flow controller (D)	Type	Rotor meter
Serial number	M14205968A	Serial number	M0205926G
Model number	F-201AV-50K-RAD-22-V	Certificate no.	Nmi/G13S3073
Rated accuracy*	±(0.5%Rd + 0.1%FS)	Uncertainty	±0.3% Rd

Customer conditions		Calibration conditions	
Fluid	CO2	Fluid	AiR
Flow	35.00 l/min	Flow	46.83 l/min (equivalent flow)
Pressure	5.0..6.0 bar (g)	Pressure	5.0 bar (a)
Temperature	20.0 °C	Temperature	22.8 °C
		Atm. pressure	1006.9 hPa (a)

Calibration and conversion results						
Output signal	Customer flow**	Equivalent flow**	Reference flow	Measured deviation*	Measurement uncertainty*	
	CO2	AiR	AiR			
99.78%	34.92 l/min	46.72 l/min	46.97 l/min	-0.54 % Rd	0.4 % Rd	
49.12%	17.19 l/min	23.36 l/min	23.47 l/min	-0.46 % Rd	0.4 % Rd	
0.00%	0.000 l/min	0.000 l/min	0.000 l/min	-	-	

Measured Deviation



Accuracy %Rd

Flow

— Rated accuracy

▲ Measured deviation

Notes

Flow unit l/min is defined at conditions 0.00 °C, 1013.25 hPa (a).

* Rated accuracy, measured deviation and measurement uncertainty are specified under calibration conditions in digital mode.

** The customer flow at customer conditions is converted to equivalent flow at calibration conditions using Bronkhorst High-Tech FLUIDAT® software.

Measurement uncertainties are based upon 95% (k=2) confidence limits. Although the item calibrated meets the specifications and performance at the time of calibration, due to any number of factors, this does not imply continuing conformance to the specifications.

Calibrator	C.L.	QC	A.F.K.
		Date	11 Jun 2014
		Signed

Multical V2.03
FLUIDAT® V5.79 (Database: 17-03-2003)
Report V1.13

Figure D.9: Thermal mass flow controller 3 calibration certificate for CO₂

References

- Agarwal, A. & Assanis, D.N., 1998. Multi-Dimensional Modeling of Natural Gas Ignition Under Compression Ignition Conditions Using Detailed Chemistry. *SAE Paper*, p.980136.
- Akansu, S., 2004. Internal combustion engines fueled by natural gas-hydrogen mixtures. *International Journal of Hydrogen Energy*, 29(14), pp.1527–1539.
- Akansu, S., Kahraman, N. & Ceper, B., 2007. Experimental study on a spark ignition engine fuelled by methane–hydrogen mixtures. *International Journal of Hydrogen Energy*, 32(17), pp.4279–4284.
- Amann, C.A. & Siegl, D.C., 2008. Diesel Particulates—What They Are and Why. *Aerosol Science and Technology*, 1(1), pp.73–101.
- Andree, A. & Pachernegg, S.J., 1969. Ignition Conditions in Diesel Engines. *SAE Paper*, p.690253.
- Aoyagi, Y., Kamimoto, T. & Matsui, Y., 1980. A gas sampling study on the formation processes of soot and NO in a DI diesel engine. *SAE Paper*, p.800254.
- Bäcker, H., Hild, O. & Lepperhoff, G., 1997. Investigation on Particle Size Distribution in the Cylinder of a Passenger Car DI Diesel Engine Using a Fast Gas Sampling Valve. *SAE Paper*, p.970875.

- Barbella, R. et al., 1989. In-cylinder sampling of high molecular weight hydrocarbons from a DI light duty diesel engine. *SAE Paper*, p.890437.
- Bari, S., 1996. Effect of carbon dioxide on the performance of biogas/diesel dual-fuel engine. *Renewable Energy*, 9(Goodger 1980), pp.1007–1010.
- Barik, D. & Murugan, S., 2014. Investigation on combustion performance and emission characteristics of a DI (direct injection) diesel engine fueled with biogas-diesel in dual fuel mode. *Energy*, 72, pp.760–771.
- Bauer, C., 2001a. Effect of hydrogen addition on the performance of methane-fueled vehicles. Part I: effect on S.I. engine performance. *International Journal of Hydrogen Energy*, 26(1), pp.55–70.
- Bauer, C., 2001b. Effect of hydrogen addition on the performance of methane-fueled vehicles. Part II: driving cycle simulations. *International Journal of Hydrogen Energy*, 26(1), pp.71–90.
- Bedoya, I.D., Arrieta, A.A. & Cadavid, F.J., 2009. Effects of mixing system and pilot fuel quality on diesel-biogas dual fuel engine performance. *Bioresource Technology*, 100(24), pp.6624–6629.

- Beeley, P., Griffiths, J.F. & Gray, P., 1980. Rapid compression studies on spontaneous ignition of isopropyl nitrate Part II: Rapid sampling, intermediate stages and reaction mechanisms. *Combustion and Flame*, 39(3), pp.269–281.
- Bennethum, J.E., Mattavi, J.N. & Toepel, R.R., 1975. Diesel Combustion Chamber Sampling - Hardware, Procedures, and Data Interpretation. *SAE Paper*, p.750849.
- Biobolsa, 2015. Sistema Biobolsa Anerobic Digester. Available at: <http://sistemabiobolsa.com/what-we-do/the-technology/> [Accessed April 5, 2015].
- Van Blarigan, P. & Keller, J.O., 1998. A hydrogen fuelled internal combustion engine designed for single speed/power operation. *International Journal of Hydrogen Energy*, 23(7), pp.603–609.
- Bora, B.J. et al., 2014. Effect of compression ratio on performance, combustion and emission characteristics of a dual fuel diesel engine run on raw biogas. *Energy Conversion and Management*, 87, pp.1000–1009.
- Bosch, R., 2004. *BOSCH: Automotive Handbook* 6th ed., Wiley-Blackwell.
- Bowman, C., 1975. Kinetics of pollutant formation and destruction in combustion. *Progress in energy and combustion science*, 1(1), pp.33–45.

- Bowman, C.T., 1973. Kinetics of nitric oxide formation in combustion processes. *Symposium (International) on Combustion*, 14(1), pp.729–738.
- Brunt, M.F.J., Rai, H. & Emtage, A.L., 1998. The Calculation of Heat Release Energy from Engine Cylinder Pressure Data. *SAE paper*, p.981052.
- Cacua, K., Amell, A. & Cadavid, F., 2012. Effects of oxygen enriched air on the operation and performance of a diesel-biogas dual fuel engine. *Biomass and Bioenergy*, 45, pp.159–167.
- Cambustion, 2011. DMS500 Fast Particulate Spectrometer. *Cambustion User Manual*.
- Cheung, H.M. & Heywood, J.B., 1993. Evaluation of a One-Zone Burn-Rate Analysis Procedure Using Production SI Engine Pressure Data. *SAE Paper*, p.932749.
- Chianese, S. et al., 2015. Hydrogen from the high temperature water gas shift reaction with an industrial Fe/Cr catalyst using biomass gasification tar rich synthesis gas. *Fuel Processing Technology*, 132, pp.39–48.
- Chiu, W.S., Shahed, S.M. & Lyn, W.T., 1976. A Transient Spray Mixing Model for Diesel Combustion. *SAE Paper*, p.760128.

- Chong, C.T. & Hochgreb, S., 2011. Measurements of laminar flame speeds of liquid fuels: Jet-A1, diesel, palm methyl esters and blends using particle imaging velocimetry (PIV). *Proceedings of the Combustion Institute*, 33(1), pp.979–986.
- Christodoulou, F. & Megaritis, A., 2013. Experimental investigation of the effects of separate hydrogen and nitrogen addition on the emissions and combustion of a diesel engine. *International Journal of Hydrogen Energy*, 38(24), pp.10126–10140.
- Chun, K.M. & Heywood, J.B., 1987. Estimating Heat-Release and Mass-of-Mixture Burned from Spark-Ignition Engine Pressure Data. *Combustion Science and Technology*, 54, pp.133–143.
- Clausse, M., Bonjour, J. & Meunier, F., 2004. Adsorption of gas mixtures in TSA adsorbers under various heat removal conditions. *Chemical Engineering Science*, 59(17), pp.3657–3670.
- COMEAP, 2001. Long-term effects of particles on mortality. *Committee on the Medical Effects of Air Pollutants*.
- COMEAP, 1998. The Quantification of the Effects of Air Pollution on Health in the United Kingdom. *Committee on the Medical Effects of Air Pollutants*.

- Das, L., 2000. A comparative evaluation of the performance characteristics of a spark ignition engine using hydrogen and compressed natural gas as alternative fuels. *International Journal of Hydrogen Energy*, 25(8), pp.783–793.
- Dec, J.E., 1997. A Conceptual Model of DI Diesel Combustion Based on Laser-Sheet Imaging. *SAE Paper*, p.970873.
- Dec, J.E. & Canaan, R.E., 1998. PLIF Imaging of NO Formation in a DI Diesel Engine. *SAE Paper*, p.980147.
- DECC, 2015. 2013 UK Greenhouse Gas Emissions, Final Figures. *Department of Energy and Climate Change*.
- DeLuchi, M.A., Johnston, R.A. & Sperling, D., 1988. Methanol vs. Natural Gas Vehicles: A Comparison of Resource Supply, Performance, Emissions, Fuel Storage, Safety, Costs, and Transitions. *SAE Paper*, p.881656.
- Demuyneck, J. et al., 2009. Local heat flux measurements in a hydrogen and methane spark ignition engine with a thermopile sensor. *International Journal of Hydrogen Energy*, 34(24), pp.9857–9868.
- Diéguez, P.M. et al., 2014. Experimental study of the performance and emission characteristics of an adapted commercial four-cylinder spark ignition engine running on hydrogen–methane mixtures. *Applied Energy*, 113, pp.1068–1076.

- Dolan, D.F. & Kittelson, D.B., 1978. Diesel Exhaust Aerosol Particle Size Distributions - Comparison of Theory and Experiment. *SAE Paper*, p.780110.
- Donahue, R.W. & Kent, R.H., 1950. A Study of Mixture Distribution. *SAE Paper*, p.500196.
- Duc, P.M. & Wattanavichien, K., 2007. Study on biogas premixed charge diesel dual fuelled engine. *Energy Conversion and Management*, 48, pp.2286–2308.
- Duggal, V.K., Priede, T. & Khan, I.M., 1978. A Study of Pollutant Formation within the Combustion Space of a Diesel Engine. *SAE Paper*, p.780227.
- Dumitrescu, C. et al., 2009. A computational study of a fast sampling valve designed to sample soot precursors inside a forming diesel spray plume. *Applied Thermal Engineering*, 29(5-6), pp.1253–1258.
- Egerton, A., Smith, F. & Ubbelohde, A., 1935. Estimation of the Combustion Products from the Cylinder of the Petrol Engine and Its Relation to “Knock.” *Philosophical Transactions of the Royal Society Of London. Series A Mathematical and Physical Sciences.*, 234(744), pp.433–521.
- European Parliament, 2009. Renewable Energy Road Map. *EU Renewable Energy Directive*.

- Faeth, G.M., 1977. Current status of droplet and liquid combustion. *Progress in Energy and Combustion Science*, 3(4), pp.191–224.
- Fenimore, C.P., 1972. Formation of nitric oxide from fuel nitrogen in ethylene flames. *Combustion and Flame*, 19(2), pp.289–296.
- Fenimore, C.P., 1971. Formation of nitric oxide in premixed hydrocarbon flames. *Symposium (International) on Combustion*, 13(1), pp.373–380.
- Ferrer, I. et al., 2008. Increasing biogas production by thermal (70°C) sludge pre-treatment prior to thermophilic anaerobic digestion. *Biochemical Engineering Journal*, 42(2), pp.186–192.
- Flynn, P.F. et al., 1999. Diesel Combustion: An Integrated View Combining Laser Diagnostics, Chemical Kinetics, And Empirical Validation. *SAE Paper*, pp.1999-01-0509.
- Fristrom, R.M., Prescott, R. & Grunfelder, C., 1957. Flame zone studies III—Techniques for the determination of composition profiles of flame fronts. *Combustion and Flame*, 1(1), pp.102–113.
- Fujiwara, Y. et al., 1984. Formation of Soot Particulates in the Combustion Chamber of a Precombustion Chamber Type Diesel Engine. *SAE Paper*, p.840417.

- Gatts, T. et al., 2010. An experimental investigation of H₂ emissions of a 2004 heavy-duty diesel engine supplemented with H₂. *International Journal of Hydrogen Energy*, 35(20), pp.11349–11356.
- Genovese, A. et al., 2011. On road experimental tests of hydrogen/natural gas blends on transit buses. *International Journal of Hydrogen Energy*, 36(2), pp.1775–1783.
- Glassman, I., 1989. Soot formation in combustion processes. *Symposium (International) on Combustion*, 22(1), pp.295–311.
- Glassman, I. & Yetter, R.A., 2008a. Combustion: Chapter 4 – Flame Phenomena in Premixed Combustible Gases. *Combustion*, pp.311–377.
- Glassman, I. & Yetter, R.A., 2008b. Combustion: Chapter 4 – Flame Phenomena in Premixed Combustible Gases. *Combustion*, pp.147–260.
- Gowdagiri, S., Wang, W. & Oehlschlaeger, M.A., 2014. A shock tube ignition delay study of conventional diesel fuel and hydroprocessed renewable diesel fuel from algal oil. *Fuel*, 128, pp.21–29.
- Gowers, A.M., Miller, B.G. & Stedman, J.R., 2014. Estimating Local Mortality Burdens associated with Particulate Air Pollution. *Public Health England*, p.40.

- Gunea, C., Razavi, M.R.M. & Karim, G.A., 1998. The Effects of Pilot Fuel Quality on Dual Fuel Engine Ignition Delay. *SAE Paper*, p.982453.
- Hayhurst, A.N., Kittelson, D.B. & Telford, N.R., 1977. Mass spectrometric sampling of ions from atmospheric pressure flames—II: Aerodynamic disturbance of a flame by the sampling system. *Combustion and Flame*, 28, pp.123–135.
- Haynes, B.S. & Wagner, H.G., 1981. Soot formation. *Progress in Energy and Combustion Science*, 7(4), pp.229–273.
- Hellier, P. et al., 2011. The Impact of Saturated and Unsaturated Fuel Molecules on Diesel Combustion and Exhaust Emissions. *SAE Paper*, pp.2011–01–1922.
- Hellier, P., 2013. *The molecular structure of future fuels*. PhD Thesis, UCL.
- Henham, a & Makkar, M., 1998. Combustion of simulated biogas in a dual-fuel diesel engine. *Energy Conversion and Management*, 39(16), pp.2001–2009.
- Heywood, J., Keck, J. & Rife, J., 1980. Final Report on Research Program: Hydrocarbon formation and oxidation in spark-ignition engines. *Sloan Automotive Laboratory, Massachusetts Institute of Technology*.
- Heywood, J.B., 1988. *Internal Combustion Engine Fundamentals* 1st ed., New York: McGraw-Hill.

Hilliard, J.C. & Wheeler, R.W., 1979. Nitrogen Dioxide in Engine Exhaust. *SAE Paper*, p.790691.

Hoekstra, R., 1995. Experimental study of a clean burning vehicle fuel. *International Journal of Hydrogen Energy*, 20(9), pp.737–745.

Horiba Instruments, 1984. *Horiba Instruments, MEXA 9100HEGR instructions manual*, Kyoto, Japan.

Imran, S. et al., 2014. Effect of pilot fuel quantity and type on performance and emissions of natural gas and hydrogen based combustion in a compression ignition engine. *International Journal of Hydrogen Energy*, 39(10), pp.5163–5175.

Kahraman, N. et al., 2009. Investigation of combustion characteristics and emissions in a spark-ignition engine fuelled with natural gas–hydrogen blends. *International Journal of Hydrogen Energy*, 34(2), pp.1026–1034.

Kajima, T. & Kawamura, Y., 1995. Development of a high-speed solenoid valve: investigation of solenoids. *IEEE Transactions on Industrial Electronics*, 42(1), pp.1–8.

Kamimoto, T. & Kobayashi, H., 1991. Combustion processes in diesel engines. *Progress in Energy and Combustion Science*, 17(2), pp.163–189.

- Karim, G., 2003. Hydrogen as a spark ignition engine fuel. *International Journal of Hydrogen Energy*, 56(6), pp.256–263.
- Karim, G., Wierzba, I. & Al-Alousi, Y., 1996. Methane-hydrogen mixtures as fuels. *International Journal of Hydrogen Energy*, 21(7), pp.625–631.
- Kato, S. et al., 1997. Investigation of Particulate Formation of DI Diesel Engine with Direct Sampling from Combustion Chamber. *SAE Paper*, p.972969.
- Kent, J.H. & Wagner, H.G., 1985. Temperature and fuel effects in sooting diffusion flames. In *Proceedings of the 20th Symposium (International) on Combustion*, The Combustion Institute. Pittsburgh, PA, USA, pp. 1007–1015.
- Khatri, N.J., Johnson, J.H. & Leddy, D.G., 1978. The Characterization of the Hydrocarbon and Sulfate Fractions of Diesel Particulate Matter. *SAE Paper*, p.780111.
- Kimura, S.G. & Walmet, G.E., 2006. Fuel Gas Purification with Permselective Membranes. *Separation Science and Technology*, 15(4), pp.1115–1133.
- Kittelson, D., Watts, W. & Johnson, J., 2002. *Diesel Aerosol Sampling Methodology* - CRC E-43, Minneapolis, USA.
- Kittelson, D.B., 1998. Engines and nanoparticles. *Journal of Aerosol Science*, 29(5-6), pp.575–588.

Kittelson, D.B. et al., 1988. In-Cylinder Measurements of Soot Production in a Direct-Injection Diesel Engine. *SAE Paper*, p.880344.

Kittelson, D.B. et al., 1986. Particle Concentrations in a Diesel Cylinder: Comparison of Theory and Experiment. *SAE Paper*, p.861569.

Klell, M., Eichseder, H. & Sartory, M., 2012. Mixtures of hydrogen and methane in the internal combustion engine – Synergies, potential and regulations. *International Journal of Hydrogen Energy*, 37(15), pp.11531–11540.

Kreith, F. & West, R.E., 2004. Fallacies of a Hydrogen Economy. In *Energy Conversion and Resources: Fuels and Combustion Technologies, Energy, Nuclear Engineering*. ASME, pp. 203–219.

Ladommatos, N., Balian, R., et al., 1996. The Effect of Exhaust Gas Recirculation on Combustion and NO_x Emissions in a High-Speed Direct-injection Diesel Engine. *SAE Paper*, p.960840.

Ladommatos, N., Abdelhalim, S. & Zhao, H., 2000. The effects of exhaust gas recirculation on diesel combustion and emissions. *International Journal of Engine Research*, 1(1), pp.107–126.

Ladommatos, N., Parsi, M. & Knowles, A., 1996. The effect of fuel cetane improver on diesel pollutant emissions. *Fuel*, 75(1), pp.8–14.

- Lambe, S. & Watson, H., 1993. Optimizing the design of a hydrogen engine with pilot diesel fuel ignition. *International journal of vehicle design*, 14(4), pp.370–389.
- Larsen, J.F. & Wallace, J.S., 1997. Comparison of Emissions and Efficiency of a Turbocharged Lean-Burn Natural Gas and Hythane-Fueled Engine. *Journal of Engineering for Gas Turbines and Power*, 119(1), p.218.
- Lavoie, G., Heywood, J. & Keck, J., 1970. Experimental and theoretical study of nitric oxide formation in internal combustion engines. *Combustion Science and Technology*, 1(1935), pp.313–326.
- Lee, R., Pedley, J. & Hobbs, C., 1998. Fuel Quality Impact on Heavy Duty Diesel Emissions:- A Literature Review. *SAE Paper*, p.982649.
- Lie, J.A. et al., 2007. Optimization of a membrane process for CO₂ capture in the steelmaking industry. *International Journal of Greenhouse Gas Control*, 1(3), pp.309–317.
- Lilik, G., Zhang, H. & Herreros, J., 2010. Hydrogen assisted diesel combustion. *International Journal of Hydrogen Energy*, 35(9), pp.4382–4398.
- Liu, X. & Kittelson, D.B., 1982. Total Cylinder Sampling from a Diesel Engine (Part II). *SAE Paper*, p.820360.

- Liu, X., Siegla, D. & Kittelson, D., 1984. In-Cylinder NO_x Histories in an Indirect Injection Diesel Engine: Comparisons Between Experimental Data and Model Predictions. *20th International Symposium on Combustion*, pp.45–52.
- Liu, Z. & Karim, G., 1995. Knock characteristics of dual-fuel engines fuelled with hydrogen fuel. *International Journal of Hydrogen Energy*, 20(11), pp.919–924.
- Lively, R.P. et al., 2012. Thermally moderated hollow fiber sorbent modules in rapidly cycled pressure swing adsorption mode for hydrogen purification. *International Journal of Hydrogen Energy*, 37(20), pp.15227–15240.
- LoRusso, J.A. et al., 1984. Electrohydraulic gas sampling valve. *Review of Scientific Instruments*, 55(5), p.786.
- LoRusso, J.A., Lavoie, G.A. & Kaiser, E.W., 1980. An Electrohydraulic Gas Sampling Valve with Application to Hydrocarbon Emissions Studies. *SAE Paper*, p.800045.
- Lovell, W.G., Coleman, J.D. & Boyd, T.A., 1927. Studies of Combustion in the Gasoline Engine 1: II—The Burning of Hydrogen and Carbon Monoxide. *Industrial & Engineering Chemistry*, 19(3), pp.376–378.

- Maizonnasse, M. et al., 2013. Investigation of the degradation of a low-cost untreated biogas engine using preheated biogas with phase separation for electric power generation. *Renewable Energy*, 55, pp.501–513.
- Makareviciene, V. et al., 2013. Performance and emission characteristics of biogas used in diesel engine operation. *Energy Conversion and Management*, 75, pp.224–233.
- Masood, M., Ishrat, M. & Reddy, A., 2007. Computational combustion and emission analysis of hydrogen–diesel blends with experimental verification. *International Journal of Hydrogen Energy*, 32(13), pp.2539–2547.
- Masood, M. & Ishrat, M.M., 2008. Computer simulation of hydrogen–diesel dual fuel exhaust gas emissions with experimental verification. *Fuel*, 87(7), pp.1372–1378.
- Matsui, K., Tanaka, T. & Ohigashi, S., 1979. Measurement of Local Mixture Strength at Spark Gap of S. I. Engines. *SAE Paper*, p.790483.
- Mayer, W.J., Lechman, D.C. & Hilden, D.L., 1980. The Contribution of Engine Oil to Diesel Exhaust Particulate Emissions. *SAE Paper*, p.800256.

- McTaggart-Cowan, G.P. et al., 2009. Combustion in a heavy-duty direct-injection engine using hydrogen–methane blend fuels. *International Journal of Engine Research*, 10(1), pp.1–13.
- Miller, J.A. & Bowman, C.T.C., 1989. Mechanism and modeling of nitrogen chemistry in combustion. *Progress in Energy and Combustion Science*, 15(4), pp.287–338.
- Musculus, M. et al., 2012. A Conceptual Model for Partially Premixed Low-Temperature Diesel Combustion Based on In-Cylinder Laser Diagnostics and Chemical Kinetics Modeling Sandia ’ s diesel conceptual model describes mixing , combustion up to end of injection. In *Directions in Engine-Efficiency and Emissions Reduction Research Conference*. Michigan.
- Mustafi, N.N., Raine, R.R. & Verhelst, S., 2013. Combustion and emissions characteristics of a dual fuel engine operated on alternative gaseous fuels. *Fuel*, 109, pp.669–678.
- Naber, J., 1998. Hydrogen combustion under diesel engine conditions. *International Journal of Hydrogen Energy*, 23(5), pp.363–371.
- Nagalingam, B., Duebel, F. & Schmillen, K., 1983. Performance study using natural gas, hydrogen-supplemented natural gas and hydrogen in AVL research engine. *International Journal of Hydrogen Energy*, 8(9), pp.715–720.

- Nightingale, D.R., 1975. A Fundamental Investigation into the Problem of NO Formation in Diesel Engines. *SAE Paper*, p.750848.
- Ning, M. et al., 1991. Soot Formation, Oxidation and Its Mechanism in Different Combustion Systems and Smoke Emission Pattern in DI Diesel Engines. *SAE Paper*, p.910230.
- Nowak, L. et al., 2008. Methodology development of a time-resolved in-cylinder fuel oxidation analysis: Homogeneous charge compression ignition combustion study application. *Combustion and Flame*, 154(3), pp.462–472.
- Ohdachi, Y. et al., 1991. Optimum design of dynamic response in automotive solenoid valve. *IEEE Transactions on Magnetics*, 27(6), pp.5226–5228.
- Ozasa, T. et al., 1991. Effect of Combustion Chamber Shape on a Lean-Burn S.I.Engine -Measurement of In-Cylinder Mixture Strength Using a Gas Sampling Technique. *JSAE Review*, 12, pp.4–10.
- Palmer, H. & Cullis, C., 1965. The formation of carbon from gases. In P. Walker, ed. *Chemistry and physics of carbon*. New York: Marcel Dekker, p. 205.
- Park, K. et al., 2003. Relationship between Particle Mass and Mobility for Diesel Exhaust Particles. *Environmental Science & Technology*, 37(3), pp.577–583.

- Patterson, T. et al., 2011. An evaluation of the policy and techno-economic factors affecting the potential for biogas upgrading for transport fuel use in the UK. *Energy Policy*, 39(3), pp.1806–1816.
- Pichayapat, K. et al., 2014. Emission characteristics of using HCNG in the internal combustion engine with minimum pilot diesel injection for greater fuel economy. *International Journal of Hydrogen Energy*, 39(23), pp.12182–12186.
- Pipho, M.J. et al., 1992. Injection Timing and Bowl Configuration Effects on In-Cylinder Particle Mass. *SAE Paper*, p.921646.
- Pope, C.A. et al., 2002. Lung cancer, cardiopulmonary mortality, and long-term exposure to fine particulate air pollution. *JAMA*, 287(9), pp.1132–41.
- Raaschou-Nielsen, O. et al., 2013. Air pollution and lung cancer incidence in 17 European cohorts: prospective analyses from the European Study of Cohorts for Air Pollution Effects (ESCAPE). *The Lancet. Oncology*, 14(9), pp.813–22.
- Raheman, H. & Ghadge, S.V., 2007. Performance of compression ignition engine with mahua (*Madhuca indica*) biodiesel. *Fuel*, 86(16), pp.2568–2573.
- Raman, V. et al., 1994. Hythane—an ultraclean transport fuel. In *10th World hydrogen Energy Conference*. Cocoa Beach, USA, pp. 1797–806.

- Rhee, K.T., Myers, P.S. & Uyehara, O.A., 1978. Time- and Space- Resolved Species Determination in Diesel Combustion Using Continuous Flow Gas Sampling. *SAE Paper*, p.780226.
- Ricardo, 1986. *The Ricardo/Cussons Standard Hydra Engine and Test Bed, Details of the Engine, Test Bed, and Control System* 8th ed., England.
- Roblee, L.H.S., 1961. A technique for sampling reaction intermediates in a rapid compression machine. *Combustion and Flame*, 5, pp.229–234.
- Sahoo, B.B., Sahoo, N. & Saha, U.K., 2009. Effect of engine parameters and type of gaseous fuel on the performance of dual-fuel gas diesel engines—A critical review. *Renewable and Sustainable Energy Reviews*, 13(6-7), pp.1151–1184.
- Saravanan, N. & Nagarajan, G., 2008a. An experimental investigation of hydrogen-enriched air induction in a diesel engine system. *International journal of hydrogen energy*, 33(6), pp.1769–1775.
- Saravanan, N. & Nagarajan, G., 2008b. Combustion analysis on a DI diesel engine with hydrogen in dual fuel mode. *Fuel*, 87(17-18), pp.3591–3599.
- Schafer, A., Heywood, J. & Weiss, M., 2006. Future fuel cell and internal combustion engine automobile technologies: A 25-year life cycle and fleet impact assessment. *Energy*, 31(12), pp.2064–2087.

- Schiermeier, Q., 2014. Energy outlook sees continuing dominance of fossil fuels. *Nature News Blog*. Available at: <http://blogs.nature.com/news/2014/11/energy-outlook-sees-continuing-dominance-of-fossil-fuels.html> [Accessed April 22, 2015].
- Schönborn, A., 2009. *Influence of the molecular structure of biofuels on combustion in a compression ignition engine*. PhD Thesis, UCL.
- Seilly, A.H., 1981. Colenoid Actuators - Further Developments in Extremely Fast Acting Solenoids. *SAE Paper*, p.810462.
- Shao, P. et al., 2012. Design and economics of a hybrid membrane–temperature swing adsorption process for upgrading biogas. *Journal of Membrane Science*, 413-414, pp.17–28.
- Shiga, S. et al., 2002. A study of the combustion and emission characteristics of compressed-natural-gas direct-injection stratified combustion using a rapid-compression-machine. *Combustion and Flame*, 129(1-2), pp.1–10.
- Shrestha, S., 1999. Hydrogen as an additive to methane for spark ignition engine applications. *International Journal of Hydrogen Energy*, 24(6), pp.577–586.

- Sierens, R. & Rosseel, E., 2000. Variable Composition Hydrogen/Natural Gas Mixtures for Increased Engine Efficiency and Decreased Emissions. *Journal of Engineering for Gas Turbines and Power*, 122(1), p.135.
- Smith, O.I., 1981. Fundamentals of soot formation in flames with application to diesel engine particulate emissions. *Progress in Energy and Combustion Science*, 7(4), pp.275–291.
- Somerville, R. et al., 2007. *Historical Overview of Climate Change*. In: *Climate Change 2007: The Physical Science Basis. Contribution of Working Group I to the Fourth Assessment Report of the Intergovernmental Panel on Climate Change* S. Solomon et al., eds., Cambridge, United Kingdom and New York, NY, USA: Cambridge University Press.
- Stelmasiak, Z., 2002. The Impact of Gas-Air Composition on Combustion Parameters of Dual Fuel Engines Fed CNG. *SAE Paper*, pp.2002–01–2235.
- Stone, R., 2012. *Introduction to Internal Combustion Engines* 4th ed., New York: Palgrave Macmillan Limited.
- Swain, M.R. et al., 1993. The Effects of Hydrogen Addition on Natural Gas Engine Operation. *SAE Paper*, p.932775.

- Symonds, J.P.R. et al., 2007. Diesel soot mass calculation in real-time with a differential mobility spectrometer. *Journal of Aerosol Science*, 38, pp.52–68.
- Szybist, J.P. et al., 2007. Biodiesel combustion, emissions and emission control. *Fuel Processing Technology*, 88(7), pp.679–691.
- Talibi, M. et al., 2014. Effect of hydrogen-diesel fuel co-combustion on exhaust emissions with verification using an in-cylinder gas sampling technique. *International Journal of Hydrogen Energy*, 39(27), pp.15088–15102.
- Taylor, C.F. & Rogowski, A.R., 1954. Scavenging the 2-Stroke Engine. *SAE Paper*, p.540258.
- Tazerout, M., Le Corre, O. & Rousseau, S., 1999. TDC Determination in IC Engines Based on the Thermodynamic Analysis of the Temperature-Entropy Diagram. *SAE Paper*, pp.1999-01-1489.
- Thi, L.D., Zhang, Y. & Huang, Z., 2014. Shock tube study on ignition delay of multi-component syngas mixtures – Effect of equivalence ratio. *International Journal of Hydrogen Energy*, 39(11), pp.6034–6043.
- Thurnheer, T., Soltic, P. & Dimopoulos Eggenschwiler, P., 2009. S.I. engine fuelled with gasoline, methane and methane/hydrogen blends: Heat release and loss analysis. *International Journal of Hydrogen Energy*, 34(5), pp.2494–2503.

- Tippayawong, N., Promwungkwa, A. & Rerkkriangkrai, P., 2007. Long-term operation of a small biogas/diesel dual-fuel engine for on-farm electricity generation. *Biosystems Engineering*, 98(1), pp.26–32.
- Tomita, E. et al., 2001. Hydrogen Combustion and Exhaust Emissions Ignited with Diesel Oil in a Dual Fuel Engine. *SAE paper*, pp.2001–01–3503.
- Tree, D.R. & Svensson, K.I., 2007. Soot processes in compression ignition engines. *Progress in Energy and Combustion Science*, 33(3), pp.272–309.
- Tricase, C. & Lombardi, M., 2009. State of the art and prospects of Italian biogas production from animal sewage: Technical-economic considerations. *Renewable Energy*, 34(3), pp.477–485.
- Tsolakis, A. & Hernandez, J., 2005. Dual fuel diesel engine operation using H₂. Effect on particulate emissions. *Energy & fuels*, (8), pp.418–425.
- Turns, S.R., 1996. *An introduction to combustion: concepts and applications*, New York: McGraw-Hill.
- Turns, S.R. & Borman, G.L., 1980. Internal combustion engine sampling probes: An experimental study of sample-gas origins and flow disturbances. *Combustion and Flame*, 38, pp.313–327.

- Varde, K.S. & Varde, L.K., 1984. Reduction of soot in diesel combustion with hydrogen and different H/C gaseous fuels. In *5th World Hydrogen Energy, Toronto, Canada*.
- Verbiezen, K. et al., 2007. Diesel combustion: In-cylinder NO concentrations in relation to injection timing. *Combustion and Flame*, 151(1-2), pp.333–346.
- Verhelst, S. et al., 2010. Impact of variable valve timing on power, emissions and backfire of a bi-fuel hydrogen/gasoline engine. *International Journal of Hydrogen Energy*, 35(9), pp.4399–4408.
- Voiculescu, I.A. & Borman, G.L., 1978. An Experimental Study of Diesel Engine Cylinder-Averaged NO_x Histories. *SAE Paper*, p.780228.
- Wallace, J. & Cattelan, A., 1994. Hythane and CNG fueled engine exhaust emission comparison. In *10th World hydrogen Energy Conference*. Cocoa Beach, USA, pp. 1761–70.
- Wang, J. et al., 2009. Numerical study of the effect of hydrogen addition on methane–air mixtures combustion. *International Journal of Hydrogen Energy*, 34(2), pp.1084–1096.
- Weaver, C.S., 1989. Natural Gas Vehicles - A Review of the State of the Art. *SAE Paper*, p.892133.

- Weiland, P., 2010. Biogas production: current state and perspectives. *Applied microbiology and biotechnology*, 85(4), pp.849–60.
- Weiss, A. et al., 2000. *On the road in 2020 A life-cycle analysis of new automobile technologies*,
- Weiss, P. & Keck, J.C., 1981. Fast Sampling Valve Measurements of Hydrocarbons in the Cylinder of a CFR Engine. *SAE Paper*, p.810149.
- Westbrook, C.K., 2000. Chemical kinetics of hydrocarbon ignition in practical combustion systems. *Proceedings of the Combustion Institute*, 28(2), pp.1563–1577.
- Whitehouse, N.D., Clough, E. & Roberts, P.S., 1977. Investigating Diesel Engine Combustion by Means of a Timed Sampling Valve. *SAE Paper*, p.770409.
- WHO, 2006. Air Quality Guidelines Global Update 2005. *World Health Organization*.
- Withrow, L., Lovell, W.G. & Boyd, T.A., 1930. Following Combustion in the Gasoline Engine by Chemical Means. *Industrial & Engineering Chemistry*, 22(9), pp.945–951.

- Würmel, J. et al., 2007. The effect of diluent gases on ignition delay times in the shock tube and in the rapid compression machine. *Combustion and Flame*, 151(1-2), pp.289–302.
- Yanagi, T., 1977. Effects of probe sampling rates on sample composition. *Combustion and Flame*, 28, pp.33–44.
- Yang, L., Ge, X., et al., 2014. Progress and perspectives in converting biogas to transportation fuels. *Renewable and Sustainable Energy Reviews*, 40, pp.1133–1152.
- Yang, L., Wang, X. & Funk, T.L., 2014. Strong influence of medium pH condition on gas-phase biofilter ammonia removal, nitrous oxide generation and microbial communities. *Bioresource technology*, 152, pp.74–9.
- Yates, D.A., 1988. The compact high-speed gas sampling valve for an internal combustion engine. In *IMechE seminar “Experimental Methods in Engine Research and Development.”*
- Yoon, S.H. & Lee, C.S., 2011. Experimental investigation on the combustion and exhaust emission characteristics of biogas-biodiesel dual-fuel combustion in a CI engine. *Fuel Processing Technology*, 92(5), pp.992–1000.

- Yu, R.C. & Shahed, S.M., 1981. Effects of Injection Timing and Exhaust Gas Recirculation on Emissions from a D.I. Diesel Engine. *SAE Paper*, p.811234.
- Zamel, N. & Li, X., 2006. Life cycle analysis of vehicles powered by a fuel cell and by internal combustion engine for Canada. *Journal of Power Sources*, 155(2), pp.297–310.
- Zeldovich, Y., Frank-Kamenetskii, D. & Sadovnikov, P., 1947. *Oxidation of Nitrogen in Combustion*, Publication House of the Academic of Sciences of USSR.
- Zhao, H. & Ladommatos, N., 2001. *Engine combustion instrumentation and diagnostics*, Society of Automotive Engineers, USA.
- Zhao, H., Lowry, G. & Ladommatos, N., 1996. Time-Resolved Measurements and Analysis of In-Cylinder Gases and Particulates in Compression-Ignition Engines. *SAE Paper*, p.961168.
- Zhou, J.H., Cheung, C.S. & Leung, C.W., 2014. Combustion, performance and emissions of a diesel engine with H₂, CH₄ and H₂–CH₄ addition. *International Journal of Hydrogen Energy*, 39(9), pp.4611–4621.
- Zvonow, V.A., 1968. Hydraulically Actuated Combustion Gas Sampling Valve. *Review of Scientific Instruments*, 39(12), p.1820.

The end
